



POLITECNICO DI MILANO

DEPARTMENT OF CHEMISTRY, MATERIALS
AND CHEMICAL ENGINEERING “GIULIO NATTA”

DOCTORAL PROGRAMME IN INDUSTRIAL CHEMISTRY
AND CHEMICAL ENGINEERING

Dendritic amphiphiles for ^{19}F -MRI and gene delivery

Doctoral dissertation of: Marta Rosati

Serial number: 892232

Supervisor: Professor Pierangelo Metrangolo

Tutor: Professor Davide Manca

The Chair of the Doctoral Program: Professor Alessio Frassoldati

2017-2020, Cycle 33

“The important thing in science is not so much to obtain new facts as to discover new ways of thinking about them.” Sir William Lawrence Bragg (1890–1971)

Table of contents

Abstract: Dendritic amphiphiles for ^{19}F-MRI and gene delivery	5
Chapter 1: Introduction	7
1.1 The bases of self-assembly in amphiphiles	7
1.1.1 The critical micelle concentration (CMC) and the molecular packing parameter	8
1.2 Types of amphiphiles: an overview on dendrimers and dendritic architectures	13
1.2.1 Dendrimers and dendritic amphiphiles	15
1.2.2 Fluorinated dendrimers	23
1.3 Gene therapy	25
1.3.1 Gene vectors: concerns and needs	25
1.3.2 Dendritic non-viral vectors: the role of fluorination and the effect of the core on gene delivery efficacy	27
1.4 Magnetic Resonance Imaging and the use of fluorine-19 (^{19}F)	30
1.4.1 Second color MRI: the role of Fluorine-19 (^{19}F)	30
Chapter 2: A new family of polyfluorinated dendritic amphiphiles	37
2.1 Results and discussion	38
2.1.1 Synthesis, purification, and characterization of the new amphiphiles	38
2.1.2 Characterization of FDG_1 , FDG_2 and FDG_3 in bulk	46
2.1.3 Self-assembly of FDG_1 , FDG_2 and FDG_3 in water	52
2.1.4 Molecular Dynamics: FDG_1 , FDG_2 and FDG_3 in comparison	61
2.2 Experimental section	66
2.2.1 Synthesis, purification, and characterization of the new amphiphiles	66
2.2.2 Characterization of FDG_1 , FDG_2 and FDG_3 in bulk	76
2.2.3 Self-assembly of FDG_1 , FDG_2 and FDG_3 in water	78
2.2.4 Molecular Dynamics: FDG_1 , FDG_2 and FDG_3 in comparison	79
Chapter 3: Development of a new ^{19}F-MRI traceable gene delivery vector ..	80
3.1 Results and discussion	81
3.1.1 Synthesis, purification and characterization of FDG_2N	81
3.1.1.1 Chemical and thermal stability of FDG_2N	83
3.1.2 Self-assembly of FDG_2N in aqueous media	86
3.1.2.1 Characterization of the aggregates in solution	89
3.1.3 Nucleic acids complexation	96
3.1.3.1 N/P ratio determination	97
3.1.3.2 <i>In vitro</i> cytotoxicity, transfection efficacy, and dendriplexes characterization	98
3.1.4 Application of FDG_2N as miRNA delivery vector	102
3.2 Experimental section	106
3.2.1 Synthesis, purification procedures and characterization of FDG_2N	106
3.2.1.1 Chemical and thermal stability of FDG_2N	108
3.2.2 Self-assembly of FDG_2N in aqueous media	109

3.2.2.1 Characterization of the aggregates in solution	110
3.2.3 Nucleic acids complexation	112
3.2.3.1 N/P ratio determination	113
3.2.3.2 <i>In vitro</i> cytotoxicity, transfection efficacy, and dendriplexes characterization	113
3.2.4 Application of FDG ₂ N as miRNA delivery vector	114
Chapter 4: Conclusions	116
Pullout	119
Tuning of Ionic Liquid Crystal Properties by Combining Halogen Bonding and Fluorous Effect	
Introduction	120
Results and discussion	122
Experimental section	130
Conclusion	131
References	132

Abstract: Dendritic amphiphiles for ^{19}F -MRI and gene delivery

Dendrimers are a class of highly structured three-dimensional macromolecules characterized by a well-defined periodically branched structure, high monodispersity and tunable size and shape. Among them amphiphilic dendrimers, in which two moieties of different hydrophilicity are covalently linked, can self-assemble in aqueous media generating many different types of aggregates whose morphology strictly depends on the balance between hydrophilic and hydrophobic portions. This allows to control their molecular conformation, the aggregation behavior both in bulk and in solution, and thus the final shape of the aggregate formed. The control of these parameters is important for the emergence of specific functions. A powerful tool for tuning the self-assembly behavior of dendritic amphiphiles and increasing their colloidal stability, also in biological media, is the introduction of linear or branched fluoroalkyl groups in their molecular structure. This enhances their tendency to segregate and influences their molecular supramolecular organization.

In this regard, the search for more sustainable fluorinated materials focused attention on shorter chains perfluorocarbons (PFCs). However, simply cutting down chain length does not lead to satisfactory results in balancing environmental impact and performance. Recently, multibranching superfluorinated derivatives obtained high attention since they combine good biocompatibility with performances assimilable to classical PFCs. Moreover, the presence of a high number of equivalent fluorine atoms in their structure renders them excellent ^{19}F -Magnetic Resonance Imaging (^{19}F -MRI) probes.

We decided to exploit the advantages of branched fluorinated chains to generate new polyfluorinated amphiphilic dendrimers suitable for gene delivery and traceable by ^{19}F -MRI, thus obtaining new theranostic systems.

Firstly, this thesis gives an overview on the literature with particular attention to amphiphiles, especially dendritic amphiphiles. Moreover, an introduction on ^{19}F -MRI probes and gene delivery vectors is also reported relative to the proposed application of the reported derivatives.

Subsequently, synthesis and characterization of new polyfluorinated dendritic amphiphiles of different generations are discussed reporting on their properties both in bulk and in solution. We observed that the self-assembly of these molecules is strictly dependent on their generation, and that we are able to tune the aggregate shape with consequent change in the magnetic relaxivities of the fluorine nuclei.

Gene delivery has become a powerful tool to treat diseases. The need to protect and deliver nucleic acids into cells requires the use of biocompatible and efficient vectors. Among those reported in literature, fluorinated dendrimers attracted high interest since they were shown to improve vector stability and enhance gene endosomal escape. Therefore, the chemical structure of the polyfluorinated dendritic amphiphiles was modified for promoting the interaction with nucleic acids. It has indeed been reported that fluorination can stabilize the formation of complexes with genes for similar compounds and facilitate their intracellular release. In this regard, the synthetic approach adopted here and the chemical characterization of the obtained derivative are discussed. Furthermore, self-assembly behavior in aqueous media of the obtained derivative is described with particular attention to the characterization of shape and stability of its aggregates. Finally, gene complexation ability and transfection efficiencies of the new dendritic vector are presented.

In the last part of this thesis, here referred as pullout, the results obtained from another project, in which the effects of fluorination on the self-assembly of small molecules are discussed. Here the tendency of fluorinated moieties to microsegregate is combined with the high directional effect driven

by halogen bond to tune the liquid crystal phase and thermal stability of new ionic liquid crystalline materials. In this final section the syntheses, crystal structures, and thermal properties of these new ionic liquid crystals are treated.

1 Introduction

1.1 The bases of self-assembly in amphiphiles

Nature shows us how self-assembly is fundamental in our lives, but what does self-assembly means? The term is composed by “assembly” which refers to put together and “self” which means on its own: therefore, it refers to the ability of isolated systems, which can be atoms, molecules, or macromolecules, to spontaneously aggregate and generate new higher complex structures thanks to the interactions that occur between single building blocks [1].

The tendency to self-assemble is characteristics of amphiphiles. The term was introduced for the first time by Hartley in 1936 to describe molecules which contain two distinct thermodynamically incompatible moieties covalently linked together; the term derives from Greek where *amphi* means “both” and *phile* means “like”[1]. Generally, the incompatibility between the two parts is due to their different solvophilicity. The simplest structure of an amphiphile shows the presence of a polar and hydrophilic part, called head, connected to an apolar and lipophilic part, called tail. The head can be neutral or ionic. In literature both cationic, anionic and zwitterionic tails are reported: the term zwitterionic refers to tails which contain both cationic and anionic centers as head groups. The different types of head groups are shown in figure 1.1. The tail can be a hydrocarbon or a fluorocarbon chain [1][2][3].

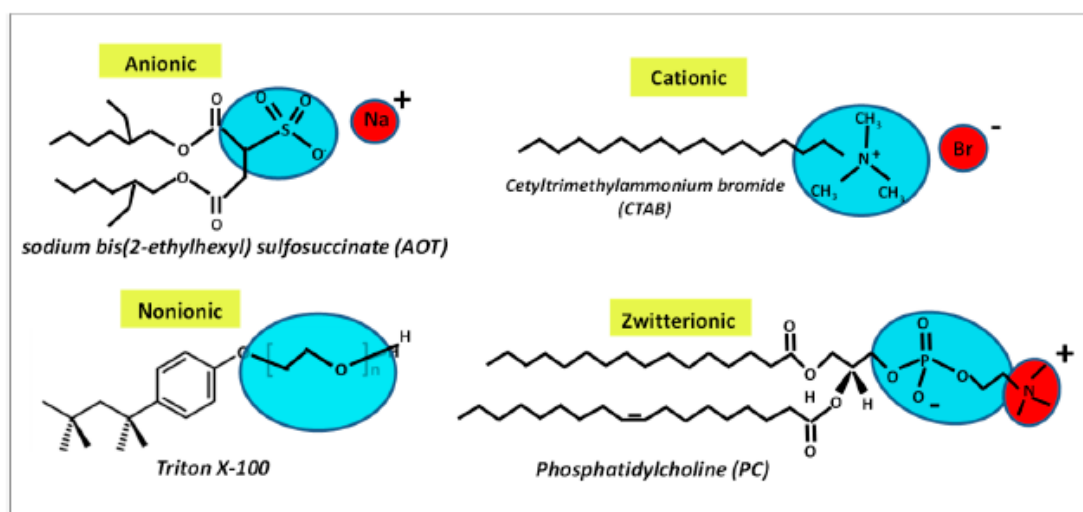


Figure 1.1 Examples of traditional ionic (cationic, anionic and zwitterionic) and nonionic head groups in classical amphiphiles, reprinted with permission from [4].

In polar solvents, such as water, for example, amphiphiles tend to adsorb at interfaces (i.e., the air-water interface), and above a certain concentration, called critical micelle concentration (CMC) better described in section 1.1.1, they tend to spontaneously self-assemble in aggregates whose morphology depends on the structure of the amphiphile.

The formation of the aggregates in water is due to both enthalpic and entropic contributions. One of the factors affecting the self-assembly is the “hydrophobic effect” [2], [5]–[7].

The hydrophobic effect is fundamental in many soft matter systems since it regulates the tendency of nonpolar molecules to self-aggregate [2]. The process is entropically driven at low temperatures: due to the rupture of the network of hydrogen bonds between the water molecules that surround the aggregates, water moves away from the large solute and forms an interface similar to that between liquid and vapor [11] which causes the reaching of a higher level of disorder. Aggregates are held

together thanks to weak noncovalent interactions which includes hydrogen bonding, hydrophobic effects, electrostatic interactions, and van der Waals forces. Table 1.1 shows the energies involved in the formation of these interactions which generally are lower than covalent bonds. The soft nature of these interactions makes possible to manipulate the morphology of these assemblies simply modifying solution conditions such as pH, temperature, concentration of the amphiphile and ionic strength of the solvent [2], [8]–[10].

Table 1.1 Strength of the interactions involved in the formation of aggregates in amphiphiles [2].

Type of interaction	Energy (kJ/mol)
Covalent bond	100–400
Ion-ioni/ion-dipole/dipole-dipole	200–300/50–200/5–50
Hydrogen bond	4–120
Cation-n(π) interaction	5–80
π-π interaction	0–50
Van der Waals interaction	0-5
Metal-ligand	0–400

The stability of the aggregates in solution is even ascribable to hydration of hydrophilic headgroups, reached by the formation of new hydrogen bonds among water molecules around the amphiphilic aggregate, and interactions among head groups at the amphiphile surface. The latter includes short range interactions, repulsive steric forces and electrical interactions. In case of neutral amphiphile the van der Waals interactions dominate, while electrostatic interactions became predominant in ionic amphiphiles [2][8][9].

1.1.1 The critical micelle concentration (CMC) and the molecular packing parameter

The International Union of Pure and Applied Chemistry (IUPAC) defined the CMC as the “relatively small range of concentrations separating the limit below which virtually no micelles are detected and the limit above which virtually all the additional surfactant forms micelles” [11]. In an amphiphile solution the system reaches a dynamic equilibrium in which the monomeric form of the amphiphile coexists with the aggregate with a continuous exchange between the two forms; the lifetime of a molecule in a small micelle is between 10^{-5} and 10^{-3} seconds [2]. For commonly used surfactants the CMC is typically less than about 0.01M; table 1.2 shows the CMC values of some of the classical surfactants [12]. Generally, CMC values are not only affected by the structure of the surfactant, but also by presence of electrolytes in solution, nature of counterions (for ionic surfactants), presence of other organic compounds in solution, and temperature [3]. The larger the hydrated radius, the weaker is the degree of binding: the presence of electrolytes in solution usually affects CMC values for ionic amphiphiles which tend to decrease by increasing ionic strength. The depression of CMC is mainly due to the shielding of the ionic head groups with a consequently decrease in electrical repulsion between them in the aggregate. Even presence of other organic molecules, such as for example proteins, can affect CMC: this is mainly due to modification in the solvent-aggregate interaction pattern or to internalization of the organic compounds in the aggregate. CMC is also affected by temperature. This is mainly caused by a balance of two opposing effects: one is decrease of hydration of the hydrophilic groups, which favors micellization, and the other is disruption of the structured

water surrounding hydrophobic groups, due to a higher mobility of the water molecules, which prevents micellization [3][13].

Table 1.2 CMC values in distilled water of some classical surfactants at 25°C [12].

Surfactant	Name	Abbreviation	CMC (mM)
Anionic	Sodium dodecylsulfate	SDS	8.20
Cationic	Dodecyltrimethylammonium bromide	DTAB	14.6–16.0
	Tetradecyltrimethylammonium bromide	TTAB	3.60–3.72
	Cetyltrimethylammonium bromide	CTAB	0.92–1.00
Nonionic	Triton X-100	TX-100	0.24–0.27
	Octaethylene glycol monododecyl ether	C ₁₂ E ₈	0.11
	Tetraethylene glycol monododecyl ether	C ₁₂ E ₄	0.064

The reach of the CMC in amphiphiles solution strongly affects the physicochemical properties of the solution, like, for example, its turbidity, surface tensions, and electrical conductivity. These changes are at the bases of some of the techniques used in the CMC determination.

Micelles are the simplest aggregates obtainable by an amphiphilic molecule, polar groups of the amphiphile tend to isolate hydrophobic tails partly or completely from water. Generally, the radius of a micelle is approximately equal to the length of the micelle-forming compound, and normally the number of molecules per micelle is between 10 and 100 nm [14].

Other than micelles, in literature are reported several types of morphologies for amphiphiles' aggregates: these include vesicles [1], disks, toroids [15], fibers [16], reversed micelles [17], and other structures [3][15][18].

Is there a link between molecular structure of the amphiphile and shape of the aggregates? The molecular packing parameter has been introduced by Israelachvili, Mitchell, and Ninham [19] and allows to predict the size and shape of an aggregate starting from a combination of molecular packing considerations and thermodynamic principles. The molecular packing parameter or critical packing parameter (c.p.p) is defined as follow:

$$c.p.p = \frac{v_0}{al_0} \quad \text{Equation 1.1}$$

where v_0 and l_0 are respectively the volume and length of the hydrophobic tail of the amphiphile, while a is defined as the polar head area per molecule [20].

Based on a series of geometrical considerations, it is possible to correlate the shape of an aggregate to the value of the critical packing parameter. Let us consider spherical micelles as an example: the total volume of a spherical aggregate of radius R composed of N amphiphilic molecules is $V = Nv_0 = 4\pi R^3/3$, where v_0 is the volume of a single molecule. Similarly, the surface area of the core $A = Na = 4\pi R^2$, and hence from simple geometrical relation $R = 3v_0/a$, where a is the area per molecule. If the micellar core is packed with amphiphilic tails without any empty space, the radius R cannot exceed the extended length of the tail (l_0). If this limit is inserted in the formula of the radius just discussed and then, inserted into the formula of the packing parameter, its value cannot exceed 1/3. Based on similar geometrical relations together with the constraint that at least one dimension of the aggregate cannot exceed l_0 , it is possible to extrapolate the connection between molecular packing parameter and aggregate shape shown in figure 1.2 [1].

The simplest aggregates which can be obtained are spherical shaped aggregates, i.e., micelles, which generally have a diameter in the range of 5-10 nm. The surfactant which self-assembles in micelles

generally shows a high surface area of hydrated groups that exceeds the diameter of the hydrophobic tail, these types of surfactants are considered as cone shaped.

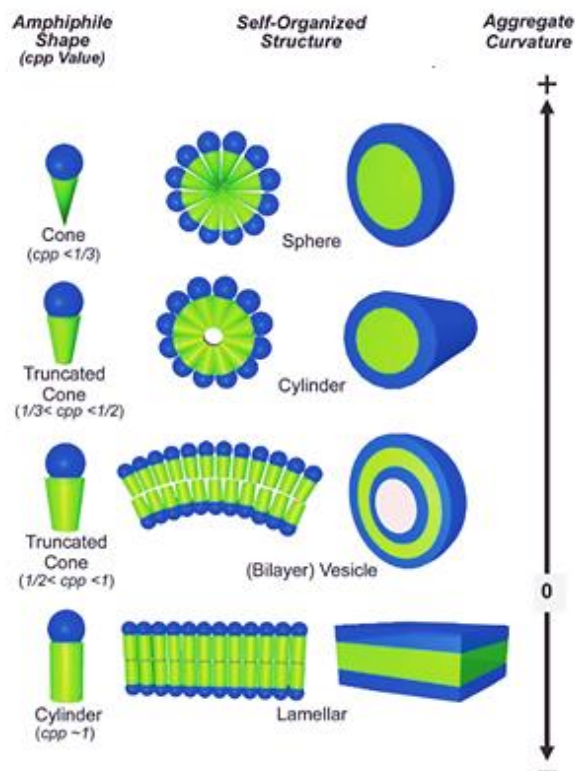


Figure 1.2 Shape of the amphiphilic molecules and c.p.p values related to the preferred aggregate structures, listed in order of decreasing curvature. Reprinted with permission from [1].

The formation of wormlike micelles is generally obtained thanks to a reduction in the surface polar area which facilitates closer packing of the molecule. In water amphiphiles showing head group surface areas similar to the cross section of the hydrophobic chain can aggregate by forming bilayers: vesicles are bilayers with a small curvature. Vesicles can be single layer, already known as unilamellar, or multi layers, as shown in figure 1.3, with an overall diameter between 10 nm to several micrometers [1].

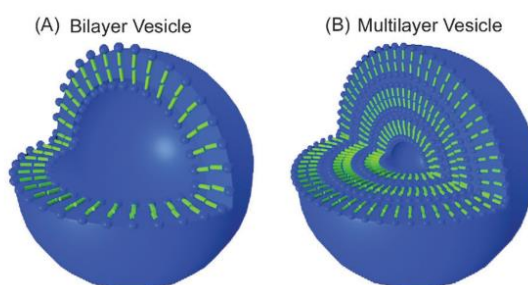


Figure 1.3 Cartoon representation of the vesicles' morphology in water media. **A)** Bilayer vesicles. **B)** Multilayer vesicles. The hydrophobic tails of two surfactants face each other while their polar groups are externally exposed; this generates an alternance of a hydrophilic layer with a hydrophobic one. Both the inner and the outer layers are hydrophilic; therefore, vesicles accommodate the water media in their internal core, reprinted with permission from [1].

Vesicles are composed of repeated molecular pairs of amphiphiles facing each other with hydrophobic tails.

Therefore, since polar groups are externally exposed, in both sides of the vesicles there is a polar environment [1][3].

Vesicles are usually thermodynamically nonequilibrium systems which can however be kinetically stable over quite long periods of time: size, polydispersity and type of vesicles obtained depend not only on surfactant structure, but also on method of preparation. Classical phospholipid vesicles are obtained by inducing the rupture of a lamellar phase dispersed in an excess of water. Generally, this method leads to small metastable vesicles with a wide size distribution. It is possible to obtain vesicles diluting a solution containing lamellar phase. Another methodology requires the fast injection in water of an organic solution of the amphiphile. Generally this method affords to giant vesicles with micrometer sizes.[1].

The stability of a vesicle is directly correlated to the stabilization of its curvature both in inner and outer sides. When this balance is perturbed, a morphological transition can occur [21]. It is reported that morphological transitions can happen altering solvent composition, temperature, pH and ionic strength, or by addition of additives to the aggregate solution [22][23][24][25]. Vesicles have been gained particular attention because they are at the base of many biological processes, which involve membrane fusion such as fertilization, synapse release, intercellular traffic, and viral infection [26][27]. Mechanisms of fusion have been studied by coarse-grained model and molecular dynamics simulations [27][28][29]. Fusion starts with an interaction between two vesicles followed by the formation of a stalk which fast evolves in a hemifusion diaphragm in which the hydrophobic tails of the surfactants in the two aggregates start to interact. This is only a metastable intermediate which then collapse to a complete fusion of the bilayer after the formation of a small fusion pore, from which water can enter between the hydrophobic tails of the two interacting aggregates, as shown in figure 1.4 [28][29]. The vesicles fusion generates bigger vesicles which can interact each other and generate new morphologies such as tubes, nanosheets and nanoribbons [24][30][31].

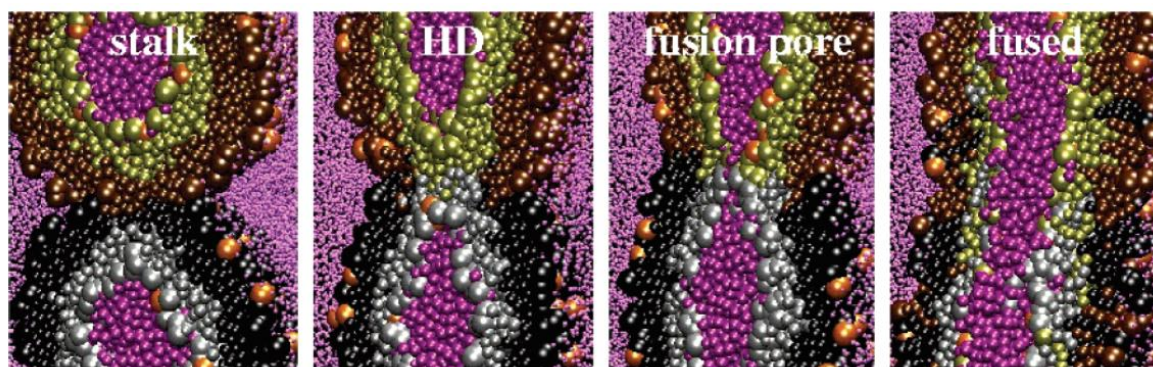


Figure 1.4 Images obtained by the in-silico simulation of two vesicles fusion. Lipid headgroups are represented by large spheres, different colors distinguish between lipids in the inner and outer monolayer and between the two vesicles. The first step is the formation of a stalk as a first interaction between vesicles; then, this quickly evolves to the hemifusion diaphragm where the hydrophobic tails of the two vesicles start to interact. Finally, after the formation of a first fusion pore in which water (purple spheres) starts to perturb the hydrophobic interactions, there is the completion of the fusion process. Reprinted with permission from [28].

In a paper published in 2013 Limin Zhai and coworkers [32] showed how aggregates obtained mixing an aromatic anion, 2-Phenylbenzimidazole 5-sulfonic acid (PBSA), with cationic alkyltrimethyl ammonium bromide of two different chain lengths (CTAB) were able to undergo a morphological evolution over time converting from vesicles to nanotubes [32].

Vesicles are isotropic structures composed by units of cuplike molecular pairs; while nanotubes are anisotropic and should be characterized by configurations of two different curvatures where one is

cylinder-like with curvature close to zero and the other is cuplike at crosswise with a high curvature close to those of micelles. Therefore, transformation from vesicles to nanotubes is strictly connected to a rearrangement of molecular pairs; one of the two interacting ions should have two different conformations which induce this reorganization. In fact, PBSA is a flat molecule, and its configuration is different depending on the side by which the molecule is placed, as shown in figure 1.5.

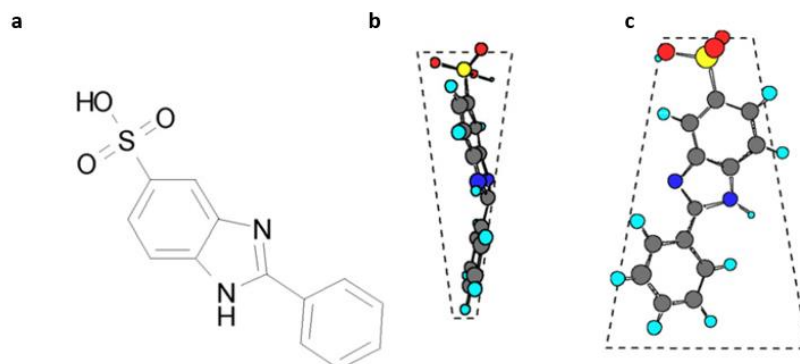


Figure 1.5 a) Structure of 2-Phenylbenzimidazole 5-sulfonic acid (PBSA), b) narrow-sided PBSS (cup-like) conformation; c) broad-sided PBSS (reverse cup-like) conformation, reprinted with permission from [32].

As schematically reported in figure 1.6, when the two configurations are randomly arranged, there is formation of large cuplike structure which form isotropic vesicles with small curvature. Otherwise, when the cylinder-like conformations are arranged side by side, the curvature of the bilayer will be close to zero while on the vertical side the curvature will be close to those of micelles: this leads to the formation of nanotubes.

The transition does not require further energy since it happens spontaneously during time; this suggested that the vesicles obtained are metastable morphologies, while nanotubes are the thermodynamic stable configurations. In nanotubes the mobility of the molecules is highly reduced and this has been confirmed by the extenuation of the NMR signals of the aggregates after the nanotubes' formation [32][33]. Generally, the aggregates transitions require high directionality and involve the self-adjustment of the hydrophobic tail, π - π stacking interactions, and intermolecular hydrogen bonds [30][34].

Is there a way to control the shape of the final aggregate? In literature are reported some examples of transition from vesicles to tubes, and, finally, ribbons [24][30][31]: the transition can be controlled by varying amphiphile concentration [30], temperature [32] or composition of the solvent [24]. Increase in the amphiphile concentration and temperature normally cause an increase in the transition rate, thus favoring the highest thermodynamically stable conformation. The modification of the polarity of the solvent, induced by the addition of an organic water miscible solvent, or the modification of the composition of the solvent can change the energies involved in the stabilization of the amphiphile in water thus influencing the final shape of the aggregate [24][31].

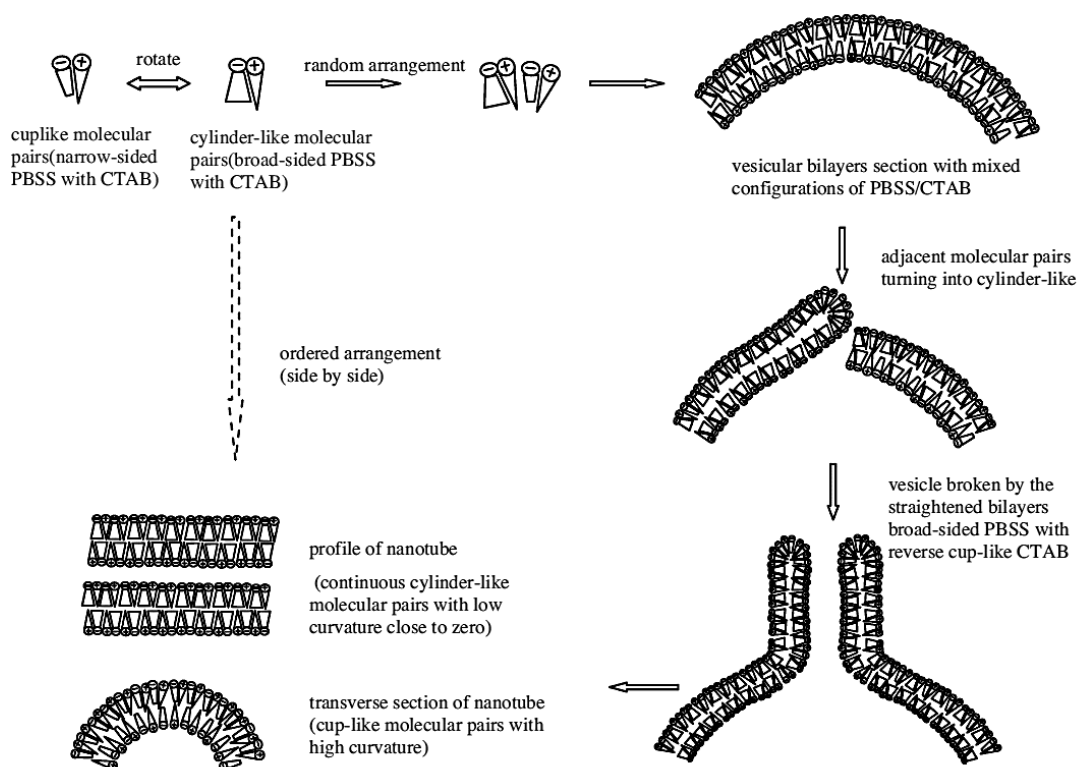


Figure 1.6 Schematic representation of nanotubes formation through the rearrangement of molecular pairs. The symbols “+” and “-” represent cetyltrimethylammonium bromide (CTAB) and PBSS, respectively. Reprinted with permission from [32].

1.2 Types of amphiphiles: an overview on dendrimers and dendritic architectures

The simplest amphiphilic structure consists of a hydrophobic chain covalently linked to a polar head group which can be ionic, nonionic or zwitterionic. This type of amphiphile is called single tailed. Often, amphiphilic compounds possess a more complicated structure and several examples of double tailed amphiphiles, gemini amphiphiles, bolaform amphiphiles and tripod amphiphiles have been reported in literature [2][3][35]. Figure 1.7 reports a schematic representation of the structure of some amphiphilic species. In double tailed surfactants, two hydrophobic chains are covalently linked to a polar head; instead, when the surfactant contains two hydrophobic chains and two hydrophilic groups it is called gemini. Amphiphilic molecules can show two head groups joined by hydrophobic spacers, these are called bola-amphiphiles or bolaforms. The tripods contain a branch point within the hydrophobic portion or within both hydrophobic and hydrophilic portions. The presence of a branch point, particularly when it is a quaternary center, provides a subtle restriction on conformational mobility relative to linear molecular fragments [35].

In gemini amphiphiles the two closer hydrophobic chains give a more compact molecular packing configuration that induces a considerably lower surface tension. This class of compounds shows intriguing properties such as submicellar aggregation and formation of thread-like micelles. Moreover, they generally have CMCs about two orders of magnitude lower than CMCs of analogue single chain surfactants [2]. The presence of two hydrophilic water-soluble groups at both ends of bolaforms yields to higher water solubilities, i.e., an increase in CMC, and a decrease in the aggregation number with respect to traditional single-headed amphiphiles. Other than classical spherical micelles, cylinders, disks and vesicles, bola amphiphiles can form helical structures from which microtubular assemblies can be produced [2].

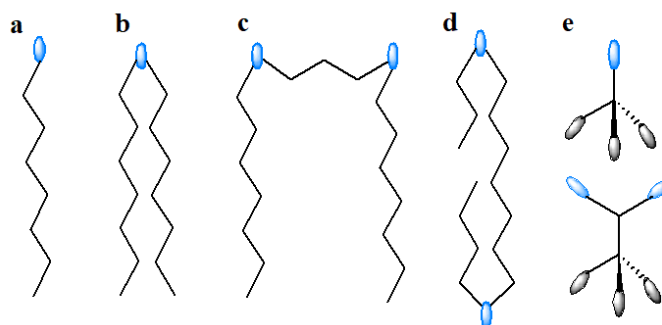


Figure 1.7 Schematic structure of classical amphiphiles: **a)** single tailed amphiphiles, **b)** double tailed amphiphiles, **c)** gemini amphiphile, **d)** bolaform amphiphiles and **e)** tripod amphiphiles. Reprinted and modified with permissions from [2] and [35].

The high potentialities of amphiphilic compounds in terms of applications prompted a strong interest in producing a huge variety of amphiphilic systems and in better understanding their self-assembling behavior. They can be mainly divided in two classes: molecular and macromolecular amphiphilic compounds. When the number of atoms in the amphiphile becomes high (major than 10^2 atoms), the complexity of the amphiphile increases and the number of possible morphologies enormously raises due to a simple combinatorial effect [36].

Depending on the characteristics of the polymers, it is possible to distinguish between four classes, which are highlighted in figure 1.8 [37].

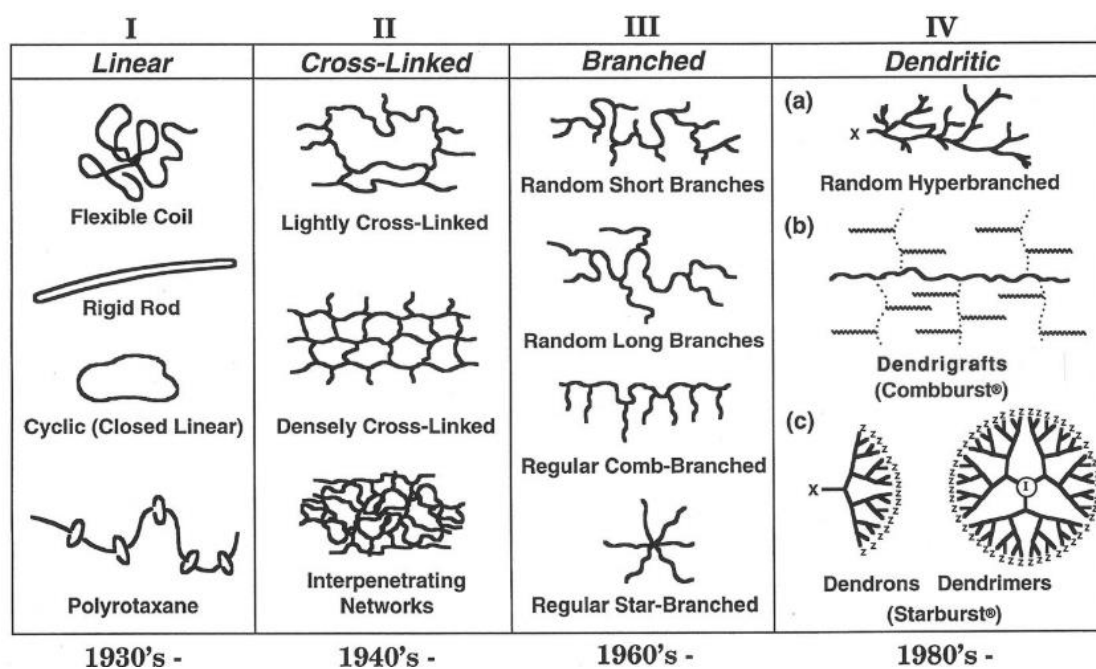


Figure 1.8 Four major classes of macromolecular architectures known to date together with the date of their first appearance, reprinted with permission from [37].

The first class of macromolecules is represented by classical linear polymers which generally possess two end-groups per molecule and a broad molecular weight distribution. The second class involves cross-linked macromolecules which generally are insoluble substances, but which can show network swelling due to penetration of the solvent. The third class includes branched polymers which show a number of end-groups per molecule higher than linear polymers. These macromolecules generally occupy smaller molecular volumes and their viscosities are generally lower than those of linear

polymers with identical molecular weight and composition. The fourth class involve macromolecules which show in their structure one or more dendritic moieties [34].

While mobility of linear polymers increases with their molecular weight, dendrimers are extremely flexible at low generations and increasing their dimension form higher compact and non-compressible globular shapes. This different behavior between linear and dendritic systems is at the base of the different properties shown by these two families. Generally, solubility of linear polymers decreases with the molecular weight; on the contrary, thanks to their branched architecture, dendrimer solubility linearly increases with generation. Another difference between linear and dendritic polymers is viscosity, which for the linear ones increases with molecular weight while for dendrimers it follows a gaussian behavior: in fact, initially it increases with the increasing of the molecular weight till to a maximum after which it returns back to a minimum [37].

1.2.1 Dendrimers and dendritic amphiphiles

Structure and synthesis of dendrimers

Dendrimers are the most recently introduced members of the polymers' family. In fact, first works about dendrimers were introduced by the groups of Vögtle, Denkewalter, Tomalia and Newkome between 1970s and 1980s [38]. The term dendrimer is strictly related to their structure which resembles a tree (*dendra* from Greek) and is referred to a polymeric structure where multiple branched monomers originate from a central core. As shown in figure 1.9, each dendrimer is composed by branched subunits called dendrons whose number depends on the multiplicity of the central core (N_c).

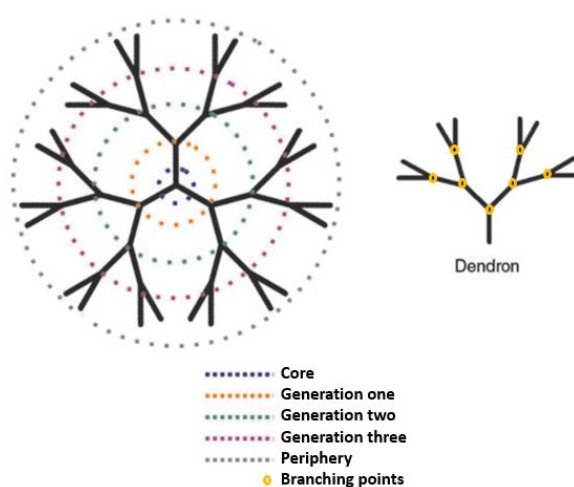


Figure 1.9 Scheme of a dendrimer structure. A dendrimer is composed by the linkage of a certain number of dendrons linked together by a branched inner core. The number of branching points defines the generation of the dendrimer. Reprinted and modified with permission from [38].

A dendron can be divided in three regions: core, branches, and periphery, already called end groups. The number of branches (N_b) extending from the core to the periphery of the dendron defines its generation (G_1, G_2, G_n). Depending on number of branching, the masses increase by the same factor, the volumes of the molecules increases cubically, and the number of surface groups (Z) increases accordingly to the expression: $Z = N_c N_b^G$, where N_c , N_b and G are multiplicity number of core, number of branching points and generation number, respectively [38].

The synthesis of dendrons and dendrimers can be done by iterative convergent or divergent methods, whose chemistry strictly depends on chemical nature of the molecules; figure 1.10 shows a schematic

representation of the two methodologies [38][39]. The divergent approach is an exponential-like growth; in fact, a branched core is iteratively decorated with branching units (AB_n). This method allows the isolation of monodisperse dendrons at low generation, while, by increasing the generation number, due to higher steric hindrance of the periphery, imperfect branching and some polydispersity may be unavoidable. Furthermore, with the increase in generations, the probability of side reactions increases accordingly. Therefore, the convergent method is most frequently used for the synthesis of dendronized topologies. This method requires the linkage of periphery units to AB_n branching units: this gives the formation of dendrons in which the number of total branches increases by a factor equal to the number of branches introduced in each branching unit. Since the total number of attachments per iteration is small, dendrons synthesized with this method can be obtained as monodisperse species with a perfect branching even at high generations. Often, the convergent approach makes difficult the assembly of high generation dendrimers due to steric issues surrounding the reactions of dendrons with the multifunctional core [40].

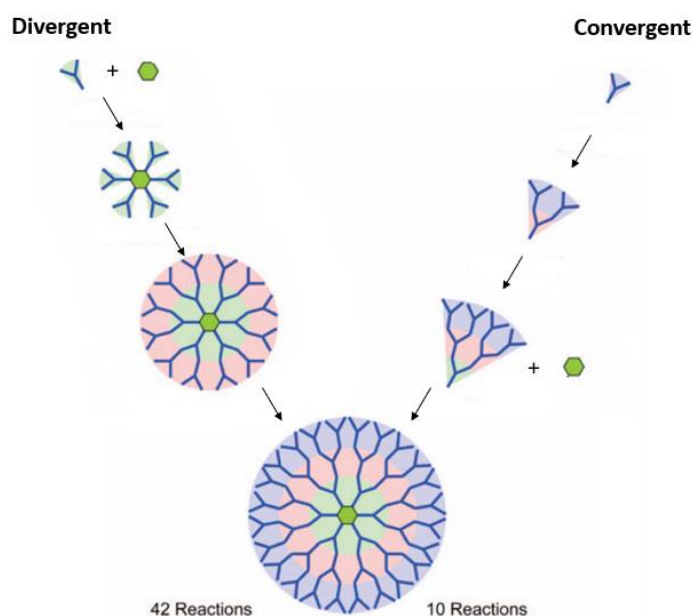


Figure 1.10 Schematic representation of the convergent and divergent synthesis of dendrimers and dendrons, reprinted and modified with permission from [39].

Types of dendrimers

In literature are reported several different dendritic structures, which can be classified by the characteristics of the monomer that is iteratively repeated in the dendrimer architecture. The monomers generally used are bifunctional moieties described as AB_n , where n is the number of branches introduced by each monomer. The A moiety is the functional group of the monomer which is connected in the *endo*-direction, toward the core of the dendritic structure, while the B domain projects in the *exo*-direction toward the periphery. The major number of dendritic structures reported in literature are composed of monomers whose branches (n) can be 2, 3, 4 or 5.

As shown in figure 1.11, since the first family of poly(propylene imine) (PPI) dendrimers, reported by Vögtle in 1978, several different other architectures with new morphologies appeared. Some of common types of dendrimers are based on polyamidoamines, polyamines, polyamides, polypeptides, polyesters, and poly(aryl ethers) or Percec-type dendrimers which have been firstly introduced in 1989 and represent the first example of self-assembling dendrons [38][39].

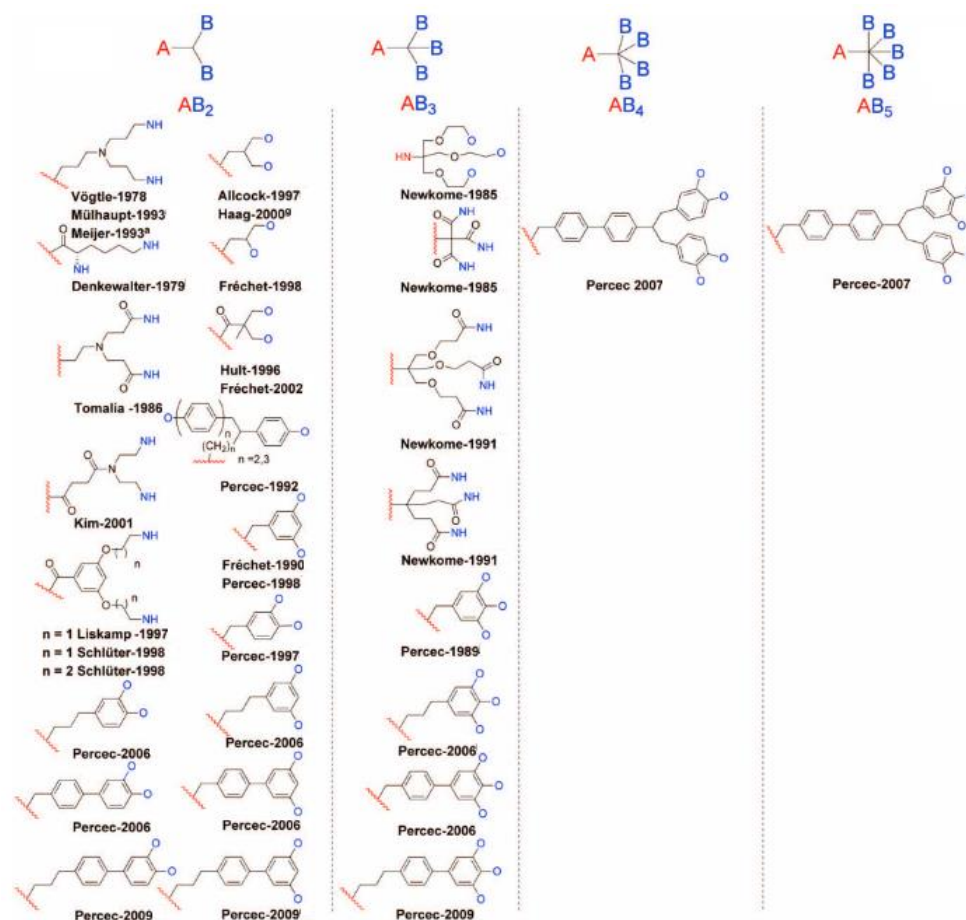


Figure 1.11 Examples of the AB_n monomers used for the constructions of self-assembling dendrons and self-organizable dendronized polymers [39].

Dendritic effect and correlations between primary, 2D and 3D structures of dendrimers

In 1825 Jacob Berzelius introduced the concept of *molecular isomerism* which states that substances with identical elemental composition, but different architectural isomerism differ in one or more properties. As already discussed at the beginning of this section, it has been found that chemically identical linear and dendritic polymers show different behaviors. This caused the introduction in 1996 of the concept of *macromolecular architectural isomerism*, which simply states that macromolecular substances containing identical building blocks in equivalent proportion, but in different architectural configurations may be expected to manifest differentiated behavior and properties [37]. Accordingly to this definition and thanks to the work of Percec and Rosen together with observation of the behavior of other reported dendritic architectures, it has been becoming even clearer that dendrimers show physico-chemical property patterns (density, glass transition temperature, self-assembly behavior and hydrodynamic diameter, and rheological properties) that are strictly dependent on their generation. On the other hand, the chemical structure can be used to tune these properties. This generational dependency is known as *dendritic effect* [37][39][41][42][43]. This gives the possibility to predict the physico-chemical behavior of dendrimers considering size, shape, surface/interior chemistry, and flexibility/compressibility. All these parameters are included in the *critical nanoscale design parameters (CNDPs)*, which are used to predict the final properties of a dendrimer.

In 2009 Percec and coworkers tested a huge number of AB_2 and AB_3 derived poly(aryl ethers) dendron libraries and, thanks to a combination of techniques, they introduced the first examples of Mendeleev-like, predictive Nano-Periodic Tables for self-assembly of aryl ether dendrons [39][41].

They found that, similarly to proteins, the primary structure of a dendrimer affects the tertiary and quaternary overall structures. On the base of the obtained results, they introduced some specific parameters useful to describe the shape of dendrons and reflecting their arrangement in bulk and solution. One of these parameters is the molecular taper angle (α'), which is defined as the projection of the solid angle α of a dendron on a plane and which is inversely proportional to the aggregation number, i.e. the number of dendrons necessary to construct a specific morphology in bulk, as shown in figure 1.12 [37][42]. Increasing the generation number, the molecular taper angle changes typically generating a transition from lamellar to columnar and, finally, to spherical self-assemblies. In fact, raising the generation number reduces the number of dendrons required to form a supramolecular sphere and the cross section of a supramolecular column. Deviations from this pattern usually indicates hollow structures or novel mechanisms of self-assembly [41].

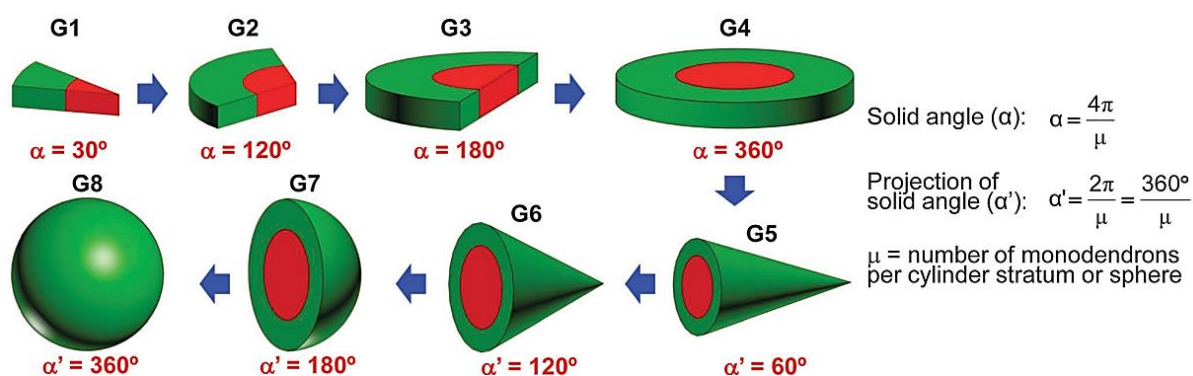


Figure 1.12 The emergence of a single sphere dendron from tapered or conical dendrons and the correlation with the projection of the solid angle (α'), reprinted with permission from [42].

Self-assembly of amphiphilic dendrimers in water and the correlation of their shape to their morphology in bulk

Dendritic amphiphiles have gained particular interest because of their advantageous features which combine characteristics of both polymeric and small molecular systems; in fact, they are as highly stable as polymeric assemblies and display membrane properties similar to small molecule assemblies. This led to the appearance in literature of several different dendritic amphiphilic architectures, which are dendrimers, Janus dendrimers, hybrid dendritic architectures like for example dendronized polymers, linear–dendritic polymers, dendritic–linear–dendritic polymers, as shown in figure 1.13.

These systems are able to self-assemble in aqueous media generating different morphologies, which include micelles, larger micelles (with diameters close to hundreds of nanometers), disk-like micelles, tapes, fibers, toroids, tubes, single layer and multi layers vesicles, and onion-like morphologies which are strictly dependent on morphology of the monomer and environment (solvent, temperature, and method of preparation) [34].

An interesting class of dendritic amphiphiles is those composed by Janus dendrimers [44][45][46]. A Janus dendrimer is formed by the linkage of two distinct dendritic building blocks, generally with different solvophilicity, this allows the formation of structures which are not spherical shaped as the classical dendrimers [44]. The dispersion of these molecules in water can be done by different methodologies, one of these requires the direct injection in water of a solution of the dendrimer in a water-miscible solvent, which can be an alcoholic or non-alcoholic solvent such as acetone, methyl ethyl ketone (MEK), 1,4-dioxane, tetrahydrofuran (THF), and acetonitrile.

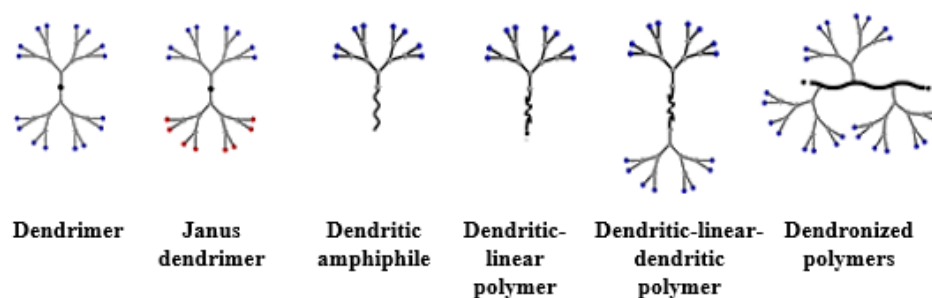


Figure 1.13 Schematic representation of different dendritic architectures present in literature, reprinted and modified with permission from [34].

Other methodologies can be based either on a reverse injection of water into a solution of the dendrimer in the previously mentioned organic solvent or on the film hydration method. Depending on the used solvent and applied method, the aggregates can change their dimensions, normally increasing by moving from direct injection to the last mentioned [44][46]. Percec synthesized a huge number of Janus dendrimers which were able to self-organize in water by generating different morphologies, as shown in figure 1.14.

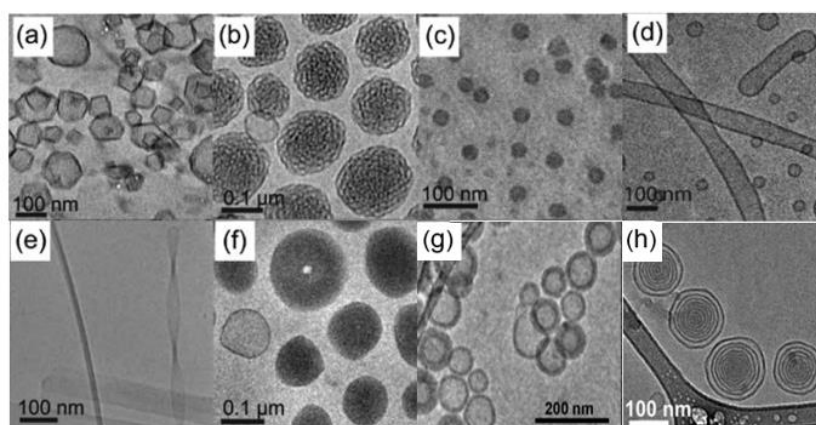


Figure 1.14 Janus dendrimers self-assembled aggregates observed in water: **a)** polygonal dendrimersomes, **b)** biscontinuous cubic particles, **c)** micelles, **d)** tubular dendrimersomes, **e)** rodlike, ribbon and helical micelles, **f)** disklike micelles and toroids, **g)** multilayers vesicles or dendrimersomes, and **h)** onion-like vesicles [44][46][47].

Comparing morphologies in bulk with aggregates observed in water and determining their dimension and shape, some important observations can be done, which are useful for the predictive determination of self-assembling behavior of Janus dendrimers. As shown in table 1.3, generally large majority of Janus dendrimers that form in solid-state lamellar phases self-assemble in water forming vesicles, also called dendrimersomes. This is due to a minor tendency of these systems to form structures with high curvature, which require a larger penalty to their free energy minimum. Otherwise, structures which form columnar or cubic phases in bulk tend to self-organize in micelles in water due to the higher tendency of the chemical structure of the amphiphilic Janus dendrimer to form structures with larger surface curvature. Deviations from this behavior can be seen and can be related to the interaction with water that provides additional energy needed to compensate for the formation of surfaces with smaller curvature, interactions that are absent in solid state [45].

Furthermore, it has been demonstrated that diameters of self-assembled aggregates increase with dendrimer concentration and, in case of dendrimersomes, even the number of layers increases with

the concentration.

Table 1.3 Correlation between the structure self-assembled in bulk and in water obtained from the analysis of amphiphilic Janus Dendrimers, modified from [45].

Structure in bulk (number of dendrimers)	Structure in water (number of dendrimers)	Percentage from the total number of structures assembled in water
Lamellar (36)	Dendrimerosomes (30)	53.6%
Columnar/ cubic (23)	Dendrimerosomes (9)	16%
Lamellar (36)	Micelles (5)	8.9%
Columnar/ cubic (23)	Micelles (12)	21.4%

The branching pattern in the primary structure of the dendrimer affects the layer thickness layers of lamellar structure in bulk and the thickness of the vesicle wall. The wall thickness of dendrimerosomes is dependent on the hydrophobic part, and an inverse proportionality between thickness of the vesicle wall and diameter of the vesicle was observed [34][45][46]. A higher interdigitation of the hydrophobic branches is responsible of a higher stability of dendrimerosomes. All these features are highlighted in figure 1.15.

Janus dendrimers can self-assemble in water forming ribbon and helical fibers. Self-assemblies like tapes, fibers, toroids, and tubes, require special directional interactions between the amphiphiles, which can be driven by π - π stacking of aromatic rings in water, along with hydrophobic interactions which allow self-assembly in a specific direction. Furthermore, the formation of a strong hydrogen bonding pattern with tendency to reduce the repulsive interactions between dendritic groups can lead to a transition from flat sheets to ribbons [34].

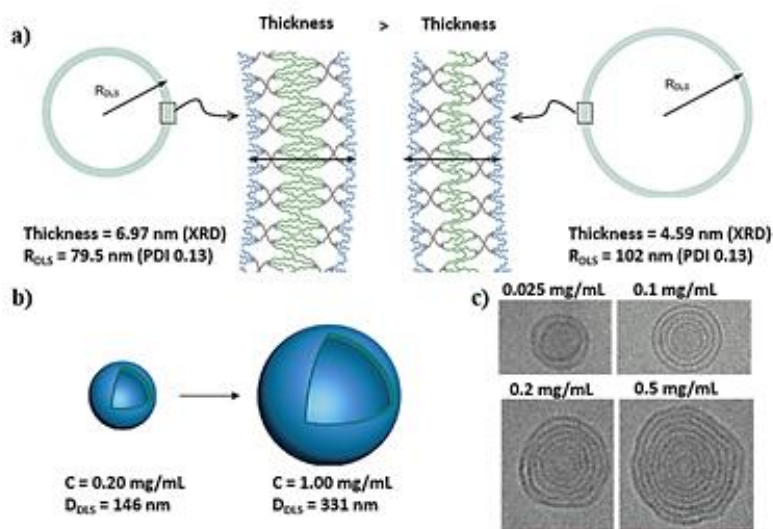


Figure 1.15 Parameters which affect size and shape of vesicular aggregates in Janus dendrimerosomes. **a)** A higher interdigitation is responsible of the reduction of the thickness of the vesicles wall which normally is lower for aggregates with bigger dimensions; **b)** For the same Janus dendrimers an increase in concentration (C) causes an increase in the vesicles diameter; **c)** for onion-like and multilayers vesicles the number of layers is proportional to the dendrimer concentration. Reprinted with permission from [45] and [46].

Applications of dendrimers in medicine

Dendrimers are good candidates in biological applications as imaging agents for diagnosis, carriers of genes, drugs, and proteins and in the development of vaccines thanks to their high structural and chemical homogeneity, which facilitate pharmacokinetic reproducibility. Furthermore, the possibility to tune their size and shape guarantees control on their biodistribution and pharmacokinetics. These

macromolecules can be functionalized with a large number of compounds and ligands, which can improve their solubility, influence their activity and define their targeting effect [48].

To date a wide variety of different dendrimer families exist with potential applications in biomedical and pharmaceutical areas, which involve polylysine, poly(propyleneimine) (PPI) and poly(amido amine) (PAMAM) dendrimers. Other architectures applied in biomedical applications are phosphorus, s-triazine, polyglycerol, polyester, and silicon-based dendrimers. The polyphenylene dendrimers are examples of nonpolar branched macromolecules that have also found applications in many biological settings [40].

Dendrimers have been used to enhance drug targeting and cellular uptake for which it has been demonstrated that the main internalization pathway is by endocytosis throughout mediation of receptors as a function of their chemical structure and periphery chemical characteristics [48].

Dendrimers can be applied as vector both for drugs and genes. Drugs can be both internalized in the hydrophobic cavity through non-covalent interactions or directly linked to the surface, where the addition of labile linkers, such as acyl hydrazone groups, ester and amide groups, and cleavable S–S bonds, can induce a controlled release of the drug.

Positive charged dendrimers, such as amino-terminated PAMAM and PPI dendrimers, have gained attention due to their capacity to bind DNA and RNA strands as transfectant systems for gene therapy. Moreover, they can show antimicrobial activity due to their membrane disrupting properties, which result in microbial membrane solubilization and pore formation, and ultimately death, thus helping to overcome antimicrobial resistance crisis. Dendritic architectures have been used in diagnostic imaging both for ^1H and ^{19}F Magnetic Resonance Imaging (MRI), as it will be discussed in section 1.4.2. Dendrimers tend to form hydrogels due to their multivalency, which can allow for high cross-link densities at low polymer concentration, and therefore have found applications as components of tissue scaffolds for promoting cell proliferation and tissue repair. Low-viscosity aqueous solutions can be injected into cavities of irregular shape to form a well-integrated polymer network. Accordingly, dendrimer hydrogels have also found applications in repairing linear and stellate corneal lacerations [40][48][49].

Several reports about dendrimers cytotoxicity suggested that cytotoxicity may be dependent on the dendrimer chemical makeup and surface functionality, generation, concentration, exposure time, cell-medium composition (e.g., serum concentration and type), and cell type under investigation. Generally, amino-terminated dendrimers induce more cytotoxicity compared to PEGylated dendrimers and species with OH, pyrrolidone, and anionic functionalities of the same generation and concentration [40][48].

Currently, some dendrimer-derived agents are in clinical trials: DEP® docetaxel, DEP® cabazitaxel for the treatment of tumors, and VivaGel® for applications as mucoadhesive gel for the treatment and prevention of bacterial vaginosis and in gel for the prevention of sexually transmitted infections. MAG-Tn3 is a vaccine for the treatment of breast cancer, ImDendrim for inoperable liver cancer, and OP-101 for X-linked adrenoleukodystrophy. Other commercially available products based on dendrimers include Alert Ticket which is a dendrimer-based anthrax detector developed by US army, PolyFect Transfection Reagent, PAMAM based dendrimers optimized for fast and easy DNA transfection of standard cell lines, Stratus® CS Acute Care TM a cardiac diagnostic testing, and finally, Superfect® a transfection agent from Qagen also based on PAMAM [48].

Biodegradable polyesters dendrimers

The search for biodegradable dendrimers has been motivated by the need of “smart” drug carriers

with no toxicity, characterized by the ability to degrade and to completely release their payloads only in a specific environment, without any drug leakage before arriving to the target sites. This would allow to reduce side effects improving drug delivery efficiency.

Biodegradable dendrimers are composed of biodegradable repeating units which will degrade into small fragments that can be excreted or eliminated through metabolic pathways.

Examples of biodegradable dendrimers are peptide dendrimers, DNA based dendrimers, polyacetal dendrimers, dendrimers composed by 1,3,5-triazaadamantane (TAA) units at each branching, polyesters dendrimers, and alternating dendrimers where the ester linkage alternates with other types of linkages which, normally, derive from orthogonal reactions.

Among all these structures, polyester dendrimers form the majority of the biodegradable dendrimers; classical monomers used for the synthesis of polyester dendrimers are succinic acid, lactic acid, adipic acid, dihydroxybenzoic acid, gallic acid together with polyethylene glycol (PEG), polyethylene oxide (PEO), and glycerol chains [50]. However, the high majority of polyester dendrimers are based on 2,2-bismethylolpropionic acid (Bis-MPA) as building block [50][51][52][53][54]. The Bis-MPA molecule is a cheap commercially available simple aliphatic, pro-chiral molecule which, being an AB₂ monomer, comprises two hydroxyls and one carboxylic group as functional units. Bis-MPA and its cyclic derivatives, like 5-methyl-5-(carboxyl)-1,3-dioxan-2-one (MCC) and the acetylene protected derivative, have been used for the development of a lot of complex architectures, as shown in figure 1.16 [51][53].

Different bis-MPA dendritic systems have been shown to be degradable, non-immunogenic, and non-cytotoxic in human cell lines and primary cultures; under physiological conditions (pH 7.5, 37 °C), hydroxyl-functional dendrimers are stable for up to 6 hours after which hydrolysis occurs, a higher stability in biological media can be achieved by addition of PEG chains.

Historically, first indication of bis-MPA's usefulness as a monomer for the synthesis of highly complex and accurate polymers was reported by Hult and coworkers in 1996 where they described the construction of monodisperse dendrimers via a convergent approach where different generation (1–4) dendrons were precisely grown from bis-MPA and finally coupled to a polyfunctional core [53]. In literature are reported several different techniques for synthesis of Bis-MPA based polyester dendrimers, which involve both convergent and divergent methodologies requiring carboxyl activation, through the use of classical coupling reagents such as those based on carbodiimide in scaffolds or uronium-based coupling agents, in presence of catalytic amount of bases like pyridine, 4-(dimethylamino)pyridine (DMAP) and 4-(dimethylamino)pyridinium-4-toluenesulfonate. Other strategies require the use of anhydrides of Bis-MPA monomers as activated form or Fluoride-Promoted Esterification (FPE) using imidazolide-activated bis-MPA monomers. Sophisticated bis-MPA-based macromolecules have been prepared by versatile click chemistry reactions such as copper-catalyzed azide-alkyne cycloaddition (CuAAC), strain-promoted azide-alkyne cycloaddition (SPAAC) and UV-initiated thiolene coupling (TEC) [53][54]. Bis-MPA dendrimers are versatile systems which can be used for thin film formation with coating applications, in the preparation of liquid crystals and other optical devices and for the synthesis of new drugs or gene delivery vectors or in the preparation of new Magnetic Resonance Imaging (MRI) contrast agents [49][51][55].

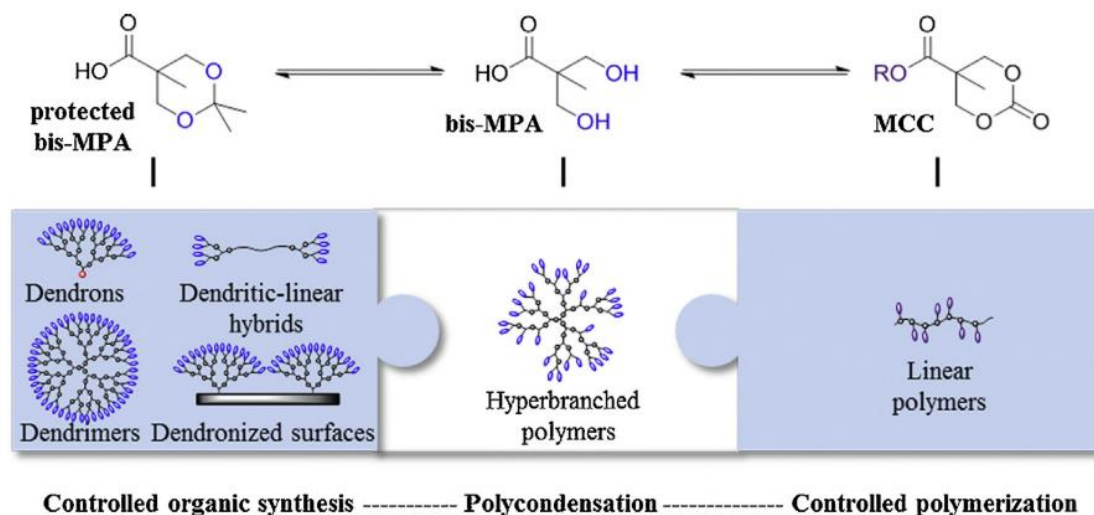


Figure 1.16 Overview on different polymeric structures based on bis-MPA as building block. Reprinted with permission from [53].

1.2.2 Fluorinated dendrimers

Fluorine is the most electronegative element of the periodic table, Pauling assigned to fluorine an electronegativity value of 4; this confers to the atom high ionization potential and low polarizability [56][57]. Even if fluorine is a relatively small atom, it is significantly larger than hydrogen (van der Waals radius 1.47 Å vs. 1.20 Å, respectively); as a consequence, perfluoroalkyl chains are bulkier than their hydrogenated counterparts, characterized by greater rigidity, and generally they assume a helical conformation to minimize steric hindrance [56]. When compared to other covalent bonds, C-F bond is the strongest in organic chemistry (105.4 kcal/mol); this is strictly related to its high polarization, with the electron density substantially on fluorine. Consequently, the particular strength of the bond can be attributed to significant electrostatic attraction between partially negative fluorine and partially positive carbon atoms involved in the bond. Table 1.4 shows Van der Waals radii of the most common elements and distances of their covalent bonds with C which are directly related to their strength [57].

Table 1.4 Van der Waals radii of the common elements present in organic molecules and average C–X bond lengths [57].

Van der Waals radii/Å	H (1.2) Si (2.1)	C (1.70) P (1.8)	N (1.55) S (1.8)	O (1.52) Cl (1.74)	F (1.47)
Bond lengths/Å	C–H (1.09) C–Si (1.85)	C–C (1.54) C–P (1.84)	C–N (1.47) C–S (1.82)	C–O (1.43) C–Cl (1.77)	C–F (1.35)

Fluorination can significantly alter the spatial conformation of a dendrimer thus generating new self-assembling properties both in bulk and solution [58]. Several different dendritic architectures have been used for this purpose including polyamidoamine (PAMAM) dendrimers, diaminobutane (DAB) dendrimers, polyether and polyarylether dendrimers, polyphenylene dendrimers, polyester, carbosilane dendrimers and phosphorus dendrimers. Linear or branched fluorinated chains not only can be linked to the surface of dendrimers (as shown in figure 1.17A) or can be grafted on the surface of dendrons by generating dendritic wedges (as shown in figure 1.17B)., Fluorinated derivatives can also be linked to the core of dendrons or can be inserted into the chemical structure of the dendrimer by substituting protons, as shown in figure 1.17 (C e D) [59].

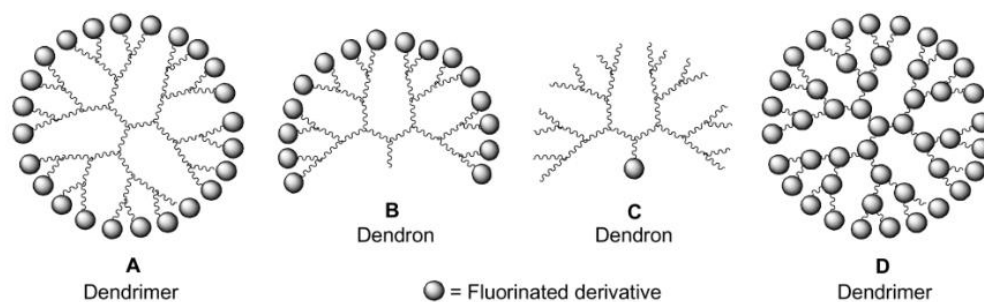


Figure 1. 17 Various types of fluorinated dendritic structures. **A)** Dendrimer with fluorine derivatives as end groups, **B)** an example of a dendritic wedge, **C)** core-functionalized dendron with fluorinated chains, and **D)** example of a dendrimer in which all the hydrogens are replaced by fluorine atoms, reprinted with permission from [59].

Fluorinated chains provide dendritic molecules with properties different from the analogous hydrogenated counterparts due to fluorophobic effect. Furthermore, the large size of fluorine atoms reduces the rotation of fluorinated chains, which infer an enhanced rigidity to the structure. Due to these distinctive properties, fluorinated chains can also produce a very pronounced microsegregation effect at molecular level, which influences the supramolecular organization of the dendritic structures, modifying mesophase type, mesophase thermal range and structural packing parameters. In some cases, all these effects can confer new liquid crystalline behavior to fluorinated dendrimers [60].

Fluorination can also have impact on the shape of self-assembled aggregates in solution and can increase aggregate stability [56]. Applications and uses of fluorinated dendrimers can be found in catalysis and extraction of proteins and small molecules from water to polyfluorinated or supercritical fluids [59][61], in constructions of new materials with improved mechanical properties [62] and in biology as drug delivery systems [63], gene vectors [64] and ^{19}F -MRI imaging agents [49]. The high hydrophobicity and low reactivity confer lower cytotoxicity [65] and higher cellular uptake [66] than non-fluorinated analogues; furthermore, their tendency to form stable aggregates in water can guarantee the delivery of fluorinated drugs thanks to fluorine-fluorine interactions [67].

1.3 Gene therapy

Gene therapy has emerged as a new and efficient modality to combat inherited and acquired diseases, such as genetic disorders, cancer, cardiovascular diseases, neurological disorders, and diabetes mellitus. In gene therapy, therapeutic deoxyribonucleic acid (DNA) and ribonucleic acid (RNA) gene molecules are capable of altering defective genes, modifying missing genes, and silencing mutated genes [68]. MicroRNAs (miRNAs) or small interfering RNAs (siRNAs) can be easily processed according to the sequence of the target mRNA and efficiently silencing the target gene of interest. SiRNA is of particular interest in cancer therapy and is based on silencing the expression of oncogene genes with specific RNA sequences. The advantages of siRNA therapy over other small anticancer drugs include its high specificity, capacity to inhibit nearly any target of interest, and low adverse effects as well as simple synthesis and purification [69]. MiRNAs consist of highly conserved 18–24 nucleotide sequences, which regulate the translation of mRNA via complimentary RNA-RNA interaction. Researchers found that some diseases are associated to an improper or suppressed expression of miRNA in specific cells. Therefore, gene therapy can be used to suppress the expression of genes by using synthetic anti-miRNAs or antagonists or restore the expression of downregulated miRNAs, a strategy known as miRNA replacement therapy. There are several ways to deliver miRNAs in cancer cells for therapeutic purposes, including introduction of synthetic miRNA mimics, DNA plasmids containing miRNA and small molecules that epigenetically alter endogenous expression of miRNAs [70]. Due to compromised blood serum stability, rapid renal clearance, nonspecific biodistribution, low transfection, poor endosomal escape, and cytoplasmic release of DNA and RNA, genes necessitate a delivery vector able to protect and assist their transfer to the targeted sites [69].

1.3.1 Gene vectors: concerns and needs

Gene vectors can be divided in two categories: viral and non-viral vectors.

Viruses are able to transfer genetic material in cells. Current viruses that are used as vectors include retroviruses, lentiviruses, poxviruses, vaccinia viruses, rubella viruses, and adenoviruses.

Genetically engineered adenovirus and adenovirus-associated virus are two common viral vectors; they are suitable to a wide range of hosts and can be targeted by gene recombination. Furthermore, they can carry relatively large exogenous gene fragments for transient expression and are not integrated into the host genome. Viral vectors are widely used as gene therapy delivery systems since their transfection and expression efficiencies are high; however, they show some disadvantages.

The major concerns are related to their immunogenicity and potential risk of mutation, which make them a potential safety hazards. Moreover, viral vectors lack targeting, have a limited length for the inserted gene, and their preparation process is complicated. Therefore, various non-viral vectors has gradually emerged as a good alternative for the development of gene delivery vectors [71].

Non-viral vectors can be divided into three categories: organic, inorganic and hybrid materials [69][71][72]; the insertion of positively charged groups guarantees the driving of genes thanks to electrostatic interactions with the negatively charged phosphate groups in the DNA and RNA sequences.

Differently from classical drugs, which can exert their therapeutic activity even if they are not internalized in cells, the genetic material must be internalized into target cell to gain the desired effect [73]. Vectors can be used to deliver DNA, mRNA and short double-strand RNA, such as small

interfering RNA (siRNA) and microRNA (miRNA) and, to be effective for *in vivo* applications, they should protect the genetic material from renal clearance and nonspecific interactions, prevent its degradation by serum endonucleases and evade immune detection [74]. Afterward, depending on the type of delivered oligonucleotides, the vector should reach the target site, which is cytosol for RNA molecules and nucleus for plasmids, as schematically illustrate in figure 1.18.

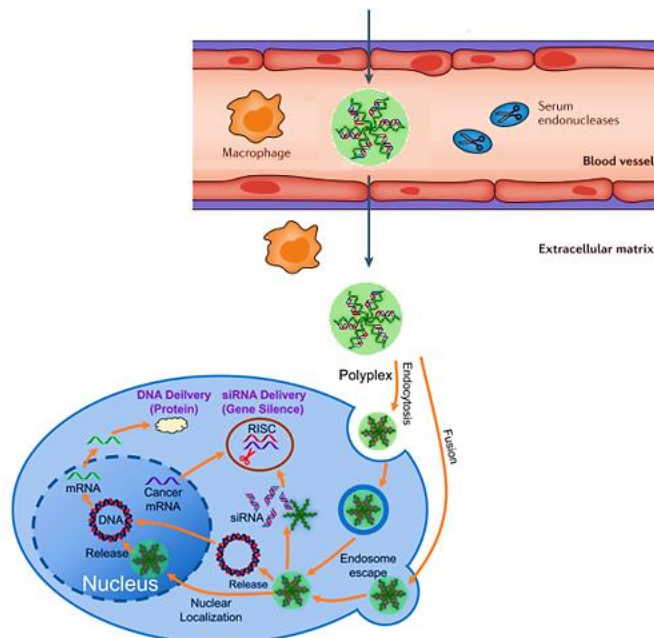


Figure 1.18 Gene delivery mechanism of polyplexes *in vivo*, reprinted and modified with permission from [68] and [74].

It has been demonstrated that the rate-determining step in non-viral gene delivery is cellular internalization, which generally occurs by endocytosis mechanisms, such as phagocytosis, clathrin-mediated endocytosis and micropinocytosis or fusion mechanism. The internalization pathway depends both on type of targeted cell and molecular composition of its surface and on size, shape and chemical composition of the used vector. Afterward, the gene complex has to escape from the acidic degradation of endosomes and lysosomes via proton-sponge mechanism or swelling causing the local rupture of their membranes. Finally, vectors need to unpack their gene payload. The unpacked siRNA or miRNA can bind its complementary sequence-specific messenger RNA (mRNA) through formation of RNA-induced silencing complexes (RISC) in cytosol to act on protein expression. Otherwise, the unpacked plasmid has to translocate to the cell nucleus for transcription mechanism and subsequent protein expression [68][70][73][74].

In order to efficiently deliver genes, it is important to tailor some properties of the vector such as density of positive charges, size and molecular weight properties directly related to the cytotoxicity and biodegradability of the used system. Since presence of positive charges is responsible for electrostatic binding to phosphate groups in oligonucleotides, a high number of positive charges guarantees a stronger interaction with genes and high polarity making these systems highly soluble in water media. However, positive charges can interact with serum proteins with consequent formation of large aggregates that can induce an immune response with their rapid clearance from the blood circulation. Another important parameter to take in account is the size of the obtained complexes, on one side vectors of larger size can be rapidly cleared from blood circulation preventing cellular internalization, whereas small ones can exhibit inefficient endocytosis leading to low gene transfection efficacy. Molecular weight is directly related to the cytotoxicity of the vector; generally,

polycations with high molecular weight show higher toxicity, even if transfection is improved. It has been shown that the use of amphiphilic systems can improve the vector efficacy. Hydrophobic interactions can contribute to the complexation with genes thanks to cooperative interactions by generating complexes of higher stability in serum; furthermore, the presence of hydrophobic chains can facilitate the interaction with the lipid bilayer of the cellular membrane enabling endocytosis, contribute to complex formation with genes and enhance their stability in serum [75]. All these features are fundamental for good gene delivery *in vivo*, however to move forward to clinical applications cationic vehicles should be made by simple and well-established biocompatible and biodegradable materials with a scalable production and a batch-to-batch reproducibility [69][76].

1.3.2 Dendritic non-viral vectors: the role of fluorination and the effect of the core on gene delivery efficacy.

Dendrimers have obtained particular attention in gene delivery due to their well-defined chemical structure, easy tunability of density of terminal groups, and ease surface modification.

Liposome-based vectors can easily enter cytoplasm by endocytosis and direct membrane fusion and release the bound DNA by lipid–phospholipid exchange, thus showing high transfection efficacies; however, they show some disadvantages including difficulties in reproducible liposome fabrication and low permeability in solid tissues as well as toxicity and instability, especially for *in vivo* application. On the contrary, cationic polymers show facile manufacturing, stable formulation, ease of modification, and high permeability; disadvantages are related to their low serum stability and cytotoxicity [77].

Dendritic-based gene vectors show properties which combine features of liposomes with those of classical polymeric vectors [77][78].

Compared to liposome-based vectors, dendritic architectures show more stable formulations, facile modification and higher permeability to tissues [78]. By synthetic procedures it is possible to link to dendritic surfaces amino groups and generate cationic dendrimers which can efficiently interact with oligonucleotides.

‘Critical nanoscale design parameters’ (CNDPs) such as size, shape, flexibility/rigidity, architecture, elemental composition, and surface chemistry of dendrimers are important parameters to be considered for the construction of the desired dendrimers. Tuning these parameters, it is possible to improve both gene delivery efficiency and cytotoxicity of dendrimers. Several libraries of cationic dendrimers have been reported, the most used ones are polyamidoamine (PAMAM), poly(propyleneimine) (PPI), poly(ether imine) (PETIM), and poly-L-Lysine dendrimers, with different surface functionalities, as it is shown in figure 1.19 [78]. It has been demonstrated that surface functionalization with fluorinated chains can greatly affect final properties of dendritic gene vectors [79][80][81][82]. Due to the unique properties of fluorinated chains, their linkage on the surface of dendrimers can enhance their ability to self-assemble thanks to fluorophilic interactions and, due to their lipophobic and hydrophobic natures, improve the affinity to lipid bilayer, facilitating both internalization in cell membrane [66] and endosomal escape of the vector [63]. Furthermore, the presence of fluorinated moieties can modulate packing and unpacking processes of the dendrimer-oligonucleotide complexes and facilitate gene release.

Compared to classical commercially available gene vectors, like Lipofectamine and jetPEI, and analogue non-fluorinated dendrimers, fluorination can improve transfection efficacy and reduce

optimal N/P ratios, the minimum ratio between amine and phosphate groups necessary for an optimal binding, reducing the needed concentration of vector and lowering cytotoxic effects.

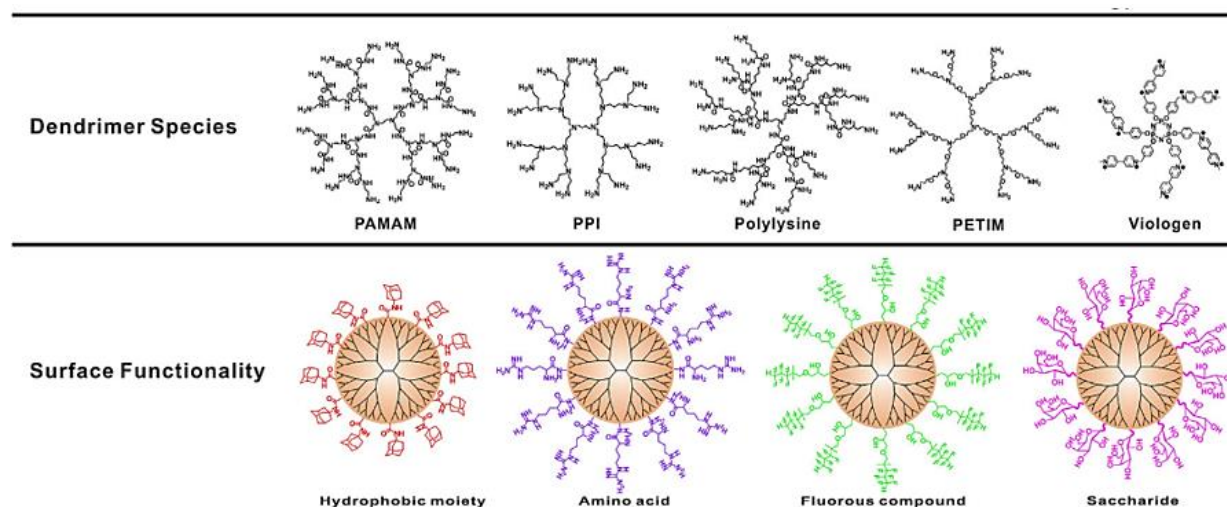


Figure 1.19 Example of classical dendritic architectures used as gene delivery vectors and types of surface functionalities explored in literature. Reprinted and modified with permission from [78].

Additionally, fluorine modified dendrimers have been used for codelivery of genes and fluorinated drugs, which can be more easily loaded thanks to fluorine-fluorine interactions, enabling the development of combination therapies [79][80][81][82].

The role of the dendrimers and dendrons core in gene delivery vector efficacy and the effect of fluorinated cores

It has been demonstrated that the core of a dendritic vector can affect gene delivery performance. In fact, beside to affect the molecular size and shape of the vector, it can also modify the flexibility of the molecule, its solvophilicity, and multivalency which are important parameters for an effective oligonucleotide binding. Generally, small dendriplexes, of about 100 nm, are preferred since larger complexes can be more easily eliminated from the blood circulation and can more difficulty pass through the cell membranes. Both dendrimer and dendron-based gene vectors functionalized with different moieties have been reported in literature and some examples are shown in figure 1.20 [83][78].

In particular, low-molecular-weight, amine-functionalized dendrons core functionalized with hydrophobic portions, shown in figure 1.20b, have gained attention as they are able to self-assemble into cationic supramolecular dendrimers, called “pseudodendrimers”, whose behavior is similar to lipids [84][85][86].

From these studies it is important to note that the presence of higher hydrophobic molecules at the core enhance transfection efficacy of the vector, while introduction of hydrolysable functional groups reduces vector toxicity facilitating gene release. Recent studies revealed that fluorinated polyethylenimine (PEI) upon self-assembly forms nanomicelles for efficient siRNA delivery, as schematically illustrated in figure 1.21 [87][88].

Fluorination not only facilitates formation of stable nanoaggregates thanks to fluororous interactions, but, compared to PEI, fluorination enhances binding affinity to siRNA with higher colloidal stability of the formed complex and reduced cytotoxicity, thus enhancing transfection efficacy.

1.4 Magnetic Resonance Imaging and the use of fluorine-19 (^{19}F)

The phenomenon of nuclear magnetic resonance (NMR) was described by Bloch and Purcell in 1946 for which they awarded the Nobel Prize for Physics in 1952. Then, the technique has been improved and, thanks to the introduction of superconducting magnets, it has been applied for clinical diagnosis. The first clinical magnetic resonance images were produced in Nottingham and Aberdeen in 1980; then applications increased, and Magnetic Resonance Imaging (MRI) has become a widely used powerful technique [89].

Contrary to other diagnostic techniques, MRI is highly sensitive non-invasive imaging method. It is particularly effective for soft-tissue diagnoses, including benign and malignant neoplasms, inflammation, and temporomandibular joint disorders.

This technique allows to produce any given tomographic image and displays blood vessels without using a contrast agent. In addition, MRI scans provide high tissue resolution.

The technique requires the use of superconducting magnet which need highly costly cryogenic liquid helium and big spaces [90][91].

1.4.1 Second color MRI: the role of Fluorine-19 (^{19}F)

Due to its large abundance in the body, ^1H has been the most widely used nucleus in MRI. However, any nucleus showing nuclear spin (I) different from zero can generate a MRI signal: this is common for atoms which show odd number of protons and neutrons, table 1.5 shows a list of some representative nuclei together with their properties [92][93][94][95].

Table 1.5 Properties of some representative MRI-active nuclei [94].

nucleus	$\gamma/2\pi$ (MHz/T)	natural abundance (%)	relative sensitivity (constant number of nuclei)	shift parameter range (ppm)
^1H	42.576	99.98	1.0	13
^3He	-32.434	0.000134	0.442	
^7Li	16.546	92.41	0.294	
^{13}C	10.705	1.108	0.0159	250
^{14}N	3.0766	99.636	0.001	
^{15}N	-4.3156	0.364	0.001	
^{17}O	-5.7716	0.038	0.0291	
^{19}F	40.076	100	0.83	400
^{23}Na	11.262	100	0.0927	
^{31}P	17.235	100	0.066	530
^{129}Xe	-11.777	26.4	0.0216	200

Among these MRI-active nuclei, ^{19}F has achieved high interest and has been the first nucleus, different from hydrogen, to be imaged in 1977 when perfluorocarbon compounds (PFC) were analyzed for the first time by ^{19}F -MRI. This nucleus received great interest for application in MRI due to its peculiar properties which include:

- 83% sensitivity of ^1H , which means high signal intensity;
- 100% natural abundance of ^{19}F isotope. All the artificial fluorine isotopes in fact are short-lived and not naturally present;
- a resonance frequency which differs only 6% from that of ^1H . This allows to get ^{19}F -MRI on existing ^1H imaging hardware, by adding a suitable ^{19}F coil and by customizing the hardware properly for this nucleus.

- Furthermore, fluorine shows an extremely broad chemical shift range and sensitivity of T1 to oxygen tension in some compounds. These properties make ^{19}F applicable for the construction of smart imaging agents or responsive markers sensible to the different microenvironment.
- ^{19}F -MR images are background free with very high specificity and allowing quantification of the signal; this is due to the low presence of fluorine in the body, which is less than 10^{-6} M. Furthermore, fluorine in the body is present in bones and teeth in the solid form; this leads to very short T2 relaxation times which are responsible of a background signal much below MRI detection limits.

The absence of detectable fluorine in the body requires the use of fluorinated tracer to acquire the images: the perfect tracer should show high fluorine content and a simple ^{19}F -NMR spectrum which allows higher sensitivity and reduce the occurrence of chemical shift artifacts due to the overlapping of different signals from non-equivalent fluorine atoms. The tracer should be characterized by short T1 and long T2. Short T1 allows for shorter echo times and, consequently, the time required for a single acquisition is reduced, while long T2 are responsible for the formation of sharper peaks. This allows for the increase in signal intensity and the improvement of the signal to noise ratio (SNR). Furthermore, a fluorinated tracer should be characterized by a facile and scalable synthesis and a simple formulation. Moreover, its chemical properties must be known together with its chemical and biological stability. The fluorinated tracer should show a long shelf life and low *in vitro* and *in vivo* toxicity [93][95].

Fluorinated tracers for ^{19}F -MRI

Among fluorinated tracers in literature, the most frequently used perfluorocarbons are perfluorooctyl bromide (PFOB), perfluorodecalin (PFDC), and perfluoro-15-crown-5-ether (PFCE) whose structures and ^{19}F -NMR spectra are shown in figure 1.22 while their relaxation times are listed in table 1.6 [94].

PFOB, also known as Perflubron, is a linear PFC with 17 fluorine atoms. It is a hydrophobic and dense liquid, with a low diffusion coefficient into blood, and displays an enhanced clearance rate from the body. It shows biological inertness, longer blood circulation time and faster body excretion than other PFCs, and it has been approved by the U.S. Food and Drug Administration (FDA). One of the main disadvantages of PFOB is related to its non-equivalent distribution of fluorine atoms, which generates a multipeak resonance spectrum, and the occurrence of chemical shift artifacts in MR images. PFDC is mostly used for blood replacement and liquid-assisted ventilation, it has been tested as an alternative non-toxic PFC for *in vivo* inflammation imaging, but its significantly low sensitivity generate weak signal intensities.

PFCE is biochemically and thermally inert which make it biocompatible; furthermore, it shows 20 chemically equivalent fluorine atoms that give one single ^{19}F -NMR signal at -92.5 ppm which guarantees high sensitivity without any chemical shift artifact; it has been demonstrated that the excretion time from the body of PFCE-based probes is highly dependent on the formulation used [96].

Perfluorocarbons are not directly dispersible in water; therefore, they need to be properly formulated: generally, PFCs can be formulated by means of lipids such as pluronics and phospholipids which form nanodroplets where the lipid generates a layer which protects the PFCs place in the interior.

In literature formulations where PFCs are encapsulated in the core of biodegradable polymeric nanoparticles based on poly(D,L-lactide-co-glycolide) (PLGA) and polyethylene glycol (PEG), which can alter and optimize the value of T1 and T2 relaxation times, can be found [93]. Other than

the PFCs just described, a lot of papers show the development of new ^{19}F -MRI tracers. In 2014 a new superfluorinated molecules with 36 equivalent fluorine atoms - called PERFECTA- (figure 1.23), showing a single intense ^{19}F -NMR peak, good relaxation times and facile formulation, has been published.

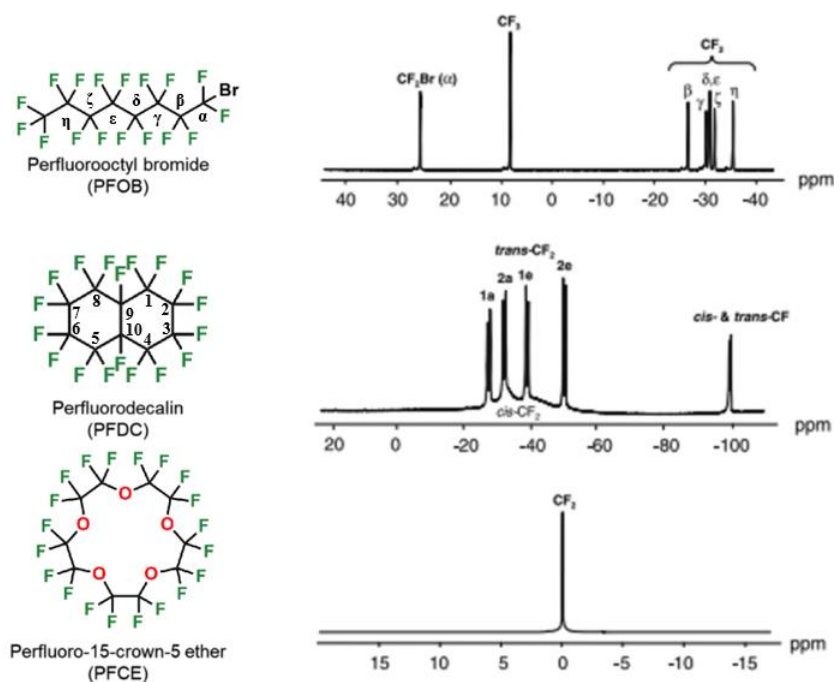


Figure 1.22 Structure of the most common ^{19}F -MRI probes together with their ^{19}F -NMR spectra, reprinted and modified with permission from [93] and [94]. Here PFCE is taken as reference for the determination of the shift of PFOB and PFDC and so its signal is set at 0 ppm.

Table 1.6 Chemical Shifts (δ) and Relaxation Times of MR Signals for PFOB, PFDC, and PFCE. The signal of PFCE is used as reference for the determination of the shift of PFOB and PFDC and set at 0 ppm (-91.8 ppm relative to CFCl_3)[94].

peak	assignment	δ (ppm)	perfluorocarbon		emulsion	
			T_1 (ms)	T_2 (ms)	T_1 (ms)	T_2 (ms)
Perfluorooctyl bromide (PFOB)						
1	CF_2Br	26.7	1420	450	550	230
2	CF_3	8.6	1865	630	610	290
3	CF_2 [β]	-27.1	1140	65	465	75
4	CF_2 [$\gamma, \delta, \epsilon, \zeta$]	-31.6	800	50	450	80
5	CF_2 [η]	-36.2	1005	70	465	75
Perfluorodecalin (PFDC)						
1	CF_2 [<i>trans</i> 1a]	-27.4	1185	80	420	45
2	CF_2 [<i>trans</i> 2a]	-32.0	1285	55	490	50
3	CF_2 [<i>trans</i> 1e]	-38.7	1050	40	425	45
4	CF_2 [<i>trans</i> 2e]	-49.6	1315	45	425	45
5	CF [<i>cis/trans</i> 9]	-98.2	1910	200	595	145
Perfluoro-15-crown-5 ether (PFCE)						
1	$(\text{CF}_2)_{10}$	0.0	1180	525	600	300

PERFECTA can be well formulated both following classical oil in water formulation just described [97] or by its encapsulation in nanoparticles obtained from classical degradable PLGA nanoparticles [98] or thanks to fluorine-fluorine interactions it can be internalized in nanoassemblies obtained by polyfluorinated amphiphiles [99]. The main advantages of using PERFECTA are related to the presence of short polyfluorinated chains which combine the benefits of a high number of fluorine

atoms with an enhanced lability and biodegradability, due to the presence of ethereal groups, than classical linear polyfluorinated chains [100].

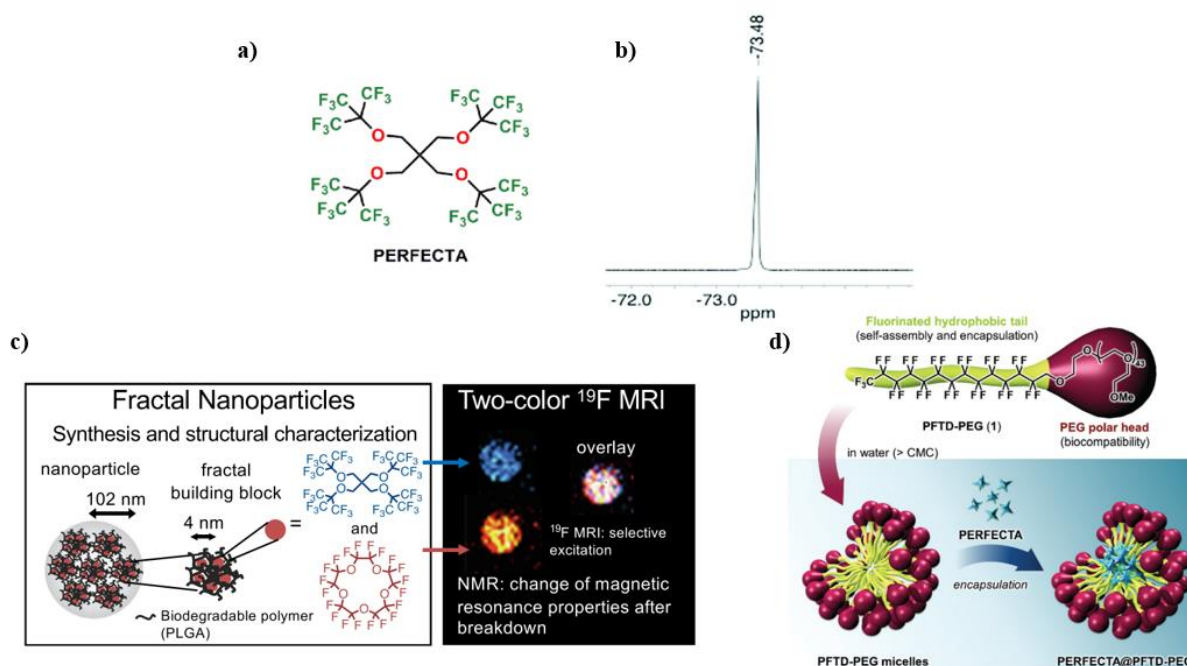
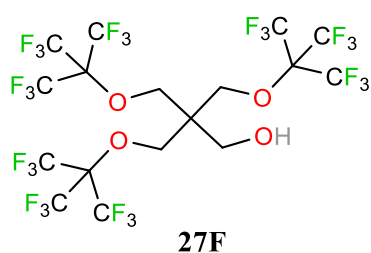


Figure 1.23 a) Chemical structure of PERFECTA, a 36 equivalent fluorine atoms containing ^{19}F -MRI-active probe, and b) the ^{19}F -NMR spectra of its oil in water formulation [97]. c) PERFECTA can be co-encapsulated with PFCE in PLGA nanoparticles. This system provides the monitoring of the colocalized two ^{19}F probes and allows the monitoring of the localization of the two probes separately, thanks to their different magnetic responses to MRI, after their release due to the rupture of the nanoparticles [98]. d) Thanks to fluorine-fluorine interactions, PERFECTA can be loaded in nanoassemblies obtained from the dispersion in water media of the fluorinated amphiphile PFTD-PEG [99].

The interest in using short polyfluorinated chains with a high number of equivalent fluorine atoms has attracted the attention of lot of scientists. In recent years much attention has been focused on the use of tri-perfluoro-*tert*-butoxyl-functionalized pentaerythritol (27F) derivatives, figure 1.24 displays the chemical structure of 27F.



- Reactive site (OH), suitable for chemical functionalization
- High number of equivalent fluorine atoms (27) suitable for ^{19}F -MRI

Figure 1.24 Chemical structure of tri-perfluoro-*tert*-butoxyl-functionalized pentaerythritol (27F). The presence of a free hydroxyl group makes the molecule suitable for the construction of new ^{19}F -MRI-active probes.

The presence of 27 equivalent fluorine atoms coming from $-\text{CF}_3$ chemical groups generates a single peak at ^{19}F -NMR, a promising characteristic for the construction of good ^{19}F -MRI probes. Furthermore, 27F shows a free hydroxyl group which is suitable for chemical functionalizations. From the first 27F derivatives reported by Bruce Yu and coworkers in 2007 [101], the library of derivates has increased and applications have been various, as shown in figure 1.25. In 2011 S. Caramori and collaborators have developed a zinc phthalocyanine complex functionalized with three hydroxyl-terminating 27F derivatives; this yielded the possibility to tune electronic distribution and

anti-aggregating properties of the photosensitizing dye suitable to application in dye-sensitized solar cells (DSCs) [102].

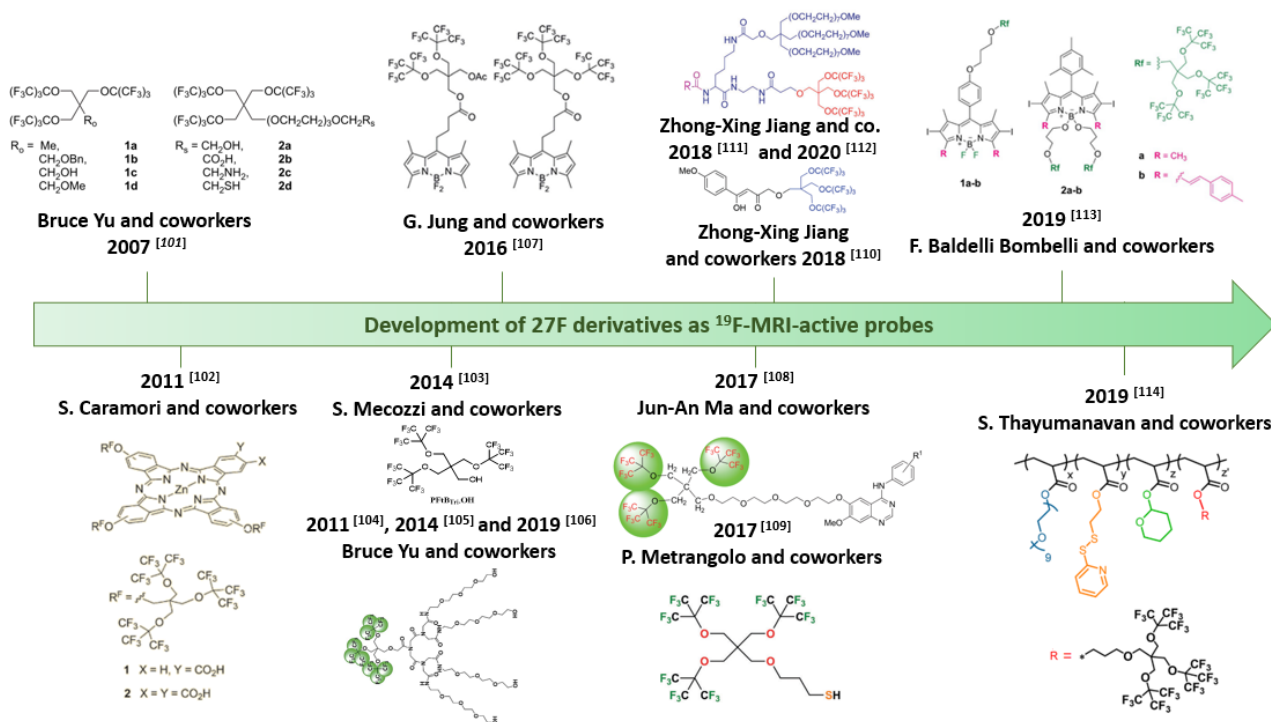


Figure 1.25 Development of new fluorinated ^{19}F -MRI active probes with 27 equivalent fluorine atoms (27-F) [101][102][103][104][105][106][107][108][109][110][111][112][113][114].

Bimodal probes can be generated combining MRI-active probes with other traceable compounds by other techniques. Boron dipyrromethene dyes, also known as BODIPY dyes, possess narrow emission bands, high quantum yields and high photostability, they are chemically stable and can be easily modified. These systems can be used in fluorescence imaging (FLI). Through BODIPY core modifications, it is possible to redshift its absorption peak to the near infrared (NIR), allowing for efficient photoacoustic imaging. The functionalization of BODIPY with a number of 27F groups at different positions has been reported; this not only allows to tune the emission spectra, but also allows for ^{19}F -MRI traceability [107][115][113]. In 2018 Zhong-Xing Jiang and collaborators developed a nanoemulsion which contained a cation chelator functionalized through an OH group to a 27F derivative coencapsulated with BODIPY. This system allowed multimodal imaging and tuning magnetic relaxation times thanks to the ability of the chelator to bind different paramagnetic cations [110]. In 2009 Yihua Bruce Yu and coworkers published the synthesis of a new water dispersible 27F derivative functionalized with four short polyethylene glycol (PEG) chains which showed good properties for applications as ^{19}F -MRI probe and peculiar self-assembling behaviors [104][105][106]. Similar promising ^{19}F -MRI properties were shown directly functionalizing the hydroxyl-terminating 27F derivative to a PEG chain which gave to the molecule the ability to self-assemble in water by forming micelles [103]. In 2017 a new 27F derivative bearing a thiol group has been used to drive the formation of superfluorinated and highly branched gold nanocrystals (AuNCs) dispersible in water media. These AuNCs showed excellent NIR photoluminescence properties and good magnetic properties, which made them applicable as multimodal devices for optical and ^{19}F -MR imaging [109]. In the same year a 27F derivative has been directly linked through a short PEG chain to a variety of 4-anilinoquinazoline derivatives; some of these derivatives showed good ^{19}F -MRI properties and are

promising for the construction of traceable targets for cancer cells [108]. Dendritic fluorinated amphiphiles based on 27F derivatives have been successfully entrapped in liposomes for the ¹⁹F-MRI-traceable *in vivo* delivery of doxorubicin with successful results. Few years later, a similar fluorinated architecture has been used by the same group to functionalize porphyrin molecules. This allowed for the construction of theranostic bimodal imaging systems traceable by fluorescence imaging and ¹⁹F-MRI able to load and release drugs [111][112]. In 2019 a 27F derivative has been used as a branching arm in random copolymers based on acrylate monomers. These polymers were able to form nanogel in water media by forming biocompatible systems with good properties for ¹⁹F-MRI applications [114].

Other examples of architectures which have been used as ¹⁹F-MRI probes can be subdivided in linear or branched polymeric architectures, fluorine-functionalized inorganic nanoparticles and multimodal imaging agents. Between linear fluorinated probes, the most used are perfluoropolyethers (PFPEs) which need to be properly formulated. These systems show similar properties with each other: in fact, generally, they show a main peak at around -92 ppm and other smaller peaks due to terminal fluorinated groups, short T1 and quite long T2. Next to linear polymers, branched architectures have been developed which show a high number of polyfluorinated groups on the periphery responsible of a higher sensitivity and better imaging performances than linear polymers. These include branched amphiphiles, star-like and branched polymers with fluorinated lateral chains, and dendrimers [93].

Applications of ¹⁹F-MRI

As highlighted in figure 1.26, ¹⁹F-MRI active probes can be useful for the development of systems which can specifically bind receptors for diagnostic purposes, can be suitable for cell tracking, can be tailored to respond to different physico-chemical stimuli, such as pH changes and oxidizing environment, and can be mixed with therapeutic molecules for the construction of theranostic probes which combine therapy and diagnostics.

Cell tracking is fundamental in stem cell therapy, tissue engineering, and immune-cellular oncology treatments. Cell tracking can explain fate, response, and effect of therapy by following their delivery into the body. Classical types of cells used for this purpose are dendritic cells (DCs), stem cells (SCs), T cells, and phagocytic cells, mainly monocytes. DCs can internalize a lot of different agents and are responsible for the initiation of immune responses, SCs are essential as regenerative therapeutics, while T cells are related to autoimmune diseases. The possibility to follow their traffic is useful to better understand autoimmune illnesses and diabetes. Monocytes accumulate in high concentrations in inflammation areas and can be useful for the diagnosis of inflammation diseases and cancer. The loading of the cells with ¹⁹F-MRI active probes can be done by *in vivo* administration or *ex vivo*. In the latter case, cells are incubated with the probe and labelled, then are reimplanted in the body. By labelling different cells with different probes, it is even possible to obtain “two color” images and obtain quantitative images which can be compared with ¹H-MR information [93][95].

¹⁹F-MRI probes have been properly functionalized with ligands, generally small molecules, antibodies, peptides, or proteins, which can specifically interact with receptor by the process known as active targeting. The majority of these ¹⁹F-MRI probes have been used to target receptors involved in vascular diseases and tumors. Even in these cases the information obtained by ¹⁹F-MR images can enrich and confirm data obtained with ¹H-MR images. Stimuli responsive ¹⁹F-MRI-active probes have been reported.

Thanks to the presence of specific binding, ions or enzyme cleavable linkage, these systems are able to change their relaxation times, caused by loss of a moiety or a conformation rearrangement, in the presence of difference in pH, redox-sensitive environments or specific enzymes.

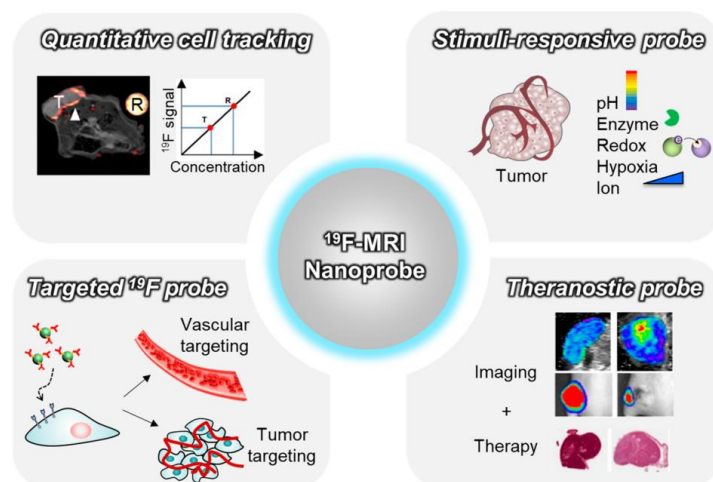


Figure 1.26 ^{19}F -MRI probes can be suitable for different applications which include cell tracking and the specific monitoring of diseases which causes differences in the environment or thanks to specific binding with receptors. Furthermore, theranostic probes can combine tracking with therapeutics. Reprinted with permission from [94].

This guarantees a probe where the ^{19}F -MRI response can be switched on or off depending on the chemical conditions. Since, generally, tumor cells are characterized by higher acidic pH, they produce higher amount of reducing glutathione and are characterized by hypoxia, fluorinated probes can be properly tailored in order to be MRI-active when in presence of such environments thus selectively mark tumor environments.

PFCs probes can be combined tanks to fluorine-fluorine interactions with fluorinated drugs or can be combined with specific systems active for chemotherapy, sonotherapy, and photothermal therapies. This allows for the constructions of theranostic nanoplateforms. These theranostic ^{19}F probes combine their localization monitoring with therapeutic effects in response to endogenous specific characteristics or exogenous physical stimuli [93][94][95].

2 A new family of polyfluorinated polyester dendritic amphiphiles

It is well known that fluorination can significantly alter the spatial conformation of a dendrimer thus generating new self-assembling properties both in bulk and solution [58]. Fluorinated chains provide dendritic molecules with properties different from the analogous hydrogenated counterparts often inducing liquid crystalline behavior in the solid state [60] and modifying the aggregates shape in solution [56]. Applications and uses of fluorinated dendrimers can be found in catalysis and extraction of proteins and small molecules from water to polyfluorinated or supercritical fluids [59][61], in constructions of new materials with improved mechanical properties [62] and in biology as drug delivery systems [63], gene vectors [64] and ^{19}F -MRI imaging agents [49]. The high hydrophobicity and low reactivity confer lower cytotoxicity [65] and higher cellular uptake [66] than non-fluorinated analogues; furthermore, their tendency to form stable aggregates in water can guarantee the delivery of fluorinated drugs thanks to fluorine-fluorine interactions [67].

To fully exploit the potential offered by fluorinated dendritic amphiphiles, there is a pressing need to design new stable, non-toxic and biocompatible fluorinated systems. In fact, great concerns have arisen around the use of perfluorocarbons (PFCs) with chains longer than six carbon atoms, due to their high persistence in the environment and their bioaccumulative potential, which make their further use environmentally not sustainable [100]. The search for less harmful materials brought the attention on shorter chains PFCs. However, simply cutting down the chain length does not lead to satisfactory results in balancing environmental impact and performance. Indeed, short chains fluorosurfactants are less efficient, self-assemble into less ordered structures and provide lower barrier properties [56][61]. The use of short branched polyfluorinated chains, as those present in PERFECTA [97], guarantees the insertion of a high number of equivalent fluorine atoms by using short branched polyfluorinated chains which combine the benefits of a high number of fluorine atoms with an enhanced lability and biodegradability, due to the presence of ethereal bonds. [100]. Yu and coworkers have already reported some tri-perfluoro-tert-butoxyl-functionalized pentaerythritol (27F) derivatives [8], suitable for the development of ^{19}F -MRI probes due to the presence of a high number of equivalent fluorine atoms. Their dendrimers have been synthesized by linking the 27F moiety to hydrophilic architectures which facilitate the dispersion in water media.

In order better understand how the balance between hydrophilic and hydrophobic portions in fluorinated dendrimers can affect their self-assembly behavior, we decided to synthesize a new family of dendrimers by attaching the same multibranched superfluorinated structure to different generations of 2,2-bismethylolpropionic acid (Bis-MPA) polyester dendrons.

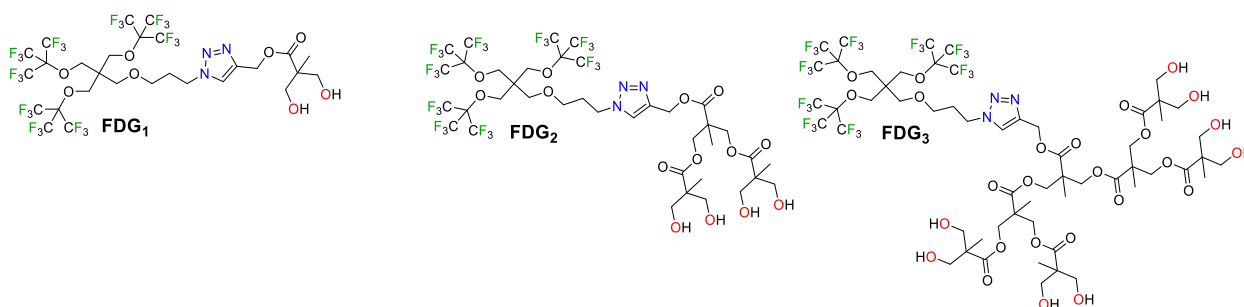


Figure 2.1 Chemical structure of the new dendritic amphiphiles.

Figure 2.1 shows the chemical structures of the new dendritic amphiphiles whose synthesis and properties will be discussed in this chapter.

We exploited the Copper-Catalyzed Azide-Alkyne Cycloaddition (CuAAC) which allows to orthogonally bind an azide group to an alkyne moiety via the copper (I) catalyzed formation of a 1,4-disubstituted triazole ring as the linker in good yields and mild conditions without the formation of by-products [116]. The CuAAC, which makes part of click reactions, has become of high interest due to its high specificity, in fact no side products are formed. Furthermore, it guarantees the linkage of the two parts with good yields and mild conditions. In CuAAC, copper (I) catalyzes the reaction, through a stepwise process, shown in figure 2.2, between the alkyne and the azide groups. Copper forms with the alkyne and the azido groups intermediate activated complexes; these intermediates evolve in the formation of a 1,4-disubstituted 1,2,3-triazole as linking group.

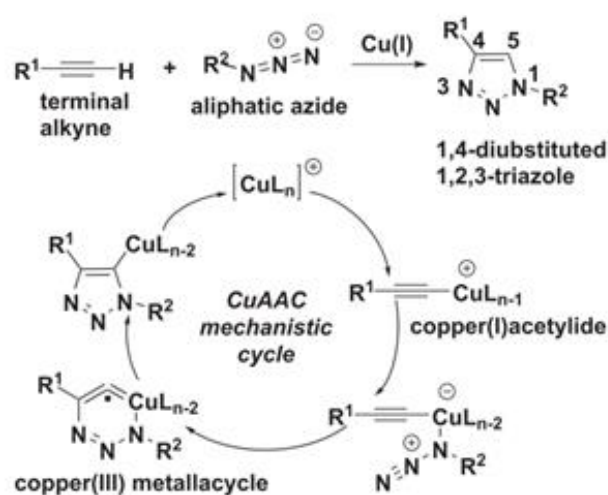


Figure 2.2 Mechanism of the copper-catalyzed azide-alkyne cycloaddition [116].

The three new molecules show a polyfluorinated moiety bearing 27 equivalent fluorine atoms which not only can be useful for the development of new ^{19}F -MRI traceable systems but acts as the hydrophobic part in the amphiphile architecture too. This high number of fluorine atoms can facilitate the self-assembly of these new systems thanks to the high tendency of fluorine atoms to segregate from water and form fluorine-fluorine interactions [104][105][106].

2.1 Results and discussion

Before entering in the description of the properties of FDG_1 , FDG_2 and FDG_3 , in section 2.1.1 the synthetic strategies used for the three amphiphiles will be reported together with their structural characterization. Afterward, in section 2.1.2 and 2.1.3 the characteristics of the three new amphiphiles in bulk and in solution will be described. Finally, in section 2.1.4 computational results will be used to better describe the behavior of the three polyfluorinated dendritic molecules observed experimentally in solutions.

2.1.1 Synthesis, purification, and characterization of the new amphiphiles

The first step for the synthesis of FDG_1 , FDG_2 and FDG_3 has been the synthesis of a new fluorinated azide ($\text{F}_{27}\text{-N}_3$), whose chemical structure is shown in figure 2.3, and its full characterization.

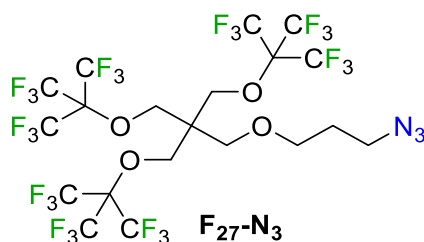


Figure 2.3 Chemical architectures of $F_{27}\text{-N}_3$, a new 27F derivative bearing an azido group suitable for the CuAAC.

$F_{27}\text{-N}_3$ has been obtained by nucleophilic substitution of the mesylate leaving group with sodium azide. The synthesis of the derivatives **a-d** has been done by slightly modifying already reported procedures; the changes have been done in order to optimize and limit the number of needed purification processes [117][109][113]. Figure 2.4 shows the reactions involved in the synthesis of the azido terminating derivative.

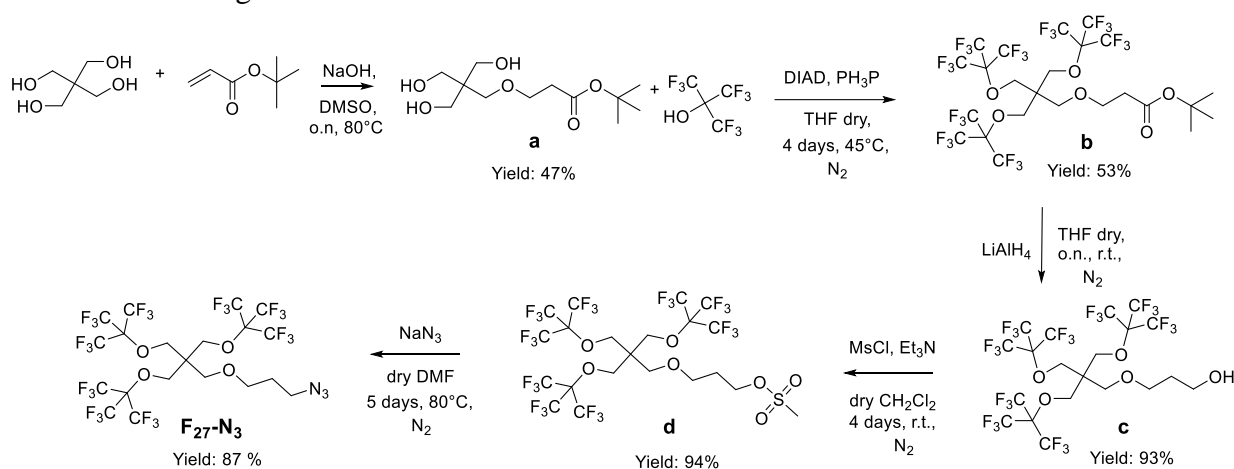


Figure 2.4 Synthesis of $F_{27}\text{-N}_3$, a new tri-perfluoro-*tert*-butoxyl-pentaerythritol derivative.

Compound **a** can be obtained by the Michael addition of *tert*-butyl acrylate on one of the four hydroxyl groups of pentaerythritol. Obviously, this is not a specific reaction and in fact it brings to the formation of an equal amount of the mono and di-substituted pentaerythritol; the trisubstituted derivative could not be isolated, probably because its formation is prevented due to steric hindrance. In this case we decided to perform a flash chromatography on silica gel by modifying the eluent used in literature, based on a mixture of dichloromethane and methanol. In fact, we used a 1:1 in volume mixture of diethyl ether and acetone which guarantees a good separation of the two products. The purification step yields to the isolation of derivative **a** with yields around 50%. Afterward compound **b** has been obtained by introducing three perfluoro-*tert*-buthyl groups on the three free hydroxyl groups of the precursor by means of the Mitsunobu reaction. Differently from the already reported procedures where the compound is purified by flash silica gel chromatography, we were able to obtain the pure product by a recrystallization in methanol which allowed the isolation of **b** with yields around 50%.

The reduction of the *tert*-buthyl ester with LiAlH₄ gave intermediate **c**; thanks to a complete conversion of the precursor in the alcohol terminating derivative **c**, we were able to isolate the clean product without flash silica gel chromatography, but just by filtrating the salts obtained after the deactivation of LiAlH₄ with a HCl solution 1M and by extracting from water the product with ethyl acetate as the organic phase. With this procedure we were able to isolate derivative **c** with a 90% yield.

Afterward the hydroxyl group has been reacted with mesyl chloride which yielded precursor **d**. By increasing the reaction times till four days, we were able to obtain a total conversion of compound **c** to the **d** one; therefore, even in this case we could avoid flash chromatography as purification step, and we were able to obtain the product with high yields just with extraction procedures. Finally, compound **d** has been converted in $F_{27}-N_3$ by nucleophilic substitution of the mesylate leaving group with sodium azide. Due to the higher hydrophobicity of the azido-derivative with respect to the other impurities, such as dimethylformamide (DMF) used as the solvent reaction, it has been possible to isolate the final product with good purity and high yields without chromatography, but just by extracting with hexane as the organic solvent.

The structure of all the intermediates just described has been confirmed by 1H -Nuclear Magnetic Resonance spectroscopy (NMR), ^{19}F -NMR and Attenuated Total Reflection Fourier-Transform Infrared spectroscopy (ATR-FTIR).

The formation of $F_{27}-N_3$ has been confirmed by ATR-FTIR with the presence of the characteristic $N=N=N$ stretching at 2100 cm^{-1} , as shown in figure 2.5.

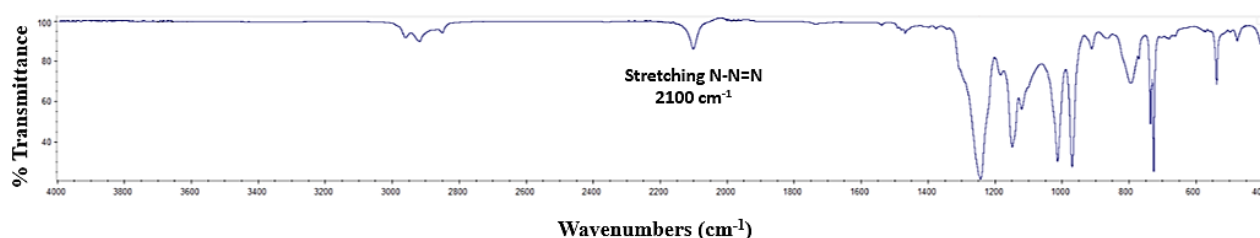


Figure 2.5 ATR-FTIR spectrum of $F_{27}-N_3$. The presence of the characteristic stretching of the azido group, at 2100 cm^{-1} , and the presence of characteristic stretching and bending of C-F between 1300 and 700 cm^{-1} confirmed the structure.

1H -NMR spectrum shows the disappearance of the signal of the protons of the ($-CH_3$) group of the mesyl derivative and the shift of the proton of the methylene group in alpha to the ($-N_3$) group in the new molecule against the same in the mesyl precursor (Δppm : 0.8) further confirming the $F_{27}-N_3$ formation. Moreover, the presence in the ^{19}F -NMR spectrum of an intense single peak is another confirmation of the purity of the compound. Figures 2.6 and 2.7 show the comparison between the 1H -NMR and ^{19}F -NMR spectra of derivative **d** and $F_{27}-N_3$.

The synthesis of dendrimers has been carried out following both a convergent and a divergent method. According to the convergent-like synthetic procedure, the new architectures were obtained by separately synthesizing the propargyl ester of the I, II and III generation Bis-MPA dendrons (DG_1 , DG_2 , and DG_3) and then by reacting them with $F_{27}-N_3$. On the other hand, we were also able to obtain the three fluorinated amphiphiles by directly growing the generation of the polyester dendron starting from FDG_1 ; therefore, by following a divergent-like procedure.

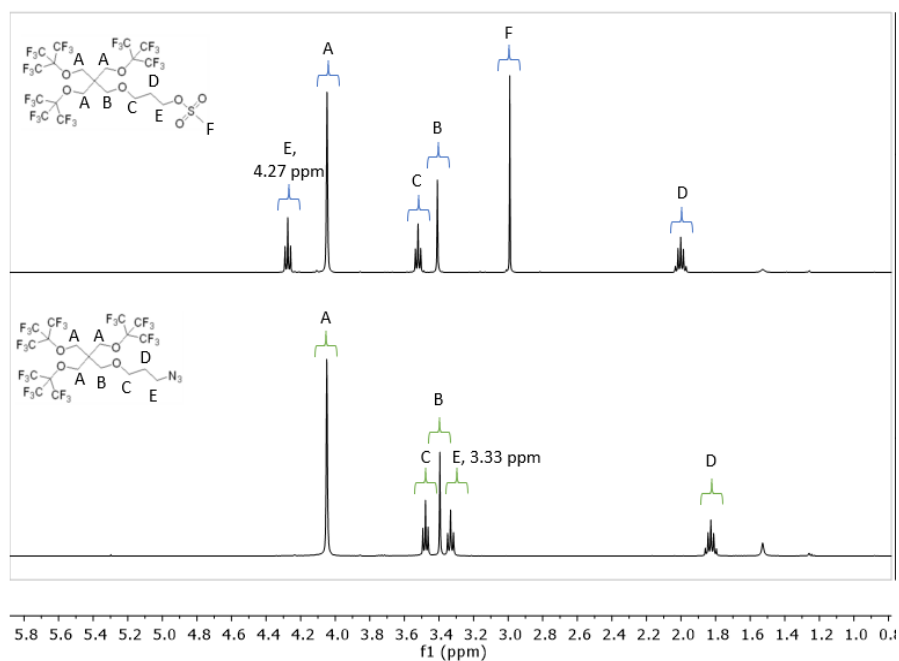


Figure 2.6 Comparison between the $^1\text{H-NMR}$ spectrum of the $\text{F}_{27}\text{-N}_3$ derivative and its mesyl precursor (compound **d**). Solvent: CDCl_3 .

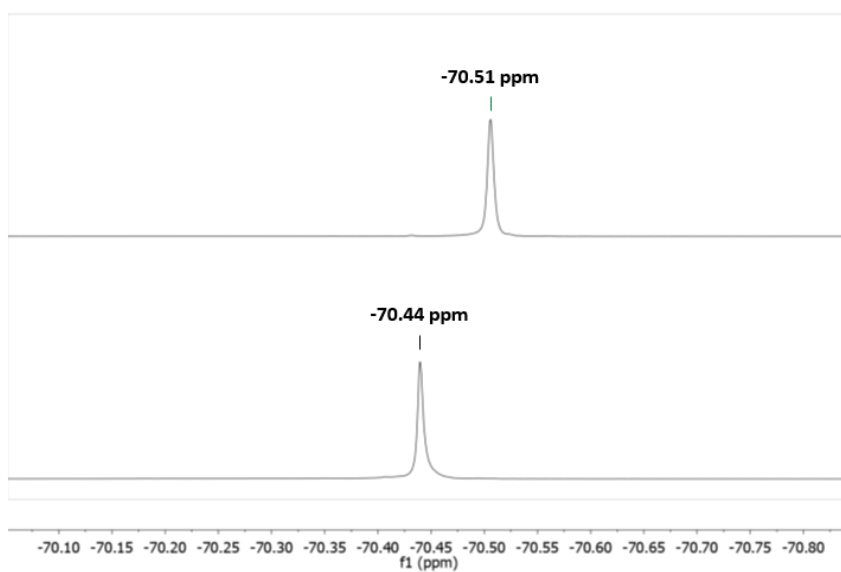


Figure 2.7 Comparison between the $^{19}\text{F-NMR}$ spectrum of $\text{F}_{27}\text{-N}_3$ (down) and compound **d** (up). Solvent: CDCl_3 .

Synthesis of FDG_1 , FDG_2 and FDG_3 by following a convergent-like methodology

The convergent method consists of coupling the different functionalized dendrons at their complementary cores, as shown in figure 2.8.

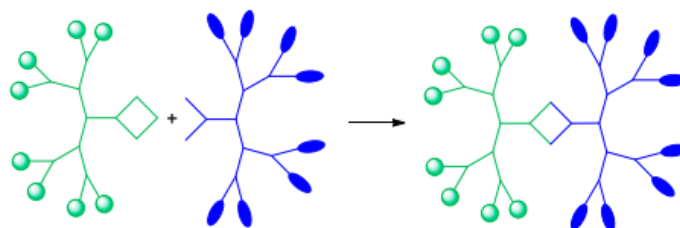


Figure 2.8 Synthesis of amphiphilic Janus Dendrimers through a convergent method. Reprinted with permission from [118].

Therefore, in our convergent-like approach we first synthesized the propargyl ester of the three Bis-MPA dendrons and then we exploited the CuAAC coupling with the F₂₇-N₃ moiety. The convergent method is generally the most used and similar procedures have been already reported in literature [118][119][120][121].

As shown in figure 2.9, the strategy requires the acetonide protection of the hydroxyl groups of Bis-MPA to form derivative **1**.

In the next step, derivative **1** is reacted with propargyl alcohol to obtain the propargyl ester derivative **2** which, after purification by flash chromatography and acetonide deprotection under acidic conditions, yielded the I generation Bis-MPA derivative (DG₁) suitable for the CuAAC reaction.

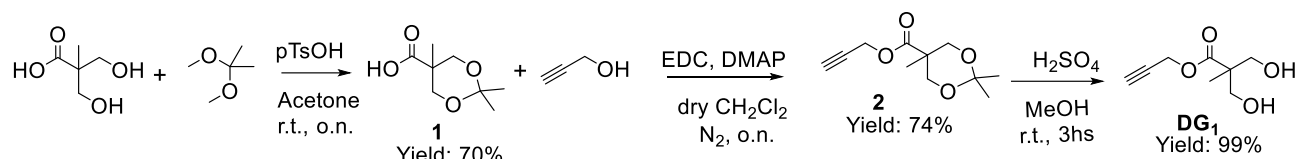


Figure 2.9 Reaction procedure adopted for the synthesis of DG₁.

To promote the ester formation, we decided to exploit the Steglich esterification, in presence of 1-ethyl-3-(3-dimethylaminopropyl)carbodiimide hydrochloride (EDC), whose chemical structure is shown in figure 2.10a, and a catalytic amount of 4-dimethylaminopyridine (DMAP) that accelerate the reaction, a schematic illustration of the mechanism of the Steglich esterification is given in figure 2.10b.

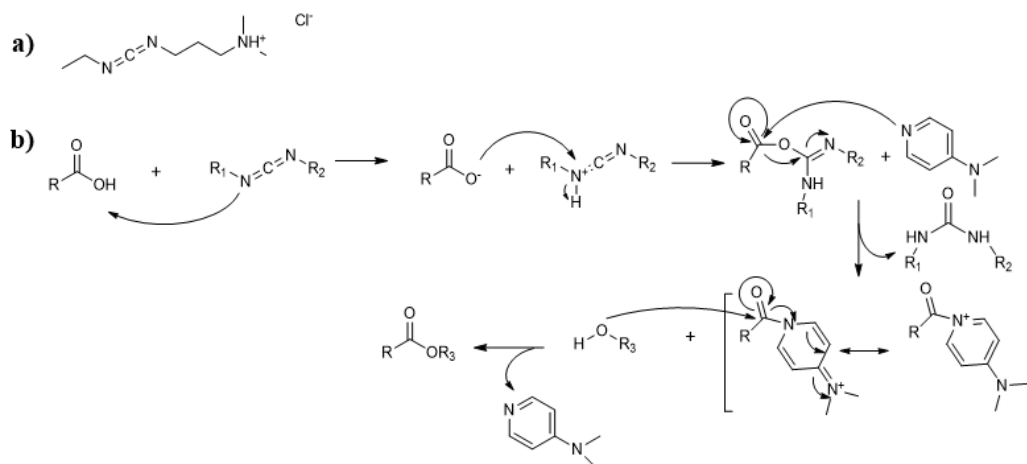


Figure 2.10 a) EDC structure. b) Mechanism of the Steglich esterification [122].

As shown in figure 2.11, the generation growth was run by the iterative alternation of the addition of the acetonide protected Bis-MPA (derivative **1**) to the smallest dendron by Steglich esterification followed by acetonide deprotection in presence of sulphuric acid.

The purification of each acetonide protected intermediate was done by column chromatography on silica gel. After the deprotection step, DG₁, DG₂, and DG₃ were purified by filtrating on celite the (NH₄)₂SO₄ salt obtained after the addition of a NH₄OH solution (30%) used to neutralize the acid.

As a high confirmation of the hydrophilicity of these dendrons, DG₁, DG₂, and DG₃ are soluble in water. In fact, after deprotection we could not isolate the polyester dendrons with extractions from water, due to their higher affinity to water than for the organic solvents generally used for extraction procedures; therefore, since precursors **3** and **4** were pure and the reaction produces byproducts can

be removed by rotary evaporation, we used DG₁, DG₂, and DG₃ directly for the next reaction without further purification.

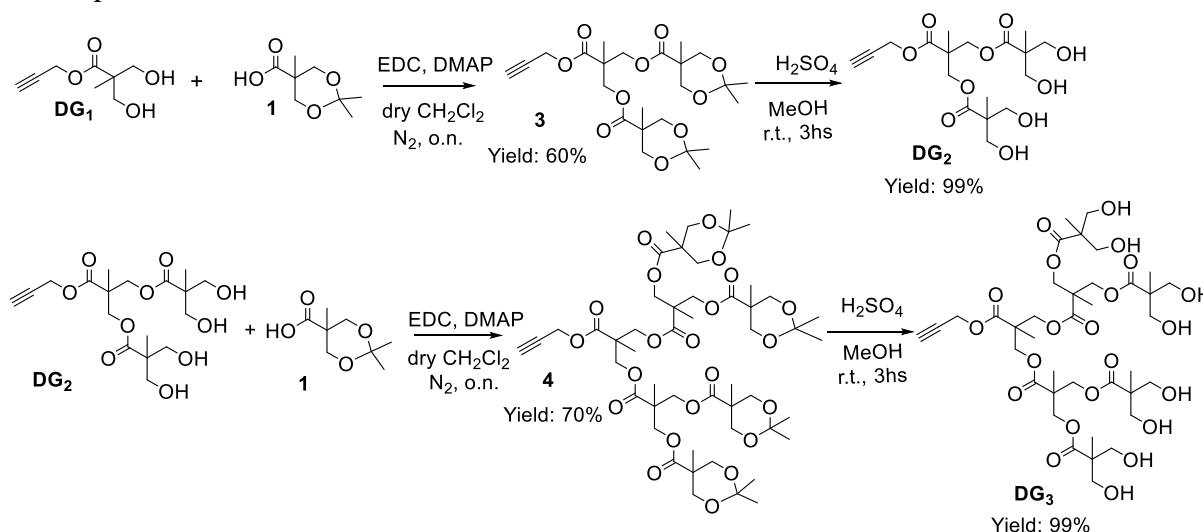


Figure 2.11 Synthesis of the higher generation dendrons DG₂ and DG₃.

As catalyst, copper can be used as copper (I) salt or as copper (II) salt in presence of sodium ascorbate which reduces in situ copper (II) in Cu (I) [116]. For our synthesis, we tried both CuI, copper acetate (I), and CuSO₄ in presence of sodium ascorbate in order to find the best reaction conditions. While we were not able to isolate the products of interest by using Cu (II), we isolated FDG₁, FDG₂, and FDG₃ in good yields by directly adopting copper (I) salts. The procedure is shown in figure 2.12 and further information are given in section 2.3. No particular differences in terms of yields, conditions or purification steps were found by changing CuI with copper acetate.

The main differences between the two catalysts are strictly related to the lower stability of CuI in organic solvents [116]: in fact, the click reaction catalyzed with CuI worked only by using dimethylformamide (DMF) as solvent while with copper (I) acetate the same products were obtained both by using tetrahydrofuran (THF) and DMF.

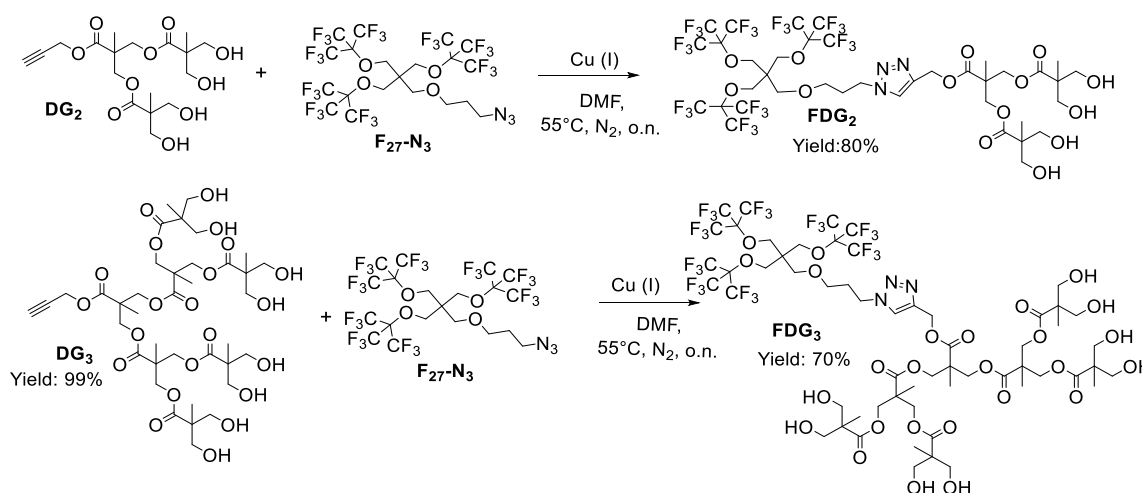


Figure 2.12 Synthesis of FDG₁, FDG₂, and FDG₃ by reacting F₂₇-N₃ with DG₁, DG₂ and DG₃.

Synthesis of FDG₁, FDG₂ and FDG₃ by following a divergent-like methodology

The divergent approach is an exponential-like growth where a branched core is iteratively decorated with branching units, as highlighted in figure 2.13.

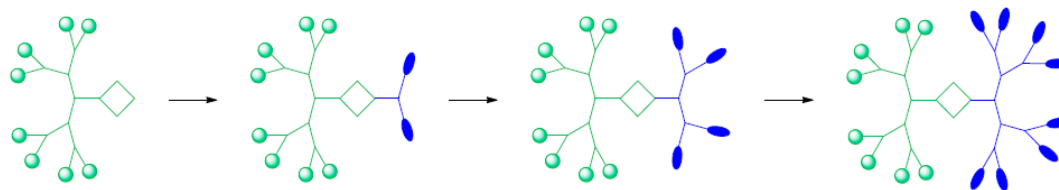


Figure 2.12 Synthesis of amphiphilic Janus Dendrimers through a divergent method. Reprinted with permission from [118].

In our case the FDG₁₋₃ synthesis started by coupling the azide derivative (F₂₇-N₃) to the acetonide protected propargyl ester of Bis-MPA, compound **2**, as shown in figure 2.14.

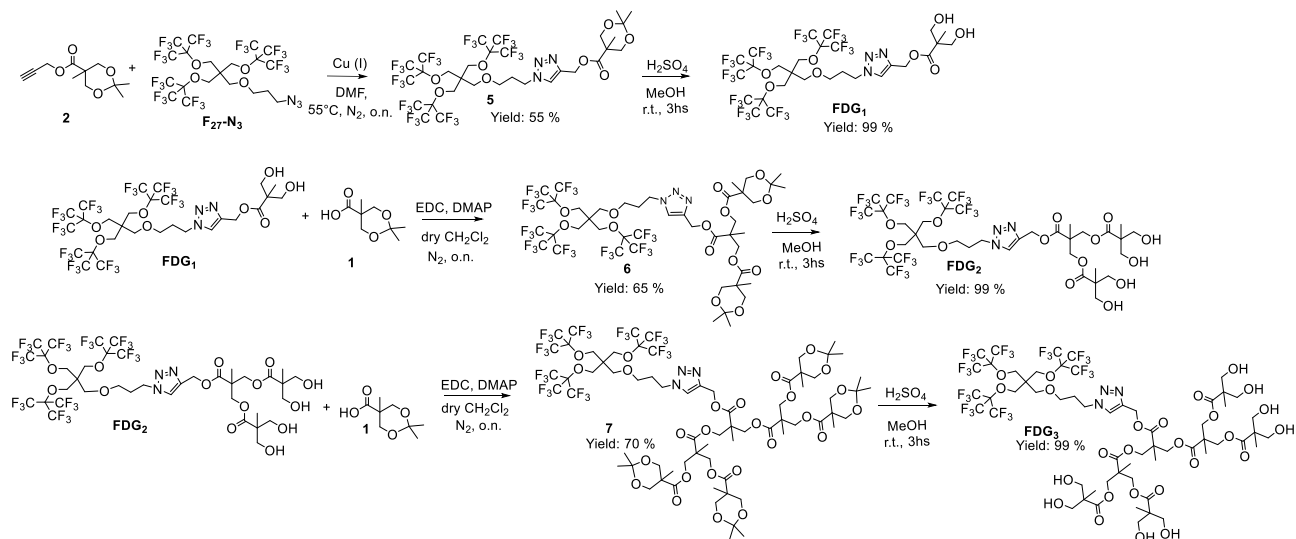


Figure 2.13 Divergent-like method: reaction steps.

The deprotection of compound **5** under acidic condition gave the first generation dendron FDG₁. Further coupling with derivative **1** by Steglich esterification followed by the acidic acetonide deprotection afforded to the higher generation dendrons FDG₂ and FDG₃. In this case each coupling reaction was followed by flash chromatography on silica gel while the final deprotected compounds were filtered on celite and dried from the solvent. The presence of the fluorinated part in the three molecules lowers their polarity; in fact, it was possible to extract the molecules from water with dichloromethane as the organic phase.

The structure of the final amphiphiles have been confirmed by ¹H-NMR and ¹⁹F NMR spectra. The appearance of the signal of the proton of the triazole ring (\approx 8ppm) combined with the shift, of about 1.07 ppm of the protons of the methylene group in alpha to the nitrogen against those in the F₂₇-N₃ precursor confirmed the formation of FDG₁, FDG₂ and FDG₃. The presence of one single peak in ¹⁹F-NMR confirmed the presence of only one fluorinated compound. In figure 2.15 and 2.16 the ¹H-NMR and ¹⁹F-NMR spectra of the three amphiphiles in comparison with those of their fluorinated precursor (F₂₇-N₃) are reported.

Further demonstrations of the formation of FDG₁, FDG₂, and FDG₃ were achieved by the ATR-FTIR analysis of the final compounds compared to their precursors. Figure 2.17 shows the comparison between the ATR-FITR spectrum of FDG₁ and its precursors, DG₁ and F₂₇-N₃, while in table 2.1 are reported the characteristics peaks observed for the three amphiphiles. The disappearance of the N=N=N stretching at 2100 cm⁻¹ of the F₂₇-N₃ reactant combined with the \equiv C-H stretching (3300 cm⁻¹) switching off of the alkyne terminating dendritic precursors gave evidence of the successful

conversion into the desired products. Furthermore, the presence of the characteristic stretching of the polyester dendrons, such as the C=O stretching at 1730 cm^{-1} and the O-H stretching between $3600\text{--}3100\text{ cm}^{-1}$, together with the presence of the C-F stretching and bending from 1300 and 700 cm^{-1} confirmed the linking between the two molecules.

Further structural confirmation of the three amphiphiles were obtained by High Resolution Electrospray Ionization Mass Spectrometry (HRESI-MS) which confirmed the chemical composition of FDG₁, FDG₂, and FDG₃.

Both the synthetic methodologies were highly efficient affording to FDG₁₋₃ with good yields. The coupling reactions applied in both the convergent and divergent methods afforded to the desired ester with yields around 70% while the acetonide deprotection occurred almost quantitatively in all cases. The click reactions occurred generally with high yields. The synthesis of FDG₃ through the convergent approach afforded for the click reaction a slightly lower yield (60%) compared with those obtained with the lower generation polyester dendrons. This is probably related to the higher steric hindrance given by the polyester branches of DG₃ which make less accessible the alkyne group during the click reaction.

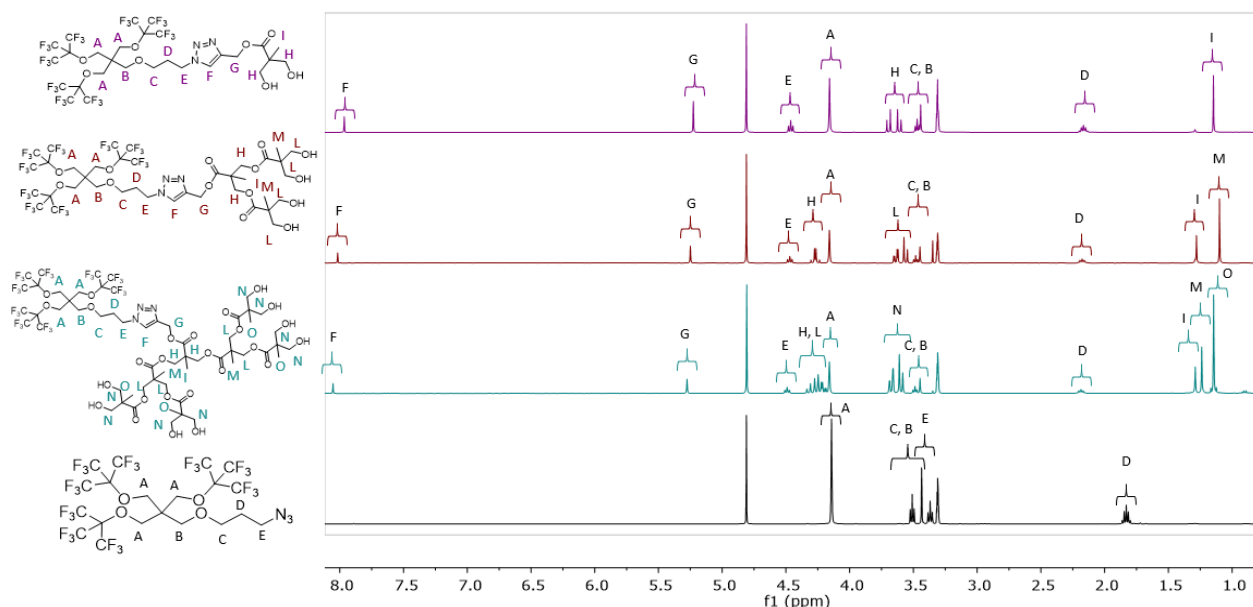


Figure 2.15 Comparison between $^1\text{H-NMR}$ spectra of FDG₁ (violet), FDG₂ (red), and FDG₃ (light blue) and their fluorinated precursor (F₂₇-N₃, black). Solvent: CD₃OD.

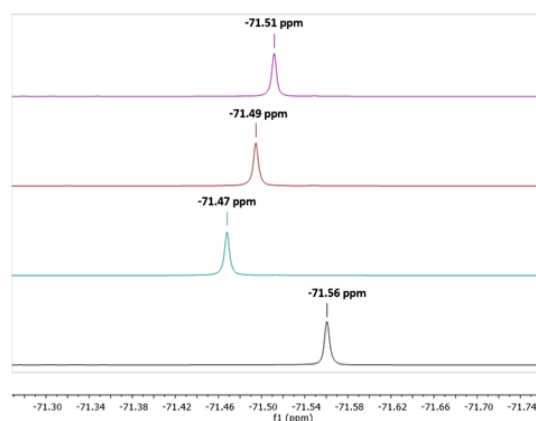


Figure 2.16 Comparison between $^{19}\text{F-NMR}$ spectra of FDG₁, FDG₂, and FDG₃ and their fluorinated precursor (F₂₇-N₃). Solvent: CD₃OD.

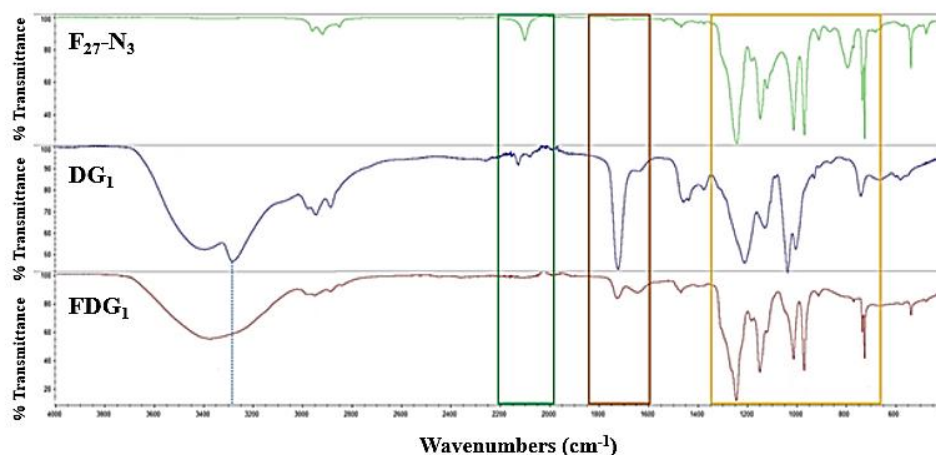


Figure 2.17 ATR-FTIR spectra comparison between FDG_1 , the DG_1 alkyne terminating precursor, and F_{27-N_3} . The disappearance of the characteristic stretching of the $N=N=N$ group of F_{27-N_3} at 2100 cm^{-1} , highlighted in the green rectangle, and the disappearance of the $\equiv\text{C-H}$ stretching of the DG_1 precursor at 3300 cm^{-1} , blue dotted line, confirmed the linkage between the two molecules. Furthermore, the presence of the C=O stretching at 1731 cm^{-1} and of the characteristic stretching and bending of the C-F groups in the range between 1300 cm^{-1} and 700 cm^{-1} confirmed the structure of FDG_1 .

Table 2.1 ATR-FTIR spectra. Characteristic peaks of FDG_1 , FDG_2 and FDG_3 .

Compound	Characteristic peaks
FDG_1	<ul style="list-style-type: none"> • Stretching O-H: 3380 cm^{-1} • Stretching C-H: $3000\text{-}2850\text{ cm}^{-1}$ • Stretching C=O: 1731 cm^{-1} • C-F stretching and bending: $1300\text{-}700\text{ cm}^{-1}$
FDG_2	<ul style="list-style-type: none"> • Stretching O-H: 3400 cm^{-1} • Stretching C-H: $3000\text{-}2850\text{ cm}^{-1}$ • Stretching C=O: 1734 cm^{-1} • C-F stretching and bending: $1300\text{-}700\text{ cm}^{-1}$
FDG_3	<ul style="list-style-type: none"> • Stretching O-H: 3401 cm^{-1} • Stretching C-H: $3000\text{-}2850\text{ cm}^{-1}$ • Stretching C=O: 1732 cm^{-1} • C-F stretching and bending: $1300\text{-}700\text{ cm}^{-1}$

2.1.2 Characterization of FDG_1 , FDG_2 and FDG_3 in bulk

It is known that the properties of dendritic architectures shown in bulk are strictly dependent on their size, shape, surface/interior chemistry, flexibility/compressibility, the parameters grouped in the so-called *critical nanoscale design parameters*, characteristics which strictly depend on the generation number of the dendritic architectures [37]. Furthermore, the properties observed in bulk are connected to the self-assembling behavior in solution [45].

Therefore, since FDG_1 , FDG_2 , and FDG_3 show an increasing generation number in their hydrophilic part while they display the same hydrophobic moiety, we decided to analyze the behavior of these three new amphiphiles both in bulk and in solution in order to discover how and if the increase in generation of the polar polyester scaffold affects the properties in bulk and in solution and how these are correlated.

The solid-state characterization of FDG_1 , FDG_2 , and FDG_3 has been done by different techniques which include single crystal and powder X-Ray diffraction, small and wide-angle X-Ray scattering (SWAXS), polarized optical microscopy (POM), thermogravimetric analysis (TGA) in nitrogen

atmosphere and differential scanning calorimetry (DSC). The single crystal structure of FDG₁ was collected at Elettra-Sincrotrone in Trieste thanks to the work of Dr. N. Demitri who collected the structure and Dr. A. Pizzi from Politecnico of Milan who resolved the structure. SWAXS was done in collaboration with Prof. B. Donnio from the Institut de Physique et de Chimie des Matériaux de Strasbourg who also performed TGA and DSC analyses which were in accordance with those collected in our laboratories.

FDG₁: a crystalline dendritic amphiphile

Examples of single crystal structures of polyester dendrimer-based molecules are reported in literature [123] and most of them are characterized by the presence in their structure of high directional groups which can interact by hydrogen bonding and π - π interactions between aromatic groups [97][100] [124]. Generally, the degree of crystallinity decreases by increasing the generation number of the dendritic architecture [125]. According to this, only FDG₁ was isolated as a white homogeneous crystalline solid. We were also able to obtain single crystals by slow evaporating a solution of FDG₁ dissolved in a mixture of acetonitrile and toluene (1:10 v/v).

Single crystals were measured at 100 K by means of synchrotron radiation. As shown in figure 2.18A, FDG₁ crystallizes in the triclinic P-1 space group, with the unit cell containing two dendritic molecules related by a crystallographic inversion center. Precisely, two facing FDG₁ molecules share the π -surface of their triazole rings, the latter being stacked in antiparallel fashion. In addition to π -stacking, the structure grows along the crystallographic axis *b* thanks to a network of hydrogen bonds involving hydroxyl groups and triazole rings of neighbor molecules.

As shown in figure 2.18B, a network of hydrogen bonds stabilizes the crystal structure: the nitrogen in position 3 (N3) in the triazole ring is a hydrogen bond acceptor and interacts with the hydrogen bound to one of the hydroxyl groups (O-H---N3) of the adjacent FDG₁ molecule. Each oxygen in the carbonyl group of FDG₁ is a hydrogen bond acceptor for the adjacent hydroxyl group of FDG₁ (O-H---O=C).

In table 2.2 are reported the distances and angles of hydrogen bonds involved in the crystal structure. The incompatibility between fluorocarbon and hydrocarbon groups forces their segregation, producing a lamellar structure with a regular alternation of fluorinated and non-fluorinated regions (figure 2.18C). Of note, the fluorocarbon layers are tightly packed, with an entangled system of weak F...F interactions that confers further stability to this supramolecular architecture. In FDG₁ the fluorinated molecule ends segregate into double layer where their cross-sectional area imposes the molecular area of the whole sequence of layers; in fact, the polar parts, represented by the I generation polyester dendron, form an intercalated monolayer to compensate for their smaller cross-sectional area. It is reasonable that similar interaction patterns are involved in the self-assembly of the higher generation dendritic amphiphiles (FDG₂ and FDG₃).

The comparison between the diffractogram obtained by powder diffraction and those extrapolated from the single crystal structure are superimposable (figure 2.19), thus confirming that the crystal structure obtained is representative of the whole solid. In case of FDG₁ the presence of the triazole ring, suitable for π - π interactions, together with the presence of the carboxyl groups of the polyester moiety and the presence of the branched polyfluorinated part, whose crystalline properties are well known [97], are at the bases of the crystallinity observed for FDG₁. DSC and SWAX analyses, whose results are reported in figure 2.20, confirmed the crystallinity of FDG₁ in the pristine state. As shown in figure 2.20b, the compound melts around 90°C to an isotropic liquid phase and freezes to a glassy

state on cooling. Only one crystal phase is observed. In table 2.3 are reported the dimensions obtained from the SWAXS analysis of FDG₁. Each FDG₁ molecule shows a higher surface area of the fluorinated part compared to the hydroxyl-terminating moiety, in accordance with geometric parameters.

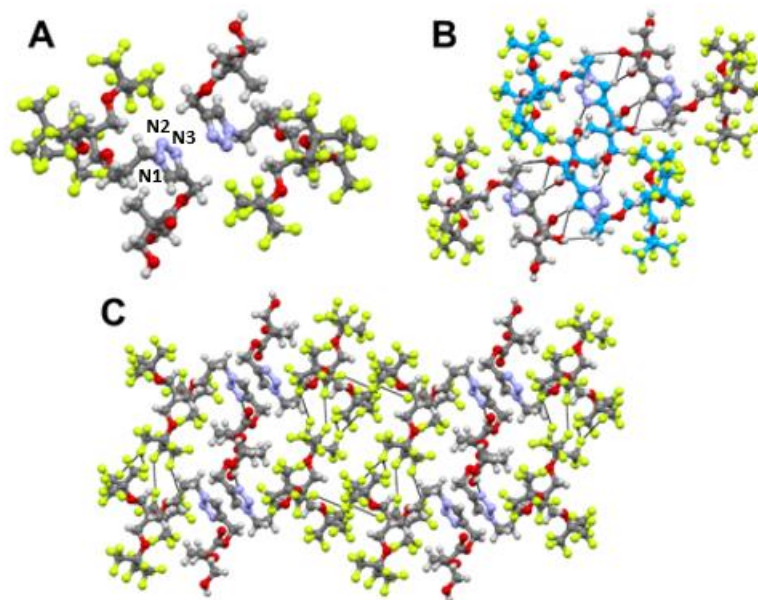


Figure 2.18 X-Ray structure of FDG₁. **A)** Dimers formed by antiparallel stacking. **B)** Network of hydrogen bonds stabilizing the hydrocarbon regions formed by the packing of FDG₁ molecules **C)** Fluorine-fluorine interactions next to $\pi\cdots\pi$ stacking generate a layered structure. Color code: C, dark grey or light blue; H, light grey; F, yellowish green; O, red; N, violet; Short contacts are depicted as black dotted lines.

Table 2.2 Distances and angles of the main hydrogen bonds involved in the stabilization of the polyester polar part in the crystal structure of FDG₁.

Atoms involved	Distances (Å)	Angles
O-H---N3	2.75	116°
O-H---O=C	2.72	112°

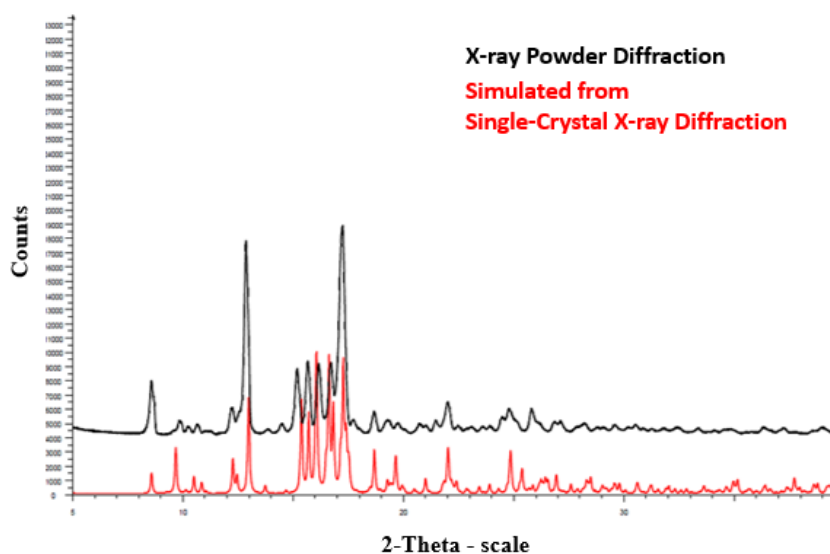


Figure 2.19 Comparison between the diffraction pattern observed from single crystal X-Ray diffraction and powder X-Ray diffraction for FDG₁.

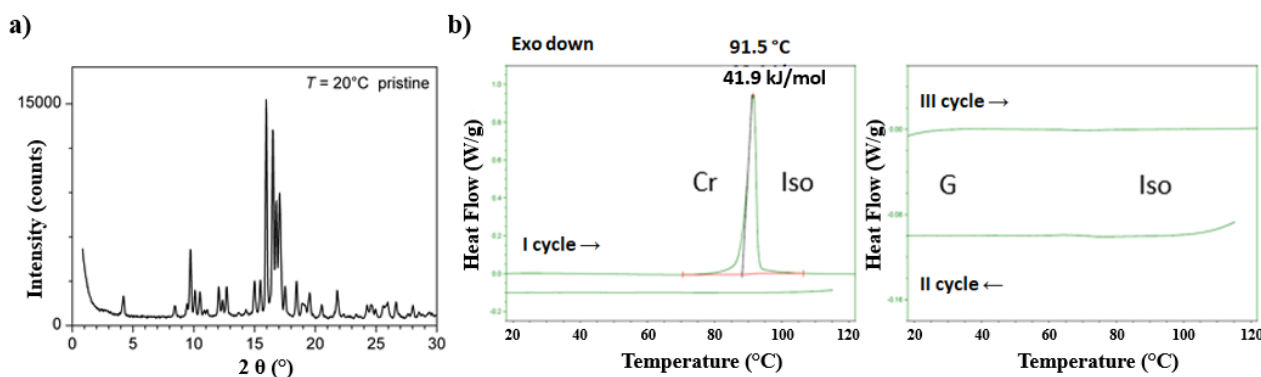


Figure 2.20 a) SWAXS diffractogram obtained at 20°C. b) DSC results: the first cycle shows a high energetic endothermic transition from a crystalline phase (Cr) to isotropic liquid phase (Iso) which is not observed on cooling (II cycle) and a on further heating (III cycle). The solid phase is amorphous (G: glassy).

Table 2.3 FDG₁: dimension parameters obtained from SWAX analysis.

Temperature (°C)	V_{mol} (Å ³)	d_{mol} (Å)	A_{mol} (Å ²)	σ_{pol} (Å ²)	σ_{F27} (Å ²)
20	1035	21	50	50	100

V_{mol} = Volume of the sequence of layers; d_{mol} = length of the sequence of layers; $A_{\text{mol}} = V_{\text{mol}}/d$ = area of the sequence of layers; σ_{pol} = cross-sectional area of the hydroxyl terminating ends; σ_{F27} = cross-sectional area of the fluorinated ends.

FDG₂: a liquid crystalline fluorinated amphiphile

Generally, the increase in generation causes a loss of crystallinity. In fact, FDG₂ is only partly crystallized in the pristine state (Cr-G) and is isolated as a sticky, pale yellow solid.

DSC and POM analyses (Figure 2.21) revealed that FDG₂ melts at 72°C to a quite fluid and non-birefringent mesophase (Cub) and exhibits a low-energetic (0.29 kJ/mol) and reversible transition around 104°C to an isotropic liquid phase (Iso). It is important to note that all these transitions occur at temperature below the degradation temperature of FDG₂. This liquid crystalline behavior can be explained considering the high tendency of fluorinated moieties to microsegregation.

The presence of a single peak at low angles in SWAXS pattern precluded phase identification, however, the total absence of birefringence at POM suggested the formation of a cubic mesophase, which is frozen during the cooling to room temperature in the glassy solid state.

In general, the liquid crystalline (LC) state is characterized by orientational or positional order in at least one direction and no fixed position for individual molecules. When only orientational order occurs, molecules adopt a parallel alignment to minimize steric hindrance and maximize intermolecular interactions; in such cases nematic phases are formed (N). When mesogens adopt a periodicity in one or two directions smectic phases (Sm) and columnar phases (Col) are formed respectively. Mesophases with periodicity in all the three dimensions can occur and cubic mesophases (Cub) are the main representatives. Cub mesophases are optically isotropic and therefore appear dark at POM [126][127][128]. Table 2.4 shows the geometric parameters obtained from SWAXS analyses.

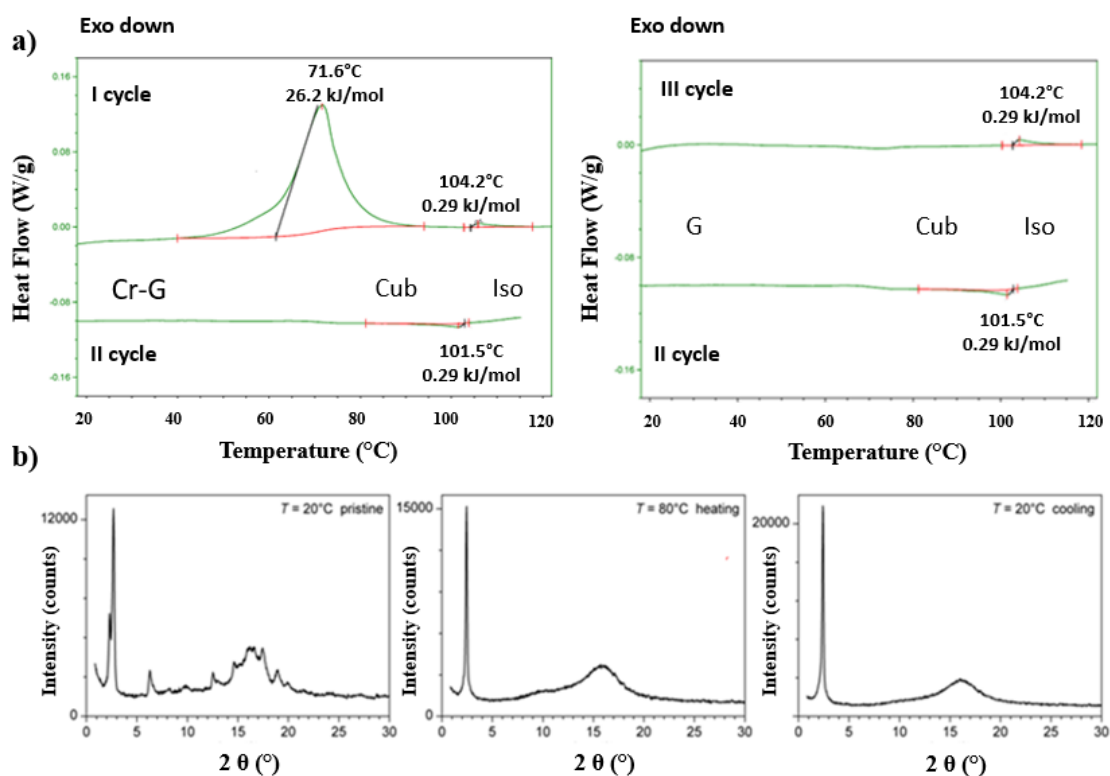


Figure 2.21 FDG₂ mesophases. **a)** DSC results. **On the left:** heating cycle (I cycle) and cooling cycle (II cycle); **on the right:** cooling cycle (II cycle) and second heating cycle (III cycle). **b)** SWAX analyses of FDG₂ in the pristine state at 20°(left), at 80°C (middle) and on cooling at 20°C (right).

Table 2.4 FDG₂: dimension parameters obtained from SWAX analysis.

Temperature (°C)	V _{mol} (Å ³)	d _{mol} (Å)	A _{mol} (Å ²)	σ _{F27} (Å ²)
20	1295	36	36	72

V_{mol} = Volume of the sequence of layers; d_{mol} = length of the sequence of layers; A_{mol} = V_{mol}/d = area of the sequence of layers; σ_{F27} = cross-sectional area of the fluorinated ends.

FDG₃: a polymorphic fluorinated dendritic amphiphile

As already discussed, the increase in the polyester dendron generation, causes changes in the ratio between the fluorinated branched part and the hydroxyl terminating moiety which consequently affect the self-assembly in bulk. Even in case of FDG₃, the increase in the Bis-MPA-based dendron affects the thermal behavior of the amphiphile. FDG₃ showed the coexistence of several phases (Cr-G) in the pristine state and showed a broad transition at 86°C at DSC, as shown in figure 2.22a, where it flowed to a liquid suspension, suggesting that a partial melting was occurring, as confirmed even by the SWAXS pattern observed at 90°C (figure 2.22c). This can suggest the presence of several polymorphs of FDG₃ which display a different thermal behavior [129][130]. Similar behaviors are reported in literature for polyester dendritic amphiphiles of the same generation [131] thus suggesting that the increased mobility of the polyester chain can induce the organization of the molecules in different morphologies responsible for the formation of different polymorphs. The low energetic transition at 106°C showed the presence of a birefringent phase at POM (figure 2.22b) whose pattern can suggest a lamellar liquid crystalline mesophase (Lam) [132]. The degradation of the compound which occurs on further heating prevents the detection of the clearing temperature for the compound.

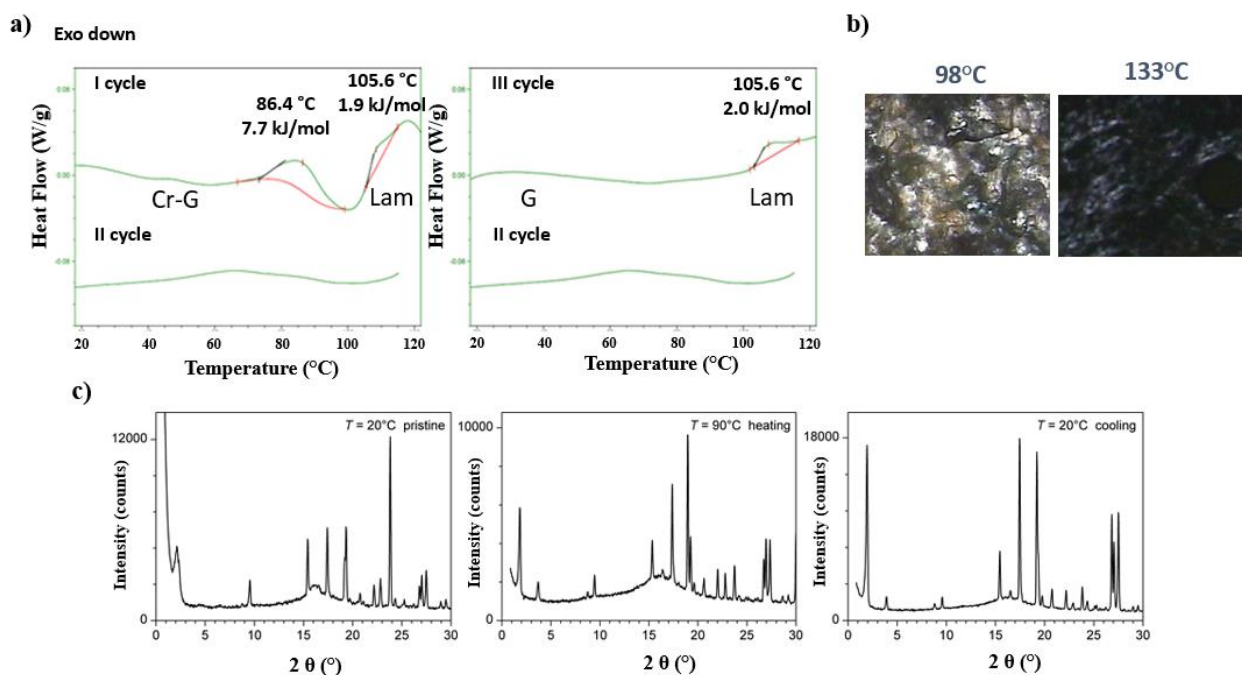


Figure 2.22 Thermal behavior of FDG₃. **a)** DSC results. **On the left:** heating cycle (I cycle) and cooling cycle (II cycle); **on the right:** cooling cycle (II cycle) and second heating cycle (III cycle). **b)** POM images: at 98°C a partial melting occurs; at 133°C birefringence is observed: the pattern suggests the reaching of a lamellar LC phase. **c)** SWAX analyses of FDG₃ in the pristine state at 20°C (**left**), at 90°C (**middle**) and on cooling at 20°C (**right**).

Thermal stability of FDG₁, FDG₂ and FDG₃ in comparison with F₂₇-N₃

The thermal stability of FDG₁, FDG₂ and FDG₃ was determined by TGA analysis and has been compared to those of their fluorinated precursor (F₂₇-N₃). As shown in figure 2.23, the linkage of the fluorinated precursor to the I generation polyester dendron affords to a high thermal stability. In fact, while F₂₇-N₃ showed a 5% weight loss at temperature close to 110°C (T5%) and a total degradation at around 170°C, FDG₁ showed a T5% at around 200°C after which the degradation continues progressively till the total decomposition of the compounds at up to 300°C. These values are in good agreement with degradation temperatures reported in literature by first generation Bis-MPA-based polyester dendrimers [120][133][131].

If compared to FDG₁, FDG₂ showed a slightly higher T5% degradation which occurs at 248°C while the total decomposition occurs at temperature close to 380°C. This means that by increasing the generation number the temperature stability of the amphiphile increases, data which are in accordance with other similar dendritic architectures reported in literature [120][133][131].

FDG₃ decomposes in a two-step process, with a first 10% weight loss at around 200°C; followed by a progressive weight loss till its total degradation that occurs at temperature higher than 400°C. This thermal degradation behavior has already been reported in literature and generally it is observed for high generation polyester dendrimers [120][131]; it can be related to the degradation of the external outer layer followed by degradation of the inner strata. This behavior can be associated to the increase in mobility of the polyester moiety which can confer a reduction in the packing density of the polar part due to a higher disorder related to entanglement of the polyester chains [131].

In this section the properties of FDG₁, FDG₂ and FDG₃ in bulk have been reported. The high tendency to microsegregation of polyfluorinated segment is clearly seen in the crystal structure of FDG₁ and is further supported by the formation of a liquid crystalline phase for FDG₂. Increasing the dimension of the polyester dendron, the ratio between the apolar and polar parts changes; this causes variations in the bulk morphology.

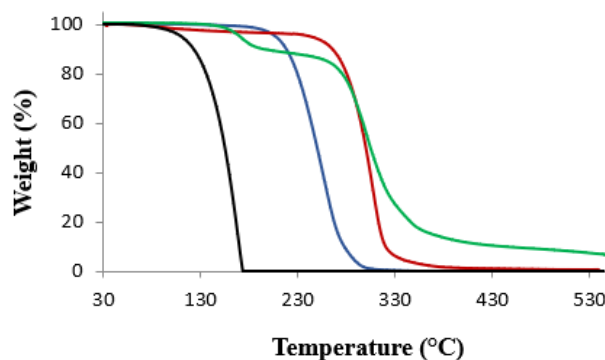


Figure 2.4 TGA analyses. Comparison between the results obtained for FDG₁, FDG₂ and FDG₃ and their fluorinated precursor F₂₇-N₃. Color code: F₂₇-N₃ = black, FDG₁ = blue, FDG₂ = red, FDG₃ = green.

2.1.3 Self-assembly of FDG₁, FDG₂ and FDG₃ in water

In this section the self-assembling properties of FDG₁, FDG₂ and FDG₃ will be described. FDG₁₋₃ are not directly soluble in water; therefore, we decided to exploit a procedure already used in literature to disperse Janus dendrimers in water. Generally, these molecules can be dispersed in water by the direct injection of a solution of the dendrimers in a water-miscible organic solvent, such as alcohols, acetone, methyl ethyl ketone (MEK), 1,4-dioxane, tetrahydrofuran (THF), and acetonitrile. Other methodologies can be based on the reverse injection of water to a solution of the dendrimers in the previously mentioned organic solvents or on the film hydration method. Since the last two methodologies generally bring to the formation of aggregates of bigger dimensions, we started with the direct injection in water [44][46]. We decided to use as water miscible organic solvent ethanol since FDG₁, FDG₂, and FDG₃ are soluble in this solvent and because it has been widely used in literature for this purpose [44][45][47]. Since the size of the aggregates depends on the concentration of the dendritic amphiphile, we tried different concentrations for the three dendrimers, as shown in table 2.5.

The general procedure employed requires the dissolution of FDG₁, FDG₂, and FDG₃ in ethanol; then, the organic solution is fast injected in a precise volume of water, afterward the obtained dispersion is mixed by means of a vortex mixer at low speed (8 rpm), further information is given in section 2.2. In the following paragraphs, we will refer to this procedure as the ethanol in water procedure. By increasing the final concentration of the three molecules, we noted an increased tendency to precipitate for FDG₁, and FDG₂, while FDG₃ showed an increase in turbidity. This could be related to the formation of aggregates of bigger dimensions. In order to compare the behavior of the three dendritic amphiphiles, we focused the attention on the dispersions obtained by adding a 10mg/mL ethanolic solution of the dendrimer in 2mL of water. Due to the different molecular weight of the three compounds, the final concentration of the three amphiphiles is different. Therefore, FDG₁ and FDG₂ dispersions have also been prepared accordingly to get a final concentration of 0.3mM, as those of FDG₃.

FDG₁, FDG₂ and FDG₃ can be dispersed in water by exploiting the ethanol in water procedure just described. The dispersion obtained has been analyzed by DLS, ¹⁹F-NMR and Cryo-TEM during time in order to study the aggregates stability.

Table 2.5 Ethanol in water procedure: weights, volumes, concentrations, and characteristics.

Compound	Weight (mg) (± 0.01)	Volume of Ethanol	Concentration in Ethanol	Water volume	Final Concentration	Stability
FDG ₁	1.1	100 μ L (5% v/v)	10 mg/mL	2 mL	0.5 mM	No precipitation
FDG ₂	1.0	100 μ L (5% v/v)	10 mg/mL	2 mL	0.4 mM	No precipitation
FDG ₃	1.1	100 μ L (5% v/v)	10 mg/mL	2 mL	0.3 mM	No precipitation
FDG ₁	0.7	100 μ L (5% v/v)	6.6 mg/mL	2 mL	0.3 mM	No precipitation
FDG ₂	0.8	100 μ L (5% v/v)	8 mg/mL	2 mL	0.3 mM	No precipitation
FDG ₃	1	100 μ L (8% v/v)	10 mg/mL	1.2 mL	0.4 mM	Slightly milky
FDG ₁	2.0	100 μ L (5% v/v)	20 mg/mL	2 mL	0.9 mM	Precipitation after 24 hs
FDG ₂	2.0	100 μ L (5% v/v)	20 mg/mL	2 mL	0.8 mM	Precipitation after 24 hs
FDG ₃	2.0	100 μ L (5% v/v)	20 mg/mL	2 mL	0.6 mM	Milky
FDG ₁	1.5	100 μ L (5% v/v)	15 mg/mL	2 mL	0.7 mM	Precipitation after 24 hs
FDG ₂	1.5	100 μ L (5% v/v)	15 mg/mL	2 mL	0.6 mM	Precipitation after 24 hs
FDG ₃	1.5	100 μ L (5% v/v)	15 mg/mL	2 mL	0.4 mM	Milky, slightly precipitate after 24 hs

FDG₁

Table 2.6 shows the solvent composition and the concentrations tested for FDG₁ in solution.

Table 2.6 Self-assembly of FDG₁: concentrations tested.

Compound	Weight (mg) (± 0.01)	Volume of Ethanol	Concentration in Ethanol	Water volume	Final Concentration
FDG ₁	1.1	100 μ L (5% v/v)	10 mg/mL	2 mL	0.5 mM
FDG ₁	0.7	100 μ L (5% v/v)	6.6 mg/mL	2 mL	0.3 mM

As already told previously in the introduction, ^{19}F -NMR is a highly sensitive technique: depending on the environment to which fluorine atoms are exposed, shifts of the peaks in the NMR spectra can be detected. It has been demonstrated that ^{19}F -NMR is a powerful technique to study changes in the aggregate shape [134][135]. DLS and Cryo-TEM analyses of the dispersions gave further information about the dimension and the shape of the aggregates. Figure 2.24 shows the results obtained by DLS and ^{19}F -NMR, while table 2.7 gives further information about the polydispersity and the hydrodynamic radii observed for the two dispersions overtime.

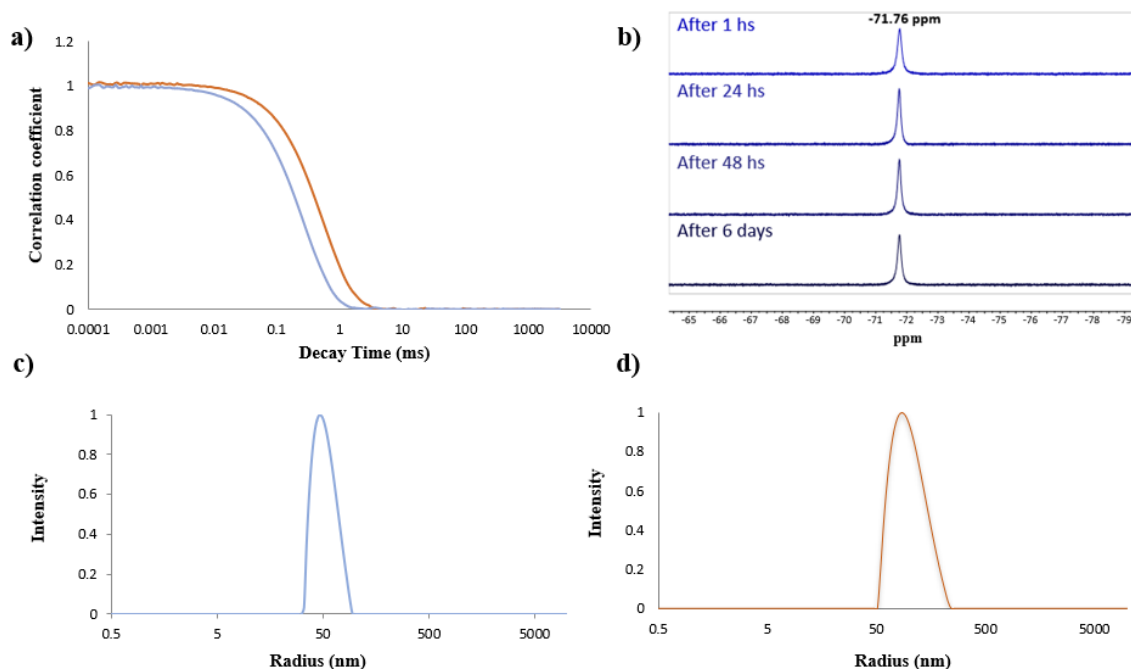


Figure 2.24 a) Comparison between the correlation functions at 90° of FDG₁ 0.3mM and 0.5mM; b) ^{19}F -NMR of FDG₁ 0.3mM overtime. Solvent: solution + D₂O (10% v/v). c) The hydrodynamic radii observed at DLS for FDG₁ at 0.3mM after 24 hs from the sample preparation d) the hydrodynamic radii observed at DLS for FDG₁ at 0.5mM after 24 hs from the sample preparation.

In DLS the decay electric field correlation factor or correlation function, $g(\tau)$, decays exponentially accordingly to equation 2.1, and is dependent on the decay constant, Γ , for macromolecules.

$$g(\tau) = e^{-\Gamma\tau} \quad \text{Equation 2.1}$$

The decay constant, Γ , is directly related to the diffusion behavior of macromolecules (D) which is inversely proportional to the hydrodynamic radius, the radius of a hypothetical sphere that diffuses at the same rate as the particle under investigation and that can be obtained using the Stokes–Einstein equation [136].

Therefore, lower is the exponential decay of the correlation function, higher is the hydrodynamic radius obtained by DLS fitting.

As shown in figure 2.24a, the correlation function of FDG₁ 0.3 mM decay faster than those of the same molecule at higher concentration: lower is the concentration, smaller is the diameter of the aggregates obtained. This is in accordance with literature [45]: it has been demonstrated in fact that, generally, an increase in concentration causes an increase in the aggregates' dimensions. Furthermore, the aggregates formed by FDG₁ are stable overtime till 6 days from the sample preparation; in fact, no significant variations are observed in the hydrodynamic radii of the aggregates, as shown in table 2.7, and in the ^{19}F -NMR spectra, in figure 2.24b.

In order to better understand the shape of the aggregates, FDG₁ dispersion at concentration 0.5 mM were imaged at Cryo-TEM thanks to the collaboration with Professor Nonappa from Tampere University of applied sciences in Finland.

Table 2.7 On the left: polydispersity index (PdI) and hydrodynamic radii (cumulant fitting, 90°) observed for FDG₁ 0.3mM overtime; on the right: polydispersity index (PdI) and hydrodynamic radii (cumulant fitting, 90°) observed for FDG₁ 0.5mM overtime.

FDG ₁ 0.3 mM			FDG ₁ 0.5 mM		
Time	PdI	Hydrodinamic Radius (nm)	Time	PdI	Hydrodinamic Radius (nm)
1 hs	0.2	47 ± 2	1 hs	0.2	75 ± 4
24 hs	0.1	51 ± 2	24 hs	0.1	84 ± 4
48 hs	0.1	52 ± 3	48 hs	0.1	80 ± 4
6 days	0.1	55 ± 3			

Cryo-TEM images (figure 2.25) showed the coexistence of two types of spherical aggregates which differentiate for their size. A statistical analysis of the imaged aggregates reveals that the 57.5% of the total number of aggregates show an averaged size of 14 nm of diameter, while the 42.5% show an averaged size of 105 nm of diameter.

At DLS, FDG₁ 0.5 mM revealed a nearly monodisperse system with low PdI and a hydrodynamic radius of about 80nm. Differently, in Cryo-TEM images two populations are found and in both cases the sizes are much smaller than those observed at DLS.

This is strictly related to the characteristics of the techniques used. The hydrodynamic radii reported in figure 2.24d are based on the intensity-weighted distribution described in equation 2.2.

$$\%I_a = \frac{a^6 \cdot 100}{N_a a^6 + N_b b^6} \quad \text{Equation 2.2}$$

The intensity distribution for a solution containing a certain number of aggregate **a** and **b** (N_a , N_b) with size a and b respectively depends to their sizes to the sixth power. When in a solution two family of aggregates of different dimensions are present, those with the biggest dimension influence much more the final value. The hydrodynamic radius is an averaged value which overestimate the real size of the object [136].

In conclusion, the results obtained indicate that FDG₁ can be dispersed in water where it forms stable spherical aggregates during time. The aggregates can be divided in two groups: small micelles of about 14 nm of diameter and bigger spherical aggregates of around 100 nm.

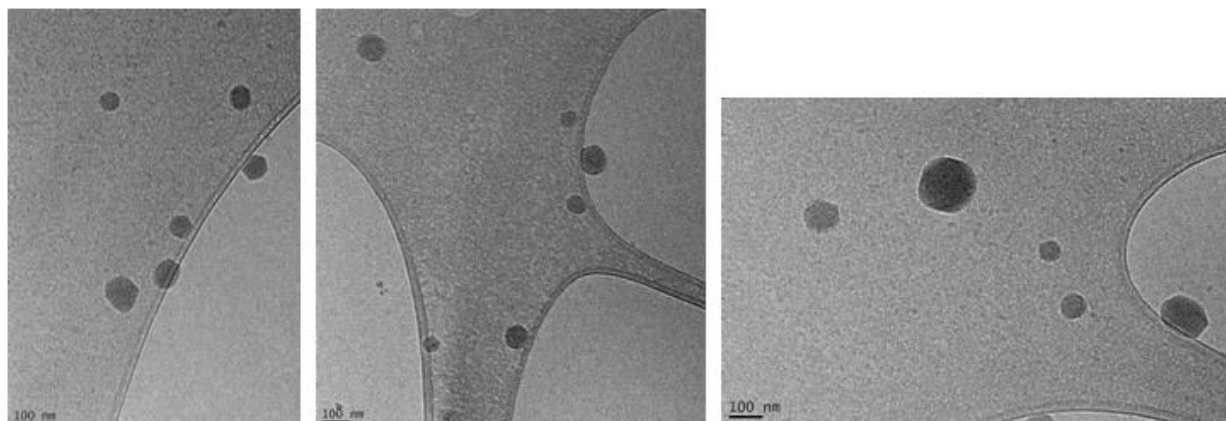


Figure 2.25 FDG₁ (0.5mM): Cryo-TEM images show the coexistence of spherical aggregates which can be divided in two groups depending on their size. Scale bar:100 nm.

FDG₂

FDG₂ can be dispersed in water by the ethanol in water procedure and table 2.8 summarizes the concentration tested for FDG₂.

Table 2.8 Self-assembly of FDG₂: concentrations tested.

Compound	Weight (mg) (± 0.01)	Volume of Ethanol	Concentration in Ethanol	Water volume	Final Concentration
FDG ₂	1.0	100 μ L (5% v/v)	10 mg/mL	2 mL	0.4 mM
FDG ₂	0.8	100 μ L (5% v/v)	8 mg/mL	2mL	0.3 mM

As for FDG₁, even FDG₂ self-assembles by forming aggregates which are stable up to six days as confirmed by both DLS and ¹⁹F-NMR. In fact, as shown in figure 2.26b, no significant changes are observed in the NMR spectra during time. Differently from FDG₁ where the change in the concentration influences the aggregate dimensions, for FDG₂ the influence of the concentration seems to less affect the aggregates dimensions. This can be related to the small differences between the concentrations tested for FDG₂, which differ only for 0.1mM. In fact, as shown in figure 2.26a, the correlation functions obtained at DLS from the two concentrations of FDG₂ showed the same decay time; a further confirmation of this can be obtained by comparing the mean hydrodynamic radii obtained from the two concentrations and reported in table 2.9. In fact, DLS fitting gave similar hydrodynamic radii.

Since the scattering objects are characterized by the same contrast and the same shape, the intensity-weighted distribution obtained at DLS (figure 2.26c) can be converted to the number-weighted distribution (figure 2.26d) that represents the number of molecules in each bin in a given histogram. The number-weighted distribution can be calculated as follow:

$$\%N_a = \frac{N_a \cdot 100}{N_a + N_b} \quad \text{Equation 2.3}$$

Where, N_a and N_b are molecules with size a and b respectively [136].

In this case the dependency on the size is not at the sixth power, and the radius observed is only calculated on the base of the number of aggregates with the same dimensions.

DLS showed the presence of two family of aggregates where the smaller one is the predominant.

Cryo-TEM images confirmed this conclusion; in fact, FDG₂ showed the presence of two types of aggregates where the most representative are the smallest one, as shown in figure 2.27. A statistical analysis of the imaged aggregates reveals that the 87.4% of the total number of micelles shows an averaged size of 14 nm of diameter, while only the 12.6% shows an averaged size of 52 nm of diameter.

As discussed in section 2.1.2, FDG₂ form cubic mesophases in bulk; in literature is reported that dendritic architectures which in bulk show cubic mesophases tend to self-assemble in solution by forming micelles [45]. FDG₂ is in line with this consideration; in fact, the high majority of the aggregates formed by FDG₂ are micelles of small dimensions.

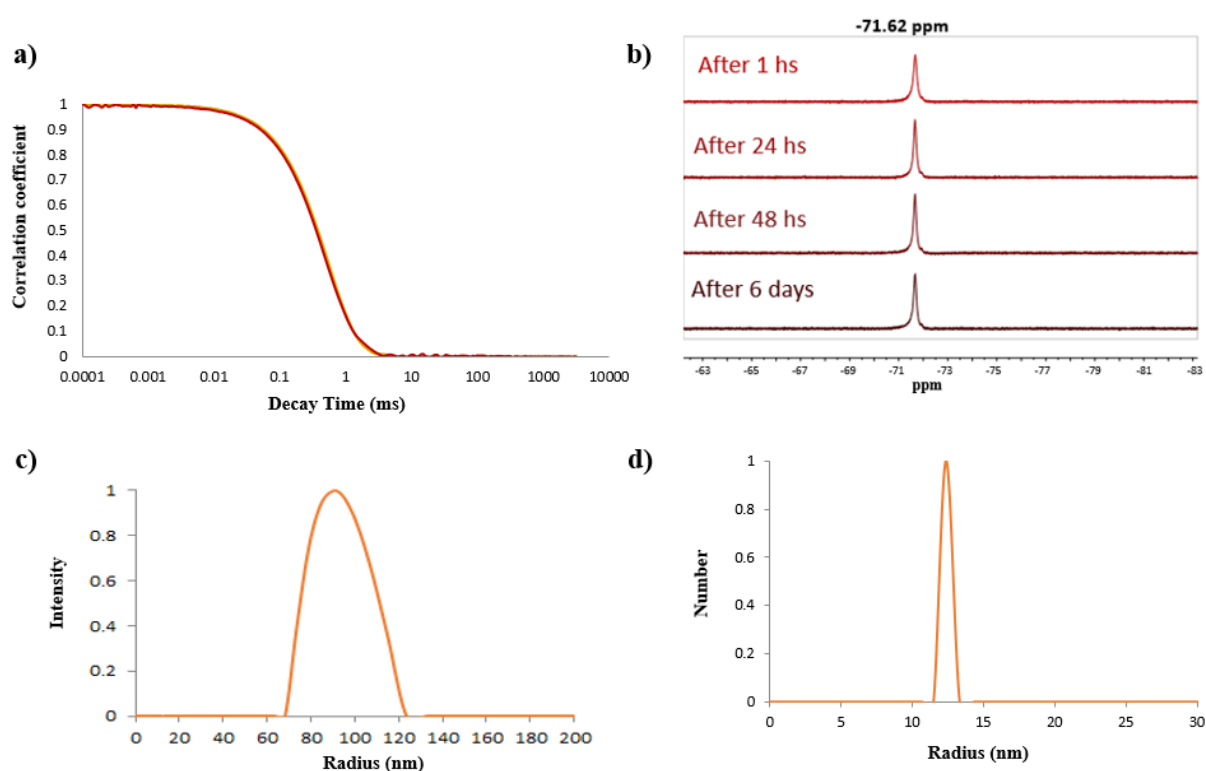


Figure 2.26 **a)** Comparison between the correlation functions at 90° of FDG₂ 0.3mM and 0.4mM; **b)** ¹⁹F-NMR of FDG₂ 0.3mM overtime. Solvent: solution + D₂O (10% v/v). **c)** the intensity-weighted hydrodynamic radius observed at DLS for FDG₁ at concentration 0.4mM after 48hs from the sample preparation. **d)** The number-weighted radius observed at the same concentration and time. Color code: FDG₂ 0.3 mM = red; FDG₂ 0.4 mM = orange.

Table 2.9 **On the left:** polydispersity index (PdI) and hydrodynamic radii (cumulant fitting, 90°) observed for FDG₂ 0.3mM overtime; **on the right:** polydispersity index (PdI) and hydrodynamic radii (cumulant fitting, 90°) observed for FDG₂ 0.4mM overtime.

FDG ₂ 0.3 mM		
Time	PdI	Hydrodynamic Radius (nm)
1 hs	0.2	72 ± 4
24 hs	0.1	73 ± 4
48 hs	0.2	70 ± 3
6 days	0.1	70 ± 3

FDG ₂ 0.4 mM		
Time	PdI	Hydrodynamic Radius (nm)
1 hs	0.1	78 ± 4
24 hs	0.1	74 ± 4
48 hs	0.1	74 ± 4

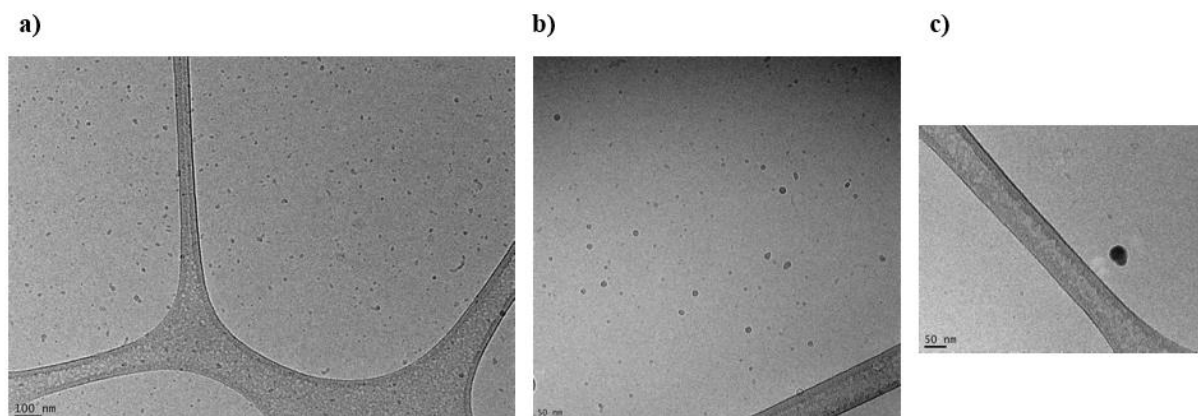


Figure 2.27 FDG₂ (0.4mM): Cryo-TEM images show the coexistence of spherical aggregates which can be divided in two groups depending on their size where the small-sized micelles are the main representative. **c)** A small number of bigger aggregates is present. Scale bar: **a)** 100 and **b, c)** 50 nm. Images were taken from Professor Nonappa.

FDG₃

Contrary to FDG₁ and FDG₂ which formed stable dispersions in water during time, a different behavior has been observed for FDG₃. In this section only the concentration 0.3mM will be described. Table 2.10 summarizes the composition of the tested FDG₃ dispersion.

Table 2.10 Self-assembly of FDG₃: concentration tested.

Compound	Weight (mg) (± 0.01)	Volume of Ethanol	Concentration in Ethanol	Water volume	Final Concentration
FDG ₃	1.1	100 μ L (5%)	10 mg/mL	2 mL	0.3 mM

As shown in figure 2.28, both DLS and ¹⁹F-NMR results revealed a change in the properties of the aggregates. The correlation function showed a significant increase of decay time and polydispersity index for the sample tested after 48 hours from its preparation. Simultaneously, a quenching of ¹⁹F NMR signal was observed. In fact, the intensity of the peak at -71.4ppm, clearly visible in the freshly prepared formulation, decreases over time till its total switching off after 48 hours from the sample preparation. Since no precipitation occurred during time, this tendency would suggest a reduced mobility of the CF₃ groups which could be related to the changes in morphology of the self-assembled structures, as suggested from literature [33].

Cryo-TEM analyses helped us to better explain what occurs during the sample aging. As shown in figure 2.29, the as prepared sample showed the presence of multilayer vesicles, denoted as dendrimersomes, whose average diameter is 70 nm, composed of up to six layers with an interlayer distance of 5 nm and a layer width of 20 nm. Upon ageing the solution at room temperature for 24 hours, vesicles start to interact and fuse with each other forming sheet like structures which gradually wrap around themselves giving rise to helical nanostructures which finally after 48 hours evolve in tubule-like structures. After 6 days of ageing just tubules are present.

A schematic illustration of the transition is given in figure 2.30.

This wide variety of morphologies, seen only for FDG₃ and absent in the case of lower generation dendrimers, would suggest the possibility to control the self-assembly behavior of dendritic amphiphiles by tuning the balance between their hydrophilic and hydrophobic portions.

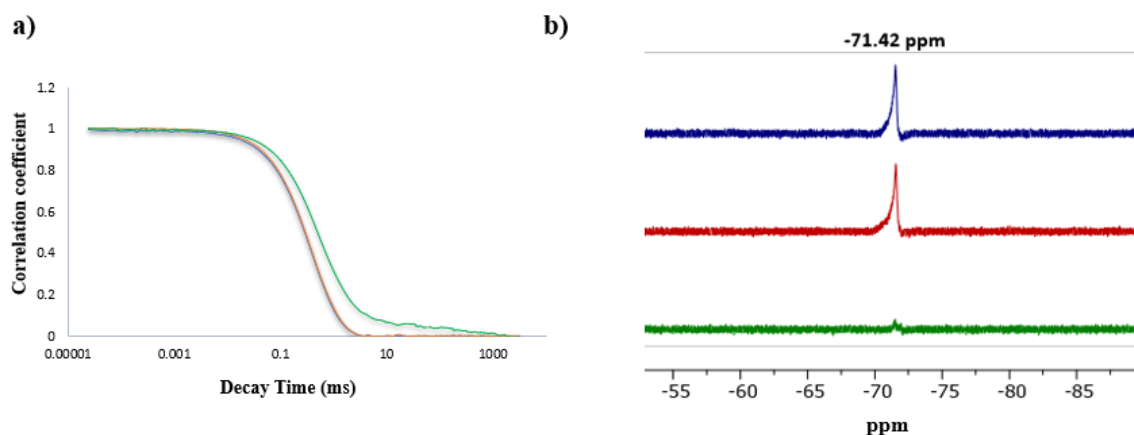


Figure 2.28 a) Comparison between the correlation functions at 90° of FDG_3 0.3mM; b) ^{19}F -NMR of FDG_3 0.3mM overtime. Solvent: solution + D_2O (10% v/v). Color code: same day of preparation = blue, after 24 hs = red, after 48 hs = green.

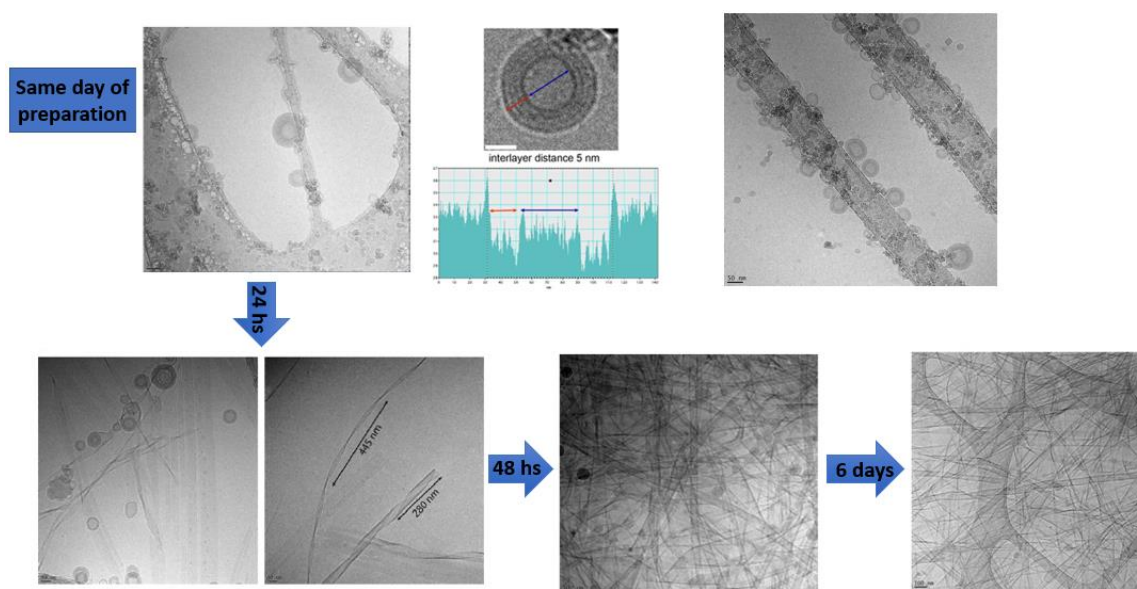


Figure 2.29 Cryo-TEM images during time. FDG_3 undergoes morphology transition from dendrimer vesicles to tubes. Taken by Professor Nonappa.

Taking into account the higher hydrophobicity of fluorinated modules and their tendency to segregate from water, we reasoned that probably the formation of multi-layered vesicles in the as prepared sample should be driven by a synergic action of fluorine-fluorine interactions, occurring between the fluorinated moieties, and hydrogen bonding involving the polar moieties. This would allow the formation of fluorinated double layers where the hydroxyl groups are exposed outside in contact with water molecules. This is further supported by the intrinsic tendency to crystallization of multibranched fluorinated molecules containing the same 27F group [93]. As suggested by cryo-TEM analyses and supported by literature [1], FDG_3 multi-layered vesicles are metastable kinetic aggregates which tend to evolve in the thermodynamic ones merging with each other and forming tubule-like structures. This transition from aggregates with higher curvature, the vesicles, to other morphologies with lower curvature, like tubules, would produce an increased structure rigidity which can cause the switching off of the ^{19}F -NMR signal. In fact, in the case of FDG_3 , CF_3 groups probably can interact much strongly in the tubules, thus probably causing a change in the relaxation times of

the fluorine atoms in the aggregates with the subsequent switching off of the signal. A similar behavior has been already reported in literature for other fluorinated molecules [33][32].



Figure 2.30 Cartoon representation of the FDG₃ transition in solution. Images were done by Professor Nonappa.

As discussed in the introduction, the polarity and the composition of the solvent can affect the shape of the aggregates.

Therefore, we decided to analyze also formulations obtained using dimethyl sulfoxide (DMSO), tetrahydrofuran (THF), acetonitrile (CH₃CN), acetone or trifluoroethanol (TFE) as organic solvent. Direct injection of DMSO or THF solution of FDG₃ in water afforded to the formation of a precipitate; on the contrary, stable dispersions were obtained in the presence of the other organic solvents.

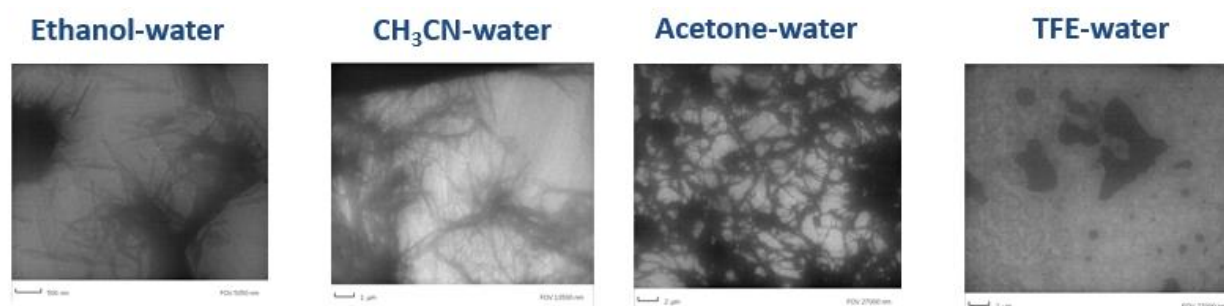


Figure 2.31 Effect of the cosolvent. TEM images showed no fibers formation after 48 hs in the dispersion obtained with TFE as cosolvent.

As shown in figure 2.31, TEM images revealed that after 48 hours fibers were present in the dispersions obtained using ethanol, CH₃CN and acetone as the organic solvent. Interestingly, no fibers were present in the case of TFE as cosolvent. Therefore, we analyzed overtime by ¹⁹F-NMR and DLS the dispersion obtained by dissolving FDG₃ in TFE (5% v/v) and adding the organic solution to 2mL of MilliQ water for a final concentration of the dendritic amphiphile of 0.3mM. As shown in figure 2.32 and in table 2.11, no significant changes in the decay time and in the hydrodynamic radii were observed during time. The peaks observed in the ¹⁹F-NMR spectra does not change after 48 hours. Trifluoroethanol seems to prevent fibers formation. Probably, the cosolvent interacts with FDG₃; thanks to fluorine-fluorine interactions with the CF₃ groups of FDG₃, TFE is able to compensate for the energy required by FDG₃ to stabilize the aggregates with higher curvature thus stabilizing vesicles.

Table 2.11 Change in the cosolvent: the effect of TFE. Polydispersity index (PdI) and hydrodynamic radii (cumulant fitting, 90°) observed for FDG₃ 0.3mM overtime.

FDG ₃ – TFE 5% v/v		
Time	PdI	Hydrodinamic Radius (nm)
1 hs	0.2	80 ± 4
24 hs	0.3	84 ± 4
48 hs	0.2	81 ± 4

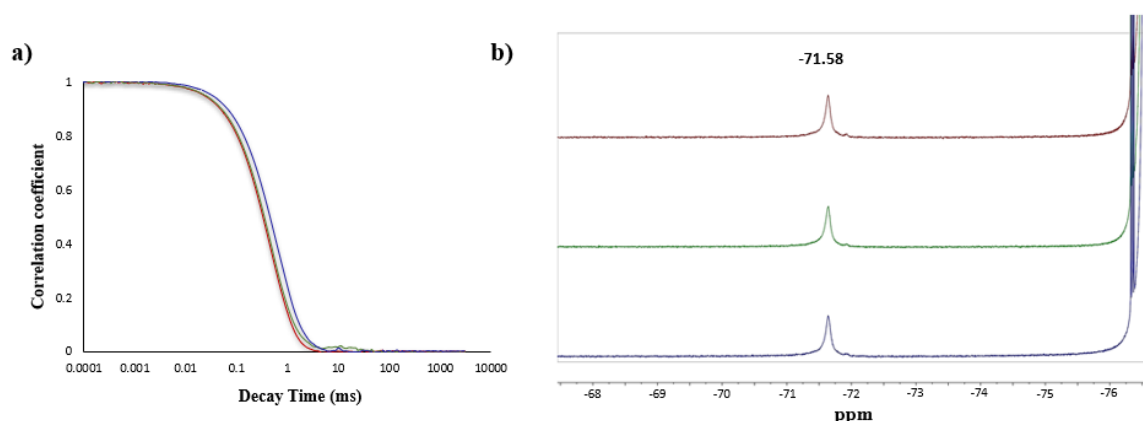


Figure 2.32 Effect of TFE as cosolvent. **a)** Comparison between the correlation functions at 90° of FDG₃ 0.3mM overtime; **b)** ^{19}F -NMR of FDG₃ 0.3mM overtime. Solvent: solution + D₂O (10%). Color code: same day of preparation = red, after 24 hs = green, after 48 hs = blue.

2.1.4 Molecular Dynamics: FDG₁, FDG₂ and FDG₃ in comparison

In order to better understand the different behavior of FDG₁, FDG₂ and FDG₃ in solution, atomistic Molecular Dynamic (MD) simulations were done, in collaboration with Professor G. Raffaini from Politecnico di Milano. In this section the self-assembling behavior of the three fluorinated dendritic amphiphiles will be compared with their energy minimized chemical structure in a cell containing water and 5% of ethanol. These conditions allow to recreate the same ones used experimentally to disperse in water the three molecules. Then, the dimensions of the three amphiphiles will be used to calculate the packing parameter which allows to correlate the size and the shape of the aggregates at equilibrium with molecular shapes and dimensions.

Energy minimization in water and ethanol (5%)

How does ethanol contribute to the dispersion of the three amphiphiles in water? To answer to this question one molecule of each amphiphile has been minimized in a box containing water and 5% of ethanol, as shown in figure 2.33.

The majority of the ethanol molecules, highlighted in green in the figure, form a sort of cage around the amphiphile with the ethyl part interacting with the hydrophobic chain of the amphiphile and the hydroxyl group of ethanol interacting with water molecules. Thanks to hydrogen bonds between water and ethanol, the ethanolic layer is probably able to better stabilize FDG₁, FDG₂ and FDG₃ in water, thus explaining why in pure water the three amphiphile are not directly dispersible.

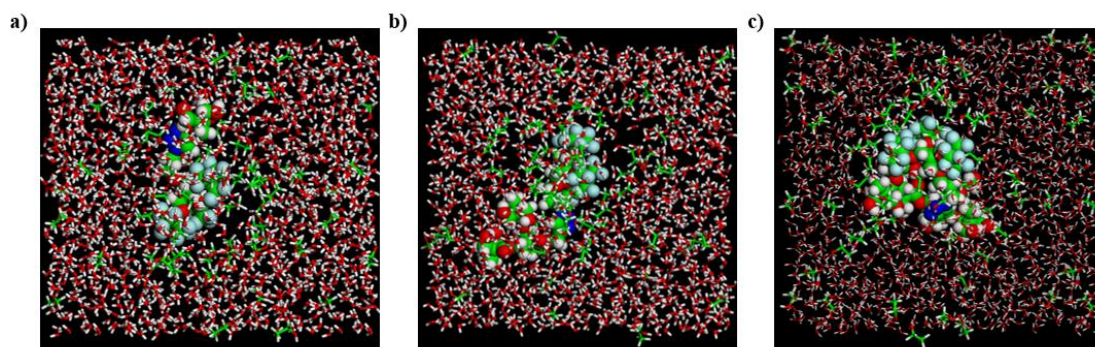


Figure 2.33 Molecular dynamics. **a)** FDG₁ (space filled) energy minimization in a box containing water and ethanol (5%); **b)** FDG₂ (space filled) energy minimization in a box containing water and ethanol (5%); **c)** FDG₃ (space filled) energy minimization in a box containing water and ethanol (5%). Color code: Oxygen = red, hydrogen = light grey, nitrogen = blue, fluorine = light blue. Ethanol molecules are highlighted in green.

Dimensions of FDG₁, FDG₂ and FDG₃: the packing parameter

Is it possible to predict the shapes of the aggregates formed by the three amphiphiles starting from the FDG₁, FDG₂ and FDG₃ dimensions through the packing parameter?

Table 2.12 shows the dimensions of the three amphiphiles minimized in water and 5% of ethanol used to calculate the packing parameters while figures 2.34 gives a schematic illustration of how the dimensions have been calculated.

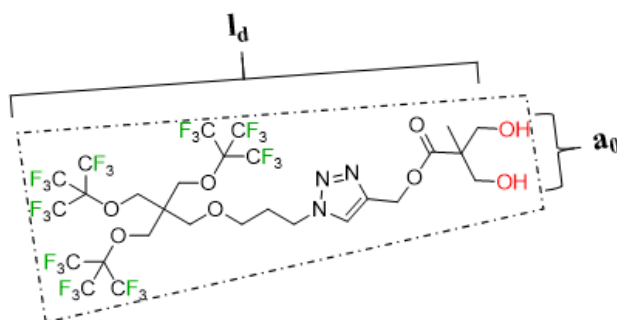


Figure 2.34 Schematic illustration of the dimensions used to calculate the packing parameters for FDG₁. The maximum extended length (l_d) has been calculated by determining the distance between the carbon atom linked to the OH group and the higher external carbon atom in CF₃. The polar surface area (a_0) has been obtained by calculating the solvent accessible area occupied by the hydroxyl groups of the amphiphile while the volume (v) is the total volume occupied by the molecule (black dotted line). The dimensions of FDG₂ and FDG₃ have been obtained in the same way.

Table 2.12 Molecular dynamics. Dimensions of the three amphiphiles minimized in water and 5% of ethanol and values of the packing parameters.

Amphiphile	Total volume (v) (Å ³)	Length (l_d): C-OH/C-F ₃ (Å)	Polar surface area (a_0) (Å ²)	Packing parameter*	Aggregates prediction
FDG ₁	803	17	157	0.30	Spherical micelles/ disk-shaped
FDG ₂	1062	21	338	0.15	Spherical micelles
FDG ₃	1508	21	702	0.10	Spherical micelles

* packing parameter = $v/(a_0 \cdot l_d)$

The packing parameter has been obtained by using the classical formula reported in table 2.12. The total volume of the minimized molecule of each amphiphile (v) has been divided for the product obtained by multiplying the solvent accessible area occupied by the hydroxyl groups (a_0) of each amphiphile and the maximum extended length of the amphiphile (l_d).

From literature, molecules showing a packing parameter < 0.33 tend to form micelles, while those with a packing parameter between 0.33 and 0.5 tend to form cylindrical or disk-shaped micelles [1]. If the experimental results are compared with the calculated packing parameter, some important considerations can be done. The packing parameter calculated for the FDG₁ is 0.30 which is close to the theoretical limit between micelles and disk-shaped micelles. Taking into account the high tendency of FDG₁ to form lamellar phases, as confirmed by the solid-state characterization, together with the value of the packing parameter, we hypothesized the formation of disk-shaped micelles. Disk-shaped micelles are bilayer micelles which generally show dimensions in the range of 30-200 nm of diameter [34].

Our experimental results revealed that FDG₁ self-assembles in water/ethanol mixtures (5% v/v of ethanol) by forming two distinct populations of aggregates in almost equal proportions: in fact, micelles of around 14 nm of diameter and bigger spherical aggregates of around 105nm coexist in the dispersion. These results are in good agreement with our predictions.

The packing parameter obtained for FDG₂, 0.15, suggests that the amphiphile tends to form micelles in solution; this is in accordance with the experimental results obtained. In fact, the amphiphile tends to self-assemble by generating almost spherical micelles of around 14 nm of diameter.

If the aggregates prediction for FDG₁ and FDG₂ are in accordance with the experimental results, a different situation is observed for FDG₃. In fact, while the packing parameter suggests that the amphiphile should self-assemble by forming micelles, experimental results revealed complex transitions from multilayer vesicles to fibers. This suggests that further considerations, other than the dimensions of the molecule, should be considered to better understand the behavior of this amphiphile in solution.

Understanding the self-assembly behavior of FDG₃: the effect of the cosolvent

Coarse-grain simulations were performed in collaboration with Dr. Angela Acocella and Professor Francesco Zerbetto from the university of Bologna (Italy). This technique allows to simplify the molecular structure of the molecule by beads able to reproduce the physico-chemical properties of a part of a molecule thus allowing to reduce the simulation times. Figure 2.35 shows the coarse-grain model adopted for FDG₃.

By molecular dynamic simulations in a box containing the FDG₃ coarse-graine model in presence of water as the solvent it was possible to observe the formation of unilamellar vesicles in presence of a low number of molecules. The number of layers increases by increasing the number of molecules of FDG₃ in the box. These results are in accordance with literature where it has been demonstrated that the number of layers in dendrimersomes depends on the final concentration of the dendritic amphiphile [45][46].

As highlighted in figure 2.36a, it was interesting to note that by reducing the hydrophilicity of FDG₃ and thus reducing the interactions between the amphiphile and water, transition from vesicles to cylinder like micelles was observed. This indicates that the strength of the interactions between the amphiphile and the solvent are at the bases of the final morphology of the aggregate.

To reproduce the experimental conditions, bites representing ethanol molecules were introduced in the box in the presence of water and the amphiphile. Interestingly, the insertion of ethanol caused a transition from vesicles to well-structured fibers thanks to the order reached by π - π interactions between the simulated triazole ring of close FDG₃ molecules, as illustrated in figure 2.36b.

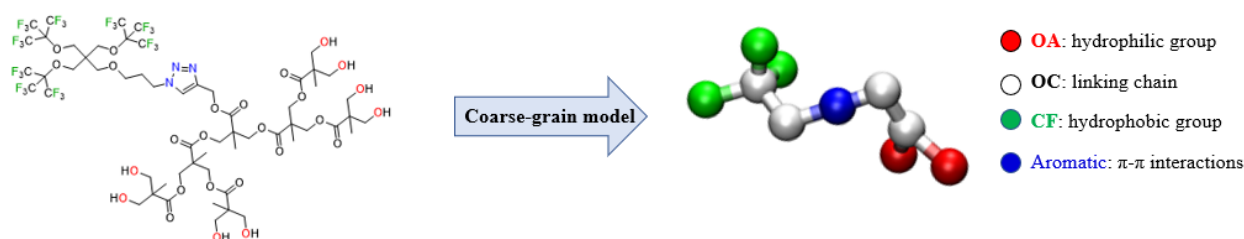


Figure 2.35 Coarse-grain model of FDG₃. The fluorinated part has been represented by three hydrophobic beads (in green), the hydroxyl terminating surface was represented by two hydrophilic beads (red) while the linking chain was mimicked with grey beads. The aromatic group has been represented with the blue bead suitable for π - π interactions.

Experimental results revealed that the substitution of ethanol with trifluoroethanol (TFE) as the cosolvent prevent the formation of fibers. Which is the reason of the different behavior observed? AMBER Molecular Dynamic simulations on FDG₃ in explicit solvent revealed that in presence of 6% of ethanol the amphiphile mostly visits bent structures with the fluorinated branched moiety and the hydrophilic polyester part arranged in a sort of *trans* conformation with an averaged dihedral

angle (θ) of about 100° , as shown in figure 2.37a. In the case of 6% of TFE, FDG₃ mostly visits bent structures with the fluorinated branched moiety and the hydrophilic groups arranged in a sort of *cis* conformation with $\theta = 56^\circ$, as illustrated in figure 2.37b.

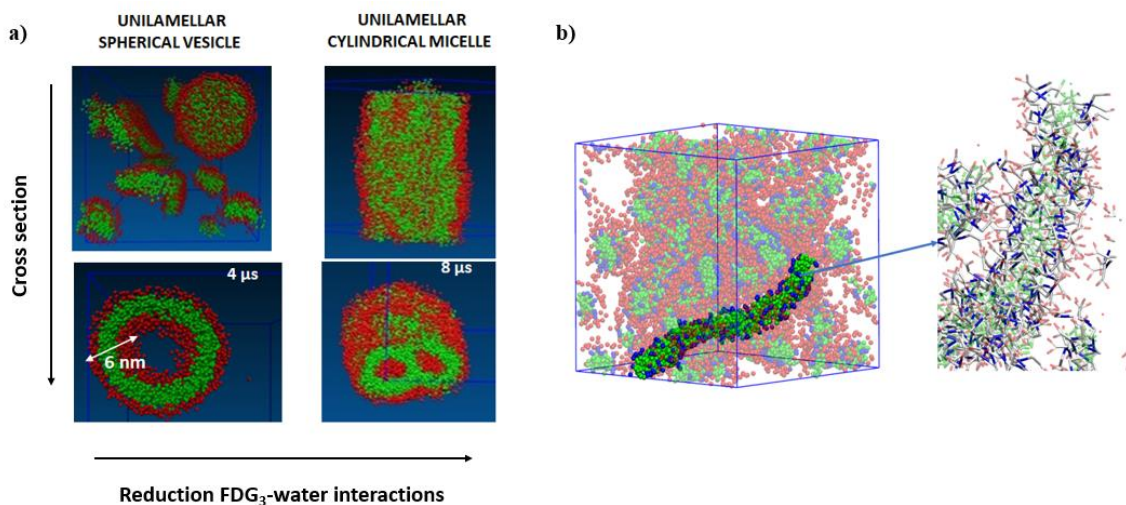


Figure 2.36 a) When interactions between FDG₃ and water are high (high hydrophilicity), unilamellar vesicles are formed (the number of layers increase by increasing the number of FDG₃ molecules in the box. Interestingly, the layer width of 6 nm is close to those observed experimentally (5 nm) thus indicating the coarse grain model well represents the chemical structure of the dendritic amphiphile. When the hydrophilicity of FDG₃ is reduced and interactions between FDG₃ molecules are maximized, cylindric micelles are formed. b) The insertion of 5% of beads representing ethanol molecules induces transition to fibers whose inner architecture is well ordered thanks to π - π interactions between the triazole rings of neighbor molecules.

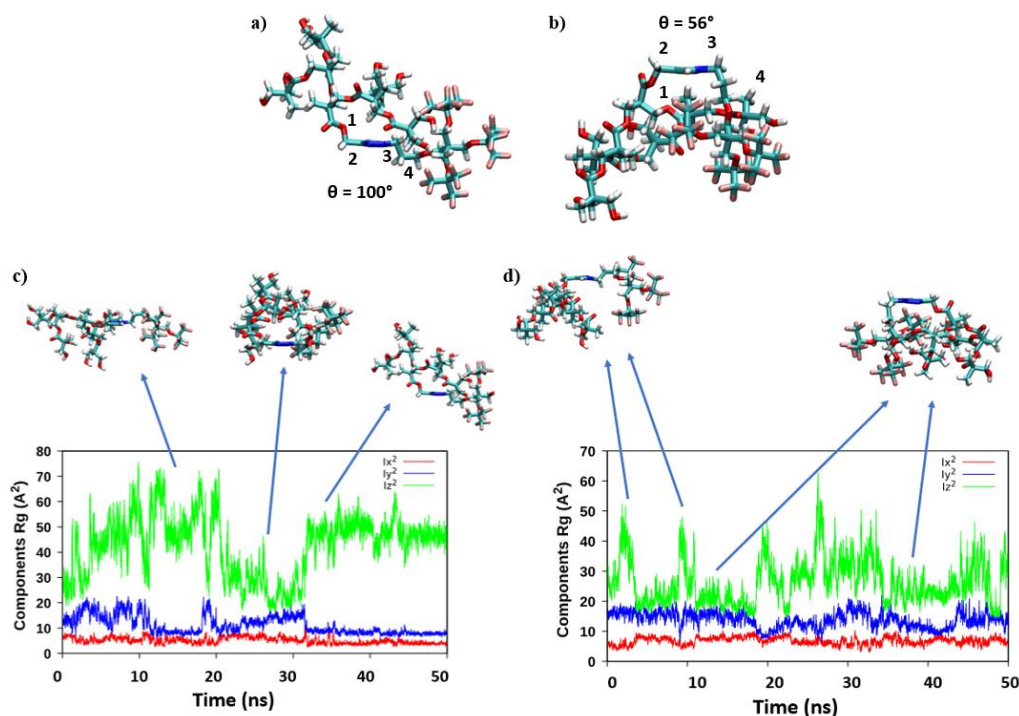


Figure 2.37 a) Trans conformation assumed by FDG₃ in presence of 6% of ethanol; b) cis conformation assumed by FDG₃ in presence of 6% of trifluoroethanol. c) MD analysis after 50 ns: components of radius of gyration assumed by FDG₃ in presence of 6% of ethanol, and relative conformation; d) MD analysis after 50 ns: components of radius of gyration assumed by FDG₃ in presence of 6% of TFE, and relative conformation. Color code: x direction: red, y direction: blue, z direction: green.

The *cis* conformation is stabilized thanks to intramolecular hydrogen bonds between OH terminal groups and the oxygen of carbonyl groups.

As highlighted in figure 2.37d, in presence of 5% of TFE, FDG₃ mostly assumes conformations where the polyfluorinated branched moiety and the polyester one are in the same direction. In the case of 5% of ethanol, FDG₃ self-organizes in a dumbbell conformation before reaching the most stable *trans* conformation, as shown in figure 2.37c. Since it has been reported, as already discussed in the introduction, that aggregates transitions which occur without any external stimuli, such as change in the pH, solvent, ionic strength, are often related to rearrangement in the conformation of the molecules [32], based on the as mentioned results, it is possible to assume that probably when FDG₃ arranges in folded conformation with high curvature, vesicles start forming. The tendency of FDG₃ to rearrange in the *trans* conformation in ethanol can be at the bases of the reorganization of the aggregates which during time tend to form fibers, as revealed by coarse grain simulations.

2.2 Experimental section

2.2.1 Synthesis, purification, and characterization of the new amphiphiles

In this section further information about the synthetic procedures and the instrument used for the synthesis of the compounds will be reported.

For the synthesis the chemicals employed as reactants and solvents were used as received without further purification and purchased with purity >97% from: ©TCI Deutschland GmbH; Sigma Aldrich, Germany; Fluorochem, U.K.

Thin layer chromatography TLC was conducted on plates precoated with silica gel Si 60-F254 (Merck, Darmstadt, Germany).

Chemical stain:

Molybdic reactant: 21g of $(\text{NH}_4)\text{Mo}_7\text{O}_{24}$ +1g of $\text{Ce}(\text{SO}_4)$ in 500 mL of deionized water and 31mL of H_2SO_4 .

Potassium permanganate: A 0.5% m/v KMnO_4 in deionized water.

Flash chromatography was carried out on J. T. Baker silica gel mesh size 230–400.

Nuclear Magnetic Resonance spectroscopy

All the NMR spectra were recorded on a Bruker AV400 Bruker AvanceIII 400 MHz spectrometer equipped with a 5 mm QNP probe (^{19}F , ^{31}P – ^{13}C / ^1H). NMR spectra were recorded at $(300 \pm 3 \text{ K})$ and chemical shifts are reported in ppm downfield from SiMe_4 with the residual proton (CHCl_3 $\delta=7.26$ ppm, CD_3OD : $\delta=3.31$ ppm) and carbon (CDCl_3 : $\delta=77.0$ ppm, CD_3OD : $\delta=49$ ppm). Proton and carbon assignments were achieved by means of ^{13}C -APT, ^1H - ^1H COSY, and ^1H - ^{13}C HSQC experiments. Coupling constant values, J , are given in Hz.

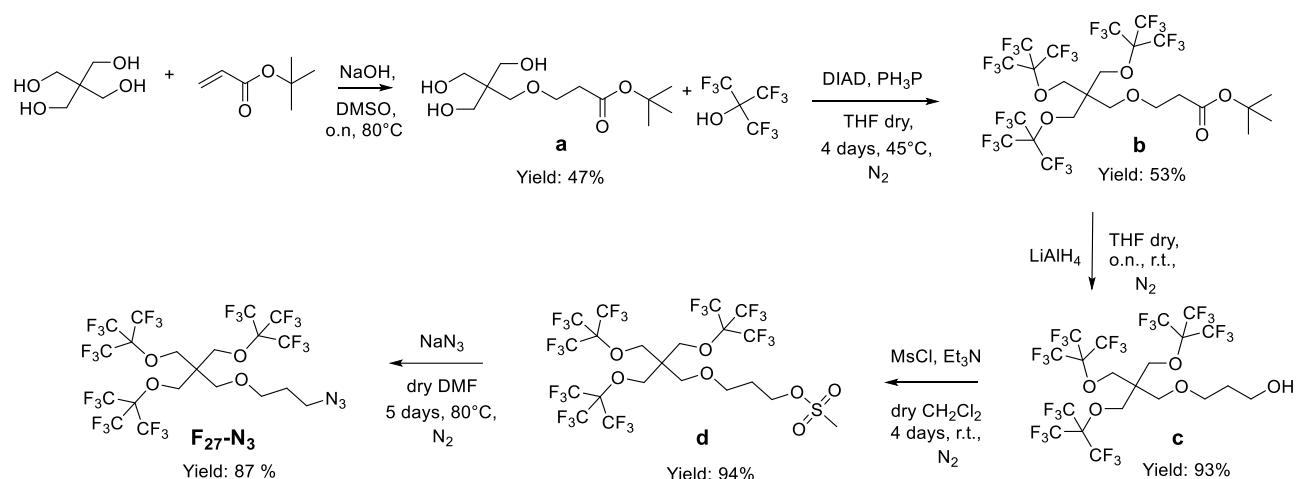
Data evaluation was done with MestreNova 10.0 from Mestre-Lab. The samples prepared for the characterization of the compound synthesized were prepared by dissolving 5-10mg in 500 μL of the deuterated solvent. Methanol- d_4 (99 atom % D) and Chloroform- d , 99.8 atom % D were purchased from Sigma Aldrich, Germany.

Attenuated Total Reflection Fourier-Transform Infrared spectroscopy

FTIR was measured with a Thermo Scientific Nicolet iS50 FTIR spectrometer, equipped with iS50 ATR accessory (Thermo Scientific, Madison, USA). The IR signal values were expressed in wavenumber (cm^{-1}) and rounded to the nearest whole number through automatic assignment using OMNICTM IR software. Air was recorded as background. The analysis was made in transmittance mode in a wavenumber window of 4000-400 cm^{-1} .

Elemental analysis was done by Redox Srl, in Monza (MB), Italy.

High resolution ESI Mass spectrometry was done by UNITECH COSPECT: Comprehensive Substances characterization via advanced spectroscopy Via C. Golgi 19, University of Milan

F₂₇-N₃, a new tri-perfluoro-*tert*-butoxyl-pentaerythritol derivative**Scheme 2.1** Synthesis of F₂₇-N₃.

Compound a. Pentaerythritol (100 g, 1 equivalent) was dissolved in 200 mL of dimethyl sulfoxide; then a solution of NaOH (40g, 0.2 equivalents) in 15 mL of deionized water was added at 0°C followed by the addition of *tert*-butyl acrylate (128 mL, 1.2 equivalents). The reaction was run under stirring at 80°C overnight. A 2M hydrochloric acid solution was added till the reaching of an acidic pH. Then an extraction was made with ethyl acetate. The crude was purified by silica gel flash chromatography using as eluent a mixture of diethyl ether and acetone (1:1) (Rf = 0.3). The compound can be isolated as an oil. (Yield: 47%)

¹H NMR (400 MHz, Chloroform-*d*) δ 3.67 (t, *J* = 5.9 Hz, 2H), 3.65 (s, 6H), 3.51 (s, 2H), 2.47 (t, *J* = 5.8 Hz, 2H), 1.45 (s, 9H).

Compound b. Compound **a** (1.363g; 1 equivalent) and triphenyl phosphine (PPh₃) (8.12g, 6 equivalents) are dissolved in 38 mL of anhydrous THF. Then, diisopropyl azodicarboxylate (DIAD) (6.1 mL, 6 equivalents) is slowly added to the reaction mixture at 0°C. The mixture is left under stirring and nitrogen atmosphere till precipitation of the adduct. Then perfluoro-*tert*-butyl alcohol (4mL, 6 equivalents) is added. The reaction is run at 45°C, under stirring and nitrogen atmosphere for four days. Then, the reaction mixture is extracted from water with dichloromethane, the organic phase is dried with Na₂SO₄, and filtered. After the removal of the solvent, the mixture is recrystallized in Methanol. The product is collected as a white crystalline solid. (Yield: 53%).

¹H NMR (400 MHz, Chloroform-*d*) δ 4.05 (s, 6H), 3.64 (t, *J* = 6.5 Hz, 2H), 3.43 (s, 2H), 2.44 (t, *J* = 6.5 Hz, 2H), 1.44 (s, 9H). ¹⁹F NMR (376 MHz, CDCl₃) δ -70.45.

Compound c. Lithium aluminum hydride (0.4g, 4 equivalents) is put under nitrogen atmosphere and is dispersed in 50 mL of anhydrous THF at 0°C. Then, compound **b** (1.363g; 1 equivalent) is slowly added to the reaction mixture at 0°C. The reaction is run at room temperature, under stirring and nitrogen atmosphere overnight. Then, then the reaction mixture is filtered and the volume of THF is reduced by rotary evaporation. Afterward an extraction from water with dichloromethane is done; the organic phase is dried with Na₂SO₄ and filtered. After the removal of the solvent, the product is collected as an uncolored oil. (Yield: 93%).

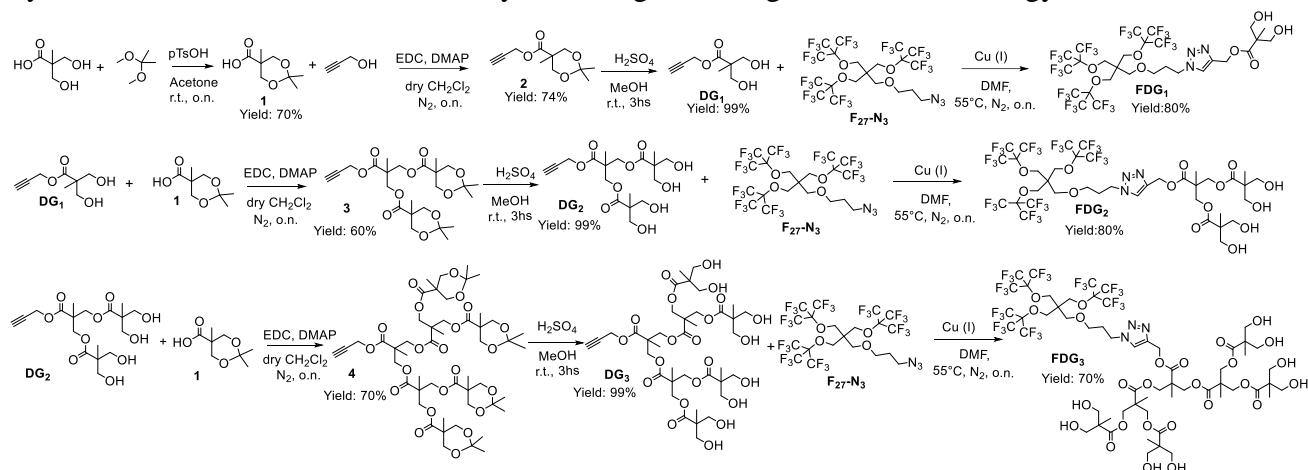
^1H NMR (400 MHz, Chloroform-*d*) δ 4.05 (s, 6H), 3.72 (t, $J = 6.2$ Hz, 2H), 3.53 (t, $J = 6.1$ Hz, 2H), 3.40 (s, 2H), 1.82 (p, $J = 6.2$ Hz, 2H). ^{19}F NMR (376 MHz, CDCl_3) δ -70.43.

Compound d. Compound **c** (0.85g; 1 equivalent) is dissolved in 26 mL of anhydrous dichloromethane. Then, triethyl amine (0.9 mL, 3 equivalents) and methanesulfonyl chloride (MsCl) (0.52 mL, 3 equivalents) are added to the reaction mixture. The reaction is run at room temperature, under stirring and nitrogen atmosphere for four days. Then, the reaction mixture is extracted from water with dichloromethane, the organic phase is dried with Na_2SO_4 , and filtered. After the removal of the solvent, the product is left under vacuum to remove all the excess of solvents. The product is collected as a pale-yellow oil. (Yield: 94%).

^1H NMR (400 MHz, Chloroform-*d*) δ 4.27 (t, $J = 6.3$ Hz, 2H), 4.05 (s, 6H), 3.52 (t, $J = 6.1$ Hz, 2H), 3.41 (s, 2H), 2.99 (s, 3H), 2.00 (p, $J = 6.2$ Hz, 2H). ^{19}F NMR (376 MHz, CDCl_3) δ -70.41.

F27-N3. Compound **d** (2.9g; 1 equivalent) is dissolved in 19 mL of dry DMF at room temperature, under N_2 atmosphere and stirring. Then, sodium azide (0.454 g; 2.2 equivalents) is added. The reaction is run at 80 °C under inert atmosphere for 5 days (to control the progress of the reaction 200 μL of the solution were collected and analyzed by ^1H -NMR). The reaction mixture is run to room temperature, added to iced water and extracted with Hexane. The organic phase is dried with NaSO_4 and the solvent was removed through rotary evaporation. The product was obtained as an uncolored oil (Yield: 87%).

^1H NMR (400 MHz, Chloroform-*d*) δ 4.27 (t, $J = 6.3$ Hz, 2H), 4.05 (s, 6H), 3.52 (t, $J = 6.1$ Hz, 2H), 3.41 (s, 2H), 2.99 (s, 3H), 2.00 (p, $J = 6.2$ Hz, 2H). ^{13}C NMR (101 MHz, Chloroform-*d*) δ 120.31 (q, $^1J_{\text{C-F}} = 292.7$ Hz), 79.85 (m, $^2J_{\text{C-F}} = 29.9$ Hz), 68.52, 66.22, 65.61, 48.42, 46.37, 28.98. ^{19}F NMR (376 MHz, Chloroform-*d*) δ -70.44. ATR-FTIR: Stretching C-H: 2962-2850 cm^{-1} ; Stretching N=N=N: 2105 cm^{-1} ; Stretching C-F: 1350 cm^{-1} ; Bending C-F: 700 cm^{-1} . El. Analysis % Calculated for $\text{C}_{20}\text{H}_{14}\text{F}_{27}\text{N}_3\text{O}_4$: theoretical C, 27.51; H, 1.62; F, 58.74; N, 4.81; O, 7.33/ Found C, 27.23; H, 1.67; N, 4.76; F, 58.03; O, 8.31.

Synthesis of FDG₁, FDG₂ and FDG₃ by following a convergent-like methodology**Scheme 2.2** FDG₁, FDG₂, and FDG₃ synthesis: convergent method.

Compound 1. Bis-MPA (5g; 1 equivalent) and para-toluensulfonic acid (0.520g; 0.1 equivalents) were put under nitrogen atmosphere; then, 2,2-dimethoxypropane (9.5 mL; 2 equivalents) was added followed by 25 mL of acetone. The reaction was run overnight at room temperature and inert atmosphere. The reaction progress was controlled by TLC using as eluent a mixture of CH₂Cl₂ and methanol (8:2) In order to remove the acid, 0.290 mL of an ammonia solution were added. Afterward, an extraction in CH₂Cl₂/water was made. The organic phase was dried with anhydrous Na₂SO₄ and, after filtration, the solvent was removed by rotary evaporation.

The compound was collected as a white solid (Yield: 70%). ¹H NMR (400 MHz, Chloroform-*d*) δ 11.14 (s, 1H), 4.18 (d, *J* = 11.9 Hz, 2H), 3.67 (d, *J* = 11.9 Hz, 2H), 1.44 (s, 3H), 1.41 (s, 3H), 1.21 (s, 3H). ¹³C NMR (101 MHz, CDCl₃) δ 180.06, 98.50, 66.03, 41.87, 25.34, 22.13, 18.56.

Compound 2. Compound 1 (252 mg; 1 equivalent), EDC (305 mg; 1.1 equivalents), and DMAP (18 mg; 0.1 equivalents) were put under nitrogen atmosphere. Then, 10 mL of anhydrous CH₂Cl₂ were added and the solution was left under stirring and inert atmosphere for 5 min. Afterward, propargyl alcohol (170 μL; 2 equivalents) was added with a syringe; the reaction was run at room temperature, under stirring and Nitrogen atmosphere overnight. To control the progress of the reaction a TLC was done using as eluent a mixture of hexane and ethyl acetate (8:2). To purify the product, a column chromatography on silica flash was made using the same eluent as those for TLC (rf: 0.42) The product was obtained as an uncolored oil (Yield: 74%).

¹H NMR (400 MHz, Chloroform-*d*) δ 4.73 (d, *J* = 2.5 Hz, 2H), 4.20 (d, *J* = 11.8 Hz, 2H), 3.65 (d, *J* = 11.8 Hz, 2H), 2.46 (t, *J* = 2.5 Hz, 1H), 1.42 (s, 3H), 1.39 (s, 3H), 1.22 (s, 3H). ¹³C NMR (101 MHz, CDCl₃) δ 172.42, 97.14, 73.93, 67.24, 64.86, 51.33, 40.90, 23.47, 21.75, 17.46.

Compound DG₁. Compound 2 (151 mg; 1 equivalent) was dissolved using 1 mL of Methanol. Separately, sulfuric acid (32μL; 0.85 equivalents) was added to another 1 mL of methanol and then, the solution was added to the previous one followed by another 1 mL of methanol. The reaction was run at room temperature, under stirring for three hours and the progress of the reaction was monitored by TLC using as eluent a mixture of hexane and ethyl acetate (8:2) and the reaction was stopped by adding to the reaction mixture an ammonia solution (128.5 μL). The salt obtained was removed by

filtration on celite and washed with methanol. The compound was obtained as a white solid after rotary evaporation of the solvent (Yield: 99%).

^1H NMR (400 MHz, Methanol- d_4) δ 4.71 (d, J = 2.4 Hz, 2H), 3.75 – 3.59 (m, 4H), 2.89 (t, J = 2.5 Hz, 1H), 1.17 (s, 3H). ^{13}C NMR (101 MHz, MeOD) δ = 175.71, 78.78, 76.18, 65.69, 52.98, 51.59, 17.19.

Compound 3. Compound **1** (566 mg; 5 equivalents), EDC (621 mg; 5 equivalents), and DMAP (40 mg; 0.5 equivalents) were put under nitrogen atmosphere for 5 minutes. Then, 3 mL of anhydrous CH_2Cl_2 were added. Separately, compound **DG₁** (172 mg; 1 equivalent) was dissolved in other 3 mL of anhydrous CH_2Cl_2 and then, transferred, by means of other 4 mL of the solvent, to the reaction mixture. The reaction was run at room temperature, under stirring and Nitrogen atmosphere overnight. To control the progress of the reaction a TLC was done using as eluent a mixture of hexane and ethyl acetate (7:3). To purify the product, a column chromatography on silica flash was made using the same eluent as those for TLC (rf: 0.4) The product was obtained as an uncolored oil (Yield: 60%).

^1H NMR (400 MHz, Chloroform- d) δ 4.71 (d, J = 2.5 Hz, 2H), 4.32 (s, 4H), 4.14 (d, J = 11.9 Hz, 4H), 3.61 (d, J = 12.0 Hz, 4H), 2.46 (t, J = 2.5 Hz, 1H), 1.40 (s, 6H), 1.35 (s, 6H), 1.31 (s, 3H), 1.15 (s, 6H). ^{13}C NMR (101 MHz, CDCl_3) δ 173.63, 171.96, 98.25, 77.34, 75.43, 66.11, 65.42, 52.81, 46.96, 42.21, 25.07, 22.44, 18.67, 17.72.

Compound DG₂. Compound **3** (170 mg; 1 equivalent) was dissolved using 2 mL of Methanol. Separately, sulfuric acid (32 μL ; 1.7 equivalents) was added to another 1 mL of methanol and then, the acid solution was added to the reaction mixture and other 2 mL of methanol were added. The reaction was run at room temperature, under stirring for three hours and the progress of the reaction was monitored by TLC using as eluent a mixture of hexane and ethyl acetate (7:3), and the reaction was stopped by adding to the reaction mixture an ammonia solution (100 μL). The salt obtained was removed by filtration on celite. The compound was obtained as a solid after rotary evaporation of the solvent (Yield: 99%).

^1H NMR (400 MHz, Methanol- d_4) δ 4.76 (d, J = 2.5 Hz, 2H), 4.29 (d, J = 2.7 Hz, 4H), 3.71 – 3.56 (m, 8H), 2.95 (t, J = 2.5 Hz, 1H), 1.31 (s, 3H), 1.15 (s, 6H). ^{13}C NMR (101 MHz, MeOD) δ = 175.88, 173.62, 78.50, 76.65, 66.31, 65.81, 53.55, 51.77, 47.87, 18.05, 17.26.

Compound 4. Compound **1** (517 mg; 8 equivalents), EDC (569 mg; 8 equivalents), and DMAP (23 mg; 0.5 equivalents) were put under nitrogen atmosphere for 5 minutes. Then, 3 mL of anhydrous CH_2Cl_2 were added and the solution was put under three cycles of vacuum/ nitrogen atmosphere. Separately, compound **DG₂** (150 mg, 1 equivalent) was dissolved in other 5 mL of anhydrous CH_2Cl_2 and then, transferred to the reaction mixture. After the addition of other 5 mL of CH_2Cl_2 , the reaction was run at room temperature, under stirring and nitrogen atmosphere overnight. To control the progress of the reaction a TLC was done using as eluent a mixture of hexane and ethyl acetate (7:3). To purify the product, a column chromatography on silica flash was made using the same eluent as those for TLC (rf: 0.4) The product was obtained as an oil (Yield: 70%). The compound was directly used for the following step.

Compound DG₃. Compound **4** (200 mg; 1 equivalent) was dissolved using 3 mL of Methanol. Separately, sulfuric acid (37 μ L; 3.4 equivalents) was mixed with 1 mL of methanol and then added to the reaction mixture. Other 3 mL of methanol were added; then, the reaction was run at room temperature, under stirring for three hours and the progress of the reaction was monitored by TLC using as eluent a mixture of hexane and ethyl acetate (7:3), and the reaction was stopped by adding to the reaction mixture an ammonia solution (100 μ L). The salt was filtered away on celite. The solvent was removed by rotary evaporation and the compound was obtained as a solid (Yield: 99%). ¹H NMR (400 MHz, Methanol-*d*₄) δ = 4.79 (d, *J*=2.5, 2H), 4.39 – 4.20 (m, 12H), 3.73 – 3.55 (m, 16H), 2.98 (t, *J*=2.5, 1H), 1.32 (s, 3H), 1.30 (s, 6H), 1.15 (s, 12H). ¹³C NMR (101 MHz, MeOD) δ = 175.92, 173.74, 173.16, 78.53, 76.99, 67.25, 66.20, 65.86, 53.77, 51.79, 47.99, 47.96, 18.24, 17.99, 17.31.

Compound FDG₁. Compound **DG₁** (313 mg; 1 equivalent) and CuI (7 mg; 0.1 equivalents) were dissolved in 500 μ L of DMF under inert atmosphere. Separately, **Spider-N₃** (62 mg; 1 equivalent) was dissolved in other 500 μ L of DMF and transferred to the reaction mixture by means of other 1.5 mL of DMF. The reaction was run under stirring and nitrogen atmosphere at 55°C overnight. The formation of the product was confirmed by analyzing at FTIR 100 μ L of the solution by monitoring the disappearance of the characteristic stretching of the azido group (2100 cm^{-1}). The reaction was stopped, added to iced water and extracted with CH_2Cl_2 ; then, the organic phase was washed two times with a 0.1 % disodium EDTA solution and 1 time with a saturated NaCl solution. The organic phase was collected, dried with Na_2SO_4 , and rotary evaporated. The compound was collected as a white solid (Yield: 80%).

¹H NMR (400 MHz, Methanol-*d*₄) δ 7.96 (s, 1H), 5.23 (s, 2H), 4.46 (t, *J* = 7.1 Hz, 2H), 4.16 (s, 7H), 3.77 – 3.53 (m, 4H), 3.47 (t, *J* = 6.1 Hz, 2H), 3.44 (s, 2H), 2.17 (p, *J* = 6.6 Hz, 2H), 1.15 (s, 3H). ¹³C NMR (101 MHz, Methanol-*d*₄) δ 176.23 , 144.36 , 125.72 (d, *J* = 50.4 Hz), 123.28 – 117.10 (m), 81.53 – 80.16 (m), 69.17 , 67.16 , 67.11 , 65.86 , 58.44 , 51.70 , 48.40 , 47.50 , 31.29 , 17.22. ¹³C NMR (101 MHz, Methanol-*d*₄) δ 176.23 , 144.36 , 125.47 , 126.28 – 117.17 (q, ¹*J*_{C-F} = 291.8 Hz), 81.83 – 80.16 (m), 69.17 , 67.16 , 67.11 , 65.86 , 58.44 , 51.70 , 48.40 , 47.50 , 31.29 , 17.22. ¹⁹F NMR (376 MHz, MeOD) δ -71.51. ATR-FTIR: Stretching O-H: 3650-3000 cm^{-1} ; Stretching C-H: 2970-2800 cm^{-1} ; Stretching C=O: 1726 cm^{-1} ; Stretching C-F: 1300 cm^{-1} ; Bending C-F: 700 cm^{-1} ; HR-MS (ESI) for $\text{C}_{28}\text{H}_{26}\text{F}_{27}\text{N}_3\text{O}_8$ - theoretical $[\text{M-Na}]^+$: 1068.1186/ Found $[\text{M-Na}]^+$: 1068.1166.

Compound FDG₂. Compound **DG₂** (110 mg; 1 equivalent) and CuI (8 mg; 0.15 equivalents) were dissolved in 1 mL of DMF under inert atmosphere. Separately, **F₂₇-N₃** (238 mg; 1 equivalent) was dissolved in other 1.5 mL of DMF and transferred to the reaction mixture. The reaction was run under stirring and nitrogen atmosphere at 55°C overnight. The formation of the product was confirmed by analyzing at FTIR 100 μ L of the solution by monitoring the disappearance of the characteristic stretching of the azido group (2100 cm^{-1}). The reaction was stopped, added to iced water and extracted with CH_2Cl_2 ; then, the organic phase was washed two times with a 0.1 % disodium EDTA solution and 1 time with a saturated NaCl solution. The organic phase was collected, dried with Na_2SO_4 , and rotary evaporated. The compound was collected as a sticky solid (Yield: 80%).

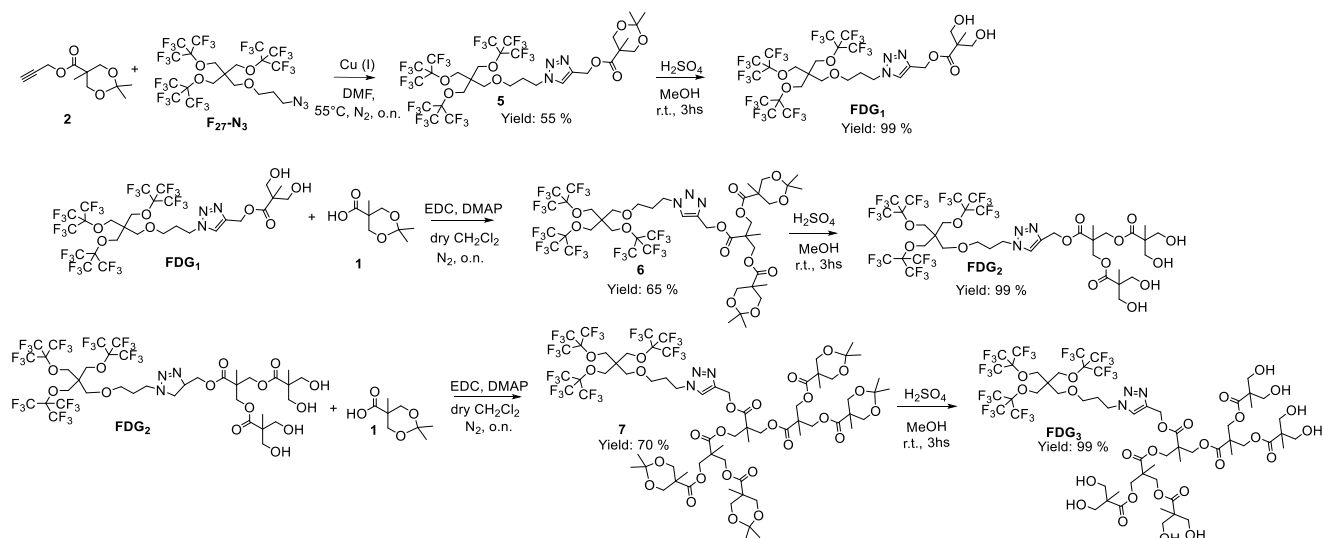
¹H NMR (400 MHz, Methanol-*d*₄) δ = 8.08 (s, 1H), 5.31 (s, 2H), 4.53 (t, *J*=7.2, 2H), 4.40 – 4.27 (m, 4H), 4.22 (s, 6H), 3.74 – 3.59 (m, 8H), 3.54 (t, *J*=6.1, 2H), 3.51 (s, 2H), 2.24 (m, 2H), 1.34 (s, 4H),

1.16 (s, 6H). ^{13}C NMR (101 MHz, Methanol- d_4) δ 126.01, 126.72 – 117.13 (q, $^1J_{\text{C-F}} = 292.3$ Hz), 80.97 (m, $^2J_{\text{C-F}} = 30.5$ Hz), 69.21, 67.12, 67.06, 66.36, 65.84, 58.98, 51.78, 48.46, 47.88, 47.51, 31.31, 18.08, 17.21. ^{19}F NMR (376 MHz, MeOD) δ -71.51.

ATR-FTIR: Stretching O-H: 3650-3100 cm^{-1} ; Stretching C-H: 3000-2850 cm^{-1} ; Stretching C=O: 1727 cm^{-1} ; Stretching C-F: 1250 cm^{-1} ; Bending C-F: 700 cm^{-1} ; HR-MS (ESI) for $\text{C}_{38}\text{H}_{42}\text{F}_{27}\text{N}_3\text{O}_{14}$ -theoretical $[\text{M-Na}]^+$: 1300.2133/ Found $[\text{M-Na}]^+$: 1300.2113.

Compound FDG₃. Compound **DG₃** (53 mg; 1 equivalent) and CuI (5.4 mg; 0.5 equivalents) were dissolved in 1 mL of DMF under inert atmosphere. Separately, **F₂₇-N₃** (52 mg; 1 equivalent) was dissolved in other 1.5 mL of DMF and transferred to the reaction mixture. The reaction was run under stirring and nitrogen atmosphere at 55°C overnight. The formation of the product was confirmed by analyzing at FTIR 100 μL of the solution by monitoring the disappearance of the characteristic stretching of the azido group (2100 cm^{-1}). The reaction was stopped, added to iced water and extracted with CH_2Cl_2 ; then, the organic phase was washed two times with a 0.1 % disodium EDTA solution and 1 time with a saturated NaCl solution. The organic phase was collected, dried with Na_2SO_4 , and rotary evaporated. The compound was collected as a white solid (Yield: 70%).

^1H NMR (400 MHz, Methanol- d_4) δ = 8.12 (s, 1H), 5.34 (s, 2H), 4.55 (t, $J=7.1$, 2H), 4.43 – 4.25 (m, 12H), 4.22 (s, 6H), 3.79 – 3.63 (m, 16H), 3.55 (t, $J=6.1$, 2H), 3.51 (s, 2H), 2.25 (m, 2H), 1.35 (s, 3H), 1.30 (s, 6H), 1.21 (s, 12H). ^{13}C NMR (101 MHz, Methanol- d_4) δ 175.93, 173.70, 143.58, 126.19, 120.15 (q, $^1J_{\text{C-F}} = 292.5$ Hz), 81.52 – 80.43 (m), 69.24, 67.24, 67.11, 67.06, 66.16, 65.87, 59.09, 51.81, 48.49, 47.97, 47.93, 47.51, 31.33, 18.17, 18.00, 17.30. ^{19}F NMR (376 MHz, MeOD) δ -71.47. ATR-FTIR: Stretching O-H: 3600-3100 cm^{-1} ; Stretching C-H: 3000-2884 cm^{-1} ; Stretching C=O: 1729 cm^{-1} ; Stretching C-F: 1230 cm^{-1} ; Bending C-F: 700 cm^{-1} ; HR-MS (ESI) for $\text{C}_{58}\text{H}_{74}\text{F}_{27}\text{N}_3\text{O}_{26}$ - theoretical $[\text{M-Na}]^+$: 1764.4027/ Found $[\text{M-Na}]^+$: 1764.4031.

Synthesis of FDG₁, FDG₂ and FDG₃ by following a divergent-like methodology**Scheme 2.3** FDG₁, FDG₂, and FDG₃ synthesis: divergent method.

Compound 5. CuI (12 mg; 0.1 equivalents) was dispersed in 0.5 mL of DMF and then, compound 2 (160 mg; 1 equivalent) was added by means of 1 mL of DMF. Finally, **F₂₇-N₃** (658 mg; 1 equivalent) was added by using other 2 mL of DMF. The reaction was run at 55°C, under inert atmosphere overnight. The formation of the product was confirmed by analyzing at FTIR 100 μ L of the solution by monitoring the disappearance of the characteristic stretching of the azido group (2100 cm^{-1}). The reaction was stopped, added to iced water and extracted with CH_2Cl_2 ; then, the organic phase was washed two times with a 0.1 % disodium EDTA solution and 1 time with a saturated NaCl solution. The organic phase was collected, dried with Na_2SO_4 , and rotary evaporated. The compound was collected as oil (Yield: 55%).

^1H NMR (400 MHz, Chloroform-*d*) δ 7.66 (s, 1H), 5.31 (s, 2H), 4.42 (t, $J = 5.6$ Hz, 2H), 4.20 (d, $J = 11.5$ Hz, 2H), 3.64 (d, $J = 11.4$ Hz, 2H), 3.46 (t, $J = 5.6$ Hz, 2H), 3.40 (s, 2H), 2.18 (m, 2H), 1.42 (s, 3H), 1.34 (s, 3H), 1.15 (s, 3H). ^{19}F NMR (376 MHz, CDCl_3) δ -70.37.

Compound FDG₁. Compound **5** (456 mg; 1 equivalent) was dissolved using 2 mL of Methanol. Separately, sulfuric acid (25 μ L; 1 equivalent) was added to another 1.5 mL of methanol and then, this solution was added to the previous one by means of other 3.5 mL of methanol. The reaction was run at room temperature, under stirring for three hours and the progress of the reaction was monitored by TLC using as eluent a mixture of hexane and ethyl acetate (7:3), and the reaction was stopped by adding to the reaction mixture an ammonia solution (267 μ L). The salt obtained was removed by filtration on celite and washed with methanol which was, then, removed by rotary evaporation. The compound was obtained as a solid (Yield: 99%).

^1H NMR (400 MHz, Methanol-*d*₄) δ 7.96 (s, 1H), 5.23 (s, 2H), 4.46 (t, $J = 7.1$ Hz, 2H), 4.16 (s, 7H), 3.77 – 3.53 (m, 4H), 3.47 (t, $J = 6.1$ Hz, 2H), 3.44 (s, 2H), 2.17 (p, $J = 6.6$ Hz, 2H), 1.15 (s, 3H). ^{13}C NMR (101 MHz, Methanol-*d*₄) δ 176.23, 144.36, 125.72 (d, $J = 50.4$ Hz), 123.28 – 117.10 (m), 81.53 – 80.16 (m), 69.17, 67.16, 67.11, 65.86, 58.44, 51.70, 48.40, 47.50, 31.29, 17.22. ^{13}C NMR (101 MHz, Methanol-*d*₄) δ 176.23, 144.36, 125.47, 126.28 – 117.17 (q, $^1J_{\text{C-F}} = 291.8$ Hz), 81.83 – 80.16 (m), 69.17, 67.16, 67.11, 65.86, 58.44, 51.70, 48.40, 47.50, 31.29, 17.22. ^{19}F

NMR (376 MHz, MeOD) δ -71.51. ATR-FTIR: Stretching O-H: 3650-3000 cm^{-1} ; Stretching C-H: 2970-2800 cm^{-1} ; Stretching C=O: 1726 cm^{-1} ; Stretching C-F: 1300 cm^{-1} ; Bending C-F: 700 cm^{-1} ; HR-MS (ESI) for $\text{C}_{28}\text{H}_{26}\text{F}_{27}\text{N}_3\text{O}_8$ - theoretical $[\text{M-Na}]^+$: 1068.1186/ Found $[\text{M-Na}]^+$: 1068.1166.

Compound 6. Compound **1** (522 mg; 6 equivalents), EDC (574 mg; 6 equivalents), and DMAP (31 mg; 0.5 equivalents) were put under nitrogen atmosphere for 5 minutes. Then, 3 mL of anhydrous CH_2Cl_2 were added and the solution was put under three cycles of vacuum/ nitrogen atmosphere. Separately, compound **FDG₁** (522 mg, 1 equivalent) was dissolved in other 5 mL of anhydrous CH_2Cl_2 and then, transferred, by means of other 7 mL of the solvent, to the reaction mixture. The reaction was run at room temperature, under stirring and nitrogen atmosphere overnight. To control the progress of the reaction a TLC was done using as eluent a mixture of hexane and ethyl acetate (7:3). To purify the product, a column chromatography on silica flash was made using the same eluent as those for TLC (rf: 0.5) The product was obtained as a pale-yellow oil (Yield: 65%). The compound was directly used for the following step.

Compound FDG₂. Compound **6** (300 mg; 1 equivalent) was dissolved in 2 mL of Methanol. Separately, sulfuric acid (24 μL ; 1.7 equivalent) was dissolved in 1mL of methanol and added to the reaction mixture. After the addition of further 3mL of methanol, the reaction was run at room temperature, under stirring for three hours and the progress of the reaction was monitored by TLC using as eluent a mixture of hexane and ethyl acetate (7:3). The reaction was stopped by adding to the reaction mixture an ammonia solution (250 μL). The salt obtained was removed by filtration on celite and washed with methanol which was, then, removed by rotary evaporation. The compound was obtained as a solid (Yield: 99%).

^1H NMR (400 MHz, Methanol- d_4) δ = 8.08 (s, 1H), 5.31 (s, 2H), 4.53 (t, $J=7.2$, 2H), 4.40 – 4.27 (m, 4H), 4.22 (s, 6H), 3.74 – 3.59 (m, 8H), 3.54 (t, $J=6.1$, 2H), 3.51 (s, 2H), 2.24 (m, 2H), 1.34 (s, 4H), 1.16 (s, 6H). ^{13}C NMR (101 MHz, Methanol- d_4) δ 126.01 , 126.72 – 117.13 (q, $^1J_{\text{C-F}} = 292.3$ Hz)), 80.97 (m, $^2J_{\text{C-F}} = 30.5$ Hz), 69.21 , 67.12 , 67.06 , 66.36 , 65.84 , 58.98 , 51.78 , 48.46 , 47.88 , 47.51 , 31.31 , 18.08 , 17.21. ^{19}F NMR (376 MHz, MeOD) δ -71.51. ATR-FTIR: Stretching O-H: 3650-3100 cm^{-1} ; Stretching C-H: 3000-2850 cm^{-1} ; Stretching C=O: 1727 cm^{-1} ; Stretching C-F: 1250 cm^{-1} ; Bending C-F: 700 cm^{-1} ; HR-MS (ESI) for $\text{C}_{38}\text{H}_{42}\text{F}_{27}\text{N}_3\text{O}_{14}$ - theoretical $[\text{M-Na}]^+$: 1300.2133/ Found $[\text{M-Na}]^+$: 1300.2113.

Compound 7. Compound **1** (246 mg; 12 equivalents), EDC (271 mg; 12 equivalents), and DMAP (17 mg; 1.1 equivalents) were put under nitrogen atmosphere for 5 minutes. Then, 2 mL of anhydrous CH_2Cl_2 were added and the solution was put under three cycles of vacuum/ nitrogen atmosphere. Separately, compound **FDG₂** was dissolved in other 3 mL of anhydrous CH_2Cl_2 to the reaction mixture. The reaction was run at room temperature, under stirring and Nitrogen atmosphere overnight. To control the progress of the reaction a TLC was done using as eluent a mixture of hexane and ethyl acetate (4:6). To purify the product, a column chromatography on silica flash was made using the same eluent as those for TLC (rf: 0.7) The product was obtained as an oil (Yield: 70%). The compound was directly used for the following step.

Compound FDG₃. Compound **7** (162 mg; 1 equivalent) was dissolved using 1.5 mL of Methanol. Separately, sulfuric acid (25 μL ; 7.7 equivalent) was added to another 0.5 mL of methanol and then,

this solution was added to the previous one by means of other 1 mL of methanol. The reaction was run at room temperature, under stirring for three hours and the progress of the reaction was monitored by TLC using as eluent a mixture of hexane and ethyl acetate (4:6), and the reaction was stopped by adding to the reaction mixture an ammonia solution (267 μ L). The salt obtained was removed by filtration on celite and washed with methanol which was, then, removed by rotary evaporation. The compound was obtained as a solid (Yield: 99%).

^1H NMR (400 MHz, Methanol- d_4) δ = 8.12 (s, 1H), 5.34 (s, 2H), 4.55 (t, $J=7.1$, 2H), 4.43 – 4.25 (m, 12H), 4.22 (s, 6H), 3.79 – 3.63 (m, 16H), 3.55 (t, $J=6.1$, 2H), 3.51 (s, 2H), 2.25 (m, 2H), 1.35 (s, 3H), 1.30 (s, 6H), 1.21 (s, 12H). ^{13}C NMR (101 MHz, Methanol- d_4) δ 175.93 , 173.70 , 143.58 , 126.19 , 120.15 (q, $^1J_{\text{C-F}} = 292.5$ Hz), 81.52 – 80.43 (m), 69.24 , 67.24 , 67.11 , 67.06 , 66.16 , 65.87 , 59.09 , 51.81 , 48.49 , 47.97 , 47.93 , 47.51 , 31.33 , 18.17 , 18.00 , 17.30. ^{19}F NMR (376 MHz, MeOD) δ - 71.47. ATR-FTIR: Stretching O-H: 3600-3100 cm^{-1} ; Stretching C-H: 3000-2884 cm^{-1} ; Stretching C=O: 1729 cm^{-1} ; Stretching C-F: 1230 cm^{-1} ; Bending C-F: 700 cm^{-1} ; HRMS (ESI) for $\text{C}_{58}\text{H}_{74}\text{F}_{27}\text{N}_3\text{O}_{26}$ - theoretical $[\text{M-Na}]^+$: 1764.4027/ Found $[\text{M-Na}]^+$: 1764.4031.

Characterization of F₂₇-N₃, FDG₁, FDG₂ and FDG₃

Figure 2.38 and 2.39 shows the comparison between the ATR-FTIR spectra of FDG₂ and FDG₃ with their alkyne terminating precursor and F₂₇-N₃.

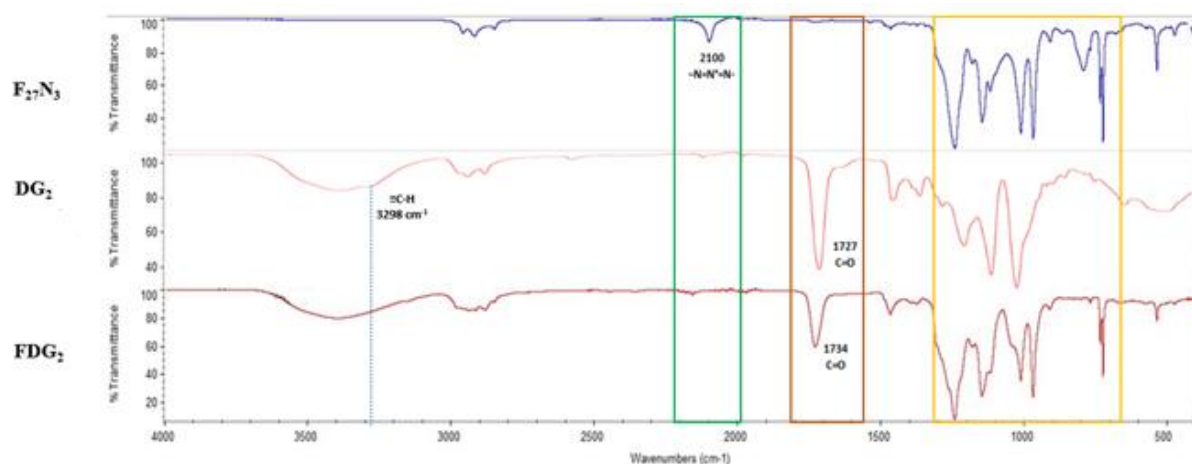


Figure 2.38 ATR-FTIR spectra comparison between FDG₂, the DG₂ alkyne terminating precursor, and F₂₇-N₃.

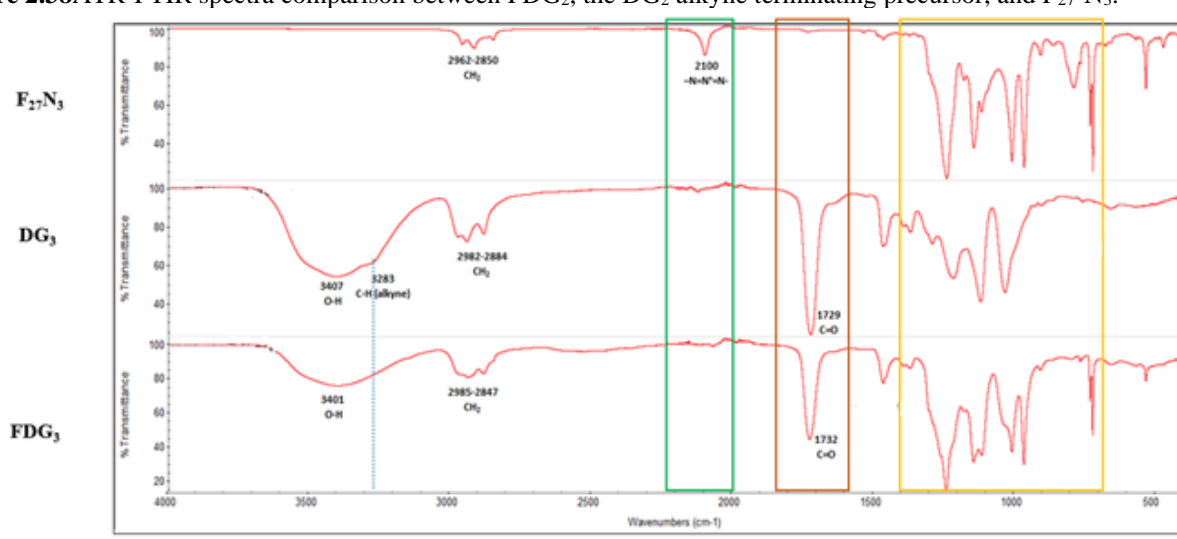


Figure 2.39 ATR-FTIR spectra comparison between FDG₃, the DG₃ alkyne terminating precursor, and F₂₇-N₃.

2.2.2 Characterization of FDG₁, FDG₂ and FDG₃ in bulk

Single Crystal X-ray diffraction analysis - Structural characterization of FDG₁

Data collections were performed at the X-ray diffraction beamline (XRD1) of the Elettra Synchrotron, Trieste (Italy). The crystals were dipped in NHV oil (Jena Bioscience, Jena, Germany) and mounted on the goniometer head with kapton loops (MiTeGen, Ithaca, USA). Complete datasets were collected at 100 K (nitrogen stream supplied through an Oxford Cryostream 700) through the rotating crystal method. Data were acquired using a monochromatic wavelength of 0.700 Å on a Pilatus 2M hybrid-pixel area detector (DECTRIS Ltd., Baden-Daettwil, Switzerland). The diffraction data were indexed and integrated using XDS. Scaling have been done using CCP4-Aimless code, merging two different datasets from two different crystals to minimize radiation damage effects.

The structures were solved by the dual space algorithm implemented in the SHELXT code. Fourier analysis and refinement were performed by the full-matrix least-squares methods based on F^2 implemented in SHELXL (version 2018/3). The Coot program was used for modelling. **FDG₁** molecules are tightly packed in a centrosymmetric triclinic unit cell and no solvent molecules have been found in the crystals. **FDG₁** molecules form dimers (related by crystallographic inversion centers) linked by hydrogen bonds, involving hydroxyl groups and triazole rings of neighbor molecules. Dimers are stacked along the crystallographic *b* axis, through contacts among closest -OH groups. $\pi \cdots \pi$ stacking interactions among triazole of neighbor dimers can be also found. Pictures were prepared using Ortep-3 and CCDC Mercury software. Table 2.13 shows the crystallographic data for **FDG₁**.

Table 2.13 Crystallographic data for **FDG₁**

Chemical Formula	C ₂₈ H ₂₆ F ₂₇ N ₃ O ₈
Crystal system	Triclinic
Space Group	<i>P</i> -1
Unit cell dimensions	<i>a</i> = 10.408(2) Å <i>b</i> = 10.676(2) Å <i>c</i> = 20.331(4) Å α = 80.69(3)° β = 88.28(3)° γ = 62.80(3)°
Volume	1980.4(9) Å ³
Density (calculated)	1.753 g·cm ⁻³
Absorption coefficient	0.196 mm ⁻¹
F(000)	1044
Crystal size	0.10·0.05·0.02 mm ³
Crystal habit	Transparent thin needles
Theta range for data collection	1.0° to 31.2°

Powder X-ray diffraction analysis - Structural characterization of **FDG₁**

Powder X-Ray diffraction data of compounds **FDG₁** were collected on Bruker AXS D8 powder diffractometer with experimental parameters as follows: Cu-K α radiation ($\lambda = 1.54056$ Å), scanning interval 4-40° at 2 θ , step size 0.016°, exposure time 1.5 s per step.

Thermogravimetric analysis

TGA was done with a Q500 instrument. 1-5 mg of the sample were placed in the melting pot and submitted to a ramp of temperature from 30 °C to 350 °C for F₂₇-N₃ and from 30 °C to 550 °C.

Polarized Optimal Microscope

The LC textures and phase transitions were studied with an Olympus BX51 polarized optical microscope equipped with a Linkam Scientific LTS 350 heating stage and a Sony CCD-IRIS/RGB video camera.

Differential Scanning Calorimetry

The enthalpies were measured by differential scanning calorimetry (DSC) with a Mettler Toledo DSC823e operated at a scanning rate of 5 °C min⁻¹ on heating and on cooling. Mettler STARe software was used for calculation. An exact amount of the solids (1-5 mg) was weighted and put on aluminum light 20 μ L sample pans.

Small and wide-angle X-Ray spectroscopy

The SWAXS patterns were obtained with a transmission Guinier-like geometry. A linear focalized monochromatic Cu K α 1 beam ($\lambda = 1.5405 \text{ \AA}$) was obtained using a sealed-tube generator (600 W) equipped with a bent quartz monochromator. The samples were filled in home-made sealed cells of 1 mm path. The sample temperature was controlled within $\pm 0.01 \text{ }^\circ\text{C}$, and exposure times were varied from 4 to 24 h. The patterns were recorded with a curved Inel CPS120 counter gas-filled detector (periodicities up to 90 \AA) and on image plates scanned by Amersham Typhoon IP with $25 \text{ }\mu\text{m}$ resolution (periodicities up to 120 \AA). I(2q) profiles were obtained from images, by using home-developed software.

2.2.3 Self-assembly of FDG₁, FDG₂ and FDG₃ in water

The ethanol in water procedure

The solid was dissolved in ethanol, then was flash injected with a syringe to MilliQ water. The dispersion was mixed at vortex for 20 seconds at 8 rpm. The dispersions were analyzed overtime.

Dynamic light scattering

Data analysis was performed according to standard procedures and the Laplace inversion of the time autocorrelation functions was obtained through a non-cumulant method using CONTIN algorithm, suitable for multimodal and polydisperse systems. Multiangle DLS was measured at ALV compact goniometer system, equipped with ALV-5000/EPP Correlator, special optical fiber detector and ALV/GCS-3 Compact goniometer, with He-Ne laser (= 633 nm, 22 mW output power) as light source. The temperature was controlled with a thermostatic bath and set at $25 \text{ }^\circ\text{C}$. A volume comprised between $800 \text{ }\mu\text{L}$ and 1 ml was used for the analysis. DLS was measured at different time points (0, 24, 48 h) and scattering angles $\theta = 70 - 130^\circ$ in 20° steps. Each measure was the result of the average of three subsequent run of 10 seconds each, with a threshold sensibility of 10%. Data analysis was done with ALV-Correlator software.

¹⁹F-NMR analysis

$400 \text{ }\mu\text{L}$ of the sample were added with $40 \text{ }\mu\text{L}$ of deuterated water (D₂O) and 256 scansions were acquired; NMR spectra for the characterization of the self-assembled aggregates were recorded at different time points (0, 24, 48 hs and 6 days).

Cryogenic Transmission Electron Microscopy (Cryo-TEM) (in collaboration with Professor Nonappa)

The cryo-TEM images were collected using JEM 3200FSC field emission microscope (JEOL) operated at 300 kV in bright field mode with Omega-type Zero-loss energy filter. For specimen preparation, 200 mesh copper grids with lacey carbon support film (Agar Scientific) were used. The TEM grids were plasma cleaned using Gatan Solarus (Model 950) plasma cleaner for 30 seconds. The specimen for Cryo-TEM imaging were prepared by placing $3 \text{ }\mu\text{L}$ of a of the sample onto TEM grids and plunge-frozen into $-170 \text{ }^\circ\text{C}$ ethane-propane (1:1) mixture using Leica automatic plunge freezer EM GP2 with 3 s blotting time under 80% humidity. The vitrified specimen was cryo-transferred to the microscope. The images were acquired with Gatan Digital Micrograph® software while the specimen temperature was maintained at $-187 \text{ }^\circ\text{C}$.

Transmission Electron Microscopy

Transmission electron microscopy (TEM) images were acquired by using a DeLong America LVEM5, equipped with a field emission gun and operating at 5 kV. Samples were prepared by placing 10 μL of the solution on 200 mesh carbon-coated copper grids, leaving the drop on the grid surface for 1 min and finally removing the excess of solvent and dry at air.

2.2.4 Molecular Dynamics: FDG₁, FDG₂ and FDG₃ in comparison

The theoretical study is based on Molecular Mechanics (MM) and Molecular Dynamics (MD) simulations. All MM and MD simulations were performed with Materials Studio, Discovery Studio packages. Using the same simulation protocol proposed in previous work [137], all calculations are performed with CVFF force field with a Morse potential for the bonded atoms, in explicit water 5% ethanol. The simulation protocol involved three sequential steps: *i*) at first the initial energy minimization; *ii*) the MD run at constant temperature; *iii*) the final geometry optimizations of the final configuration assumed by the system at the end of MD run. All energy minimizations were carried out up to an energy gradient lower than $4 \times 10^{-3} \text{ kJ mol}^{-1} \text{ \AA}^{-1}$. The MD simulations were performed at a constant temperature (300 K), controlled through the Berendsen thermostat. Integration of the dynamical equations was carried out with the Verlet algorithm using a time step of 1 fs, and the instantaneous coordinates were periodically saved for further analysis or geometry optimization.

3 Development of a new ^{19}F -MRI traceable gene delivery vector

Dendritic scaffolds have been widely applied in the development of non-viral gene delivery vectors. Among dendritic gene delivery vectors reported in literature, only few examples are based on Bis-MPA monomer [138][139]. The cationic Bis-MPA-based dendritic vectors reported showed good ability to bind genes, lower cytotoxicity [138], and higher biodegradability [140] when compared to classical PAMAM vectors of the same generation. The covalent or non-covalent addition of fluorinated chains is a promising strategy to enhance the serum stability of dendriplexes and facilitate their endosomal escape [141], reduce the N/P ratio [79], enhance cellular uptake and transfection efficiencies [142], and reduce cytotoxicity [66]. The most commonly studied dendritic-based fluorinated gene delivery vectors are polyamidoamine (PAMAM) [77][79][80][143][144], poly(propyleneimine) (PPI) [145], and poly-L-lysine dendrimers [146][147] of different generations. New strategies in the development of dendritic non-viral vectors are based on the modification of hydrophilic amine-functionalized dendrons of low generation with hydrophobic portions. This leads to the construction of cationic dendritic amphiphiles which, due to their amphiphilic nature, are able to self-assemble in water forming supramolecular dendrimers, also called *pseudodendrimers*. Low generations Bis-MPA [148], PAMAM [149][150] and polyglycerol-based dendrons [86][151] have been linked to both linear hydrocarbon chains, rigid hydrophobic scaffolds like cholesterol, and lipids. It has been demonstrated that the characteristics of the hydrophobic portion strongly influence the binding efficacy of the genetic materials: higher is the amphiphile self-assembling attitude, higher is the gene binding efficacy [148].

As discussed in chapter 2, FDG_1 , FDG_2 and FDG_3 are promising molecules for the development of ^{19}F -MRI traceable probes. Due to their different balance between the sizes of the polyester polar dendron and the branched fluorinated hydrophobic portion, these molecules showed different properties both in bulk and in water.

Important characteristics to be taken into account for the development of a good gene vector are surface density of positive charges, fundamental for an efficient gene binding, colloidal stability, and size of the aggregates. It has been demonstrated in fact that small micelles tend to form more stable complexes with genes [83][152]. Considering self-assembly properties shown by the three new fluorinated dendritic amphiphiles (see chapter 2), FDG_2 has been selected as the most promising candidate to be further functionalized in order to design a new fluorinated gene delivery vector. In fact, this molecule showed a good balance between fluorinated and polyester moieties and self-assembled forming colloidally stable micelles in solution. Furthermore, the four hydroxyl terminal groups on the polyester moiety can be easily chemically modified to form four positively charged primary ammonium groups able to bind the negatively charged nucleic acids. Therefore, FDG_2 has been converted in a tetravalent ammonium cation showing four trifluoroacetate ions as counterions. The new molecule, FDG_2N shown in figure 3.1, is an optimal candidate to function as ^{19}F -MRI traceable gene delivery vector. The presence of the branched polyfluorinated core can impact on the oligonucleotides binding efficacy and on the transfection efficiency as suggested by literature.

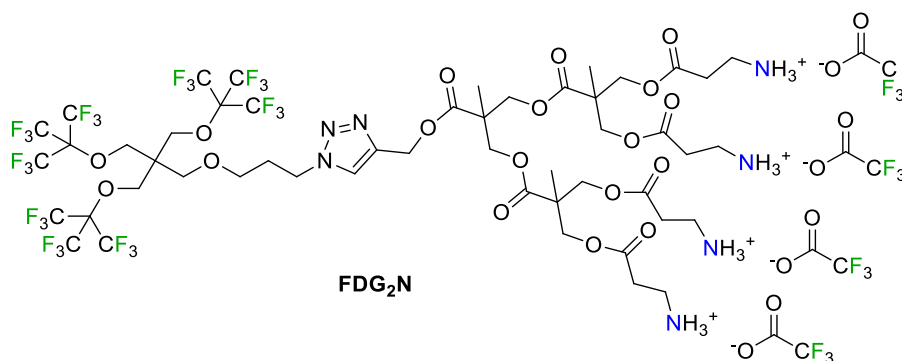


Figure 3.1 Structure of FDG₂N, a new cationic polyfluorinated Bis-MPA-based dendritic amphiphile suitable for gene delivery and ¹⁹F-MRI traceability applications.

3.1 Results and discussion

In the following section the synthetic strategy adopted to modify FDG₂ will be described together with the structural characterization of FDG₂N. Then, in section 3.1.2, self-assembling properties of the cationic amphiphile in water media and effects on the aggregate shape caused by the presence of electrolytes in water will be discussed. In the same section, relaxation times of the fluorine atoms present in the inner cavity of the aggregates formed by FDG₂N will be reported. In section 3.1.3, the characteristics of FDG₂N as gene delivery vector will be presented. The characterization of the dendriplexes, complexes formed between dendrimers and nucleic acids, will be reported and then the gene binding efficacy and cytotoxicity will be described. Finally, in section 3.1.4, some preliminary results about the *in vitro* efficacy of FDG₂N as miRNA delivery vector will also be reported.

3.1.1 Synthesis, purification and characterization of FDG₂N

As shown in figure 3.2, the synthesis of FDG₂N started from FDG₂, whose synthesis has been already described in the previous chapter.

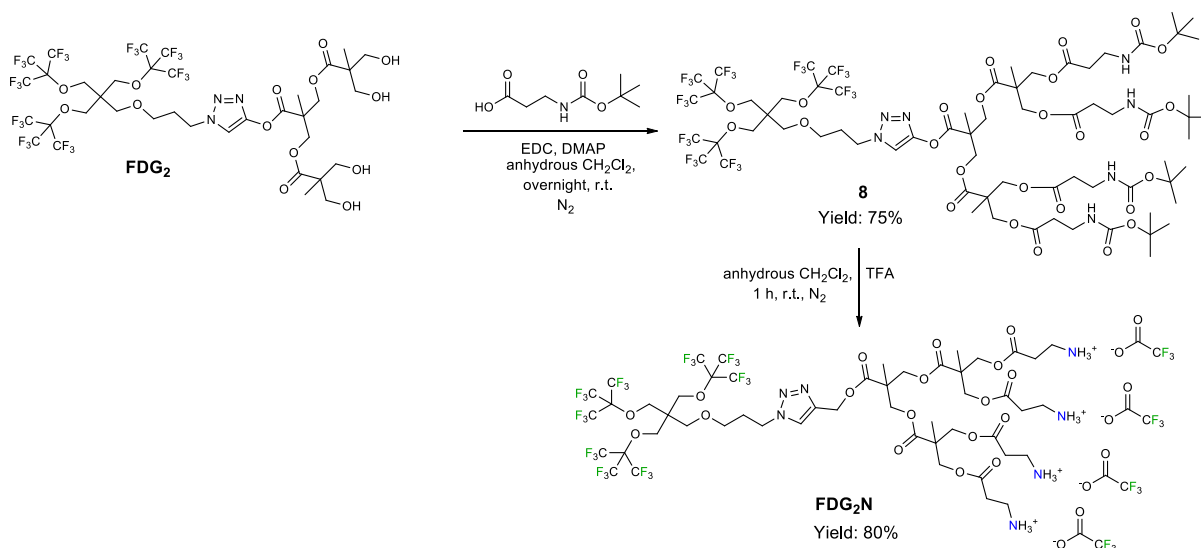


Figure 3.2 Synthesis of FDG₂N starting from FDG₂ as the precursor.

The Steglich esterification was performed to obtain an ester bond among the hydroxyl groups of FDG₂ and 3-[(2-methylpropan-2-yl)oxycarbonylamino]propanoic acid, also called Boc-beta-alanine. EDC and DMAP were used as coupling agents. After evaporation of CH₂Cl₂, used as reaction solvent, the crude obtained from the reaction was purified by silica gel flash chromatography with a mixture

of hexane and ethyl acetate (1:1 v/v) as eluent. Then, excess of the unreacted Boc-beta-alanine was totally removed washing the product with 10% m/v aqueous solution of NaHCO₃ and extracting it with CH₂Cl₂ as organic phase. The product was obtained after removal of the organic solvent by rotary evaporation.

The formation of the product was confirmed by ¹H-NMR. In particular, the presence of all the peaks of the precursor together with two triplets at 3.36 and 2.5 ppm relative to the methylene groups of the linked Boc-beta-alanine and the peak of the methyl protons of the Boc-protecting group at 1.41 ppm confirmed the formation of intermediate **8** (Figure 3.2). This derivative can be isolated at high yield (75%). FDG₂N can be obtained deprotecting the amino groups of intermediate **8** in acidic condition; this deprotection was performed in presence of trifluoroacetic acid (TFA) and therefore, the product was isolated as a salt with four TFA anions as counter ions.

Thanks to fluorine-fluorine interactions, excess of TFA was removed dissolving the product in hexafluoro-2-propanol and evaporating the solvent by rotary evaporation, afterward a precipitation in presence of cold diethyl ether was performed. FDG₂N was finally obtained as a white solid upon freeze-drying from a solution of the compound in water at 80% yield. ¹H-NMR analysis confirmed the formation of the desired product (figure 3.3a). The lack of the peak relative to the methyl groups of the boc-protecting group of intermediate **8** confirmed that the deprotection of the amine groups was successful. Furthermore, the ¹⁹F-NMR spectrum of the pure compound is shown in figure 3.3b, in which the fluorine peaks of the compound and of TFA anions are visible. In this spectrum, setting the integral of the peak at -71.56 ppm relative to FDG₂N at 27, which is the number of fluorine atoms per molecule, the integral of the TFA at -76.8 ppm becomes 12, which confirms the presence of four TFA anions and no excess of TFA is present.

FTIR analysis confirmed the molecular structure of FDG₂N. Comparing the spectrum of FDG₂ with that of the cationic derivative (figure 3.4) it could be observed the disappearance of the intense and sharper peak related to the stretching of the -OH groups with the presence of less intense and broader peak relative to the stretching of -NH₃ groups in the same region. Moreover, the FTIR spectrum of FDG₂N shows two peaks at 1745 and 1674 cm⁻¹ related to the C=O stretchings of the carboxyl groups of the cationic derivative and its TFA counterions. Similarly to FDG₂ the characteristic stretching bands of the C-F bonds in the range between 1300 and 650 cm⁻¹ are clearly observed. As a new molecule, FDG₂N has also been characterized by HRESI-MS that was in agreement with the chemical structure shown in Figure 3.2.

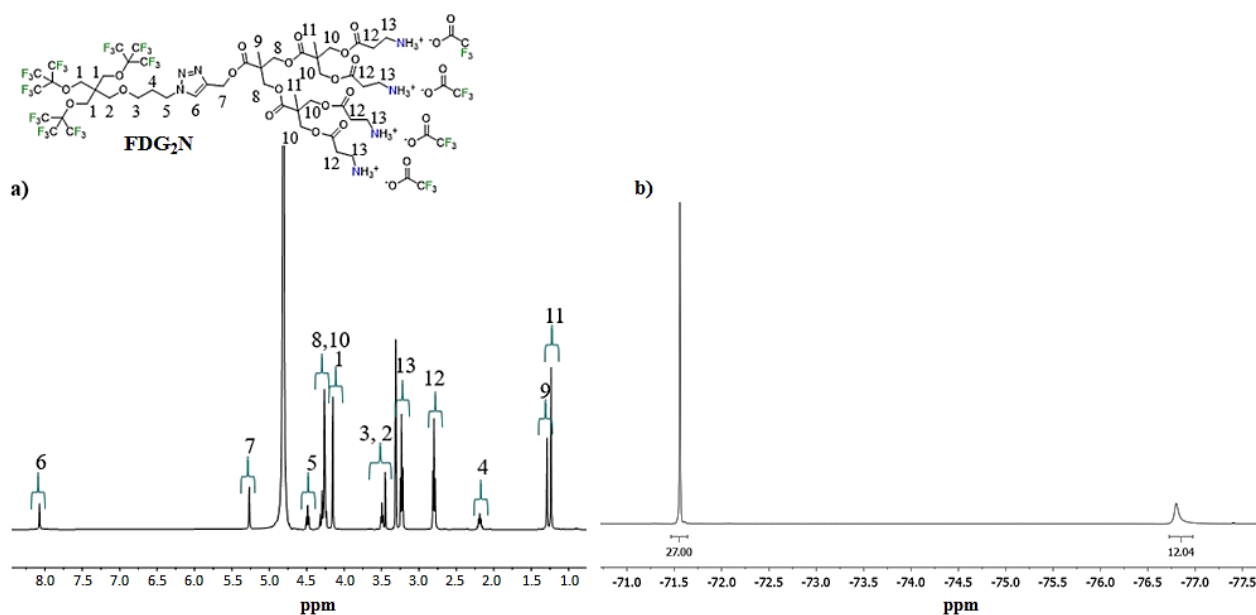


Figure 3.3 a) ¹H-NMR spectrum of FDG₂N and peak assignment. b) ¹⁹F-NMR spectrum of FDG₂N. As shown by the integration, each molecule of the cationic amphiphile bears 27 fluorine atoms and 4 TFA anions as counter ions. Solvent: CD₃OD.

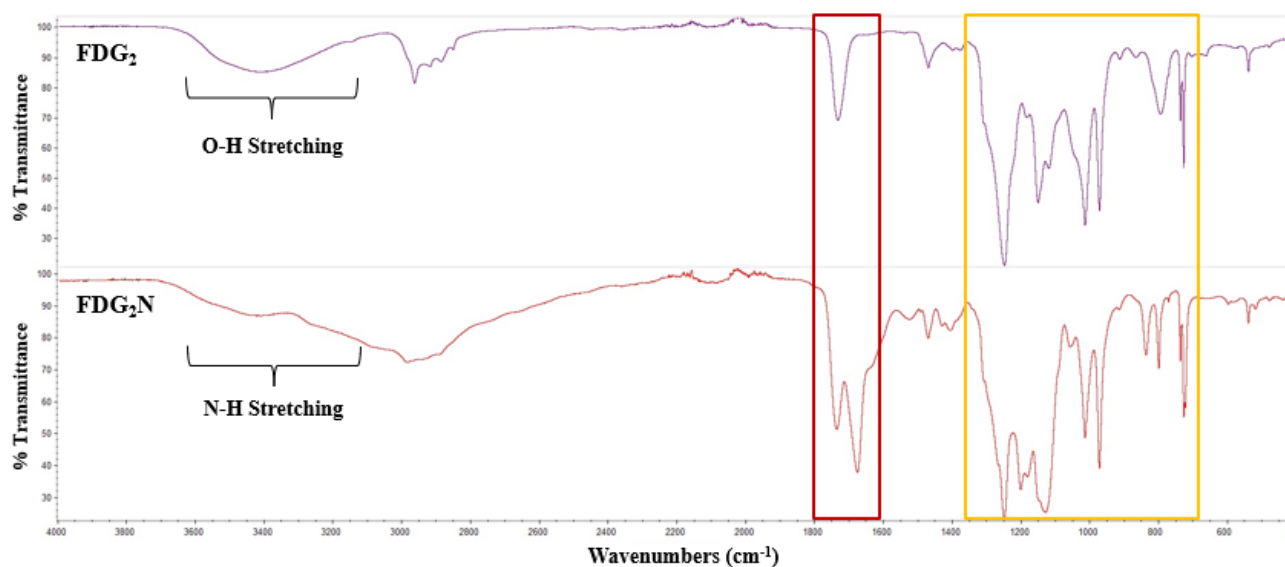


Figure 3.4 Comparison between ATR-FTIR spectra of FDG₂, the second generation Bis-MPA based hydroxyl terminating precursor, see chapter 2, (up) and its cationic derivative FDG₂N (down). The presence of the characteristic stretching and bending of C-F bonds (highlighted in the yellow rectangle) in both spectra together with the appearance of a second peak in the C=O stretching region (red rectangle), related to the presence of TFA as counter ion and to the carboxyl groups of the polyester structure, and the disappearance of the O-H stretching of FDG₂ which is substituted with a broader and less intense peak in the same region in the FDG₂N spectrum confirmed the product structure.

3.1.1.1 Chemical and thermal stability of FDG₂N

We evaluated the thermal stability of FDG₂N by TGA. As shown in figure 3.5, the cationic derivative is stable till high temperature as it showed a 5% weight loss (T5%) at 204°C with a two steps degradation pathway.

The first degradation step caused 13% weight loss at 228°C followed by a progressive weight loss until to the total degradation of the compound which occurred at about 400°C.

We were able to measure $^1\text{H-NMR}$ and $^{19}\text{F-NMR}$ spectra of FDG_2N after first degradation step at 204°C . As shown in figure 3.6a, the first degradation step is related to the partial loss of TFA ions detectable from the $^{19}\text{F-NMR}$ spectrum. In fact, there is a clear reduction of the intensity of the peak at -76.8 ppm upon degradation. Furthermore, the broadness of the peak related to the fluorine atoms of FDG_2N suggests that at 204°C even the molecular structure of the amphiphile starts to degrade. Indeed, $^1\text{H-NMR}$ spectrum of the degraded FDG_2N , reported in figure 3.6b, shows the disappearance of the signals of the protons of the methylene groups in *alfa* and *beta* position to the ammonium groups in the molecule suggesting that at this temperature FDG_2N starts its degradation from the outer polar periphery.

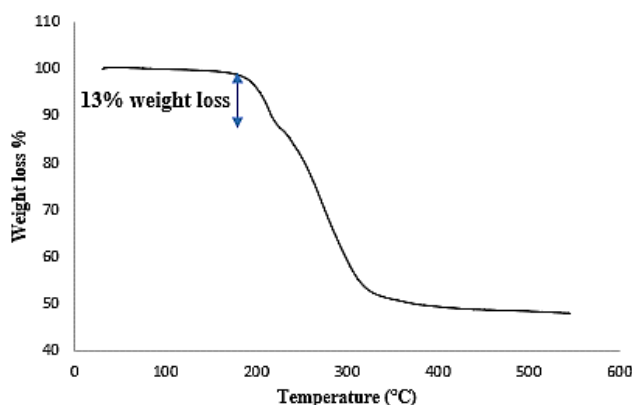


Figure 3.5 Thermal stability of FDG_2N , TGA results. A 13% weight loss (highlighted with the blue arrow) was observed at 228°C . The total degradation of the compound occurs at temperature higher than 400°C .

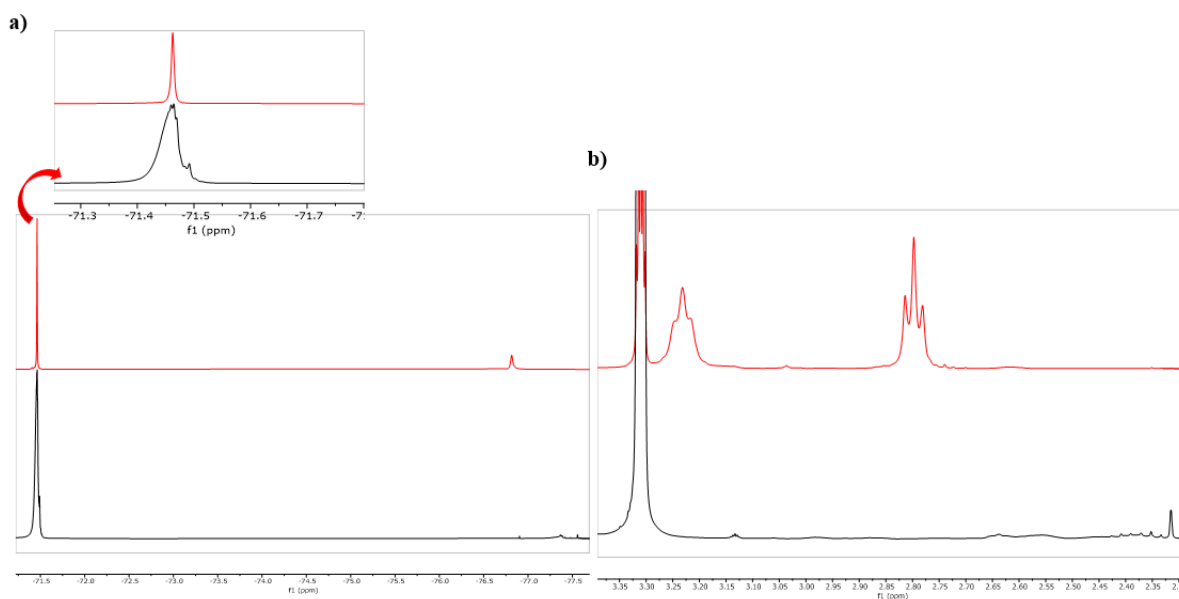


Figure 3.6 a) $^{19}\text{F-NMR}$ spectra of FDG_2N and b) $^1\text{H-NMR}$ spectra of FDG_2N in the pristine state and after the first degradation step seen at TGA at 204°C . Color code: red = pristine state, black = after the degradation.

It has been reported in literature that Bis-MPA-based polyester dendrimers, surface functionalized with beta-alanine, tend to degrade in aqueous media. In these works, the stability of the dendrimers in water has been monitored by MALDI-TOF Mass spectrometry over time. The authors showed a progressive decrease in the intensity of the molecular ion peaks and an increase in the number of the peaks related to the degraded molecules even at acidic pH. This is due to both intermolecular reactions and ester bonds hydrolysis in water, which starts from the rupture of the ester bonds in the outer layers

[139][153]. Therefore, we evaluated the chemical stability of FDG₂N in aqueous solution analyzing it by MALDI-TOF Mass spectrometry directly after compound dissolution and after 24 and 48 hr from the sample preparation. The spectra are compared with those of the amphiphile dissolved in methanol, where it is expected higher stability. Mass analyses were performed in collaboration with Dr. Roberto Milani at VTT Technical Research Centre of Finland, Espoo, Finland.

As shown in figure 3.7, the mass spectrum of the water solution of FDG₂N did not show differences over time and it was comparable to that obtained in methanol. In Table 3.1 assignment of the peaks observed in the mass spectra are reported, the observed peaks can be associated to fragmentations of the molecule, which occurred during the analysis. In fact, fragmentation is strictly related to the laser power used for the analysis: the same spectra measured at decreasing laser powers showed a decrease in the intensity of the fragments' peaks. Therefore, from the results obtained it is possible to conclude that no degradation occurred at least until 48 hr after FDG₂N dispersion in water. As it will be described in the following section FDG₂N self-assembles in water forming aggregates, this can be responsible of a reduction in the reactivity of the ester bond due to steric hindrance which can contribute to a reduction in the degradation rate.

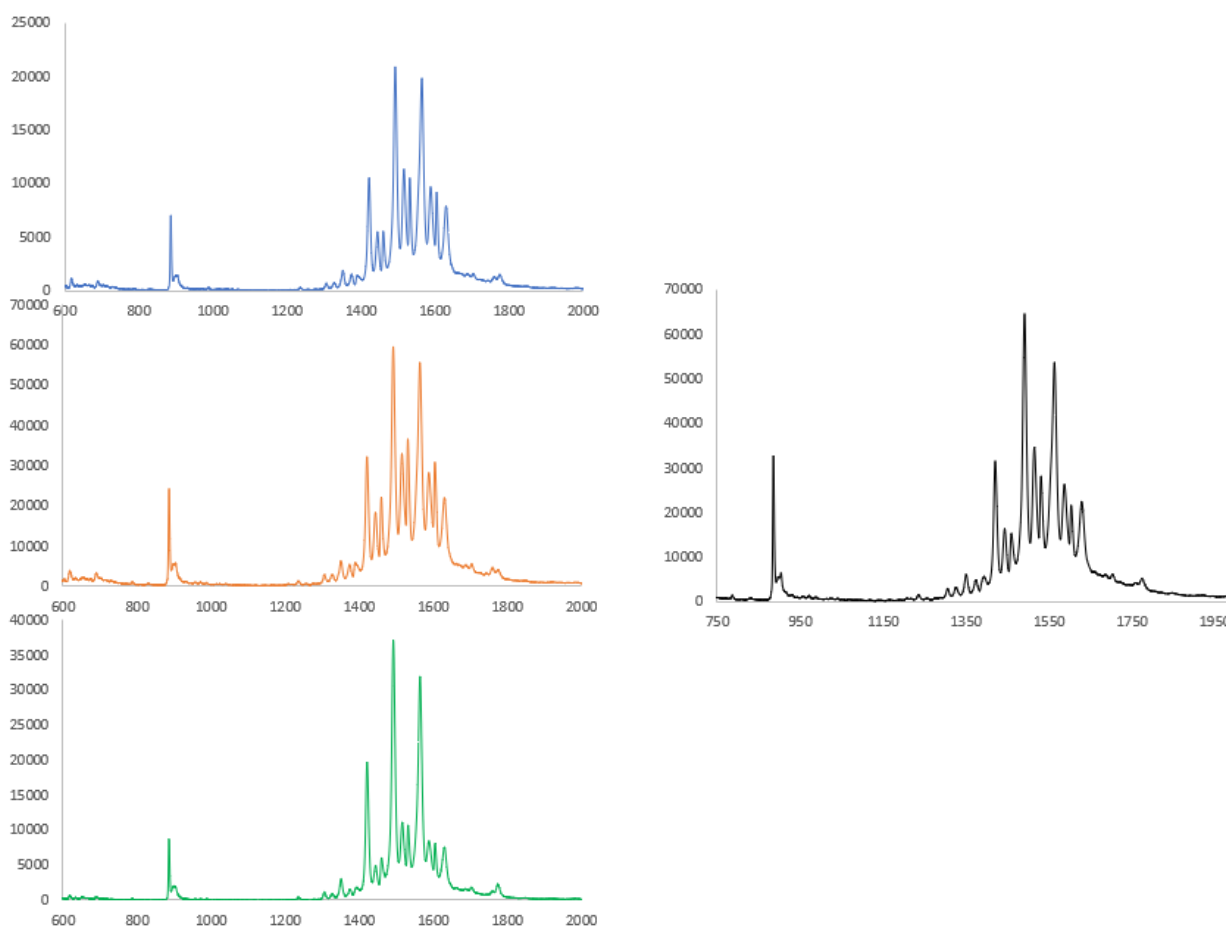
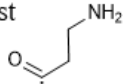


Figure 3.7 Mass spectra obtained from the MALDI-TOF MS analysis of the solution of FDG₂N dissolved in water and in methanol. Color code: water, after dissolution = blue; water, after 24 hs = orange; water, after 48 hs = green; methanol after dissolution = black.

Table 3.1 MALDI-TOF MS analysis, peaks assignment.

Peaks	Structure	Related peaks
<ul style="list-style-type: none"> $T_0 = 1565.4$ $T_{24} = 1564.5$ $T_{48} = 1565$ 	Molecular Ion	<ul style="list-style-type: none"> $1588 = 1565 + 23$ (Na) $1605 = 1565 + 39$ (K) $1630 = 1565 + 65$ (Cu)
<ul style="list-style-type: none"> $T_0 = 1493.8$ ($1565.4 - 71.6$) $T_{24} = 1492.7$ ($1564.5 - 71.8$) $T_{48} = 1493$ ($1565 - 72$) 	Fragment lost  Chemical Formula: $C_3H_6NO^+$ Exact Mass: 72.04	<ul style="list-style-type: none"> $1517 = 1493 + 24$ (Na)
<ul style="list-style-type: none"> $T_0 = 1422.9$ ($1493.8 - 71$) $T_{24} = 1422$ ($1492.7 - 71$) $T_{48} = 1422$ ($1493 - 71$) 	Fragment lost $C_3H_6NO^*$	<ul style="list-style-type: none"> $1444 = 1422 + 22$ (Na) $1461 = 1422 + 39$ (K)
<ul style="list-style-type: none"> $T_0 = 1351.5$ ($1422 - 71.4$) $T_{24} = 1351.5$ ($1422 - 71.4$) $T_{48} = 1351.5$ ($1422 - 71.4$) 	Fragment lost: $C_3H_6NO^*$	

3.1.2 Self-assembly of FDG₂N in aqueous media

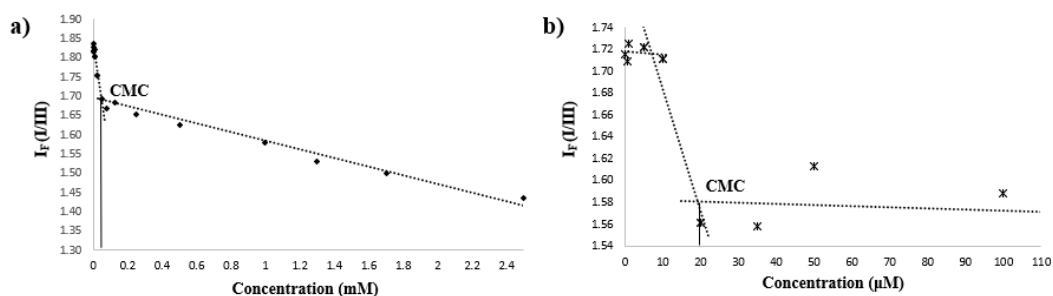
FDG₂N is directly dispersible in aqueous media. We firstly evaluated the critical micelle concentration (CMC) in pure water and in 150 mM NaCl aqueous solution monitoring the fluorescence of pyrene, used as probe. The fluorescence emission spectrum of pyrene is composed of five characteristic bands whose intensities are strictly dependent on the chemical environment around pyrene. Above CMC, due to the low polarity of pyrene, the probe is internalized in the hydrophobic inner cavity of the aggregates with the subsequent change of the intensity of the pyrene bands. CMC value can be determined plotting the ratio between the intensities of first and third pyrene bands versus amphiphile concentration [14][154][155].

CMC values were obtained at the intersection of the linear fit of the data at the change of the slope of the curve, following already reported procedures [86].

In figure 3.8 CMC graphs of FDG₂N obtained in two media are reported, while table 3.2 shows CMC values obtained for FDG₂N in pure water and in 150 mM NaCl aqueous solution.

Table 3.2 CMC values for FDG₂N in MilliQ water and in NaCl (150mM) obtained by the fluorescence method.

Solution	FDG ₂ N in MilliQ water	FDG ₂ N in NaCl (150mM)
CMC value	50 μ M	20 μ M

**Figure 3.8** CMC graphs. a) FDG₂N in MilliQ water, linear fitting. b) FDG₂N in NaCl (150mM), linear fitting.

Theoretically it is expected that an increase in the ionic strength causes a reduction in CMC values, since the presence of electrolytes in solution tends to shield the positive repulsive charges of the polar heads reducing the repulsion between them with subsequent increase in their tendency to self-assemble [3]. Due to a balance between hydrophobic effect and repulsive electrostatic interactions, FDG₂N showed a CMC in water of 0.05 mM; its self-assembling tendency increases in the presence of NaCl ions with a final CMC value almost twice lower than that observed in pure water. If compared to similar core-functionalized cationic Bis-MPA dendrons, FDG₂N showed, in presence of electrolytes, a CMC value comparable to those observed for Bis-MPA polyester dendrons of second generation core functionalized with linear hydrocarbon chains [148].

In the literature, it was reported an alternative method to evaluate CMC of fluorinated amphiphiles through ¹⁹F-NMR monitoring the shift of the high environmental sensitive trifluoromethyl group of polyfluorinated surfactants [156]. Above CMC aggregates start forming and therefore fluorine atoms in the micelles are shielded and this causes an upfield shift of the signal upon aggregation. If the exchange rate between free monomer and aggregate is fast with respect to NMR analysis time scale, the shift of the peak observed after micellization is a mean value of the monomer and aggregate resonances [156][157]. Therefore, we decided to determine the CMC of FDG₂N in pure water by ¹⁹F-NMR to compare these results with those observed by fluorescence.

If ¹⁹F-NMR spectra of FDG₂N at different concentrations are compared, as in figure 3.9, two sets of data can be observed whose intensities are dependent on the amphiphile concentration.

Downfield signals (between -71.6 and -71.35 ppm) can be related to the resonance of the fluorine atoms in the monomer form, as the fluorine atoms of the free monomer are in contact with the highly polarizable aqueous medium responsible for fluorine nucleus deshielding. Upfield signals (between -72.6 and -72.38) can be associated to the resonance of the shielded fluorine atoms in the inner cavity of the aggregates. The presence of both peaks in the spectra suggests that the exchange rate between monomer and aggregate is slow with respect to the NMR time scale. The simultaneous detection of the monomer and aggregate signals has been already reported for anionic polyfluorinated surfactants and fluorinated polymers. Generally, low exchange rates can be ascribed to the presence of interactions preventing aggregate disassembly [158]. In the case of FDG₂N the low exchange rate can be related to the strength of fluorine-fluorine interactions among branched fluorinated chains in the aggregate, which reduces the disaggregation rate of the micelles. Plotting the observed differences in the chemical shift of the peaks *versus* the inverse of the concentration it is possible to evaluate the CMC as the concentration at which the curve shows a breakpoint [156][157]. Figure 3.10 shows the graph obtained in pure water for FDG₂N, on the y-axis of the graph is reported the difference in ppm (Δ ppm) between the chemical shifts of the aggregates' peaks and the chemical shift of the monomeric form. All the chemical shifts are obtained by using the peak of TFA anions as an internal standard by setting its chemical shift at -76.55 ppm. As shown by the CMC graph, two distinct breakpoints can be observed one at 0.25 mM, and a second one at 1.7 mM. Similar behaviors have already been reported in literature for linear cationic fluorinated surfactants, and generally the breakpoint at lower concentration is related to the CMC while that at higher concentration is ascribed to the formation of a different type of aggregates [159]. Being the peaks of monomeric and aggregate forms present in the spectra at all the concentrations, we can speculate that both breaking points observed in the CMC graph can be related to changes in aggregates rather to the CMC onset. These results are in accordance with those obtained by fluorescence of pyrene, where the CMC was detected at 0.05 mM. Unfortunately, spectra performed at lower concentrations than 0.05 mM could not be detected due to

limits in the sensitivity of the ^{19}F -NMR.

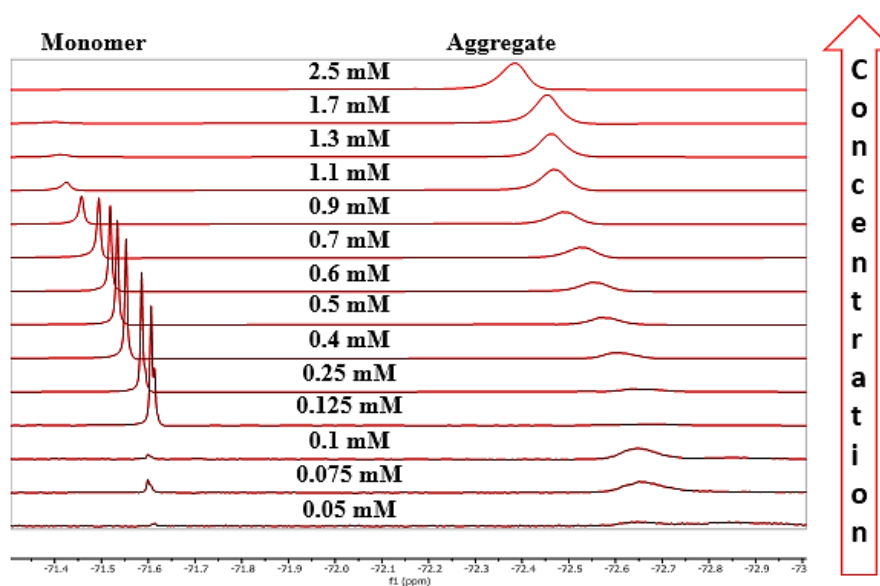


Figure 3.9 Comparison between the ^{19}F -NMR spectra obtained at the increasing in the FDG_2N concentrations. Solvent: FDG_2N solution + D_2O (10:1 v/v).

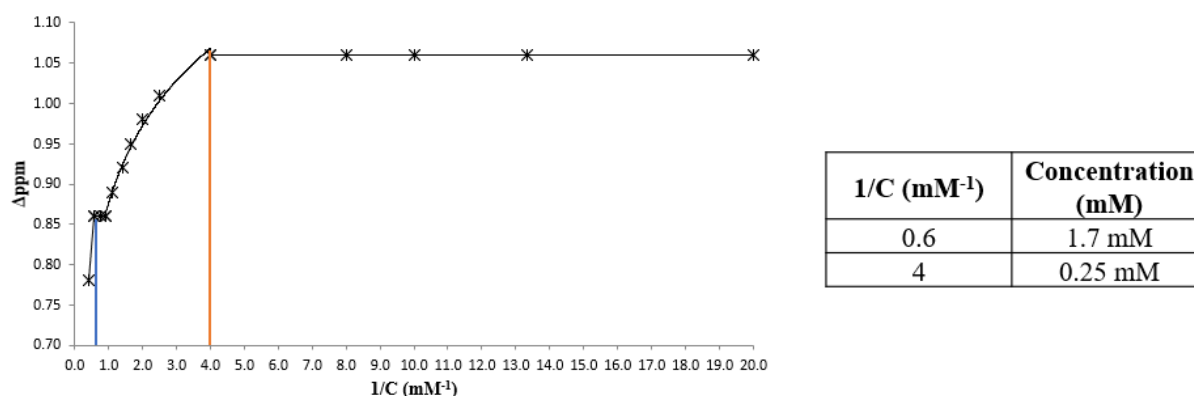


Figure 3.10 CMC graph obtained by plotting the difference between the shift of the monomer and the aggregate peaks observed in the ^{19}F -NMR spectra against the inverse of the FDG_2N concentrations. The table shows the corresponding concentration at the breaking points of the graph.

Figure 3.11 shows the shifts of the monomer and aggregate species against the concentration of FDG_2N .

In the graph reported in figure 3.11, two different situations can be observed. While at low concentrations (below 0.25mM) and between 1 and 1.7mM no shifts are observed for both the species, between 0.25mM and 1mM and at concentration of 2.5mM downfield shifts are observed for both the monomeric and aggregate forms. This can be attributed to changes in the dispersion composition. When the system is in equilibrium, the chemical shifts of both the species are constant; otherwise, when the system changes the chemical shifts change accordingly, thus indicating variations in the fluorine microenvironment.

At the increase in the FDG_2N concentration, the density of charges increases and probably the fluorine atoms are surrounded by a higher polarizable environment, responsible for the downfield shift of the aggregate peaks.

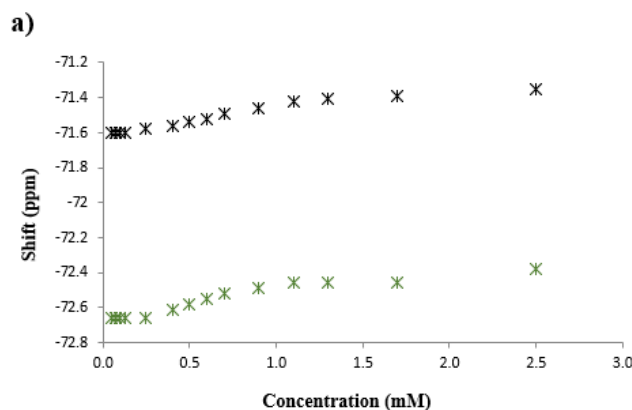


Figure 3.11 Chemical shifts observed in the ^{19}F -NMR spectra at the increasing in the concentrations of FDG₂N. Color code: black = monomeric form, green = aggregate form.

3.1.2.1 Characterization of the aggregates in solution

FDG₂N is directly dispersible in aqueous solutions forming aggregates from a concentration of at least 0.05 mM. Due to the low exchange rate between monomer and aggregate in aqueous solutions, ^{19}F -NMR spectra show the presence of the peaks of both the species. In this section the properties of the aggregates formed by FDG₂N in aqueous solutions will be discussed. The characterization of the aggregates in solution was done by DLS, ^{19}F -NMR, and Z potential monitoring eventual pH changes in the experimental environment. To determine dispersion stability, the samples were also studied overtime.

Characterization of the aggregates in pure water

FDG₂N self-assembly seems to be strictly dependent on the final concentration of the amphiphile in water. As just discussed, ^{19}F -NMR studies showed that the aggregates formed by FDG₂N seem to change their properties above 1.7 mM concentration. Therefore, we decided to study the properties of the aggregates at the concentrations of 0.5 mM, below this breaking point (figure 3.10), and 2.5 mM, above this point, overtime to monitor the stability of the colloidal dispersions.

Superimposing the correlation functions observed at DLS overtime for the two colloidal dispersions at $\theta=90^\circ$, as shown in figure 3.12a and 3.12b, it can be observed that no significant changes occur in the sample at 0.5 mM and 2.5 mM over 48 hr. This suggests that the dispersions are stable during this time. Furthermore, the correlation functions obtained for FDG₂N at concentration 2.5 mM is less noisy than those observed for FDG₂N at 0.5 mM. Table 3.3 shows the mean hydrodynamic radii obtained by cumulant fitting for the two analyzed colloidal dispersions. The obtained sizes are comparable for the two concentrations confirming that the lower scattering intensities is simply related to the lower concentration of the aggregates at 0.5 mM. Of note, the polydispersity indexes (PdI) obtained by cumulant analysis suggest that these colloidal dispersions are very polydisperse and thus populations of aggregates of different size are simultaneously present. By considering that different populations of aggregates are characterized by the same contrast and the same shape, on this base, in figure 3.13, the number weighted size distributions at the two different concentrations are reported together with the relative ^{19}F -NMR spectra overtime. The number weighted distributions, reported in figures 3.13a and 3.13c, suggest that the majority of the aggregates at the two concentrations are micelles of small size with a mean hydrodynamic radius of about 15 and 8 nm for

the 2.5 mM and 0.5 mM concentrations, respectively.

As shown in figures 3.13b and 3.13d, ^{19}F -NMR spectra of both colloidal dispersions do not change upon 48 hr ageing in agreement with DLS results. Furthermore, from the spectra it is clear that both monomeric and aggregated species are present in the two dispersions, but in different ratio. If the peaks of monomer and aggregate in the obtained spectra at 0.5 mM are integrated, it can be observed that 63% of the fluorine atoms resonate as aggregate, while remaining 37% as monomeric form. In the case of the 2.5 mM dispersion, the peak of the monomer is very low in intensity representing only 2% of the fluorine nuclei, while the remaining 98% are in the aggregated form.

As previously observed, the peak of the aggregate at 0.5 mM is more shielded (-72.58 ppm) than that at the 2.5 mM concentration (-72.38 ppm) and the aggregates formed by FDG₂N are smaller at the lower concentration. Presumably, fluorine atoms in the smaller aggregates are higher compressed with respect to the bigger ones and this can be responsible of a higher shielding of the fluorine nuclei from the water media with the consequent shift of the peak at lower ppm.

One of the important characteristics for a good gene complexation is the presence of positive charges. We thus evaluated the Z potential of the aggregates formed in water. For both tested concentrations in pure water, FDG₂N showed values higher than +30 mV that is promising in the perspective to use them as gene delivery vectors.

The peaks related to the aggregated form in the ^{19}F -NMR spectra are broader than those of the free monomer; this is due to the effect of self-assembly on the relaxation times of the fluorine atoms. It is known that self-assembly causes a reduction of the relaxation times, responsible of such broadening of the peaks [160]. For determining if FDG₂N can be a promising ^{19}F -MRI probe, T1 and T2 relaxation times of fluorine were measured in the self-assembled state. Therefore, the relaxation times of FDG₂N dispersions in pure water at a concentration of 2.5 mM were measured by ^{19}F -NMR. In these conditions FDG₂N showed a T1 of 465 ms and a T2 equal to 85.4 ms. If we compare these values to those of the classical ^{19}F -MRI probes such as perfluorooctyl bromide (PFOB), perfluorodecalin (PFDC), and perfluoro-15-crown-5- ether (PFCE) formulated as emulsions, T1 is comparable and sufficiently low, as low T1 are important for the reduction of the experimental time in MRI analysis. Instead, generally a short T2 is responsible of a worst signal to noise ratio (SNR) at MRI. In literature it is reported that to obtain good SNRs, T2 must be longer than 10 ms [161]. The value obtained for FDG₂N in water is promising since it is comparable with perfluoropolyether-based probes [162] and to hyperbranched-star amphiphilic fluoropolymers [163] which showed good performances as ^{19}F -MRI probes. All these preliminary results reveal that FDG₂N is promising as ^{19}F -MRI tracer.

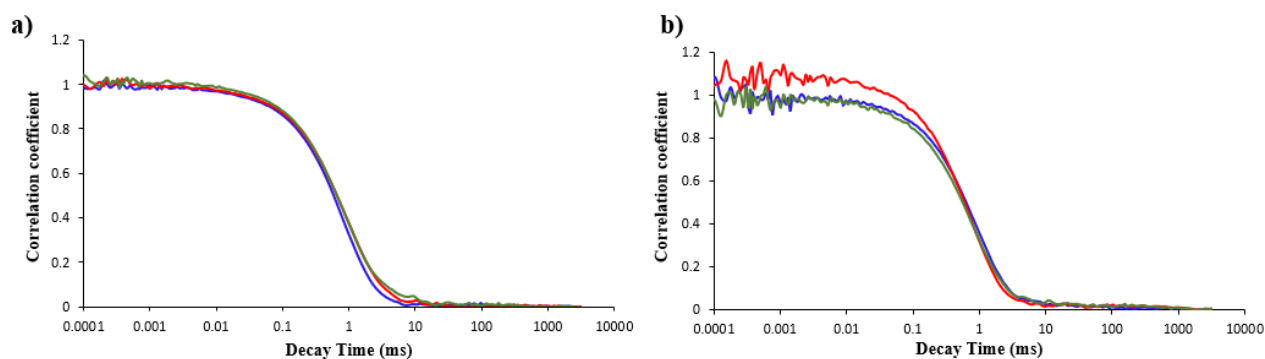


Figure 3.12 a, b) a) FDG₂N 2.5 mM in water. Comparison between the correlation function obtained at 90° at DLS overtime; **b)** FDG₂N 0.5 mM in water. Comparison between the correlation functions obtained at 90° at DLS overtime; **d)** intensity of the scattered light at 90°. Color code: 1 hr = blue, 24 hr = red, 48 hr = green.

Table 3.3 Hydrodynamic radii and polydispersity index of FDG₂N 2.5 mM and 0.5 mM in water overtime. R_H and PdI were obtained by cumulant fitting at 90°.

0.5 mM			2.5 mM		
90°			90°		
Time	Hydrodinamic Radius (nm)	PdI	Time	Hydrodinamic Radius (nm)	PdI
0	147 ± 7	0.4	0	140 ± 7	0.3
24	120 ± 5	0.3	24	153 ± 8	0.4
48	130 ± 6	0.4	48	148 ± 7	0.4

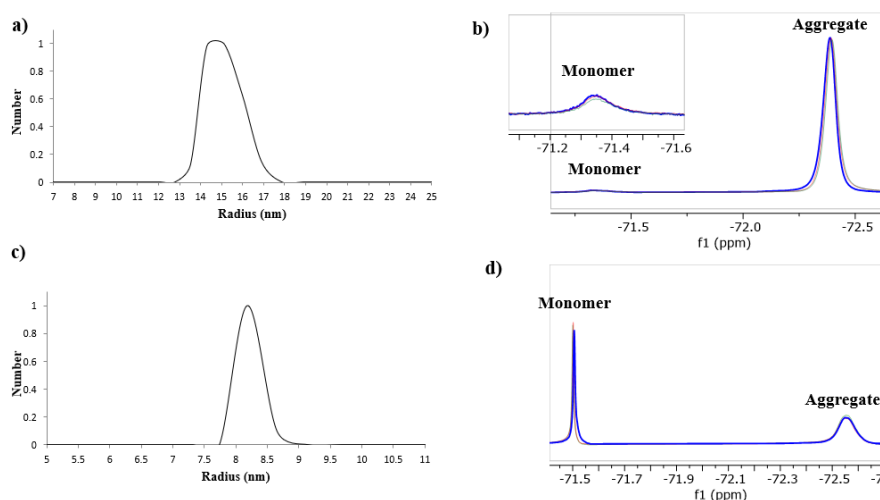


Figure 3.13 a, b) FDG₂N 2.5 mM in water. **a)** Number weighted distribution at 90° after 48 hr of ageing; **b)** Superimposition of the ¹⁹F-NMR spectra obtained after 1hr, 24 hr and 48 hr of ageing. **c, d)** FDG₂N 0.5 mM in water. **c)** Number weighted distribution at 90° after 48 hr of ageing; **d)** Superimposition of the ¹⁹F-NMR spectra obtained after 1 hr, 24 hr and 48 hr of ageing. Color code: after 1 hour of ageing = blue, after 24 hr = red, after 48 hr = green. ¹⁹F-NMR solvent: FDG₂N solution + D₂O (10:1 v/v).

Molecular Dynamics: FDG₂N in water

To better elucidate self-assembling properties of FDG₂N, molecular dynamics simulations have been performed in collaboration with Professor Giuseppina Raffaini (DCMIC, Politecnico di Milano). In particular, energy minimization of one FDG₂N molecule was obtained in a box containing only water molecules to mimic the experimental conditions. Table 3.4 shows the molecular parameters and the dipole moment resulting from these simulations, which were used to predict the packing parameter and aggregate shape of the amphiphile in aqueous solutions.

Table 3.4 Molecular dynamics simulations. Dimensions, dipole moment, and packing parameter calculated for FDG₂N

Amphiphile	Dipole moment (Debye)	Total volume (v) (Å ³)	Length (l _d) C-OH/C-F ₃ (Å)	Polar surface area (a ₀) (Å ²)	Packing parameter*	Aggregates prediction
FDG ₂ N	86	1387	23	631	0.1	Spherical micelles

* packing parameter = $v/(a_0 \cdot l_d)$

The high value of the dipole moment of FDG₂N, almost 26 times higher than that of its precursor FDG₂, which in pure water showed a dipole moment of 3.24 Debye, justifies its dispersibility in water without the use of ethanol as co-solvent.

The calculated packing parameter (about 0.1) suggests the formation of micelles in water which is in good agreement with the experiments as shown by DLS and SAXS experiments.

Characterization of the aggregates in NaCl solution and in HEPES Buffer

The good dispersibility in water with the formation of nano-scaled assemblies and its high positive zeta-potential make FDG₂N a good candidate as gene delivery vector. The most common solvents used for gene complexation studies are 10 mM HEPES buffer (pH = 7.4) and NaCl 150 mM [164]. The use of these media guaranteed monitoring of FDG₂N self-assembly at physiological pH and in presence of electrolytes. Tables 3.5 and 3.6 show the obtained characterization of FDG₂N in these two aqueous solutions at 2.5 mM and 0.5 mM. The pH variation is higher as the FDG₂N concentration increases; furthermore, as shown by table 3.5, HEPES buffer is able to stabilize the pH only for the lower FDG₂N concentration. This is related to the low buffer concentration; in fact, the use of HEPES buffer 25 mM guaranteed a higher stability of the pH even for the FDG₂N concentration of 2.5mM, as shown in table 3.7.

Table 3.5 Self-assembly of FDG₂N in HEPES buffer 10 mM pH 7.4. Z potential has been measured after 48 hours of ageing. R_H and PdI were obtained by cumulant fitting at 90°.

HEPES 10 mM (pH=7.4)					HEPES 10 mM (pH=7.4)				
FDG ₂ N concentration 0.5 mM					FDG ₂ N concentration 2.5 mM				
Time	pH	R _H (nm)	PdI	Z potential (mV)	Time	pH	R _H (nm)	PdI	Z potential (mV)
1 hr	7.3	60 ± 3	0.5	+ 56	1 hr	6.9	193 ± 10	0.4	+ 90
24 hr	7.3	32 ± 2	0.4		24 hr	6.5	128 ± 6	0.4	
48 hr	7.2	32 ± 2	0.3		48 hr	5.8	119 ± 6	0.3	

Table 3.6 Self-assembly of FDG₂N in NaCl 150 mM. Z potential has been measured after 1 hour of ageing. R_H and PdI were obtained by cumulant fitting at 90°.

NaCl 150 mM (pH=7.2)					NaCl 150 mM (pH=7.2)				
FDG ₂ N concentration 0.5 mM					FDG ₂ N concentration 2.5 mM				
Time	pH	R _H (nm)	PdI	Z potential (mV)	Time	pH	R _H (nm)	PdI	Z potential (mV)
1 hr	6.6	272 ± 14	0.4	+ 40	1 hr	6	576 ± 29	0.3	+ 88
24 hr	7.0	455 ± 23	0.5		24 hr	6.3	467 ± 23	0.4	

Table 3.7 Self-assembly of FDG₂N in HEPES buffer 25 mM pH 7.4. Z potential has been measured after 48 hours of ageing. R_H and PdI were obtained by cumulant fitting at 90°.

HEPES 25 mM (pH=7.4)			
FDG ₂ N concentration 2.5 mM			
Time	pH	R _H (nm)	PdI
1 hr	6.8	122 ± 6	0.5
48 hr	6.5	30 ± 2	0.2

In both media, as observed from the PdI values close to 0.4, FDG₂N forms quite polydisperse assemblies, for which hydrodynamic radii increase with amphiphile concentration. Furthermore, larger assemblies are formed in NaCl 150 mM, where the size increases at the low concentration overtime while decreases over time at high concentration. In HEPES the hydrodynamic radii instead decrease overtime reaching a sort of “equilibrium” value after 24 hours of ageing. This different behavior can be ascribed to different interactions between cationic assemblies and ions present in the different media enhanced by different final pH values of the dispersions (causing different protonation of the amine groups and diverse salt concentrations (higher for NaCl).

Figure 3.14, instead, shows a comparison among number weighted distributions of the hydrodynamic radii in HEPES 10 mM and in NaCl 150 mM. With all the limits of fitting analysis to pass from intensity to number weighted size distributions, and supposing that the scattering objects are characterized by the same contrast and the same shape, these results clearly suggest that high majority of these assemblies are small size micelles with hydrodynamic radii of about 3-5 nm. Presumably, the ratio between bigger and smaller aggregates is different in the two media. This is further confirmed if the dispersions are filtered on 0.22µm filters. As it is shown in figures 3.15a and 3.15b, while the dispersion in HEPES buffer at 0.5 mM showed no changes of the correlation functions and in scattered light intensities before and after filtration. A different behavior was observed for the same FDG₂N concentration in NaCl. In fact, the scattered light intensity significantly decreases, and the autocorrelation function shifts to lower timescales (smaller size) and appears noisier. This suggests that FDG₂N forms larger assemblies in NaCl that cannot pass through the filter pores.

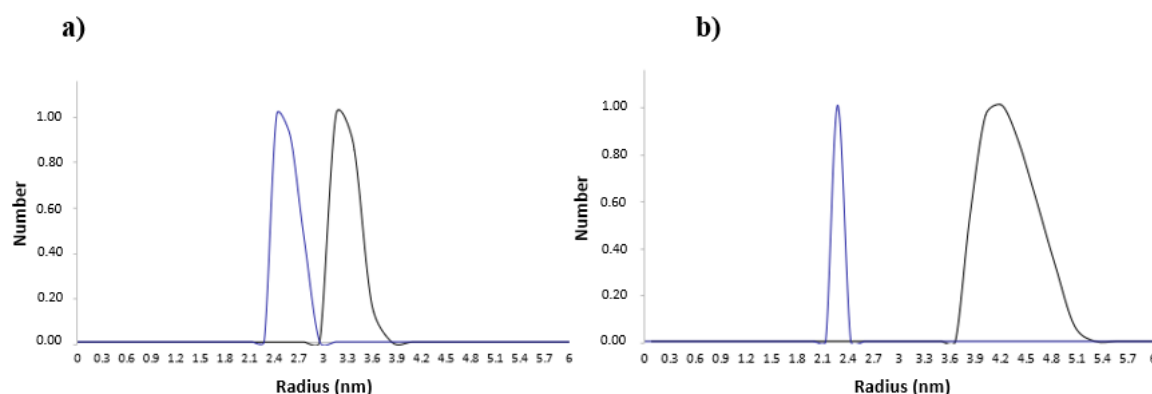


Figure 3.14 Number weighted distribution at DLS after 24 hours of samples ageing. **a)** FDG₂N 2.5 mM, **b)** FDG₂N 0.5mM. Color code: blue = HEPES 10 mM; black = NaCl 150 mM.

Another confirmation of the different sizes observed in the two media has been obtained from Cryo-TEM images which were done in collaboration with Professor Nonappa from Tampere University of applied sciences in Finland and Cryo-EM images in collaboration with Dr. Antonio Chaves-Sanjuan from Cryo-EM Lab, Department of Biosciences, University of Milan.

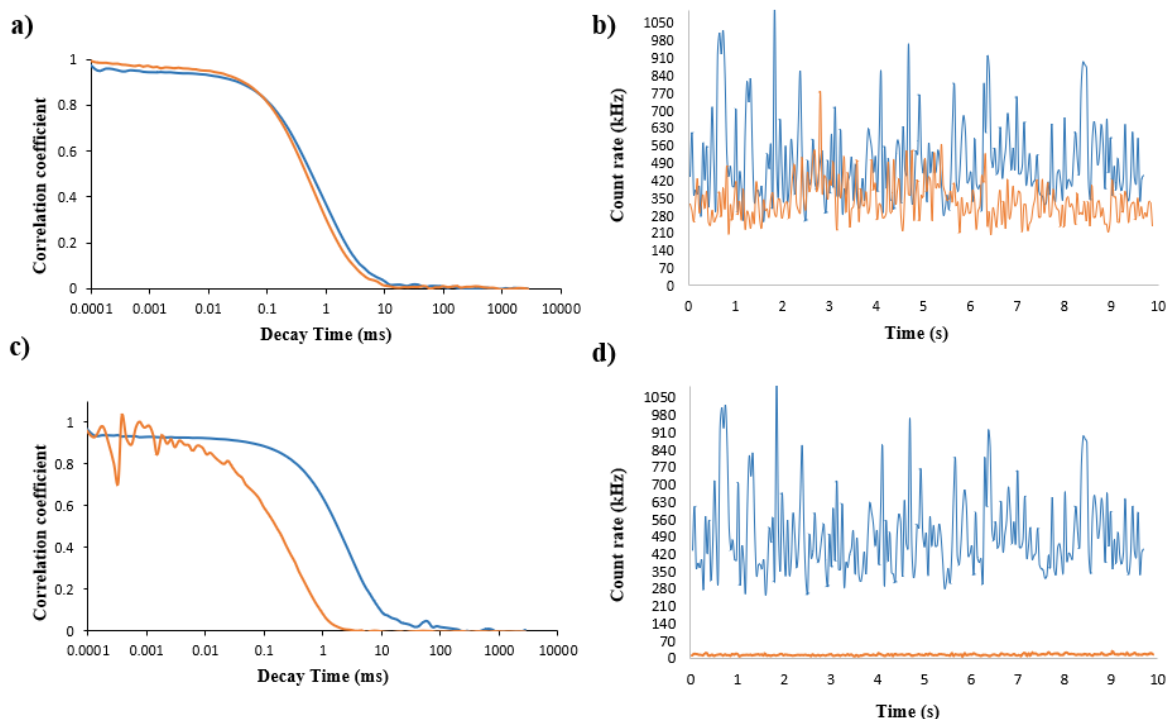


Figure 3.15 Effect of filtration on 0.5 mM FDG₂N dispersions after 24 hours ageing by DLS. **a)** Correlation functions at 90° of FDG₂N in HEPES buffer before and after filtration; **b)** Intensity of the scattered light during DLS analyses in HEPES buffer before and after filtration. **c)** Correlation functions at 90° of FDG₂N in NaCl 150 mM before and after filtration; **d)** Intensity of the scattered light during DLS analysis in NaCl 150 mM before and after filtration. Color code: blue = before filtration; orange = after filtration.

Figure 3.16 shows images of the dispersions obtained by dissolving FDG₂N at a 2.5 mM concentration in HEPES buffer 10 mM and in NaCl 150 mM.

The high majority of the aggregates present in HEPES 10 mM are small micelles with a mean size (diameter) of about 5-10 nm. The dimensions of the aggregates in HEPES were confirmed even by SAXS analyses which were done at the Chemistry Department of University La Sapienza in Rome by Dr. Alessandra Del Giudice. SAXS spectrum of 2.5 mM FDG₂N suspension in HEPES (10 mM, pH = 7.4) is reported in Figure 3.17 as red scatterers. The curve has been fitted by a combination of a spherical form factor with a log-normal distribution and a structure factor for a system of charged, spheroidal objects in dielectric medium. This allowed for inclusion of the interparticle interference effects due to screened coulomb repulsion between charged particles. The fitting curve is reported in the figure as a solid black line. The sample can be well approximated to a quite polydisperse population of spheres and the resulting mean radius is 2.5 nm, in accordance with DLS and Cryo-TEM results.

When FDG₂N is dissolved in NaCl 150 mM at 2.5 mM, close to micelles of small dimensions (15-20 nm of diameter), spherical aggregates of bigger dimensions, 50-100 nm averaged, are present. These bigger aggregates are probably responsible for the high hydrodynamic radii obtained at DLS by the cumulant fitting. Figure 3.18 shows the ¹⁹F-NMR spectra of the four colloidal dispersions just described. Even in this case the chemical shifts of the peaks are related to those of the TFA anions, set at -76.55 ppm.

¹⁹F-MRI can be a useful tool to monitor self-assembling behavior in water [134]. The first difference between NMR spectra observed in pure water and those reported in figure 3.18 is the lack of the peaks related to the monomeric form. This can be ascribed to an increase in the exchange rate between monomer and aggregate in the presence of an increased concentration of ions. It is interesting to note

that over time the peaks shift: in 10 mM HEPES we observed that the aggregates tend to decrease in their size reaching an equilibrium after 48 h.

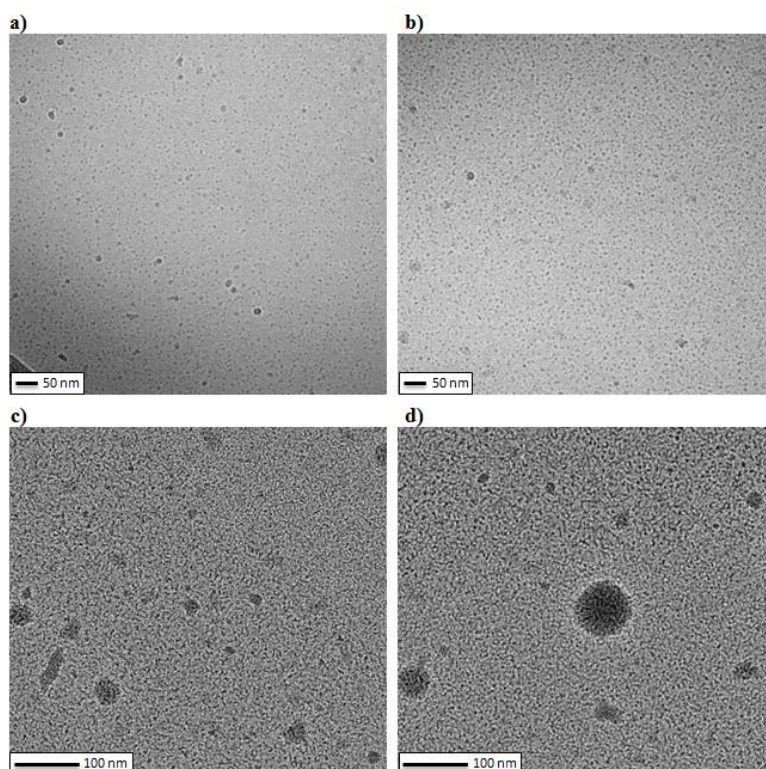


Figure 3.16 a, b) FDG₂N 2.5 mM in HEPES buffer 10 mM (pH 7.4), fresh sample: Cryo-TEM images highlight the presence of small micelles of about 5-10 nm of diameter. **c, d)** FDG₂N 2.5 mM in NaCl 150 mM, fresh sample: Cryo-EM images show the coexistence of small micelles (10-20 nm of diameter) and bigger spherical aggregates (around 50-100 nm).

As it is shown in figure 3.18a and 3.18b, the peak of the 2.5 mM and the 0.5 mM concentrations of the amphiphile in HEPES shifts upfield (0.05 and 0.26 Δ ppm, respectively) after 24 hours of ageing and then no further shift is observed.

The reduction in size, higher for the lower concentration, seems to hide more fluorine atoms from the polarizable external environment (chemical shift up shielded). In 150 mM NaCl the dispersions at 2.5 mM showed no significant differences upon 24 hours ageing by ¹⁹F-NMR, shown in figure 3.18c, in agreement with DLS results. At the lower concentration, 0.5 mM, the size of the aggregates was found to increase over time and accordingly NMR spectra showed a shift of 0.04 Δ ppm down shielded, as shown in figure 3.18d. Depending on amphiphile concentration and experimental conditions (i.e. concentration and nature of the medium) multiple peaks can be observed. In this regard, it has been reported that the splitting of the signal of chemically equivalent fluorine atoms can be related to the presence of different types of aggregates in the dispersion [158] or to a different chemical environment around the fluorine atoms. However, assemblies formed in pure water were characterized by higher PDI values with the formation of different populations, but no splitting of the NMR signal was observed. This suggests that the presence of multiple peaks is more related to a different chemical environment around the fluorine atoms caused by specific interactions with the ions present in the media. It might also be that these interactions are different for the diverse assemblies present in the dispersions. Clearly, further analyses must be done to elucidate better the reasons of this splitting.

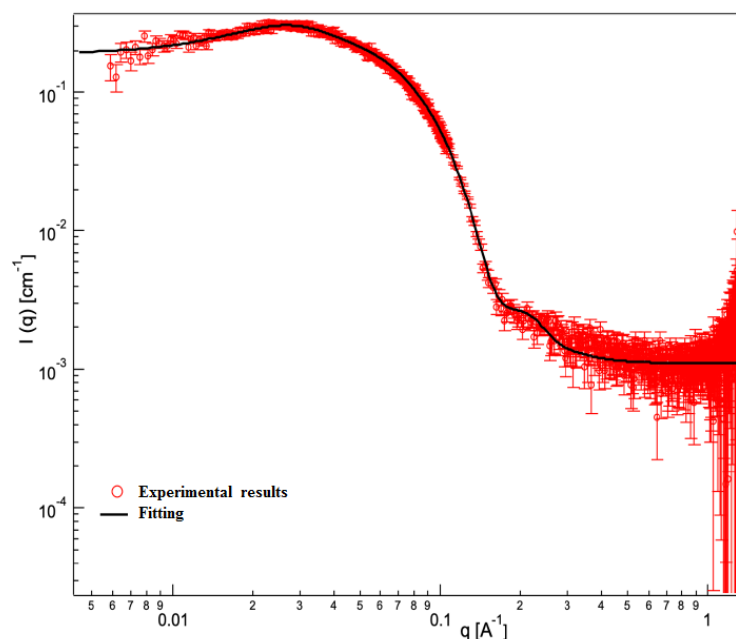


Figure 3.17 SAXS analysis of 2.5 mM FDG₂N in HEPES buffer (10 mM, pH 7.4). Structure factor (the Fourier transform of the pair correlation function $g(r)$ for a system of charged, spheroidal objects in a dielectric medium) here is combined with an appropriate form factor (such as spherical with a log-normal distribution of size) and allows for inclusion of the interparticle interference effects due to screened coulomb repulsion between charged particles. The red scatterers represent the SAXS spectrum of the analyzed dispersion, while the solid black line represents the fitting curve.

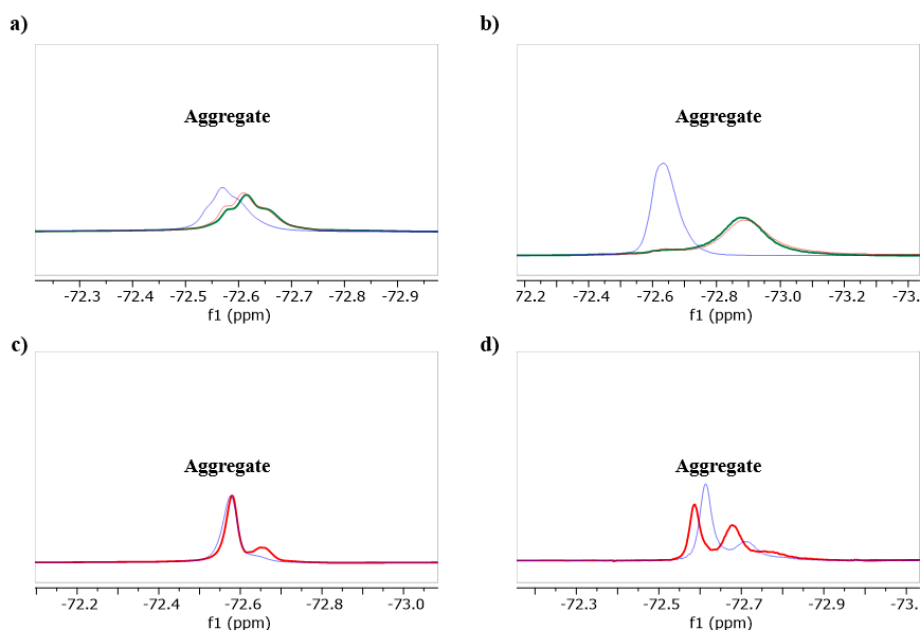


Figure 3.18 ^{19}F -NMR spectra of the tested FDG₂N dispersions overtime. **a)** 2.5 mM concentration in 10 mM HEPES buffer; **b)** 0.5 mM concentration in 10 mM HEPES buffer. **c)** 2.5 mM concentration in NaCl 150 mM; **d)** 0.5 mM concentration in NaCl 150 mM. Color code: after 1 hour of ageing = blue, after 24 hs = red, after 48 hs = green. ^{19}F -NMR solvent: FDG₂N solution + D₂O (10:1 v/v).

3.1.3 Nucleic acids complexation

In this section the binding ability of FDG₂N as gene delivery vector will be discussed, important parameters for this complexation such as the nitrogen to phosphorous (N/P) ratio, the lowest amount of ammonium groups necessary to completely complex oligonucleotides, will be reported. Then,

transfection efficacy and cytotoxicity of dendriplexes on L929 murine fibroblasts and SH-5YSY human neuroblasts will be discussed.

Finally, the characterization of dendriplexes will be reported. Complexation tests and cytotoxicity studies have been performed in collaboration with Dr. Nina Bono and Professor Gabriele Candiani at the Department of Chemistry, Materials and Chemical Engineering of Politecnico di Milano.

3.1.3.1 N/P ratio determination

The binding ability of FDG₂N to complex nucleic acids has been determined for both DNA and siRNA sequences in HEPES buffer 10 mM or in NaCl 150 mM. In particular, salmon sperm DNA, composed by 2000 base pairs, and Luciferase GL3, double strand siRNA (CUUACGCUGAGUACUUCGA), were used. The N/P ratio was determined monitoring the fluorescence emission of SYBR® green in presence of a constant amount of the nucleic acid and an increasing amount of FDG₂N.

The binding between nucleic acid sequences and SYBR® green leads to the formation of a fluorescent complex: when no FDG₂N is present with N/P equal to zero, all SYBR® is intercalated in the DNA helix leading to the maximum of fluorescence emission. When FDG₂N is instead added to the nucleic acid solution, the N/P ratio increases and SYBR® green competes with the nucleic acid to interact with the ammonium groups of FDG₂N with a consequent decrease in fluorescence emission. Data are reported as relative fluorescence values normalized to the fluorescence of the uncomplexed nucleic acid as a function of the theoretical N/P ratio of the mixture (figure 3.19). The N/P ratio related to a consistent decrease in the fluorescence emission represents the value at which maximum complexation occurs. Starting from FDG₂N concentration of 2.5 mM in 10 mM HEPES buffer (pH = 7.4) different N/P ratios were tested at different times from the preparation of the mixture, i.e. after 48 hours and 20 days ageing. As shown in figure 3.19a, FDG₂N showed complete complexation at a N/P ratio of 2.5 for DNA, this value is in line with N/P ratios observed for similar cationic Bis-MPA-based low generation amphiphiles [148] and for classical commercially available polymeric vectors, like linear PLL and branched PEI polymers [165]. After 48 hours from preparation, the amphiphile showed no changes in its binding ability for DNA, while a different behavior is observed after 20 days of ageing, as N/P increases almost ten times. This behavior suggests that the compound lost its binding ability probably due to both deprotonation of the ammonium groups and amphiphile degradation.

It has been reported that a change of the medium can affect the N/P ratio of a gene vector, even if small differences are generally observed between HEPES 10 mM and NaCl 150 mM [164][166]. As shown in figure 3.19b, a different N/P ratio was observed in NaCl 150 mM (N/P = 2) and in HEPES buffer (N/P = 7) for RNA; this can be related to different properties (size, surface change) of dendriplexes in the two media due to changes in ionic strength and pH [166].

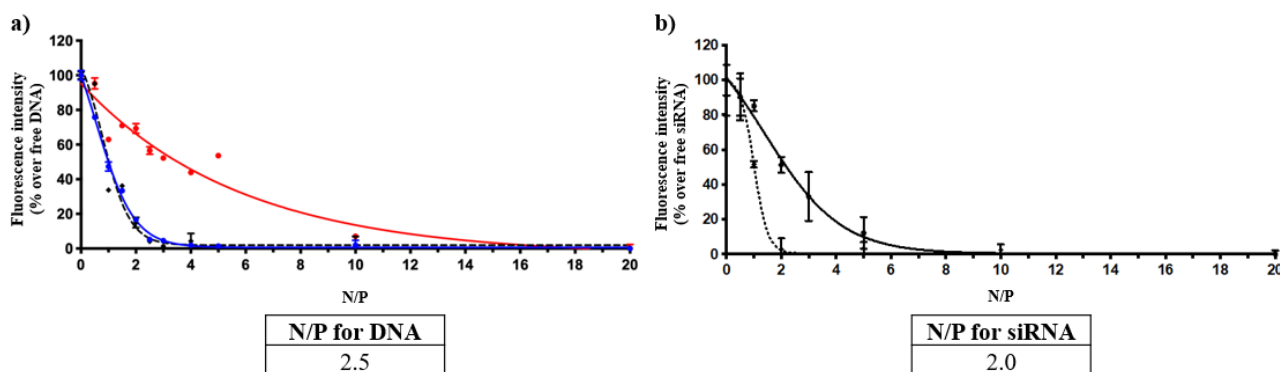


Figure 3.19 N/P ratio determination for FDG₂N. **a)** Normalized fluorescence intensity for increasing amounts of amphiphile in solutions containing a constant concentration of salmon sperm DNA in HEPES buffer 10 mM (pH:7.4). Color code: fresh FDG₂N solution = blue, aged FDG₂N solution (48 hr) = black, aged FDG₂N solution (20 days) = red. **b)** Normalized fluorescence intensity for increasing amounts of amphiphile in solutions containing a constant concentration of siRNA in HEPES buffer 10 mM (pH 7.4), black line, and in NaCl 150 mM, dotted line.

3.1.3.2 *In vitro* cytotoxicity, transfection efficacy, and dendriplexes characterization

In the previous paragraph we showed that FDG₂N is able to efficiently complex genes, in this section cytotoxicity of the dendriplexes obtained at different N/P ratios will be compared with their transfection efficacy: this is important to find the best condition for a good delivery and release of the genetic material into cells at a low cytotoxicity.

For these studies two different types of cell lines have been used: L929 murine fibroblasts from subcutaneous connective tissue and SH-5YSY human neuroblasts. Viability of untransfected cells was assigned to 100% and cytotoxicity was calculated as reported in section 3.2.3.2. The transfection efficiency was evaluated measuring luciferase activity: for these analyses pGLuc-Basic 2 (pDNA) was used. It is a plasmid composed by 4958 base pairs encoding the secreted luciferase from the copepod *Gaussia* princeps. Transfection efficiencies are thus expressed as luminescence signal (in relative light units, RLU). pGLuc was complexed in 150 mM NaCl with FDG₂N at different N/Ps; cells were incubated with the complexes for 24 hours and then cytotoxicity and transfection efficiency were determined. Data are compared with jetPEI®, a commercially available non-viral gene delivery vector for which the optimal conditions of transfection are set for DNA at a concentration of 75 μM corresponding to a N/P = 5 [167].

Figure 3.20 shows cytotoxicity and transfection results obtained for the two cell lines with respect to the increasing concentration of FDG₂N at a constant concentration of pDNA.

As shown in figure 3.20b and 3.20d, FDG₂N showed a transfection efficacy strictly dependent on the type of used cell line. While the optimal conditions of cell viability and transfection efficiency are comparable in terms of FDG₂N concentration for the two cell lines (23 μM and 31 μM), a higher efficiency was observed for the fibroblasts. In this case, it is interesting that in order to obtain comparable transfection efficiency it is necessary almost a double concentration of the commercial vector jetPEI®.

Furthermore, at FDG₂N concentration of 31 μM cytotoxicity is lower than that for jetPEI® at 75 μM. For the neuroblasts, (figure 3.20b), the optimal transfection efficacy of FDG₂N at 31 μM is lower than that of the commercial vector, but cytotoxicity is almost five times lower than those observed for jetPEI®. The different behavior observed for FDG₂N can be related to a lower internalization of the amphiphile in neuroblasts than in fibroblasts; this is further confirmed by the lower cytotoxicity of the polyfluorinated amphiphile for neuroblasts than for fibroblasts at the same concentration.

Probably this behavior can be ascribed to a different mechanism of internalization of the two cell lines. Table 3.8 shows the relation between the FDG₂N concentrations and the tested N/P ratios. As just discussed, independently of cell culture a good compromise between the lowest cytotoxicity and optimal transfection efficacy is reached at a concentration of FDG₂N equal to 31 μ M which, as shown in table 3.8, corresponds to a N/P ratio of 40 which is in line with those required from classical polymeric cationic vectors such as 25 kDa linear PEI, and 50–100 kDa branched PEI [165].

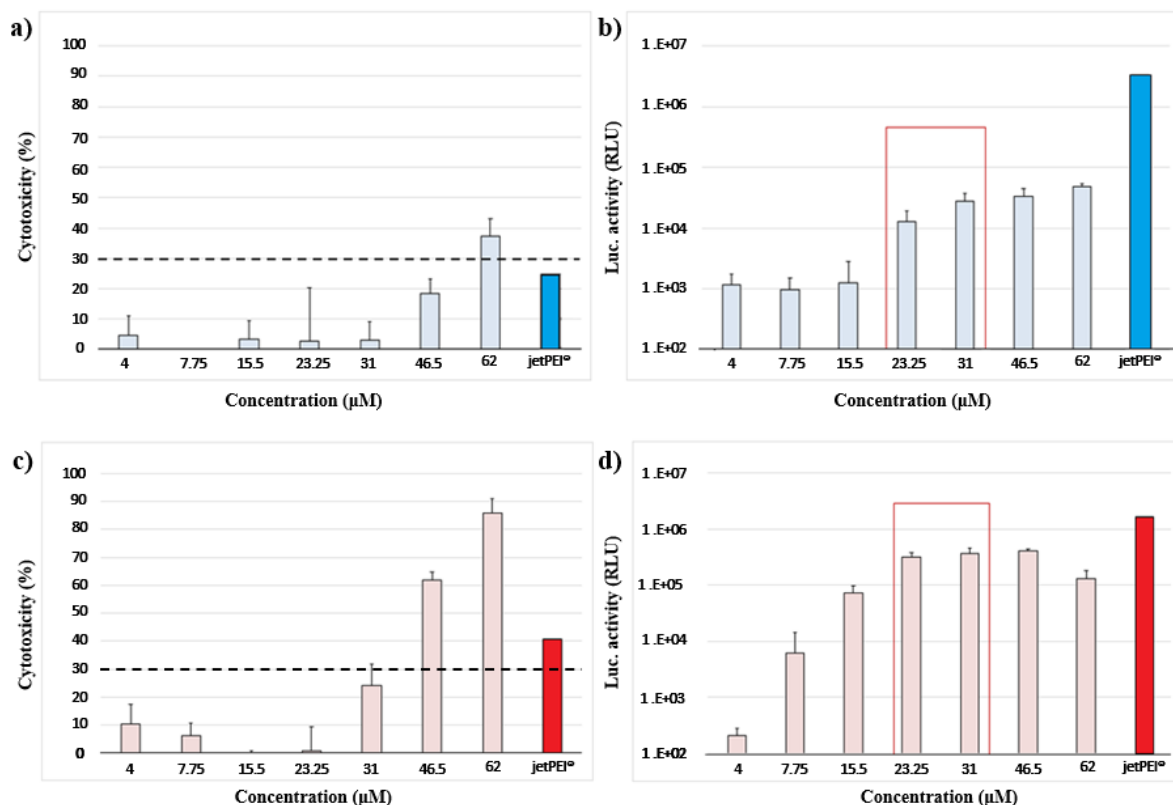


Figure 3.20 Comparison between the results observed by using FDG₂N and jetPEI® as vectors for pGLuc-Basic 2. **a)** Cytotoxicity results and **b)** transfection efficacies on SH-5YSY human neuroblasts. **c)** Cytotoxicity results and **d)** transfection efficacies on L929 murine fibroblasts.

Table 3.8 Cytotoxicity and transfections experiments. Correlation between the FDG₂N concentrations tested, the concentration of ammonium groups and the N/P ratios.

FDG ₂ N concentration (μ M)	Concentration of ammonium groups* (μ M)	N/P
4	16	5
7.75	31	10
15.5	62	20
23.25	93	30
31	124	40
46.5	186	60
62	248	80

* Concentration of ammonium groups if a 100% FDG₂N protonation is considered.

Taking into account these data, we decided to study the dendriplexes obtained in NaCl 150 mM at N/P = 40 by DLS, ¹⁹F-NMR, Z potential and Cryo-EM. The results, reported in table 3.9, are compared with the analysis of the dispersions obtained at the same concentration of FDG₂N without

pDNA.

Table 3.9 Dendriplexes characterization. Comparison between DLS and Z potential results obtained on the dendriplexes dispersion (N/P = 40, FDG₂N concentration = 0.557 mM) and FDG₂N alone. R_H and PdI were obtained by cumulant fitting at 173°.

Solution tested	R _H (nm)	PdI	Z potential (mV)
FDG ₂ N 557 μM	120 ± 46	0.6	+ 54
Dendriplexes N/P = 40	74 ± 34	0.2	+ 42

As shown by the results, the addition of pDNA to the dendrimer dispersion causes a reduction in the mean hydrodynamic radius (from 120 to 74 nm) as well as in the polydispersity of the system, in fact the PdI goes from 0.6 for FDG₂N to 0.2 for the mixture. All these results confirm that complexation between dendrimer and pDNA has occurred. This is further confirmed by the Z potential reduction, caused by the neutralization of some of the positive charges upon interaction with negatively charged phosphate groups of pDNA. The presence of an excess of positive charges, which is required for a good transfection [165], is confirmed by the positive value observed at Z potential after the complexation. Cryo-EM images seem to confirm this behavior; in fact, as shown in figure 3.21 in presence of pDNA the spherical aggregates maintain their shapes and interact each other thus forming clusters of aggregates of an averaged size of 50 nm of diameter. Figure 3.22 shows a schematic representation of the formation of dendriplexes upon pDNA addition. After the pDNA addition, driven by electrostatic interactions with the nucleic acid, the mobile aggregates of FDG₂N, that in water media tend to form micelles and a minor number of particles of bigger dimensions, reorganize. Micelles, surrounded by a shielded positive charge due to the presence of DNA, interact better with each other thus forming the final dendriplexes.

SAXS and small-angle neutron scattering (SANS) are in progress: these can help for a deeper understanding of the real morphology of the final dendriplexes.

Figure 3.23 shows the comparison between ¹⁹F-NMR spectra of FDG₂N dispersion at 0.557 mM and dendriplexes at the same FDG₂N concentration with N/P = 40.

As highlighted in the figure, the ¹⁹F-NMR spectrum of dendriplexes showed an upfield shift of the fluorine nuclei with respect to that of the pure amphiphile at the same concentration. This is in accordance with reduction of the mean size of the aggregates observed upon DNA complexation. Furthermore, in both cases two peaks are observed: since PdI significantly changes, if the presence of the double peak is related to the simultaneous presence of different types of aggregates in solution, the shape of the NMR peak should change upon complexation. However, no significant changes were detected in the two spectra. This can strengthen the hypothesis that the presence of different peaks in the ¹⁹F-NMR spectra can be related to a different environment to which inner and outer fluorine atoms in the aggregates are exposed rather to different resonance of fluorine nuclei in different aggregates.

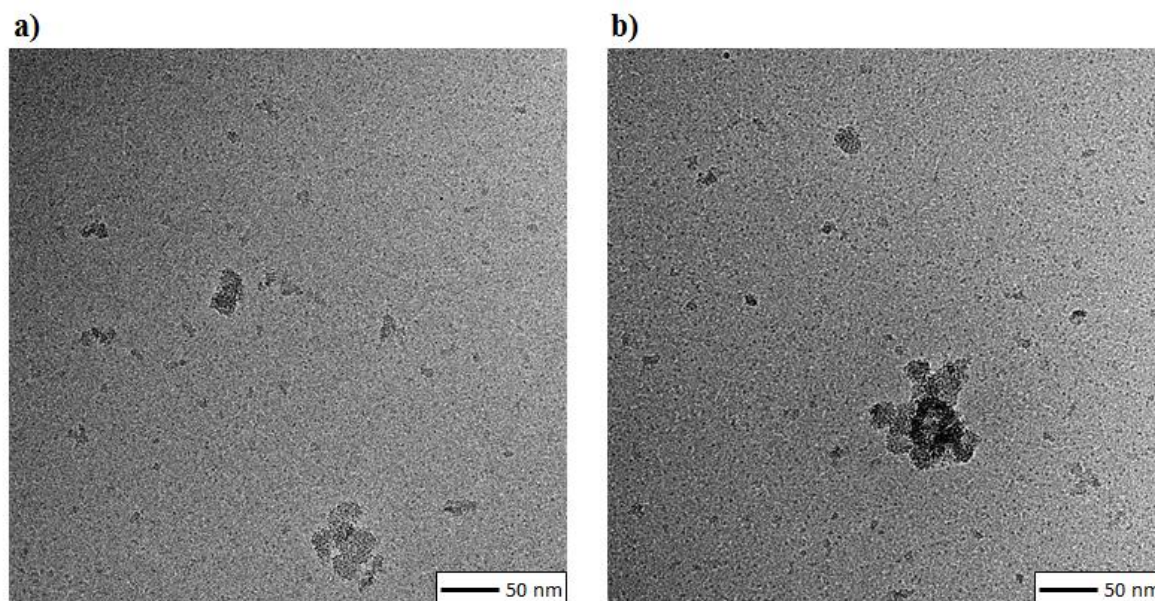


Figure 3.21 a, b) Cryo-EM images obtained from the analysis of the fresh dendriplexes obtained from a FDG₂N concentration 0.557 mM at N/P = 40 and pDNA. From the images it seems that the aggregates formed by FDG₂N maintain their spherical shape and tend to interact each other thus forming clusters of aggregates in which probably pDNA is entrapped (in collaboration with Dr. Antonio Chaves-Sanjuan from Cryo-EM Lab, Department of Biosciences, University of Milan).

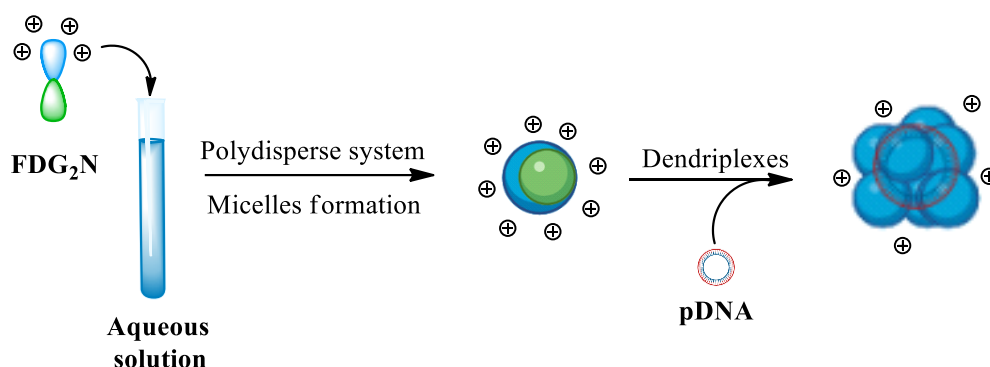


Figure 3.22 Schematic representation of the effect of the pDNA complexation with FDG₂N. The dissolution of the amphiphile in water is responsible for the formation of a polydisperse colloidal dispersion where the high majority of aggregates are micelles of small dimensions, characterized by an inner fluorinated cavity and an outer positively charged surface. After the addition of pDNA, the FDG₂N aggregates, driven by electrostatic interaction with the phosphate groups of the nucleic acids, self-organize to neutralize pDNA thus generating complexes in a higher monodisperse dispersion. Color code: green: fluorinated moiety; blue = ammonium terminating part.

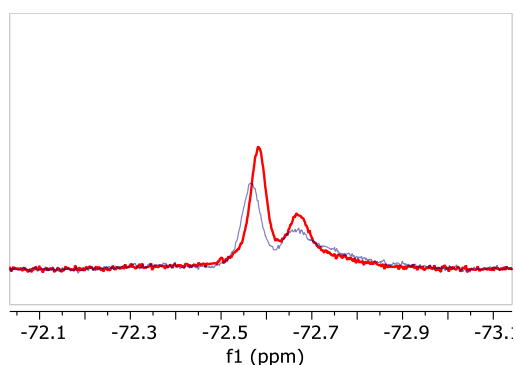


Figure 3.23 Dendriplexes characterization. Comparison between ¹⁹F-NMR spectra of the dendriplexes dispersion (N/P = 40, FDG₂N concentration = 0.557 mM), in red, and those of FDG₂N alone (FDG₂N concentration = 0.557 mM), in blue, after 1 hs from the samples' preparation. ¹⁹F-NMR solvent: FDG₂N solution + D₂O (10:1 v/v).

3.1.4 Application of FDG₂N as miRNA delivery vector

As just discussed, FDG₂N is able to complex nucleic acids at low N/P ratios with maximum transfection efficiencies reached at N/P=30-40, furthermore, the highly fluorinated amphiphile shows lower cytotoxicity if compared to a commercially available non-viral vector, like jetPEI®. All these results suggest that FDG₂N is a promising gene vector. In this section preliminary results will be presented for *in vitro* application of FDG₂N as miRNA delivery vector; the results will be useful to understand the FDG₂N potentialities in the construction of new gene therapies for the treatment of amyotrophic lateral sclerosis (ALS). ALS is a fatal progressive disorder responsible for the motoneuron degeneration in the cortex, brainstem, and spinal cord. Most cases are sporadic (SALS) and of unknown etiology; while the 12-23% of cases are due to the genetic mutation of superoxide dismutase 1, known as familial ALS (FALS). SALS and FALS are clinically indistinguishable and current therapies are not able to prevent the motoneuron degeneration, but they can only retard the progress of the disease of few months [168]. Adult neural stem cells are responsible for maintaining and repairing central nervous system tissues; several trauma and neurodegenerative diseases are accompanied by an extensive proliferation of ependymal stem progenitor cells (epSPCs) to the injured region. EpSPCs are able to differentiate and contribute neurons, astrocytes and oligodendrocytes to the injured tissue [169][170]. The maintenance and proliferation of epSPCs is governed by miRNAs and the expressions of miR-9, miR-124a, miR-19a and miR-19b is known to be crucial during neurogenesis and cell regulation. G93A-SOD1 transgenic mice are widely used ALS animal models and show an increase proliferation of epSPCs and altered proportions of the differentiated cell types, compared to control mice. In fact, G93A-SOD1 epSPCs have an altered neurogenic potential, differentiating more into neurons than into astrocytes. This differentiation is related to an altered expression of miRNAs in 93A-SOD1 than in control mice; the reduced differentiation of astrocytes and the increase of differentiated neurons is related to the upregulation of miR-9 and miR-124a in stem cells of diseased mice [168]. The different expression of genes in ill mice than in the control ones open the doors to new possible ALS therapies: a possibility can be the modulation of the miRNA expression, through endogenous stem cell stimulation, to improve the survival of motoneurons in the spinal neurodegeneration.

MiR-124a (sequence: CGUGUUCACAGCGGACCUUGAU) is an extensively studied oligonucleotide and promotes differentiation of neuronal progenitors into mature neurons [171][172]. To test the properties of FDG₂N as miRNA delivery vector on epSPCs, the amphiphile was complexed with a mimic miRNA-124. The experiments were performed in collaboration with Dr. Stefania Marcuzzo and Prof. Giuseppe Lauria Pinter from the Istituto neurologico “Carlo Besta” in Milan. In order to understand the aggregates shapes of dendriplexes obtained between FDG₂N and miR-124a, we imaged the aggregates obtained by dissolving FDG₂N at a 0.557 mM concentration at N/P = 40 with a double strand siRNA (CUUACGCUGAGUACUUCGA) of similar dimensions as the miRNA used for the *in vitro* tests shown in the following paragraph (figure 3.24). ¹⁹F-NMR and DLS analyses are scheduled to complete dendriplexes characterization. Cryo-EM images revealed that in presence of siRNA, probably due to its smaller dimensions when compared to pDNA, FDG₂N reorganizes and form new spherical aggregates of 100 nm as the averaged diameter.

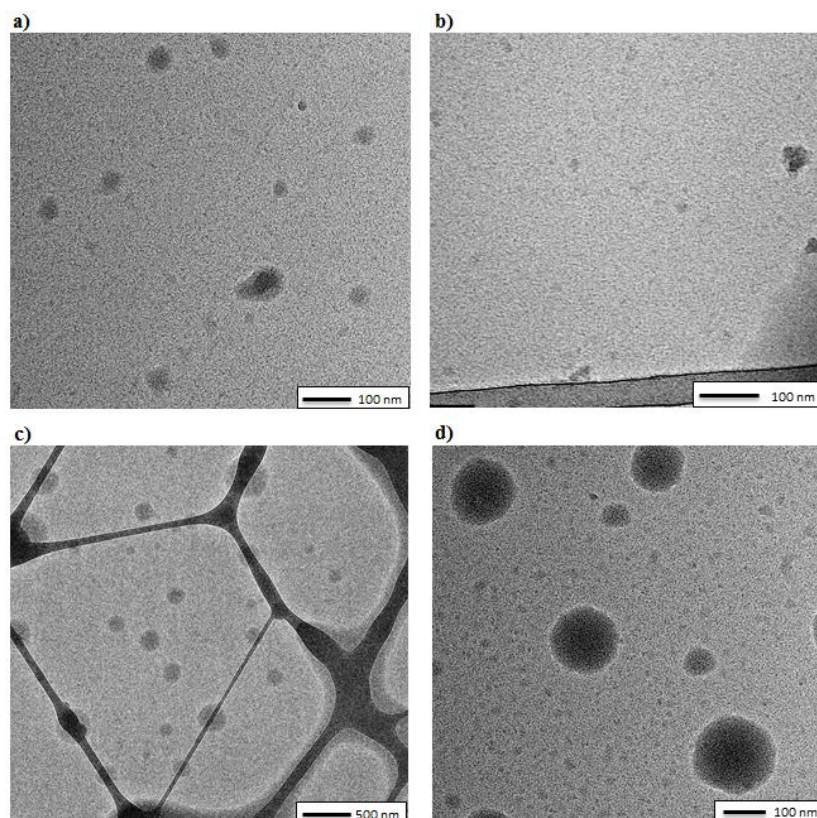


Figure 3.24 Cryo-EM images (in collaboration with Dr. Antonio Chaves-Sanjuan from Cryo-EM Lab, Department of Biosciences, University of Milan). **a, b** FDG₂N 0.557 mM in NaCl 150 mM alone (fresh sample). Images show the coexistence of aggregates of different dimensions in accordance with those observed for the FDG₂N 2.5 mM in NaCl 150 mM (see figure 3.16c and d). **c, d** Dendriplexes obtained by dissolving FDG₂N in NaCl 150 mM at a concentration 0.557 mM at N/P = 40. Differently from dendriplexes imaged with pDNA (figure 3.21), here FDG₂N reorganizes and form new spherical aggregates of an averaged diameter of 100 nm when bound to siRNA.

Transfection efficiencies of FDG₂N as miRNA delivery vector: *in vitro* preliminary results

EpSPCs neurosphere were isolated from whole spinal cords of adult control mice (18 weeks-old) and cultured *in vitro* for two days and then treated with dendriplexes of FDG₂N and miRNA (hsa-miR-124-3p; mature sequence: UAAGGCACGCGGUGAAUGCC) at different N/P ratios. The results are also compared with controls of cells treated with either culture medium (Optimem), or nanovector or miRNA (basal). Data are reported in relation to the expression of cells treated with a negative control oligonucleotide to remove aspecific effects. Furthermore, to compare the effect of the FDG₂N as vector, the results are compared with those obtained on the cells treated with Lipofectamine® RNAiMAX reagent, here referred as *Lipo*, a commercially available RNA delivery vector. Figure 3.25 shows the relative expression of miRNA124a for the tested samples and reports the microscopy images of the cells after 72 hours of treatments with the tested solutions.

As shown in figure 3.25a, FDG₂N was able to drive in cells the genetic material as confirmed by the increased relative expression of miRNA-124a in the cell treated with the dendriplexes even at N/P = 5. If compared to *Lipo*, FDG₂N showed a three times lower miRNA expression but, as shown in figure 3.25b and c, epSPCs treated with polyplexes of *Lipo* presented an altered morphology compared to the cells treated with the FDG₂N dendriplexes at N/P=30, thus suggesting a higher toxicity of *Lipo* on epSPCs.

Previous studies have shown that miRNA-124a regulates the expression of Jagged 1 (Jag1), SRY (sex determining region Y)-box 9 (Sox9), and distal-less homeobox 2 (Dlx2) [168]. Therefore, the expression of these genes has been quantified to determine the effect of the increased expression of

miRNA-124a on the expression of its target genes. Figure 3.26 shows the relative expressions of the target genes after the treatments of epSPCs with the samples' solutions.

As shown in the graphs, epSPCs treated with dendriplexes of FDG₂N and miRNA showed an increased expression of the target genes Jag1, at N/P = 20 and 30, and of Dlx2, at N/P = 30, compared to untreated cells and to those treated with miRNA polyplexes of *Lipo*. This suggests that miR-124a and FDG₂N established a significant impact on the cellular pathways involved in the self-renewal and proliferation of epSPCs, thus providing an impetus to the design of novel approaches in neurological diseases.

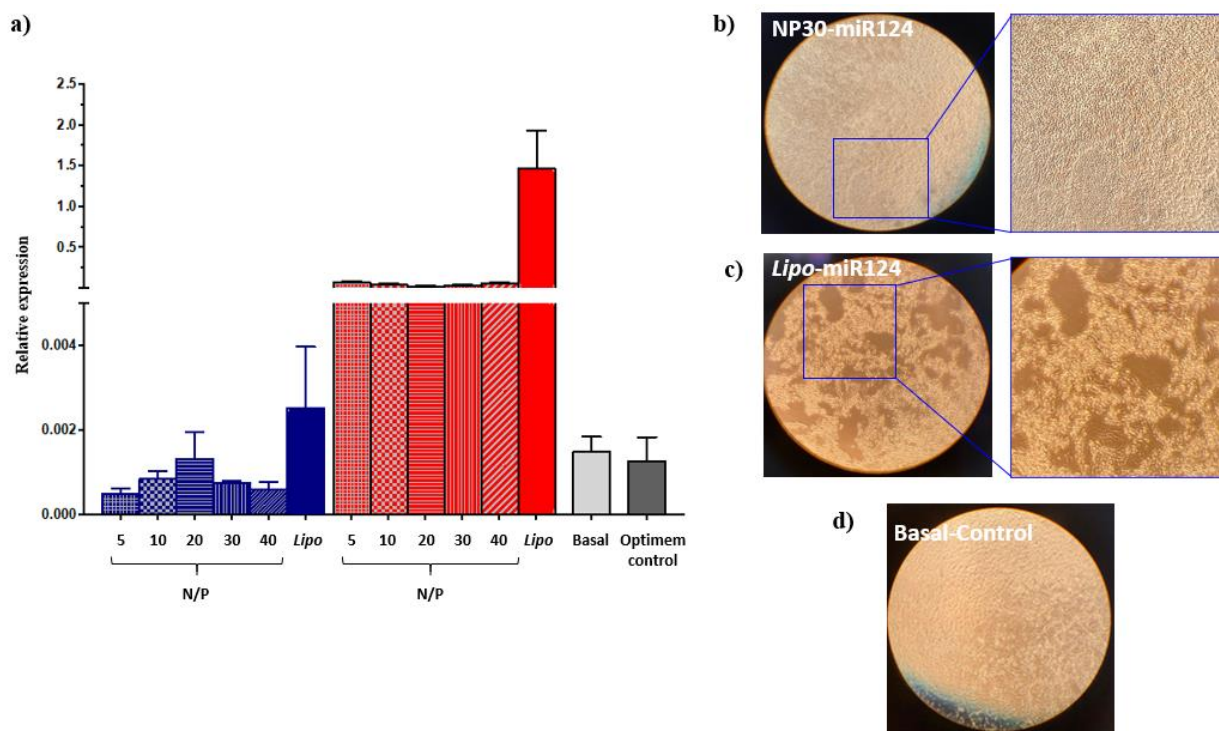


Figure 3.25 a) Relative expression of miRNA-124a in cells treated with dendriplexes of FDG₂N at different N/P ratios and comparison between those obtained on cells treated with polyplexes of *Lipo*. Data are compared to cells treated with nanovectors alone, to the basal control and to the results obtained on cells treated only with culture medium (Optimem). Color code: nanovectors alone = blue; dendriplexes/polyplexes = red; basal control = light grey; Optimem control = dark grey. b) Microscopy images taken on cells after 72 hours of treatment with the FDG₂N dendriplexes solution (N/P = 30); c) microscopy images taken on cells after 72 hours of treatment with *Lipo* polyplexes; d) microscopy images taken on cells after 72 hours of treatment with the miRNA alone (Basal-Control).

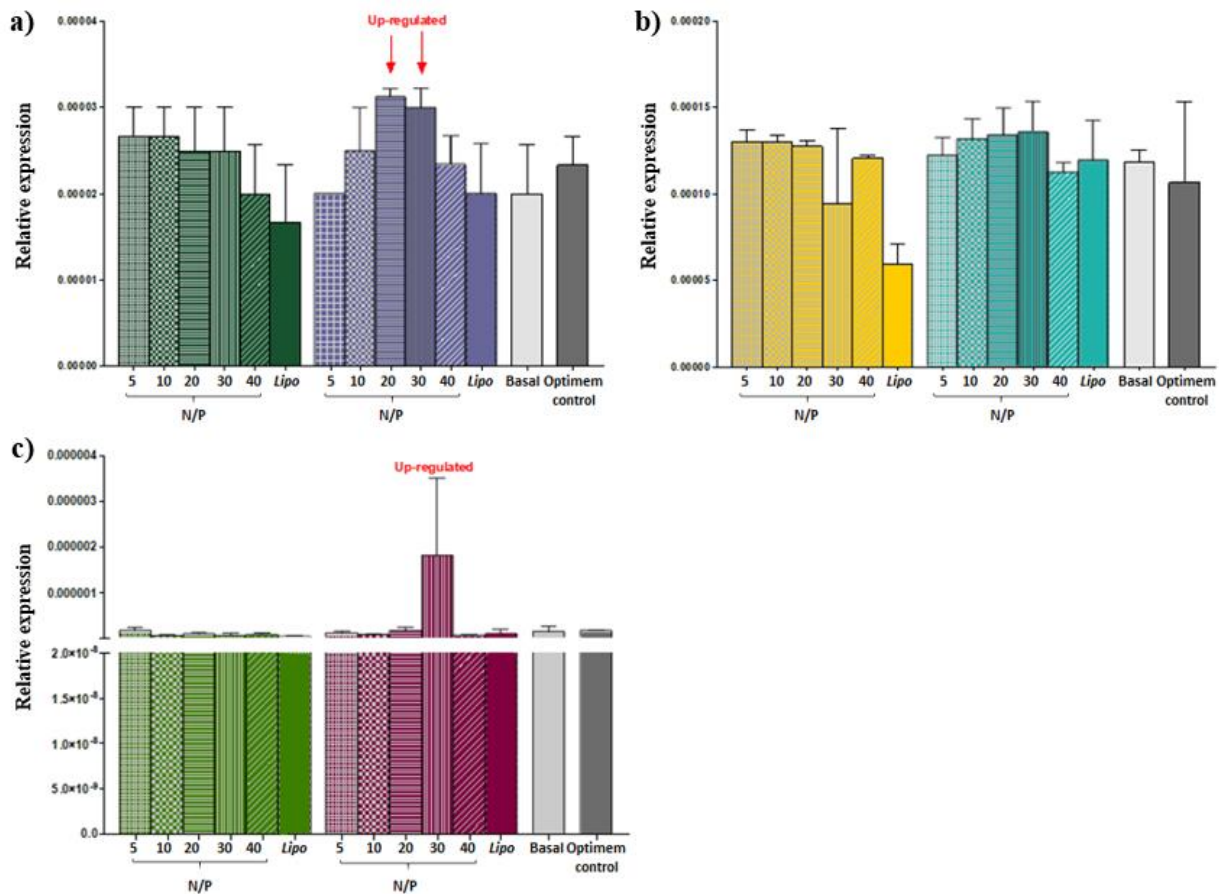


Figure 3.26 Relative expression of the miRNA-124 target genes. **a)** Relative expression of Jagged 1 (Jag1). Color code: nanovectors alone = green; dendriplexes/polyplexes = blue; basal control = light grey; Optimem control = dark grey. **b)** Relative expression of SRY (sex determining region Y)-box 9 (Sox9). Color code: nanovectors alone = yellow; dendriplexes/polyplexes = light blue; basal control = light grey; Optimem control = dark grey. **c)** Relative expression of distal-less homeobox 2 (Dlx2). Color code: nanovectors alone = green; dendriplexes/polyplexes = purple; basal control = light grey; Optimem control = dark grey.

3.2 Experimental section

In this section further information about the synthetic procedures and the instrument used for the synthesis of the compounds will be reported.

For the synthesis the chemicals employed as reactants and solvents were used as received without further purification and purchased with purity >97% from: ©TCI Deutschland GmbH; Sigma Aldrich, Germany; Fluorochem, U.K.

Thin layer chromatography TLC was conducted on plates precoated with silica gel Si 60-F254 (Merck, Darmstadt, Germany).

Chemical stain:

Ninhydrin solution: 0.2g of ninhydrin in 100mL of ethanol. Reagent used for its selective reactions with amine groups to yields imines.

Flash chromatography was carried out on J. T. Baker silica gel mesh size 230–400.

3.2.1 Synthesis, purification and characterization of FDG₂N

Nuclear Magnetic Resonance spectroscopy

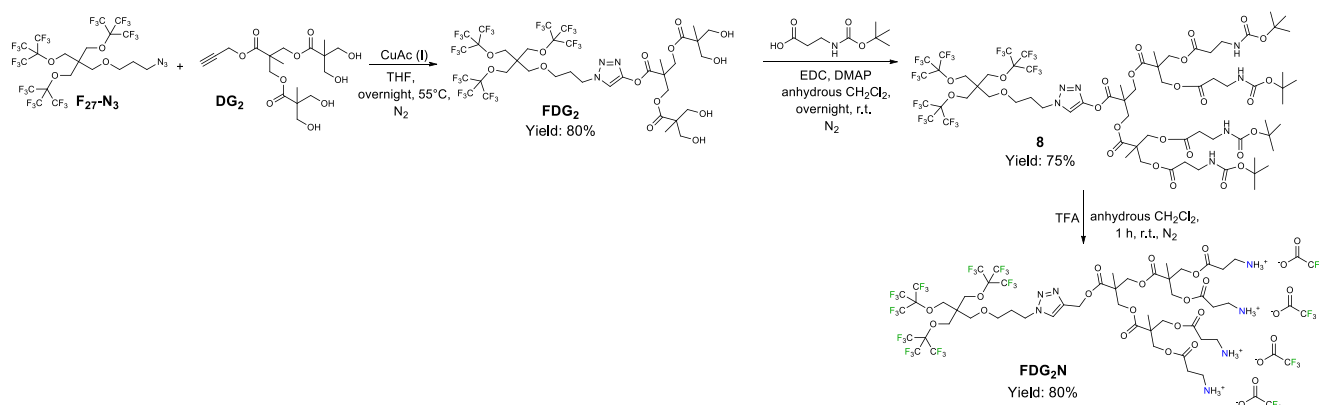
All the NMR spectra were recorded on a Bruker AV400 Bruker AvanceIII 400 MHz spectrometer equipped with a 5 mm QNP probe (¹⁹F, ³¹P-¹³C/¹H). NMR spectra were recorded at (300 ± 3 K) and chemical shifts are reported in ppm downfield from SiMe₄ with the residual proton (CHCl₃ d=7.26 ppm, CD₃OD: d=3.31 ppm) and carbon (CDCl₃: d=77.0 ppm, CD₃OD: d=49.0 ppm). Proton and carbon assignments were achieved by means of ¹³C-APT, ¹H-¹H COSY, and ¹H-¹³C-HSQC experiments. Coupling constant values, J, are given in Hz.

Data evaluation was done with MestreNova 10.0 from Mestre-Lab. The samples prepared for the characterization of the compound synthesized were prepared by dissolving 5-10mg in 500μL of deuterated solvent. Methanol-d₄ (99 atom % D), deuterated water (D₂O, 99 atom % D) and Chloroform-d, 99.8 atom % D were purchased from Sigma Aldrich, Germany.

Attenuated Total Reflection Fourier-Transform Infrared spectroscopy

FTIR was measured with a Thermo Scientific Nicolet iS50 FTIR spectrometer, equipped with iS50 ATR accessory (Thermo Scientific, Madison, USA). The IR signal values were expressed in wavenumber (cm⁻¹) and rounded to the nearest whole number through automatic assignment using OMNICTM IR software. Air was recorded as background. The analysis was made in transmittance mode in a wavenumber window of 4000-400 cm⁻¹.

High resolution ESI Mass spectrometry was done by UNITECH COSPECT: Comprehensive Substances characterization via advanced spectroscopy, Via C. Golgi 19, University of Milan



Scheme 3.1 Synthesis of FDG_2N starting from the azido terminating fluorinated derivative ($\text{F}_{27}\text{-N}_3$) and the alkyne functionalized II generation Bis-MPA based dendron (DG_2).

The synthesis of compound $\text{F}_{27}\text{-N}_3$ and DG_2 has been done by following the procedures reported in section 2.3.1.

Compound FDG_2 . Compound DG_2 (113.5 mg; 1 equivalent) and Copper (I) acetate (3.8 mg; 0.1 equivalents) were dissolved in 1 mL of THF under inert atmosphere. Separately, $\text{F}_{27}\text{-N}_3$ (244 mg; 1 equivalent) was dissolved in other 2 mL of THF and transferred to the reaction mixture. The reaction was run under stirring and nitrogen atmosphere at 55°C overnight. The formation of the product was confirmed by analyzing at FTIR 100 μL of the solution by monitoring the disappearance of the characteristic stretching of the azido group (2100 cm^{-1}). The reaction was stopped, added to iced water and extracted with CH_2Cl_2 ; then, the organic phase was washed two times with a 0.1 % disodium EDTA solution and with a saturated NaCl solution. The organic phase was collected, dried with Na_2SO_4 , and rotary evaporated. The compound was collected as a sticky solid (Yield: 80%).

^1H NMR (400 MHz, Methanol- d_4) δ = 8.12 (s, 1H), 5.34 (s, 2H), 4.55 (t, $J=7.1$, 2H), 4.43 – 4.25 (m, 12H), 4.22 (s, 6H), 3.79 – 3.63 (m, 16H), 3.55 (t, $J=6.1$, 2H), 3.51 (s, 2H), 2.25 (m, 2H), 1.35 (s, 3H), 1.30 (s, 6H), 1.21 (s, 12H). ^{13}C NMR (101 MHz, Methanol- d_4) δ 175.93 , 173.70 , 143.58 , 126.19 , 120.15 (q, $^1J_{\text{C-F}} = 292.5\text{ Hz}$), 81.52 – 80.43 (m), 69.24 , 67.24 , 67.11 , 67.06 , 66.16 , 65.87 , 59.09 , 51.81 , 48.49 , 47.97 , 47.93 , 47.51 , 31.33 , 18.17 , 18.00 , 17.30. ^{19}F NMR (376 MHz, MeOD) δ - 71.47. ATR-FTIR: Stretching O-H: $3600\text{-}3100\text{ cm}^{-1}$; Stretching C-H: $3000\text{-}2884\text{ cm}^{-1}$; Stretching C=O: 1729 cm^{-1} ; Stretching C-F: 1230 cm^{-1} ; Bending C-F: 700 cm^{-1} ; HR-MS (ESI) for $\text{C}_{58}\text{H}_{74}\text{F}_{27}\text{N}_3\text{O}_{26}$ - theoretical $[\text{M-Na}]^+$: 1764.4027/ Found $[\text{M-Na}]^+$: 1764.4031.

Compound 8. Boc-beta-alanine (312 mg; 12 equivalents), EDC (317 mg; 12 equivalents), and DMAP (8.4 mg; 0.5 equivalents) were put under nitrogen atmosphere for 5 minutes. Then, 4 mL of anhydrous CH_2Cl_2 were added. Separately, compound DG_1 (176 mg; 1 equivalent) was dissolved in other 3 mL of anhydrous CH_2Cl_2 and then, transferred, by means of other 3 mL of the solvent, to the reaction mixture. The reaction was run at room temperature, under stirring and nitrogen atmosphere overnight. To control the progress of the reaction a TLC was done using as eluent a mixture of hexane and ethyl acetate (1:1). To purify the product, a column chromatography on silica flash was made using the same eluent as those for TLC (rf: 0.3). To remove the excess of boc-beta-alanine, the purified mixture was dissolved in CH_2Cl_2 and washed twice with a 10% aqueous NaHCO_3 solution. The organic phase was dried on Na_2SO_4 and a pale-yellow oil was recovered after the removal of the solvent by rotary evaporation. (Yield: 75%).

^1H NMR (400 MHz, CDCl_3) δ 7.73 (s, 1H), 5.27 (s, 2H), 4.43 (t, $J = 7.3$ Hz, 2H), 4.30 – 4.10 (m, 12H), 4.05 (s, 6H), 3.48 (t, $J = 6.0$ Hz, 2H), 3.37 (t, $J = 6.1$ Hz, 8H), 2.53 (t, $J = 6.1$ Hz, 8H), 2.26 – 2.16 (m, 2H), 1.43 (s, 36H), 1.25 (s, 3H), 1.20 (s, 6H). ^{19}F NMR (376 MHz, CDCl_3) δ -70.36.

Compound FDG₂N. Compound **8** (195 mg; 1 equivalent) was dissolved in 2 ml of anhydrous CH_2Cl_2 , under nitrogen atmosphere. Then trifluoroacetic acid (TFA, 2mL) was slowly added. The reaction was run till the total conversion of the precursor, confirmed by TLC by using as eluent a mixture of hexane and ethyl acetate (1:1). The time required is around 1 hour. The reaction was stopped by drying the compound through rotary evaporation. Then the compound was solubilized in hexafluoro-2-propanol and dried again three times to remove the excess of TFA. Then the compound was solubilized in 250 μl of cold methanol and transferred slowly into a vial containing 5 ml of cold ether: after the precipitation at the bottom of the vial of an immiscible oily phase, the supernatant was removed, and the precipitate was dissolved in water and freeze-dried. The compound was collected as a white hygroscopic amorphous solid. (Yield: 80%).

^1H NMR (400 MHz, MeOD) δ 8.07 (s, 1H), 5.27 (s, 2H), 4.49 (t, $J = 7.2$ Hz, 2H), 4.34 – 4.21 (m, 12H), 4.15 (s, 6H), 3.50 (t, $J = 6.1$ Hz, 2H), 3.45 (s, 2H), 3.23 (t, $J = 6.7$ Hz, 8H), 2.80 (t, $J = 6.7$ Hz, 8H), 2.19 (p, $J = 6.4$ Hz, 2H), 1.29 (s, 3H), 1.24 (s, 6H). ^{13}C NMR (101 MHz, MeOD) δ 173.48, 171.80, 126.23, 121.59 (q, $J = 293.1$ Hz), 80.50-81.0 (m), 69.24, 67.13, 67.03, 66.93, 66.85, 59.05, 47.98, 47.48, 36.31, 31.32, 17.91, 17.83. ^{19}F NMR (376 MHz, MeOD) δ -71.46, -76.82. ATR-FTIR: Stretching N-H: 3600-3350 cm^{-1} ; Stretching C-H: 3200-2850 cm^{-1} ; Stretching C=O: 1735 cm^{-1} , 1674 cm^{-1} ; Stretching C-F: 1230 cm^{-1} ; Bending C-F: 736 cm^{-1} ; HRMS (ESI) for $\text{C}_{50}\text{H}_{63}\text{N}_7\text{O}_{18}\text{F}_{27}$ - theoretical $[\text{M}-\text{H}]^+$: 1562.3798/ Found $[\text{M}-\text{H}]^+$: 1562.3794.

Figure 3.27 shows the ATR-FTIR spectrum collected for FDG₂N.

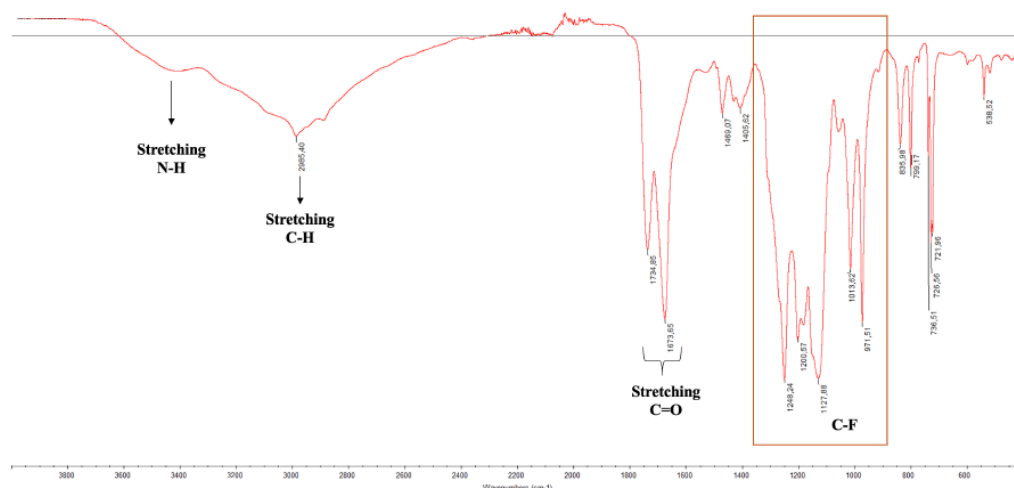


Figure 3.27 ATR-FTIR spectrum of FDG₂N.

3.2.1.1 Chemical and thermal stability of FDG₂N

Thermogravimetric analysis (TGA)

TGA was done with a Q500 instrument. 1-5 mg of the sample were placed in the melting pot and submitted to a ramp of temperature from 30 $^{\circ}\text{C}$ to 550 $^{\circ}\text{C}$.

Degradation studies:

3.79 mg of FDG₂N were placed in the melting pot and submitted to a ramp from 30° to 229°C, followed by an isothermal for 5 minutes. After the ramp 2.97 mg of compound remained and were dissolved in deuterated methanol (450µL) and analyzed by ¹H and ¹⁹F-NMR.

MALDI-TOF Mass Spectrometry (In collaboration with Dr. Roberto Milani at VTT Technical Research Centre of Finland, Espoo, Finland).

FDG₂N was dissolved in water or methanol at concentrations 4mg/mL. The initial matrix used was DHB (2,5-Dihydroxybenzoic acid), dissolved in TA20 mixture (2 parts 0.1% aqueous TFA, 1 part acetonitrile). 1.5 µL of sample solution was mixed with 1.5 µL of matrix solution, then the mixture was spotted as 0.6 µL aliquots. Unless otherwise specified, measurements were done in positive ion mode, in the range 0-10 kDa. There was no suitable calibration standard available for the 0-5 kDa range, however calibration was made with the protein standard I (4-20 kDa range). It is not optimal, but we can estimate peak position errors as a few Daltons at most. Usually, several laser powers were used (expressed as %). A too low laser power will result in weak or no spectrum at all while a too strong laser power will result in fragmentation of the compound and possible appearance of artifacts. Initial dissolution in water and methanol yielded a clear solution. It was possible to obtain spectra in DHB. Spectra were taken at time zero and at 24h and 48h aging in water at +4C. No significant differences observed over time.

3.2.2 Self-assembly of FDG₂N in aqueous media

CMC determination by the fluorescence of pyrene

Procedure

The procedure was done by slightly modifying an already reported procedure [14].

- Prepare a pyrene solution by dissolving 5 mg in 10 mL of methanol (2.5mM).
- Dilute this solution 400 times with Methanol (pyrene: 6.25µM).
- To prepare the working mixtures for fluorescence measurements, a small aliquot (17 µL) of the latter pyrene solution is transferred to the solution of FDG₂N till a final volume of 1 mL (pyrene: 100nM).

Fluorescence emission and excitation spectra were obtained with a commercial spectrofluorimeter (Jasco, FP-6500). Table 3.10 shows the input parameter used to set the experiments.

Tables 3.11a and b show the concentrations of the FDG₂N solution tested for the CMC determination in water and in NaCl 150mM respectively.

Table 3.10 CMC determination by the fluorescence emission of pyrene. Input parameters used to set the fluorescence measurements.

Input parameter	
Measurement range (λ)	344 - 480 nm
Excitation wavelength (λ)	334.0 nm
Light source	Xe lamp

Table 3.11 FDG₂N concentrations tested and relative ratio between the first ($\lambda = 373$ nm) and the third ($\lambda = 383$ nm) peaks of the emission spectra of pyrene **a)** CMC determination in MilliQ water and **b)** CMC determination in NaCl 150mM.

a)	Concentration (mM)	I _F (I/III)	b)	Concentration (μ M)	I _F (I/III)
	0.00000	1.82		0.00000	1.72
	0.00125	1.81		0.50000	1.71
	0.00250	1.83		1.00000	1.73
	0.00500	1.84		5.00000	1.72
	0.00750	1.82		10.00000	1.71
	0.01250	1.80		20.00000	1.56
	0.02500	1.75		35.00000	1.56
	0.05000	1.69		50.00000	1.61
	0.07500	1.67		100.00000	1.59
	0.12500	1.68		500.00000	1.51
	0.25000	1.65		1000.00000	1.48
	0.50000	1.62			
	1.00000	1.58			
	1.30000	1.53			
	1.70000	1.50			
	2.50000	1.43			

CMC determination by ¹⁹F-NMR in water

Table 3.12 shows the concentration tested for the determination of the CMC by ¹⁹F-NMR in water. All the solution were prepared with a final volume of 500 μ L to which 50 μ L of deuterated water were added to performed to lock at NMR. Spectra were collected by setting 256 number of scans as input parameter. The peak of the TFA anions has been set at -76.55ppm while Δ ppm are reported against the peak of the monomer shift at the lowest concentration of FDG₂N (-71.6 ppm).

Table 3.12 CMC determination of FDG₂N in water by ¹⁹F-NMR. Concentrations tested and relative chemical shifts of the monomer and aggregate form.

Concentration (mM)	1/conc (mM ⁻¹)	Aggregated shift (ppm)	Δ ppm	Monomer shift (ppm)
2.5	0.4	-72.38	0.78	-71.35
1.7	0.6	-72.46	0.86	-71.39
1.3	0.8	-72.46	0.86	-71.41
1.1	0.9	-72.46	0.86	-71.42
0.9	1.1	-72.49	0.89	-71.46
0.7	1.4	-72.52	0.92	-71.49
0.6	1.7	-72.55	0.95	-71.52
0.5	2.0	-72.58	0.98	-71.54
0.4	2.5	-72.61	1.01	-71.56
0.25	4.0	-72.66	1.06	-71.58
0.125	8.0	-72.66	1.06	-71.6
0.1	10	-72.66	1.06	-71.6
0.075	13.3	-72.66	1.06	-71.6
0.05	20	-72.66	1.06	-71.6

3.2.2.1 Characterization of the aggregates in solution

Solutions of FDG₂N were obtained by directly dispersing the amount of the solid required to obtain the desired concentrations (2.5mM and 0.5mM) in the final solvent: MilliQ water, NaCl 150mM, and

HEPES (4-(2-hydroxyethyl)-1-piperazineethanesulfonic acid)) 10mM whose pH was adjusted with a NaOH 1M solution till the reaching of a pH = 7.4. Milli-Q water (mQw, 18.2 mΩ/cm) used to prepare the aqueous dispersions was obtained by the purification system provided by Simplicity®. HEPES was purchased from Merck, Germany, and NaCl (purity 99%) was purchased from Sigma Aldrich. The solutions were aged at a constant temperature (25°C) and analyzed after 1 hour from the sample preparation, after 24 hours and 48 hours of ageing as previously discussed.

pH determination

A drop of each solution was analyzed in triplicate by a Pocket ISFET pH Meter Model 24006 whose calibration was performed as reported by the vendor instructions.

Dynamic light scattering measurements

Multiangle DLS was measured at ALV compact goniometer system, equipped with ALV-5000/EPP Correlator, special optical fiber detector and ALV/GCS-3 compact goniometer, with He-Ne laser ($\lambda = 633$ nm, 22 mW output power) as light source. The temperature was controlled with a thermostatic bath and set at 25 °C. A volume comprised between 800 μ L and 1 ml was used for the analysis. DLS was measured at different time points (0, 24, 48 h) and scattering angles $\theta = 70 - 130^\circ$ in 20° steps. Each measure was the result of the average of three subsequent run of 10 seconds each, with a threshold sensibility of 10%. Data analysis was done with ALV-Correlator software. The apparent hydrodynamic radii at different angles were obtained from an intensity weighted and a number weighted fitting of the autocorrelation function. Hydrodynamic radii (R_H) and polydispersity indexes (PdI) were calculated using the cumulant fitting. For a more accurate analysis, precluded with cumulant fitting due to the high polydispersity of the samples, CONTIN analyses were performed, and sizes distributions are reported according to intensity and number weighted equations (see chapter 2, equation 2.2 and 2.3).

Z potential measurements

Z potential was measured at 25°C in folded capillary cells (U-shaped cells with two gold plated beryllium/copper electrodes at the top) 48 hours later the colloidal dispersion preparation with a Zetasizer Nano ZS (Malvern Instrument, Malvern, Worcestershire, UK), equipped with a 633 nm laser. Before each measure, the cells were cleaned with MilliQ water and then filled up with approximately 1 ml of sample solution, checking that the gold-plated electrodes were immersed and that there were no bubbles inside the cell.

^{19}F -NMR spectra

To perform the ^{19}F -NMR spectra 500 μ L of the 2.5 and the 0.5mM FDG₂N solutions were mixed with 50 μ L of deuterated water, added to perform the lock at the NMR instrument. Spectra were collected by setting 256 number of scans as input parameter. The peak of the TFA anions has been set at -76.55ppm.

T1 and T2 measurements were obtained on the FDG₂N solution 2.5mM in MilliQ water. The fitting of the data was performed by a single exponential fit and raw data were analyzed by the Bruker TopSpin software and the MestReNova software. Figure 3.28 shows the T1 and the T2 data and their fitting curves.

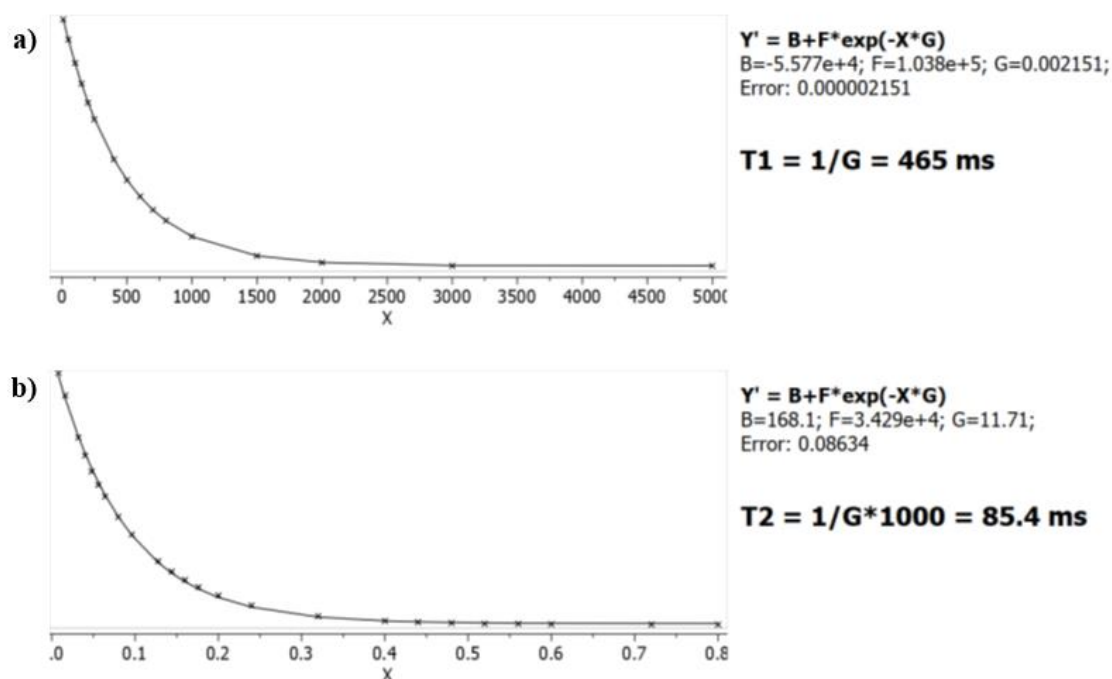


Figure 3.28 a) T1 results and b) T2 results obtained by analyzing a 2.5mM FDG₂N solution in water by ¹⁹F-NMR. Solvent: FDG₂N solution + 10% of D₂O put as external solvent reference (coaxial tube).

Molecular Dynamics: FDG₂N in water

The theoretical study is based on Molecular Mechanics (MM) and Molecular Dynamics (MD) simulations. All MM and MD simulations were performed with Materials Studio, Discovery Studio packages. Using the same simulation protocol proposed in previous work [137], all calculations are performed with CVFF force field with a Morse potential for the bonded atoms, in explicit water 5% ethanol. The simulation protocol involved three sequential steps: *i*) at first the initial energy minimization; *ii*) the MD run at constant temperature; *iii*) the final geometry optimizations of the final configuration assumed by the system at the end of MD run. All energy minimizations were carried out up to an energy gradient lower than 4×10^{-3} kJ mol⁻¹ Å⁻¹. The MD simulations were performed at a constant temperature (300 K), controlled through the Berendsen thermostat. Integration of the dynamical equations was carried out with the Verlet algorithm using a time step of 1 fs, and the instantaneous coordinates were periodically saved for further analysis or geometry optimization.

3.2.3 Nucleic acids complexation

L929 (murine fibroblast from subcutaneous connective tissue; ATCC[®]-CCL-1[™]) and SH-5YSY (human neuroblast, ATCC[®] CRL-2266[™]) cell lines were purchased from the American Type Culture Collection (ATCC, Manassas, VA, USA). AlamarBlue Cell Viability Assay was from Life Technologies Italia (Monza, Italy), while BCA Protein Assay Kit was from ThermoFisher (Monza, Italy). pDNA encoding the secreted luciferase from the copepod *Gaussia princeps* (pGLuc-Basic 2 (pGLuc), 4.958 kbp) and BioLux[®] *Gaussia* Luciferase Assay Kit were obtained from New England Biolabs Inc. (MA, USA). siMAX siRNA control – Luciferase GL3 was purchased from Eurofins – Genomics. pDNA solution concentration 0.25 μg/mL.

3.2.3.1 N/P ratio determination

Preparation of transfectant solution.

FDG₂N was diluted in 150 mM NaCl or HEPES buffer 10mM to a final concentration of 2.5 mM and a final concentration of positive charges [N] = [+] = 10mM, if a 100% protonation is considered.

Preparation of FDG₂N/ pDNA complexes.

Complexes were prepared by mixing (through vigorous pipetting) the pDNA and transfectant solutions, prepared at the desired concentration to yield different ammine-to-phosphate ratios (N/Ps) (i.e., 5, 10, 20, 30, 40, 60 and 80), followed by 20 minutes of incubation at room temperature.

Evaluation of the oligonucleotides binding ability.

The binding ability of FDG₂N was monitored by a fluorophore-displacement assay, as reported elsewhere [165][166][173]. Briefly, complexes were invariably prepared by mixing 1.0 μL of pDNA in 1.0 μL of SYBR Green I ($\lambda_{\text{ex}} = 497 \text{ nm}$, $\lambda_{\text{em}} = 520 \text{ nm}$) with 11.8 μL of the FDG₂N solutions at different concentrations, yielding different CRs. Afterwards, complexes were incubated for 20 minutes at room temperature in the dark, then diluted to a final volume of 200 μL in the solvent. Fluorescence measurements (n = 3) were performed with a Synergy H1 spectrophotometer (BioTek, Italy) in 384-multiwell black plates ($\lambda_{\text{ex}} = 487 \text{ nm}$, $\lambda_{\text{em}} = 528 \text{ nm}$). Data are given as relative fluorescence values normalized to the fluorescence of uncomplexed pDNA.

3.2.3.2 *In vitro* cytotoxicity, transfection efficacy, and dendriplexes characterization

L929 were cultured in Dulbecco's modified Eagle's medium (DMEM) containing 1 mM sodium pyruvate, 10 mM HEPES buffer, 100 U/mL penicillin, 0.1 mg/mL streptomycin, 2 mM glutamine and supplemented with 10% (v/v) fetal bovine serum (FBS) in a humidified atmosphere under constant supply of 5% CO₂ and at 37°C (hereinafter referred as to standard culture condition).

SH-5YSY cells were cultured in 40% (v/v) Eagle's Minimum Essential Medium (EMEM), 40% (v/v) F12 medium, 1% (v/v) NEAA, 100 U/mL penicillin, 0.1 mg/mL streptomycin, 2 mM glutamine and supplemented with 15% (v/v) FBS in a standard culture condition.

Twenty-four hours before transfection assays, cells were seeded onto 96-well plates at a density of 2×10^4 cells/cm² and maintained in standard culture conditions. Next, 320 ng/well of pGLuc were complexed in 150 mM NaCl with FDG₂N solutions to yield different N/P ratios, as described herein above, and cells were incubated with complexes in 100 μL/well of culture medium under standard culture conditions for 24 hours.

Following a 24 hours transfection, cytotoxicity was evaluated by means of AlamarBlue assay according to manufacturer's instructions. This test allows to determine cell viability and exploits the natural reducing power of living cells to convert resazurin to resorufin, a fluorescent molecule. When AlamarBlue, composed by resazurin, enters into cells, it is reduced to resorufin and a bright red fluorescence is observed. Briefly, medium was removed, and each well was loaded with 100 μL of 1× resazurin dye-containing culture medium. Cells were next incubated in standard culture conditions for 2 hours, then the fluorescence of the medium was read with a Synergy H1 spectrophotometer (BioTek, Italy) ($\lambda_{\text{ex}} = 540 \text{ nm}$; $\lambda_{\text{em}} = 595 \text{ nm}$). Viability of untransfected cells (CTRL) was assigned to 100% and cytotoxicity was calculated as follows:

$$\text{cytotoxicity (\%)} = 1 - [\text{RFU}_{\text{transfected cells}} / \text{RFU}_{\text{CTRL}}] \times 100$$

Transfection efficiency was evaluated measuring the luciferase activity by means of the Luciferase Assay System, according to manufacturer's instructions. The test measures *Gaussia* Luciferase (GLuc) activity that catalyzes the oxidation of the substrate, coelenterazine, in a reaction producing light. The luminescence measured from the supernatant of cultured cells transfected with a plasmid expressing GLuc is proportional to the amount of enzyme produced and reflects the level of transcription. Briefly, from each well, 10 μ L of supernatant were added to 50 μ L of Luciferase Assay Reagent and luminescence was measured by means of a Synergy H1 spectrophotometer. Transfection efficiencies were thus expressed as luminescence signal (expressed as relative light units, RLU) of each sample.

Figure 3.29 shows the cytotoxicity evaluated for FDG₂N alone on SH-5YSY cells.

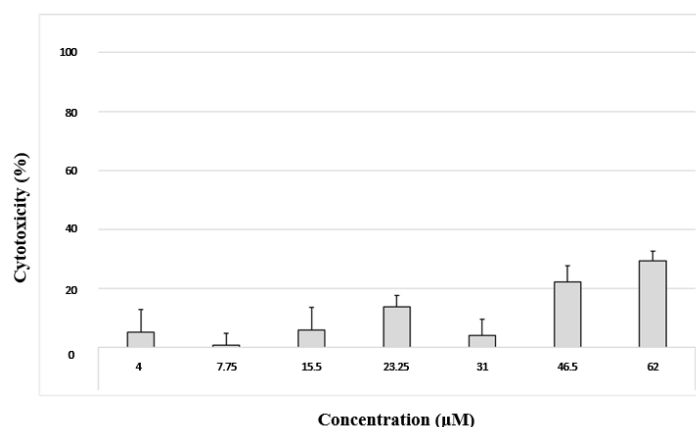


Figure 3.29 FDG₂N cytotoxicity evaluated for the amphiphile alone on SH-5YSY cells.

Dendriplexes characterization.

Complexes were prepared as described above. Briefly, 40 μ L of pDNA was mixed with 460 μ L of transfectant solutions to yield a final N/P ratio of 40 and incubated for 20 min at room temperature. Hydrodynamic radius and surface charge of complexes were measured at 25°C by Dynamic Light Scattering and Electrophoretic Light Scattering using a Malvern Zetasizer Nano instrument (Malvern, Italy), fitted with a 5 mV He-Ne laser ($\lambda = 633$ nm) and a scattering angle of 173°. The results have been compared to those obtained on the same concentration of FDG₂N alone in NaCl 150mM (concentration of FDG₂N = 0.557mM). ¹⁹F-NMR analyses were performed on 500 μ L of the solutions to which 50 μ L of D₂O were added (Number of scans = 256).

3.2.4 Application of FDG₂N as miRNA delivery vector

MISSION® microRNA Mimic hsa-miR-124-3p was purchased from Signa Aldrich.

Ependymal progenitor stem cells were isolated from the spinal cord of adult male control mice (18 weeks old) as previously described [168]. Cells were plated on Matrigel (adhesion substrate) 80,000 cells per well of 12 (19mm diameter) multi well in triplicate for each condition. The cells were kept for two days in proliferative medium and then treated with nanovectors / miRNA 124 for 72 hours. after 72hs, RNA was collected and extracted by Trizol.

Sample preparation:

2.0 μ L miRNA in were diluted in 125.0 mL Opti-MEM® Medium per each well that has to be treated. Then, 125 μ L of the diluted miRNA solution (0.5 μ M) were added to 125 μ L of the diluted Lipofectamine® RNAiMAX Reagent (Cat. n. 13778-075 Thermo Fisher) (1:1 ratio), used as control, or with the diluted FDG₂N solution. The solutions were incubated for 5 minutes at room temperature.

The cells medium was substituted to remove dead cells. Then, 1750 μL of fresh medium were added. 250 μL of relative miRNA complexes solution were added to the wells. Cells were incubated for 72 hours at 37°C and then were analyzed.

As controls the cells treated with Optimem alone, cells treated with vectors alone and cells treated with a negative control oligonucleotide to evaluate aspecific effects were analyzed.

miRNA real-time polymerase chain reaction (PCR):

Total RNA was extracted using Trizol from 1 to 2×10^6 undifferentiated epSPCs. RNA quality was checked using a2100Nano Bioanalyzer (Agilent Technologies, Waldbron, Germany). Total RNA was reverse transcribed using a TaqMan MicroRNA Reverse Transcription Kit with primers specific for miR-124a, and U6, used as control. The cDNA (corresponding to 15 ng total RNA) was amplified in triplicate by quantitative real-time PCR, using Universal PCR master mix and pre-designed TaqMan MicroRNA assays, as indicated above, on the Applied Biosystems PRIMS 7500 Fast Real-Time PCR System. All the results were normalized against U6 and the relative miRNA expression levels were calculated using the ΔCt method.

Functional analysis of miRNA target genes.

MiRNA gene target prediction In-silico prediction of miRNA targets was performed using theDIANA-microT-3.0-Strict algorithm from the DIANA miRNA database using the default score cut-off (<http://diana.cslab.ece.ntua.gr/microT/>). We also identified potential dysregulated gene targets from literature (Delaloy et al., 2010; Krichevsky et al., 2006; Zhao et al., 2009). These included genes implicated in cell-cycle regulation, cell function signaling, migration, proliferation, and neural cell fate. We identified ten genes to further investigate for their expression levels in relation to miRNA regulators: cyclin D2 (Ccnd2), Dlx2, Jagged 1 (Jag1), (sex determining region Y)-box 9 (Sox9).

mRNA real-time PCR.

Total RNA extracted from undifferentiated epSPCs previously examined for miRNA expression was retrotranscribed using SuperScript Vilo cDNA Synthesis kit. cDNA (corresponding to 100 ng total RNA) was amplified by quantitative real-time PCR, in triplicate, using Universal PCR master mix and Taqman Array Fast Plate assembled by Life Technologies with primer and probe sets for 3 miRNA target genes (Dlx2, Jag1, Sox9) and one housekeeping gene (18s) on Applied Biosystems PRIMS 7500 Fast Real-Time PCR System.

4 Conclusions

Fluorinated chains provide dendritic molecules with properties different from the analogous hydrogenated counterparts thus finding application in a lot of different fields. The high hydrophobicity and low reactivity confer lower cytotoxicity and higher cellular uptake than non-fluorinated analogues; while their tendency to form stable aggregates in water can guarantee the delivery of fluorinated drugs thanks to fluorine-fluorine interactions.

To fully exploit the potential offered by fluorinated dendritic amphiphiles, there is a pressing need to design new stable, non-toxic and biocompatible fluorinated systems. The use of short branched polyfluorinated chains guarantees the insertion of a high number of equivalent fluorine atoms by using short branched polyfluorinated chains which combine the benefits of a high number of fluorine atoms with an enhanced lability and biodegradability.

In order better understand how the balance between hydrophilic and hydrophobic portions in fluorinated dendrimers can affect their self-assembly behavior, we decided to synthesize a new family of dendrimers by attaching the same branched fluorinated structure to different generations of 2,2-bismethylolpropionic acid (Bis-MPA) polyester dendrons.

Thanks to the synthesis of a new hyperbranched fluorinated azide, $F_{27}-N_3$, we were able to obtain a new family of polyfluorinated amphiphilic dendrimers which bears 27 equivalent fluorine atoms. The three amphiphiles have been obtained by linking three small generation polyester dendrons based on Bis-MPA monomer to $F_{27}-N_3$ by exploiting the Copper-Catalyzed Azide-alkyne Cycloaddition. The new polyfluorinated dendritic amphiphiles bear the same hydrophobic part and a hydrophilic moiety which increases in size, flexibility and number of hydroxyl groups exposed from FDG_1 to FDG_3 .

From experimental results we observed that the crystallinity of our dendritic amphiphiles decreases with the increase in generation. Moreover, the generation of the polyester moiety affects the temperature stability and thermal behavior of the three molecules. In fact, FDG_2 showed a higher degradation temperature than FDG_1 . On the contrary, FDG_3 showed a decrease in the temperature stability and a degradation pathway which suggests an initial degradation of the outer layers followed by degradation of the inner strata. DSC, POM and SWAX analyses revealed that FDG_2 has mesomorphic properties and forms a cubic mesophase, while, probably due to the higher mobility of the polyester chains, FDG_3 self-assembles in bulk in different polymorphs characterized by different thermal behaviors.

FDG_1 , FDG_2 and FDG_3 are dispersible by the ethanol in water procedure; this allowed us to observe that the generation dependency is confirmed even in solution. In fact, we observed that in solution FDG_1 forms micelles and bigger spherical aggregates in similar proportion which are stable up to six days, in accordance with the lamellar architecture observed in the crystal structure. FDG_2 forms stable dispersions in water media where predominantly small sized micelles are present as typically observed for dendritic cubic mesogens. In both cases the ^{19}F -NMR spectra show a single peak with good signal to noise ratio, a promising characteristic for application of FDG_1 and FDG_2 as ^{19}F -MRI traceable probes. Known the high tendency of fluorinated chains to microsegregate from water, we can suppose that micelles are composed by a fluorinated inner core which should be suitable for fluorinated drug encapsulation and delivery, as suggested by literature.

On the contrary FDG_3 revealed a complex self-assembly behavior, in accordance with its tendency to form polymorphs in the solid state. In fact, in presence of ethanol, it forms dendrimersomes, multilayer vesicles, which undergo morphology transition to fibers over 48 hours of ageing. The transition to fibers causes the switching off of the ^{19}F -NMR signal thus suggesting that the relaxation times of the fluorine atoms increase, probably due to a higher rigidity of the branched polyfluorinated

chain in fibers. Interestingly, by replacing ethanol with its fluorinated derivative trifluoroethanol as the water miscible organic solvent, the FDG₃ transition to fibers is prevented and the switching off of the ¹⁹F-NMR signal can be avoided. From the calculated critical packing parameters of FDG₁, FDG₂, and FDG₃, interestingly we observed that the theoretical results obtained for FDG₁ and FDG₂ agreed with experimental results. On the contrary, even if the packing parameter calculated for FDG₃ was not able to predict the peculiar behavior observed in solution, this suggested that other forces than molecular dimensions are involved in its self-assembly. From coarse-grain simulations we were able to observe the formation of vesicles in water which convert in fibers in presence of ethanol. Furthermore, we observed that, probably due to the high mobility of the polyester chains, FDG₃ has two conformations, here referred as *cis* and *trans*, where the polyester moiety and the fluorinated branched part are respectively directed in the same and opposite directions. In presence of 6% of TFE, FDG₃ assumes preferably the *cis* conformation while in ethanol the *trans* conformation is preferred. Presumably, this is at the bases of the peculiar self-assembly observed experimentally in solution, suggesting that when FDG₃ self-organizes in the conformation of high curvature, vesicles are preferred and ¹⁹F-NMR is on, while the tendency of the amphiphile to self-adjust in the *trans* conformation in presence of ethanol can be at the bases of the transition to fibers.

Comprehensively, the results described reveal that by modulating the ratio between the branched fluorinated chain and the polyester part it is possible to change the self-assembling behavior of the final compound both in bulk and in solution, and that these are interconnected. Furthermore, we confirmed the high tendency of the branched polyfluorinated chain to microsegregate and to interact with each other by fluorine-fluorine interactions which cause high rigidity and crystallinity to the supramolecular architecture.

Since dendritic scaffolds have been widely applied in the development of non-viral gene delivery vectors and, among dendritic gene delivery vectors reported in literature, only few examples are based on Bis-MPA monomer, we decided to synthesize a new branched polyfluorinated gene delivery vector starting from one of the hydroxyl terminating one. In this way we could combine the positive effects given by the presence of fluorinated chains with ¹⁹F-MRI traceability. Since important characteristics to be taken into account for the development of a good gene vector are surface density of positive charges, colloidal stability, and size of the aggregates, by considering self-assembly properties shown by the new hydroxyl-terminating polyfluorinated dendritic amphiphiles, FDG₂ has been selected as the most promising candidate to be modified as gene delivery vector. In fact, this molecule showed a good balance between fluorinated and polyester moieties and self-assembled forming colloidally stable micelles in water. The four hydroxyl terminal groups of FDG₂ have been chemically modified to form four positively charged primary ammonium groups, FDG₂N, with high yields and purity. The presence of cationic groups in the amphiphile's structure makes it directly dispersible in water without means of a cosolvent where it forms small micelles with a stable ¹⁹F-NMR signal and promising relaxation times of the fluorine nuclei which make it promising as ¹⁹F-MRI probe. In presence of electrolytes, FDG₂N showed the tendency to self-assemble forming small sized micelles as main aggregates with an increased attitude to form larger aggregates at higher salt concentrations. In all the cases Z-potential measurements confirmed that the aggregates are positively charged and can be used to electrostatically bind nucleic acids functioning as gene delivery vectors. For determining the properties of the amphiphile as gene delivery vector, the optimal N/P ratio for gene complexations was measured for DNA and RNA sequences. FDG₂N showed low N/P ratios for both species with values in line with N/P ratios observed for classical synthetic cationic vectors. To

evaluate the best compromise between cytotoxicity and transfection efficacy, *in vitro* analyses were performed with two different cell lines. FDG₂N showed good transfection efficacy and a lower cytotoxicity if compared to jetPEI®, a commercially available cationic gene vector. The dendriplexes characterization showed a decrease in the polydispersity of the colloidal dispersion upon DNA complexation accompanied by a lowering of the averaged hydrodynamic radius, thus indicating a good ability of FDG₂N to efficiently bind DNA.

Given the positive results obtained for FDG₂N as gene vector, we decided to study the ability of the amphiphile to transfect miRNA into ependymal stem progenitor cells (epSPCs), whose excessive proliferation and altered differentiation in neurons and astrocytes characterize the occurrence of amyotrophic lateral sclerosis (ALS), a progressive neurodegenerative disorder for which no efficient therapies are now present. Preliminary *in vitro* experiments were performed on epSPCs to evaluate the ability of FDG₂N to efficiently transfect into the cells a mimic miRNA124a, one of the miRNAs overexpressed in epSPCs in ALS and responsible of their cells' differentiation. From the first results, FDG₂N showed a good transfection efficacy and a minor cytotoxicity on epSPCs with respect to Lipofectamine® RNAiMAX, a commercially available RNA cationic vector. Interestingly, we observed that the miRNA124a transfected with FDG₂N was able to induce the upregulation of Jagged 1 (Jag1) and distal-less homeobox 2 (Dlx2), its target genes, thus confirming the efficacy of FDG₂N to transfect and release the miRNA into the cytoplasm.

Further analyses must be done to evaluate the stability of FDG₂N in serum media and to better understand the internalization pathways adopted from cells to internalize the dendriplexes formed by this new cationic amphiphile; however, the results show that FDG₂N is a promising gene delivery vector with low cytotoxicity and good performances both to transfect RNA than DNA. Moreover, the decrease in the N/P ratio detected on the aged FDG₂N samples suggests that the amphiphile has a high tendency to degrade, an important characteristic for a higher biodegradability of the amphiphile. To better understand the effects given by the fluorinated chains to the final properties of the amphiphile, it should be interesting to compare FDG₂N with its non-fluorinated, cationic derivative. Nevertheless, the presence of fluorine nuclei not only makes FDG₂N applicable as ¹⁹F-MRI tracer, but the presence of an inner fluorinated cavity makes this new amphiphile applicable for the delivery of fluorinated drugs, thus opening new opportunities for the construction of combined therapies.

Pullout

Tuning of Ionic Liquid Crystal Properties by Combining Halogen Bonding and Fluorous Effect [174]

Introduction

Ionic liquid crystals (ILCs) are ionic liquid-crystalline materials that consist of cations and anions and that show at least one, either enantiotropic or monotropic, liquid crystalline mesophase [175]. The first report on ILCs was reported by Knight and Shaw in 1938. Generally, the reaching of mesophases is obtained by introducing long alkyl chains to either or both the cation and anion; as cations quaternary ammonium, pyridinium, imidazolium, phosphonium, and viologen ILCs has received great attention due to their relatively facile preparation by quaternization with alkyl halides. ILCs can be classified in thermotropic and lyotropic even if often they show amphitropic behaviour and are classified on the bases of the cation used. Cations carrying simple long alkyl chains (figure 1a) are the most representative among ILCs and show an amphiphilic character which is at the bases of their lyotropic mesomorphism; the cationic group can be directly linked or by means of flexible chains to a rigid aromatic mesogen, thus generating nonsymmetric dimers (figure 1b and 1c, respectively). Wedge-shaped ILCs (figure 1d) can form cylindrical supramolecular aggregates which tend to generate columnar and cubic mesophases [175][176].

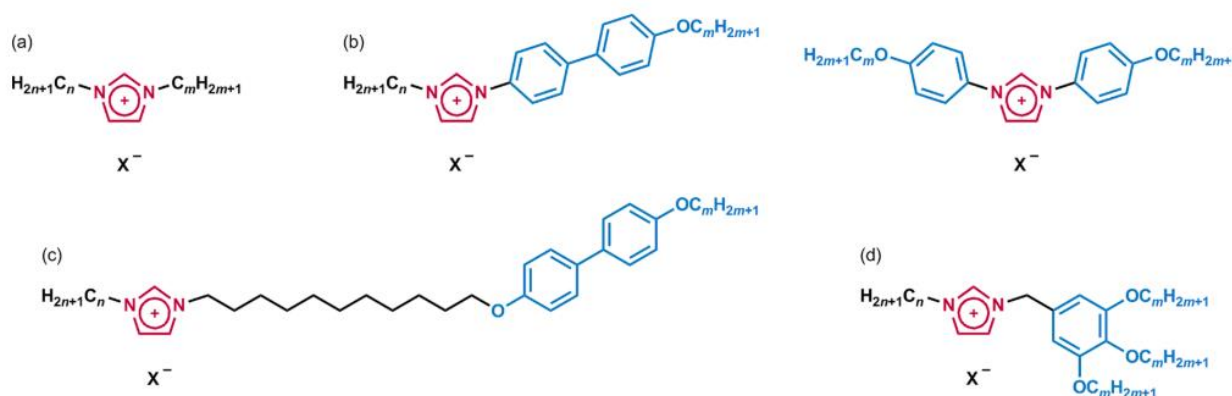


Figure 1 Molecular structure of ILCs based on imidazolium ring as the organic cation. Reprinted with permission from [175].

The principal characteristics of ILCs include orientability, due to their viscosity and magnetic susceptibility some ILCs are, in fact, macroscopically orientable by shear forces, show miscibility with various species like hydrophobic, hydrophilic, ionic, and nonionic compounds, due to the simultaneous presence in their structure of aliphatic and ionic parts, phase stability and packing tunability. The microsegregation of aliphatic and ionic moieties in ILCs generates polar nanochannel with precise structures which can transport polar and ionic species. All these features make ILCs promising for application for guest recognition, and as separation membranes, ion-/proton-conducting membranes, reaction media, and optoelectronic materials [176]. Mesophases can be introduced by exploiting supramolecular interactions: among them, halogen bonding can induce and stabilize LC phases. It has been observed that this interaction not only can introduce LC phases when the building components are not mesogenic, but, in the case of molecules that already exhibit a mesophase, the insertion of halogen bond donors can impact on the phase structure and stability [177]. In 2013 IUPAC defined that “a halogen bond occurs when there is evidence of a net attractive interaction between an electrophilic region associated with a halogen atom in a molecular entity and a nucleophilic region in another, or the same, molecular entity” [178]. The polarizability of halogens is at the bases of halogen bond; when a halogen is involved in the formation of a covalent bond the halogen shows a region of higher electron density, where the electrostatic potential is negative in

nearly all cases, and a region of lower electron density, called σ -hole, where the potential is frequently positive, mainly in the heavier halogens, which generates a cap of depleted electron density on the elongation of the covalent bond. This region can form attractive interactions with electron-rich sites thus forming halogen bond. In figure 2 is reported a schematic representation of the halogen bond: R-X is the halogen bond donor and X is a halogen atom covalently bound to the R group showing an electrophilic region. Y is the halogen bond acceptor and can be an anion or a neutral species possessing at least one nucleophilic region, like a lone-pair-possessing atom or π -system. Halogen bond (XB) is a high directional, hydrophobic interaction where the halogen-bond-donor ability, which determines how strong the halogen-bond interaction will be, changes with the order $I > Br > Cl > F$, and this rank order can be explained through the increase of positive electrostatic potential which increases with the polarizability and decreases with the electronegativity of the halogen atoms. Furthermore, the strength of halogen bonding can be tuned by inserting in the R chain electron-withdrawing groups [178].

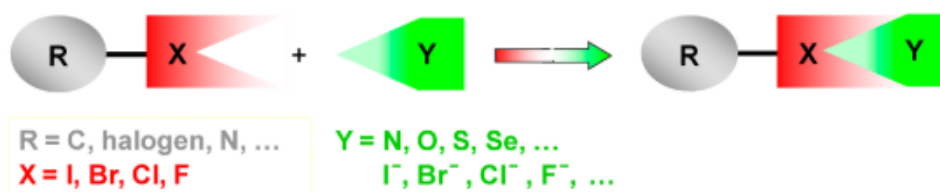


Figure 2 Schematic representation of the halogen bond. Reprinted with permission from [178].

In 2016 G. Cavallo et al. [179] published a first family of ILCs based on 1-alkyl-3-methylimidazolium iodides of varying alkyl chain length where the liquid crystallinity was enabled by the formation of supramolecular, halogen-bonded trimeric anions containing 1-iodoperfluoroalkane units. Iodide, as a strong halogen bond acceptor, interacted with the terminal iodine of 1-iodoperfluoroalkane units, thus forming the supramolecular $C-I \cdots I^- \cdots I-C$ synthon which acted as a mesogenic core driving mesophase formation, as shown in figure 3. The segregation of the perfluorocarbon chains promoted the self-organization of the obtained ILCs which exhibited liquid crystallinity even at room temperature.

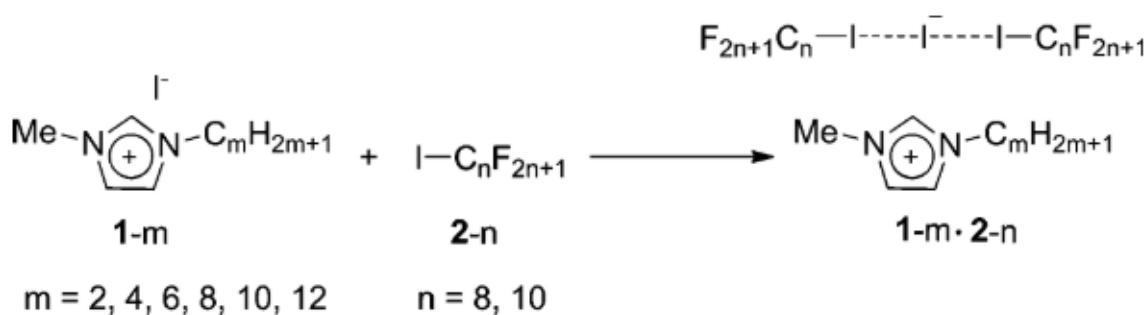


Figure 3 Chemical structures of the used imidazolium salts (1-m) and iodoperfluoroalkanes (2-n), and their halogen-bonded complexes (1-m·2-n). Reprinted with permission from [179].

Results and discussion

Room-temperature ionic liquids (RTILs) have attracted considerable scientific interest over the past years; this is due to their unique and useful properties, such as negligible vapor pressure, thermal stability, high ionic conductivity, and a large electrochemical window [180], which make them ideal electrolytes in various iono-optic and electrochemical devices [181][182]. Physico-chemical properties of ILs may easily be tuned through a careful choice of the organic cation and its counterion. In particular, it has been reported that introducing specific pendants on several cations induces the formation of mesophases, thus generating ionic liquid crystalline (ILC) materials. Due to the unique properties of the fluorine atom, fluorination has been exploited to control properties and self-assembly behavior of ILs; fluorinated ILs display a higher oxygen solubility and lower surface energy if compared to their non-fluorinated analogues and have found applications, among others, in (electro)catalysis and energy storage technologies. Moreover, functionalizing mesogens with perfluorocarbon chains allows to control their mesomorphic behavior thanks to the fluorous effect [183][184][185].

With the hypothesis in mind of exploiting the synergistic combination of halogen bond and fluorous effect to drive mesogen self-assembly and tune transition temperatures, we pursued supramolecular complexes between 1-polyfluoroalkyl-3-alkylimidazolium iodides **1** and **2m**, and long-chain iodoperfluoroalkanes **3p** and **4**, as reported in figure 4.

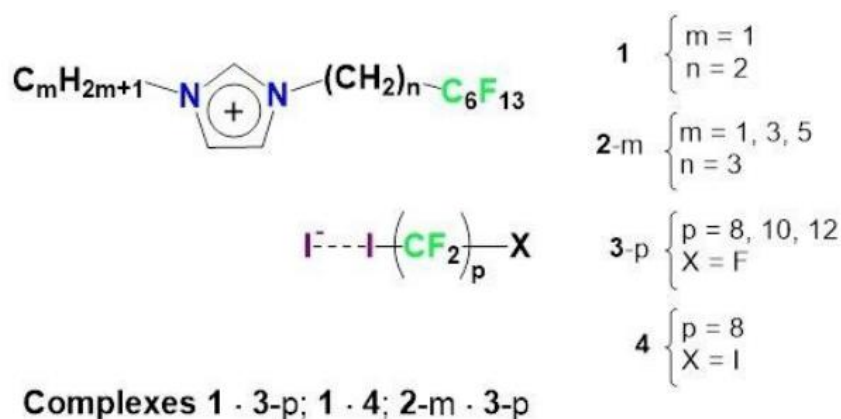


Figure 4 Chemical structures of the used polyfluorinated imidazolium salts (**1** and **2-m**) and iodoperfluoroalkanes (**3p** and **4**), and their halogen-bonded complexes **1 · 3-p**, **1 · 4**, **2-m · 3-p**, and **2-m · 4**, [174].

Synthesis of 1-polyfluoroalkyl-3-alkylimidazolium iodides and complex preparation

All the 1-polyfluoroalkyl-3-alkylimidazolium iodides (**1** and **2-m**) were prepared as previously reported [183]. The general scheme of the reactions is reported in figure 5.

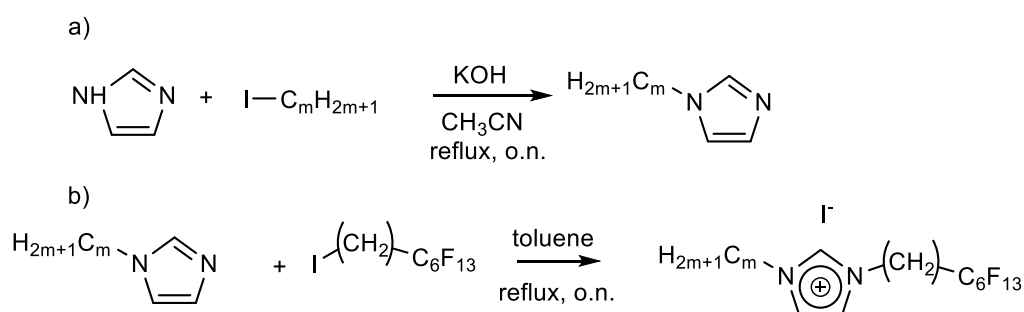


Figure 5 Scheme of the reactions involved in the synthesis of the imidazolium salts.

All the compounds could be isolated with good yield (higher than 70%) and purity and their structure was confirmed by ^1H and ^{19}F -NMR. The final complexes were obtained by mixing 1- polyfluoroalkyl-3-alkylimidazolium iodides 1 and 2-m with iodoperfluoroalkanes of different chain lengths (3p) or 1,8- diiodoperfluorooctane (4). Notably, the starting imidazolium salts 1 and 2-1 show enantiotropic smectic A mesophases, while 2-3 and 2-5 are non-mesomorphic in nature, suggesting that the flexibility of propyl and pentyl chains may impact liquid crystallinity. We reasoned that by halogen bonding a long-chain iodoperfluoroalkane to the Γ ion of the ILs 2-3 and 2-5 could result in a more efficient segregation of the hydrocarbon segments of the molecules and a more compact fluororous layer, thus resulting in a lamellar organization and likely promoting the emergence of a mesophase. In particular, the number of halogen bonds that Γ ions usually form, depends on the geometry of the interacting moieties, the accessibility of the XB-donor moiety, and the overall requirements of the crystal packing. Therefore, it is quite common to have Γ ions functioning as monodentate, bidentate or tridentate XB-acceptors, although higher coordination numbers are also possible [186]. To establish the correct stoichiometric ratio between the imidazolium salt and the iodoperfluoroalkane, we prepared the XB-complexes by isothermal crystallization at RT starting from chloroform solutions containing the XB-donor and acceptor, in either 1:1 or 2:1 ratio. All the complexes were obtained as white microcrystalline solids that have been fully characterized by ^1H and ^{19}F -NMR, DSC, and POM analyses. Good-quality single crystals were also grown for several complexes and submitted to X-ray diffraction analyses.

Single-crystal X-ray structural analyses and ^{19}F -NMR results

Single-crystal X-ray diffraction analyses of samples 1·3-8, 1·3-10, 1·4, 2-1·3-10, and 2-1·4 revealed common patterns of noncovalent interactions, highlighting how the XB drives the self-assembly between the starting modules. Notably, in all of the cocrystals, the Γ ion functions as monodentate XB-acceptor towards the I atoms of the polyfluorinated modules. The XB- donor/acceptor ratio in the systems thus depends exclusively on the topicity of the XB-donor. In fact, in complexes 1·3-8, 1·3-10, and 2-1·3-10 where the XB-donors are monoiodinated, the XB-donor/acceptor ratio is 1:1 and dimeric halogen-bonded complexes are, thus, formed (Figure 6A). Similarly, in the complexes 1·4 and 2-1·4, where the XB-donor is diiodoperfluorooctane 4, which functions as a ditopic XB-donor, the 1/4 and 2-1/4 ratios are 2:1 and trimeric complexes are obtained (Figure 6B).

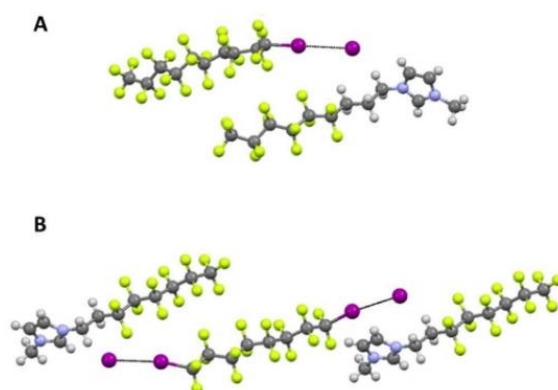


Figure 6 A: The asymmetric unit of the complex 2-1 · 3-10. Halogen bonding drives the self-assembly of the imidazolium salt 2-1 and the iodoperfluorodecane 3-10 into a dimeric supramolecular complex. **B:** The asymmetric unit of the complex 1 · 4. Halogen bonding drives the self-assembly of the imidazolium salt 1 and diiodoperfluorooctane 4 into a trimeric supramolecular complex. Color code: gray=carbon, blue=nitrogen; magenta=iodine; green=fluorine; light gray=hydrogen. Black dotted lines indicate the halogen bonds, [174].

In all of the structures obtained, the C-I...I XBs, are linear, with C-I...I angles between 170.2 and 177.5°) and relatively short, as shown in table 1, confirming the existence of strong and directional interactions. All the C-I...I distances are quite similar, ranging between 3.434 and 3.503 Å, which corresponds to an almost 13% reduction of the sum of the van der Waals and Pauling radii for I and I and are perfectly in line with those reported in the literature for analogous XB-complexes [187]. Furthermore, in all of the analyzed complexes, the I⁻ ions form weak hydrogen bonds (HBs) with the H atom in position 2 of the imidazolium cation, as a consequence of the strong electron-withdrawing effect of the positively charged ring, which increases the Lewis-acid character of this H atom. The average H...I distance in the complexes is ~3 Å, which is in line with those reported in the literature for similar systems [188]. Other weak HBs involve the I⁻ ions and the methyl group of a nearby ring in cocrystals 1·3-8, 1·3-10, and 1·4. As far as the crystal packing is concerned, a lamellar organization is observed in all of the complexes elicited by the segregation between the perfluoroalkyl chains and the charged moieties (Figure 7A). The positively charged rings and the iodide anions form a well-defined hydrocarbon layer where each I⁻ unit is surrounded by four imidazolium rings. Specifically, the iodide anion is placed at the center of a supramolecular cube formed by the imidazole rings and shows several short contacts with the electron deficient aromatic area of two imidazolium units and several hydrogen bonding contacts with the H atom in position 2 and the CH₂ units of two other imidazolium cations. The hydrocarbon layers are then surrounded by the fluorinated layers composed by the polyfluorinated halogen bonding donor units and the polyfluorinated part of the imidazolium moieties. Notably an extended network of F...F contacts, highlighted in figure 7A, is present in the fluorinated layers promoting the formation of dense and robust fluorinated lamellar systems. The resulting lamellar organization, if preserved in the molten state, would most likely determine an LC behavior with smectic mesophases, as planned in our design. The content of fluorine atoms in these complexes is exceptionally high, picking up to over 53% in 1·3-10. Therefore, it was no surprise that perfluoroalkyl chains showed an extensive disorder. This behavior is quite common in highly fluorinated crystalline systems and is mainly due to the low ability of fluorine atoms to engage with strong intermolecular interactions, commonly resulting in poorly crystalline materials. Although for some of the reported structures the disorder of the fluorinated chains was quite severe, we were able to locate all the fluorine atoms.

Table 1. Geometrical features of XB in crystallized complexes.			
Complex	d _{I...I} ⁻ [Å]	N _c ^[a]	C-I...I ⁻ Angle [°]
1·3-8	3.502	0.87	174.5
1·3-10	3.434	0.85	174.0
1·4	3.468	0.85	170.2
2-1·3-10	3.503	0.87	177.5
2-1·4	3.527	0.87	172.8

(a) N_c: Normalized contacts, expressed as the ratio between the XB distance over the sum of the vdW and Pauling radii of the atoms involved in the interaction.

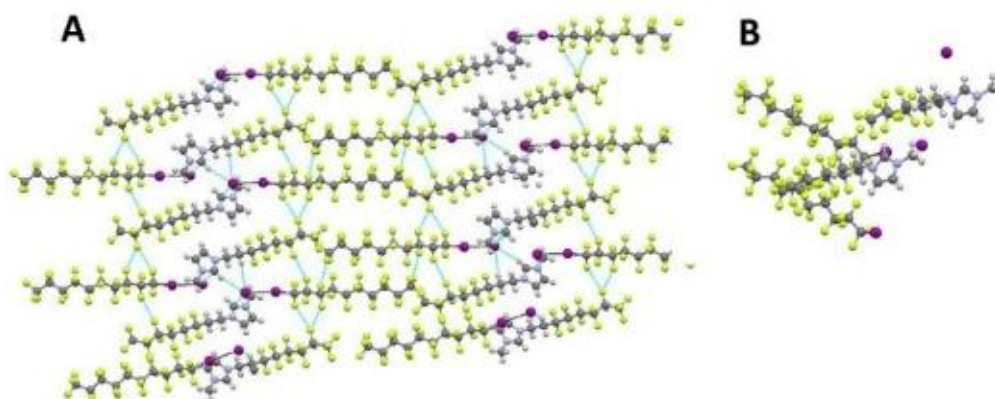


Figure 7 **A)** Packing of 2-1·3-10 viewed along the crystallographic *b* axis, showing the segregation between the imidazolium ring and the iodoperfluorooctane module, resulting in a lamellar organization; **B)** Interdigitation of fluorinated chains from the cation and the halogen-bonded superanion. Color code: grey, carbon; blue, nitrogen; magenta, iodine; green, fluorine; light grey, hydrogen. Black lines indicate the halogen bonds; light blue lines indicate other short contacts, [174].

^{19}F -NMR spectroscopy was used to determine whether the bulk crystalline samples had the same composition of the analyzed single crystals, thus determining the stoichiometric ratio between the imidazolium salt and the iodoperfluoroalkane in all of the complexes under study. In particular, iodoperfluoroalkanes **3p** showed a triplet at -59.86 ppm and a multiplet at -113.12 ppm, due, respectively, to the α and β difluoromethylene groups; similarly, the diiodoperfluorooctane **4** showed a triplet at -59.34 ppm and a multiplet at -113.08 ppm. The imidazolium salts on the contrary showed a multiplet at -113.58 ppm due to the $-\text{CH}_2\text{CF}_2-$ group. The ratios between the $-\text{CH}_2\text{CF}_2-$ signal area, derived from the imidazolium cation, and the $(\text{I}-\text{CF}_2\text{CF}_2-)$ signal areas, derived from the iodoperfluoroalkane, were 1:1 in all of the crystallized complexes (figure 8), independent of the starting stoichiometry between XB-donor and XB-acceptor modules used in the experiments. This result is perfectly in line with X-ray data, see figure 6. It confirms that the I^- functions as monodentate XB-acceptor in all of the bulk complexes and the imidazolium/ perfluoroalkane ratios, 1:1 for complexes containing **3p** and 1:2 for complexes containing **4**, found in single crystals are representative of the whole bulk samples.

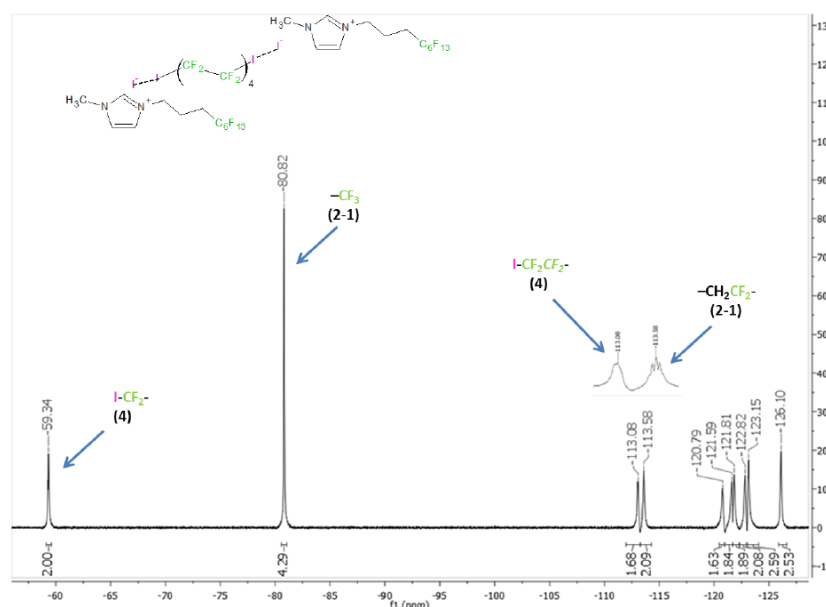


Figure 8 ^{19}F -NMR spectra in CDCl_3 of the XB complex 2-1·3-10, [174].

Thermal characterization

The LC properties of the starting imidazolium salts and of all the obtained complexes were established by a combination of Polarised-light Optical Microscopy (POM) and Differential Scanning Calorimetry (DSC) performed on the powder crystalline samples. Starting imidazolium salts displayed decreasing melting temperatures with increasing hydrocarbon chain lengths. Indeed, while imidazolium salts 1 and 2-1 have melting points (mp) slightly below 100°C, both 2-3 and 2-5 are highly viscous liquids at room temperature (mp of -8 and -32°C, respectively). Furthermore, both 1 and 2-1 also showed SmA LC properties with clearing points $\geq 200^\circ\text{C}$. Noteworthy, all the obtained complexes showed thermotropic LC properties. Transition temperatures are reported in Table 2.

Table 2. Phase transition temperatures and mesophase temperature ranges measured on heating the halogen-bonded complexes 1·3 p, 1·4, and 2 m·3 p.			
Complex	Transition ^[a]	Temperature [°C]	ΔT [°C]
1	Cr–SmA	94	130
	SmA–Iso	224	
1·3-8	Cr–SmA	107	127
	SmA–Iso	234	
1·3-10	Cr–SmA	99	134
	SmA–Iso	233	
1·3-12	Cr–SmA	116	111
	SmA–Iso	227	
1·4	Cr–SmA	86	75
	SmA–Iso	161	
2-1	Cr–SmA	86	112
	SmA–Iso	198	
2-1·3-8	Cr–SmA	90	55
	SmA–Iso	145	
2-1·3-10	Cr–SmA	98	37
	SmA–Iso	135	
2-1·3-12	Cr–SmA	120	43
	SmA–Iso	163	
2-3	Cr–Iso	-8	
2-3·3-8	Cr–SmA	< 23	97
	(SmA–SmB) ^[b]	108	
	SmA–Iso	120	
2-3·3-10	Cr–SmA	73	62
	(SmA–SmB) ^[b]	122	
	SmA–Iso	135	
2-3·3-12	Cr–SmA	78	61
	(SmA–SmB) ^[b]	105	
	SmA–Iso	139	
2-5	Cr–Iso	-32	
2-5·3-8	Cr–SmA	< 19	80
	SmA–Iso	99	
2-5·3-10	Cr–SmA	53	65
	SmA–Iso	118	
2-5·3-12	Cr–SmA	52	75
	SmA–ISO	127	

[a] Crystal phase (Cr), smectic A phase (SmA), smectic B phase (SmB), and isotropic phase (Iso). [b] Seen only on cooling.

All of the complexes displayed enantiotropic mesomorphism with smectic A phases displaying characteristic optical textures on cooling, as shown in figure 9. This result is consistent with XRD analyses and is a manifestation of the lamellar organization of perfluorocarbon and hydrocarbon modules. Notably, 2-3-3p and 2-5-3p, although starting imidazolium salts were not LC, all showed the emergence of mesophases. In particular, all of the complexes containing 2-3 and 2-5 showed mp lower than 80°C and, noteworthy, 2-3-3-8 and 2-5-3-8 were LC at RT. This result is relevant because RT-LC materials displaying high ionic conductivity are attractive candidates for applications in several electrochemical devices. All of 2-3-3p and 2-5-3p complexes showed clearing points, i. e., SmA-Iso transitions temperatures at $\leq 100^\circ\text{C}$ and increasing with the length of the halogen-bonded perfluoroalkyl chains. The mesomorphism of 2-3-3p complexes also showed on cooling an intermediate phase, identified by microscopy through the appearance of striations across the back of the fans, as reported in figure 9E), which disappeared on cooling further below the transition. POM texture would suggest the formation of a SmB phase, however other smectic phases or crystal modifications cannot be excluded. Complexes 1-3p all showed melting ($\geq 100^\circ\text{C}$) and clearing points ($\geq 200^\circ\text{C}$) higher than the pure 1, and, in general, provided with the highest transition temperatures and the broadest LC ranges of the whole series of obtained complexes (Figure 10). Conversely, the complex 1-4 showed a lower transition temperature. On the other hand, 2-1-3p complexes showed higher melting points while lower clearing points than the pure imidazolium salt 2-1. In both cases, no particular trends related to the chain length of the polyfluorinated modules were observed. As far as the length of the alkyl chains on the imidazolium cations, instead, transition temperatures consistently decreased with the increase of the chain length from 1 to 2m.

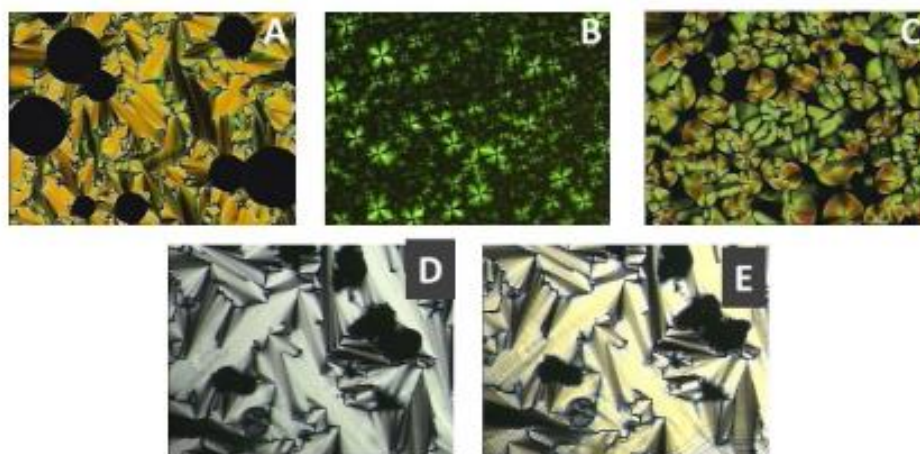


Figure 9 Optical textures observed on cooling from the isotropic state for: **A)** 1-3-8 at 220°C; **B)** 2-1-3-10 at 133°C; **C)** 2-5-3-8 at 97°C; **D)** 2-3-3-10 at 126°C (SmA phase); **E)** 2-3-3-10 at 114°C (SmB phase), [174].

Despite the high clearing points, DSC analyses confirmed the stability of such complexes (figures 11 and 12). Repeated heating and cooling cycles demonstrated that the LC properties were fully reversible over, at least, three cycles, and typical POM features were perfectly reproducible even after several excursions into the isotropic phases.

Since 2-3 and 2-5 are not mesomorphic, this implies that the XB between the I⁻ ion and the iodoperfluorocarbon survives in the mesophase and is responsible for the LC behaviors of the obtained supramolecular structures. In addition, the formation of halogen bonds also plays a key role in the assembly and stabilization of the observed lamellar arrangements and thus on the formation of the ordered SmA phases. Specifically, the selected XB acceptor modules, composed by an ionic head

and a fluorinated tail, are self-assembled amphiphilic systems in nature and their assembly is promoted by strong electrostatic interactions in the layers of the ion pair units (namely the imidazolium ring and the iodide anion) and by multiple $F\cdots F$ contacts for the organization of the fluorinated tails in the fluorinated layers. This amphiphilic character is clearly observed in the XRD studies, and it is responsible for the overall lamellar arrangement of the complexes. Here the addition of polyfluorinated XB donors has two-folds effect on the overall organization. First there is, for all the complexes, an elongation of the polyfluorinated portion which adds a further stabilization of the fluorinated layers thanks to the formation of additional $F\cdots F$ contacts. Latter it is able to induce, for the non-mesomorphic salts 2-3 and 2-5, the LC behavior. Therefore, the formation of liquid crystalline phases with lamellar order can be affected by a careful selection of the length of polyfluorinated chains which can be added using a supramolecular approach driven by halogen bond.

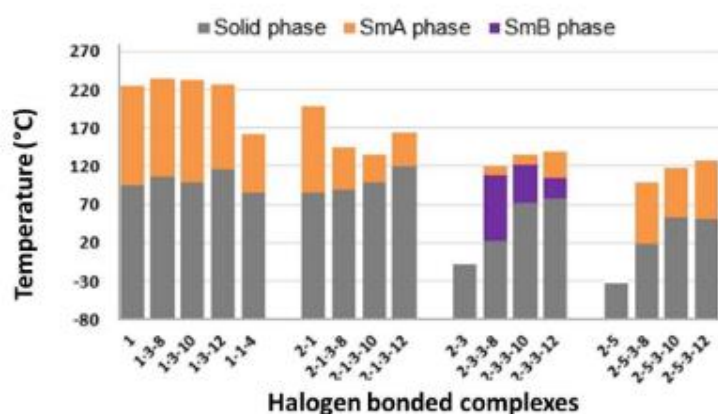


Figure 10 Phase transition temperatures and mesophase temperature ranges measured on heating the halogen-bonded complexes under a hot-stage polarized optical microscope. The smectic B phase has been seen only on cooling for complexes containing 2-3 p, [174].

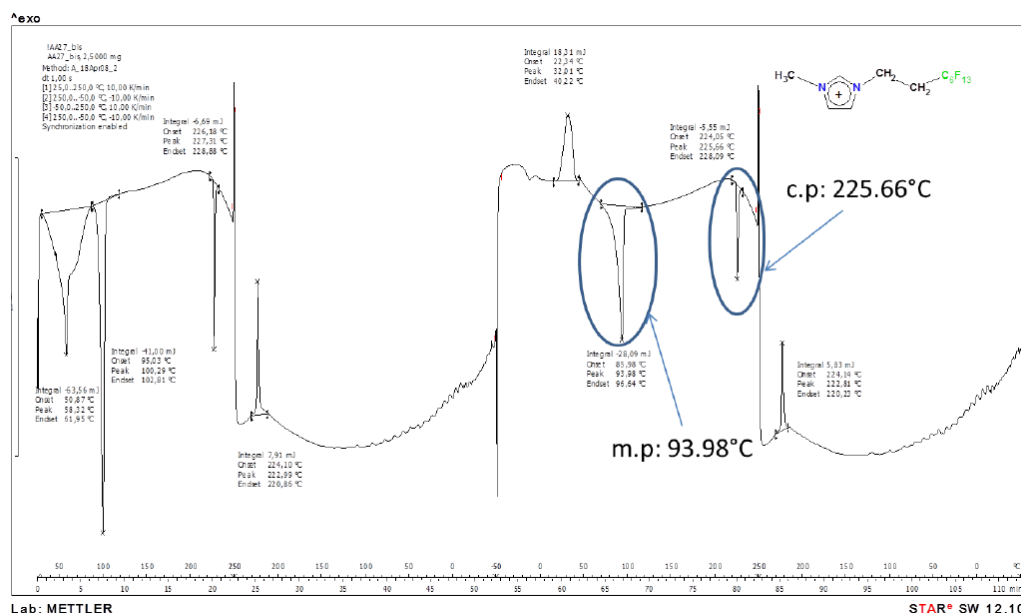


Figure 11 DSC thermogram of pure 1, [174].

Experimental section

Materials and Methods

The starting materials were purchased from Sigma-Aldrich, Acros Organics, and Apollo Scientific and they were used as received. Commercial HPLC-grade solvents were used without further purification. The LC textures were studied with an Olympus BX51 polarized optical microscope equipped with a Linkam Scientific LTS 350 heating stage and a Sony CCD-IRIS/RGB video camera. DSC analysis was performed with a Mettler Toledo DSC823e instrument, using aluminum light 20 μL sample pans and Mettler STARe software for calculation. $^1\text{H-NMR}$ and $^{19}\text{F-NMR}$ spectra were recorded at 25°C with a Bruker AV 500 spectrometer using CDCl_3 as a solvent. TMS and CFCl_3 were used as internal standards for calibrating chemical shifts in $^1\text{H-NMR}$ and $^{19}\text{F-NMR}$, respectively. The single-crystal X-ray structures were determined on a Bruker Kappa Apex II diffractometer.

Synthesis

All the 1-polyfluoroalkyl-3-alkylimidazolium iodides (1 and 2-m) were prepared as previously reported [183].

The supramolecular complexes were synthesized as follows: the 1-polyfluoroalkyl-3-alkyl imidazolium iodides and the appropriate iodoperfluoroalkanes were dissolved separately in chloroform. The two solutions were mixed in an open, clear borosilicate glass vial to obtain a 1 :1 or a 1 :2 imidazolium/perfluorocarbon molar ratio. The slow evaporation of the solvent at room temperature afforded to microcrystalline powders which have been characterized by ^1H and $^{19}\text{F-NMR}$.

Single crystal X-ray diffraction analysis

Single crystals suitable for X-Ray diffraction analysis were obtained through free-interface diffusion crystallization experiments carried out at the interface between chloroform and hexane. In this case, the imidazolium salts were dissolved in chloroform, while perfluorocarbons were dissolved in hexane. The hexane solution was then stratified on the chloroform solution and the slow diffusion of the hexane in chloroform afforded to good quality single crystals. Deposition Numbers 784681 (for 1·3-8), 784679 (for 1·3-10), 784677 (for 1·4), 784680 (for 2-1·3-10) and 784678 (for 2-1·4) contain the supplementary crystallographic data for this paper. These data are provided free of charge by the joint Cambridge Crystallographic Data Centre and Fachinformationszentrum Karlsruhe Access Structures service www.ccdc.cam.ac.uk/structures.

Conclusion

We have described the synthesis of new supramolecular complexes obtained upon XB-driven self-assembly of 1-poly-fluoroalkyl-3-alkylimidazolium iodides (1 and 2m) and mono-iodoperfluoroalkanes of different chain lengths (3p) or diiodoperfluorooctane (4). Single crystal X-ray diffraction analyses proved that I...I halogen bonds are primarily responsible for the self-assembly of the complementary modules, driving the formation of polyfluorinated superanions. The partial interdigitation of fluorinated chains of anions and cations interacting through weak F...F contacts enhances the segregation between perfluorocarbon and hydrocarbon moieties promoting the formation of the segregated layered structure. All of the complexes displayed thermotropic liquid-crystalline behavior over a wide range of temperatures, with enantiotropic smectic phases, which are reminiscent of the lamellar phase observed in the crystal state. Notably, some complexes are liquid crystalline at room temperature providing new fluorinated ionic liquid crystalline materials. Our results highlight the ability of the XB to persist in the molten/liquid phase and work as an efficient supramolecular tool for the introduction of long perfluoroalkyl chains on the anions of imidazolium salts, thus providing novel design principles for supramolecular ionic conductors.

References

- [1] M. Ramanathan, L. Kumar Shrestha, T. Mori, Q. Ji, J. P. Hillbc, K. Ariga, “Amphiphile nanoarchitectonics: from basic physical chemistry to advanced applications” *Phys.Chem.Chem.Phys.*, vol. 15, pp. 10580–10611, 2013, doi: 10.1039/c3cp50620g.
- [2] P. C. Domenico Lombardo, Mikhail A. Kiselev, Salvatore Magazù, “Amphiphiles self-assembly: Basic concepts and future perspectives of supramolecular approaches,” *Adv. Condens. Matter Phys.*, pp. 1–22, 2015, doi: 10.1155/2015/151683.
- [3] N. P. Sampad Ghosha, A. Ray, “Self-assembly of surfactants: An overview on general aspects of amphiphiles,” *Biophys. Chem.*, vol. 265, pp. 106429–106440, 2020, doi: 10.1016/j.bpc.2020.106429.
- [4] D. Lombardo, P. Calandra, L. Pasqua, S. Magazù, “Self-assembly of organic nanomaterials and biomaterials: The bottom-up approach for functional nanostructures formation and advanced applications,” *Materials (Basel)*, vol. 13, no. 5, 2020, doi: 10.3390/ma13051048.
- [5] Q. Sun, “The physical origin of hydrophobic effects,” *Chem. Phys. Lett.*, vol. 672, pp. 21–25, 2017, doi: 10.1016/j.cplett.2017.01.057.
- [6] N. T. Southall, K. A. Dill, A. D. J. Haymet, “A view of the hydrophobic effect,” *J. Phys. Chem. B*, vol. 106, no. 3, pp. 521–533, 2002, doi: 10.1021/jp015514e.
- [7] D. Chandler, “Interfaces and the driving force of hydrophobic assembly,” *Nature*, vol. 437, pp. 640–647, 2005.
- [8] R. Nagarajan, “Amphiphilic surfactants and amphiphilic polymers: Principles of molecular assembly,” *ACS Symp. Ser.*, vol. 1070, pp. 1–22, 2011, doi: 10.1021/bk-2011-1070.ch001.
- [9] R. Nagarajan, E. Ruckenstein, “Theory of Surfactant Self-Assembly: A Predictive Molecular Thermodynamic Approach,” *Langmuir*, vol. 7, no. 12, pp. 2934–2969, 1991, doi: 10.1021/la00060a012.
- [10] J. Israelachvili, *Intermolecular and Surface Forces - 3rd Edition*, Third edit. Academic Press, 2011. Accessed: Jan. 16, 2021. [Online]. Available: <https://www.elsevier.com/books/intermolecular-and-surface-forces/israelachvili/978-0-12-391927-4>
- [11] K. Nesměřák, I. Němcová, “Determination of critical micelle concentration by electrochemical means,” *Anal. Lett.*, vol. 39, no. 6, pp. 1023–1040, 2006, doi: 10.1080/00032710600620302.
- [12] J. Aguiar, P. Carpena, J. A. Molina-Bolívar, C. Carnero Ruiz, “On the determination of the critical micelle concentration by the pyrene 1:3 ratio method,” *J. Colloid Interface Sci.*, vol. 258, no. 1, pp. 116–122, 2003, doi: 10.1016/S0021-9797(02)00082-6.
- [13] S. Svenson, “Self-assembly and self-organization: Important processes, but can we predict them?,” *J. Dispers. Sci. Technol.*, vol. 25, no. 2, pp. 101–118, 2004, doi: 10.1081/DIS-120030657.
- [14] A. Domínguez, A. Fernández, N. Gonzalez, E. Iglesias, L. Montenegro, “Determination of critical micelle concentration of some surfactants by three techniques,” *J. Chem. Educ.*, vol. 74, no. 10, pp. 1227–1231, 1997, doi: 10.1021/ed074p1227.
- [15] S. J. Holder, N. A. J. M. Sommerdijk, “New micellar morphologies from amphiphilic block copolymers: Disks, toroids and bicontinuous micelles,” *Polym. Chem.*, vol. 2, no. 5, pp. 1018–1028, 2011, doi: 10.1039/c0py00379d.
- [16] Y. Wang, X. Du, Z. Liu, S. Shi, and H. Lv, “Dendritic fibrous nano-particles (DFNPs): Rising stars of mesoporous materials,” *J. Mater. Chem. A*, vol. 7, no. 10, pp. 5111–5152, 2019, doi: 10.1039/c8ta09815h.
- [17] L. Qiu, J. Zhang, M. Yan, Y. Jin, K. Zhu, “Reverse self-assemblies based on amphiphilic polyphosphazenes for encapsulation of water-soluble molecules,” *Nanotechnology*, vol. 18, no. 47, pp. 475602–475611, 2007, doi: 10.1088/0957-4484/18/47/475602.
- [18] H. Liu, J. Xu, Y. Li, Y. Li, “Aggregate nanostructures of organic molecular materials,” *Acc. Chem. Res.*, vol. 43, no. 12, pp. 1496–1508, 2010, doi: 10.1021/ar100084y.
- [19] R. Nagarajan, “Molecular Packing Parameter and Surfactant Self-Assembly: The Neglected Role of the Surfactant Tail,” *Langmuir*, vol. 18, pp. 31–38, 2002, doi: 10.1021/la010831y.
- [20] P. A. Hassan, S. L. Gawali, “Directing Amphiphilic Self-Assembly: From Microstructure Control to Interfacial Engineering,” *Langmuir*, vol. 35, no. 30, pp. 9635–9646, 2019, doi: 10.1021/acs.langmuir.8b02921.

- [21] S. E. Burke, A. Eisenberg, "Kinetic and mechanistic details of the vesicle-to-rod transition in aggregates of PS310-b-PAA52 in dioxane-water mixtures," *Polymer*, vol. 42, no. 21, pp. 9111–9120, 2001, doi: 10.1016/S0032-3861(01)00385-8.
- [22] Y. Shen, J. Hao, H. Hoffmann, Z. Wu, "Reversible phase transition from vesicles to lamellar network structures triggered by chain melting," *Soft Matter*, vol. 4, no. 4, pp. 805–810, 2008, doi: 10.1039/b717097a.
- [23] J. Zhao, H. Y. Zhang, H. L. Sun, Y. Liu, "Supramolecular nanoassemblies of an amphiphilic porphyrin-cyclodextrin conjugate and their morphological transition from vesicle to network," *Chem. - A Eur. J.*, vol. 21, no. 11, pp. 4457–4464, 2015, doi: 10.1002/chem.201405943.
- [24] D. Mandal, S. Dinda, P. Choudhury, P. K. Das, "Solvent induced morphological evolution of cholesterol based glucose tailored amphiphiles: Transformation from vesicles to nanoribbons," *Langmuir*, vol. 32, no. 38, pp. 9780–9789, 2016, doi: 10.1021/acs.langmuir.6b02165.
- [25] Z. Gong, X. Liu, J. Dong, W. Zhang, Y. Jiang, J. Zhang, W. Feng, K. Chenc, J. Bai, "Transition from vesicles to nanofibres in the enzymatic self-assemblies of an amphiphilic peptide as an antitumour drug carrier," *Nanoscale*, vol. 11, no. 33, pp. 15479–15486, 2019, doi: 10.1039/c9nr02874a.
- [26] G. J. A. Sevink, A. V. Zvelindovsky, "Self-assembly of complex vesicles," *Macromolecules*, vol. 38, no. 17, pp. 7502–7513, 2005, doi: 10.1021/ma0506740.
- [27] A. H. De Vries, A. E. Mark, S. J. Marrink, "Molecular Dynamics Simulation of the Spontaneous Formation of a Small DPPC Vesicle in Water in Atomistic Detail," *J. Am. Chem. Soc.*, vol. 126, no. 14, pp. 4488–4489, 2004, doi: 10.1021/ja0398417.
- [28] S. J. Marrink, A. E. Mark, "The mechanism of vesicle fusion as revealed by molecular dynamics simulations," *J. Am. Chem. Soc.*, vol. 125, no. 37, pp. 11144–11145, 2003, doi: 10.1021/ja036138+.
- [29] V. Knecht, S. J. Marrink, "Molecular dynamics simulations of lipid vesicle fusion in atomic detail," *Biophys. J.*, vol. 92, no. 12, pp. 4254–4261, 2007, doi: 10.1529/biophysj.106.103572.
- [30] X. Yu, P. Zhang, Y. Li, L. Chen, T. Yi, Z. Ma, "Vesicle-tube-ribbon evolution via spontaneous fusion in a self-correcting supramolecular tissue," *CrystEngComm*, vol. 17, no. 42, pp. 8039–8046, 2015, doi: 10.1039/c5ce00636h.
- [31] H. Wu, Y. Q. Zhang, M. B. Hu, L. J. Ren, Y. Lin, W. Wang, "Creating Quasi Two-Dimensional Cluster-Assembled Materials through Self-Assembly of a Janus Polyoxometalate-Silsesquioxane Co-Cluster," *Langmuir*, vol. 33, no. 21, pp. 5283–5290, 2017, doi: 10.1021/acs.langmuir.7b01015.
- [32] J. Yu, D. Sun, H. Ai, X. Wang, L. Zhai, "Novel mechanism for nanotube formation from vesicle: A transition induced by the rearrangement of molecular pairs," *Colloids Surfaces A Physicochem. Eng. Asp.*, vol. 422, pp. 148–154, 2013, doi: 10.1016/j.colsurfa.2012.11.042.
- [33] A. T. Preslar, F. Tantakitti, K. Park, S. Zhang, S. I. Stupp, T. J. Meade, "19F Magnetic Resonance Imaging Signals from Peptide Amphiphile Nanostructures Are Strongly Affected by Their Shape," *ACS Nano*, vol. 10, no. 8, pp. 7376–7384, 2016, doi: 10.1021/acs.nano.6b00267.
- [34] B. N. S. Thota, L. H. Urner, R. Haag, "Supramolecular architectures of dendritic amphiphiles in water," *Chem. Rev.*, vol. 116, no. 4, pp. 2079–2102, 2016, doi: 10.1021/acs.chemrev.5b00417.
- [35] P. S. Chae, P. D. Laible, S. H. Gellman, "Tripod amphiphiles for membrane protein manipulation," *Mol. Biosyst.*, vol. 6, no. 1, pp. 89–94, 2009, doi: 10.1039/b915162c.
- [36] A. Halperin, "Polymeric vs. monomeric amphiphiles: Design parameters," *Polym. Rev.*, vol. 46, no. 2, pp. 173–214, 2006, doi: 10.1080/15321790600724369.
- [37] D. A. Tomalia, "Dendritic effects: Dependency of dendritic nano-periodic property patterns on critical nanoscale design parameters (CNDPs)," *New J. Chem.*, vol. 36, no. 2, pp. 264–281, 2012, doi: 10.1039/c1nj20501c.
- [38] C. C. Lee, J. A. MacKay, J. M. J. Fréchet, F. C. Szoka, "Designing dendrimers for biological applications," *Nat. Biotechnol.*, vol. 23, no. 12, pp. 1517–1526, 2005, doi: 10.1038/nbt1171.
- [39] B. M. Rosen, C. J. Wilson, D. A. Wilson, M. Peterca, M. R. Imam, V. Percec, "Dendron-mediated self-assembly, disassembly, and self-organization of complex systems," *Chem. Rev.*, vol. 109, no. 11, pp. 6275–6540, 2009, doi: 10.1021/cr900157q.

- [40] L. P. Wu, M. Ficker, J. B. Christensen, P. N. Trohopoulos, S. M. Moghimi, "Dendrimers in Medicine: Therapeutic Concepts and Pharmaceutical Challenges," *Bioconjug. Chem.*, vol. 26, no. 7, pp. 1198–1211, 2015, doi: 10.1021/acs.bioconjchem.5b00031.
- [41] B. M. Rosen, D. A. Wilson, C. J. Wilson, M. Peterca, B. C. Won, C. Huang, L. R. Lipski, X. Zeng, G. Ungar, P. A. Heiney, V. Percec, "Predicting the structure of supramolecular dendrimers via the analysis of libraries of AB₃ and constitutional isomeric AB₂ biphenylpropyl ether self-assembling dendrons," *J. Am. Chem. Soc.*, vol. 131, no. 47, pp. 17500–17521, 2009, doi: 10.1021/ja907882n.
- [42] H. J. Sun, S. Zhang, V. Percec, "From structure to function via complex supramolecular dendrimer systems," *Chem. Soc. Rev.*, vol. 44, no. 12, pp. 3900–3923, 2015, doi: 10.1039/c4cs00249k.
- [43] D. A. Tomalia, "Architecturally driven properties based on the dendritic state," *High Perform. Polym.*, vol. 13, no. 2, 2001, doi: 10.1088/0954-0083/13/2/301.
- [44] V. Percec, D. A. Wilson, P. Leowanawat, C. J. Wilson, A. D. Hughes, M. S. Kaucher, D. A. Hammer, D. H. Levine, A. J. Kim, F. S. Bates, K. P. Davis, T. P. Lodge, M. L. Klein, R. H. DeVane, E. Aqad, B. M. Rosen, A. O. Argintaru, M. J. Sienkowska, K. Rissanen, S. Nummelin, J. Ropponen, "Self-Assembly of Janus Dendrimers into Uniform Dendrimersomes and other Complex Architectures," *Science.*, vol. 328, no. May, pp. 1009–1015, 2010.
- [45] M. Peterca, V. Percec, P. Leowanawat, A. Bertin, "Predicting the size and properties of dendrimersomes from the lamellar structure of their amphiphilic janus dendrimers," *J. Am. Chem. Soc.*, vol. 133, no. 50, pp. 20507–20520, 2011, doi: 10.1021/ja208762u.
- [46] S. Zhang, H.-J. Sun, A. D. Hughes, R.-O. Moussodia, A. Bertin, Y. Chen, D. J. Pochan, P. A. Heiney, M. L. Klein, V. Percec, "Self-assembly of amphiphilic Janus dendrimers into uniform onion-like dendrimersomes with predictable size and number of bilayers," *Proc. Natl. Acad. Sci. U. S. A.*, vol. 111, no. 25, pp. 9058–9063, 2014, doi: 10.1073/pnas.1402858111.
- [47] V. Percec, P. Leowanawat, H.-J. Sun, O. Kulikov, C. D. Nusbaum, T. M. Tran, A. Bertin, D. A. Wilson, M. Peterca, S. Zhang, N. P. Kamat, K. Vargo, D. Moock, E. D. Johnston, D. A. Hammer, D. J. Pochan, Y. Chen, Y. M. Chabre, T. C. Shiao, M. Bergeron-Brlek, S. André, R. Roy, H.-J. Gabius, P. A. Heiney, "Modular synthesis of amphiphilic Janus glycodendrimers and their self-assembly into glycodendrimersomes and other complex architectures with bioactivity to biomedically relevant lectins," *J. Am. Chem. Soc.*, vol. 135, no. 24, pp. 9055–9077, 2013, doi: 10.1021/ja403323y.
- [48] A. P. Dias, S. da Silva Santos, J. V. da Silva, R. Parise-Filhoa, E. I. Ferreira, O. El Seoud, J. Giaroll, "Dendrimers in the context of nanomedicine," *Int. J. Pharm.*, vol. 573, no. November 2019, 2020, doi: 10.1016/j.ijpharm.2019.118814.
- [49] M. T. McMahon, J. W. M. Bulte, "Two decades of dendrimers as versatile MRI agents: a tale with and without metals," *Wiley Interdiscip. Rev. Nanomedicine Nanobiotechnology*, vol. 10, no. 3, pp. 1–17, 2018, doi: 10.1002/wnan.1496.
- [50] D. Huang, D. Wu, "Biodegradable dendrimers for drug delivery," *Mater. Sci. Eng. C*, vol. 90, no. March, pp. 713–727, 2018, doi: 10.1016/j.msec.2018.03.002.
- [51] A. Carlmark, E. Malmström, M. Malkoch, "Dendritic architectures based on bis-MPA: Functional polymeric scaffolds for application-driven research," *Chem. Soc. Rev.*, vol. 42, no. 13, pp. 5858–5879, 2013, doi: 10.1039/c3cs60101c.
- [52] R. d'Arcy, J. Burke, N. Tirelli, "Branched polyesters: Preparative strategies and applications," *Adv. Drug Deliv. Rev.*, vol. 107, pp. 60–81, 2016, doi: 10.1016/j.addr.2016.05.005.
- [53] S. García-Gallego, A. M. Nyström, M. Malkoch, "Chemistry of multifunctional polymers based on bis-MPA and their cutting-edge applications," *Prog. Polym. Sci.*, vol. 48, pp. 85–110, 2015, doi: 10.1016/j.progpolymsci.2015.04.006.
- [54] J.-d'A. K. Twibanire, T. B. Grindley, "Polyester dendrimers," *Polymers*, vol. 4, no. 1, pp. 794–879, 2012, doi: 10.3390/polym4010794.
- [55] J. Zhao, G. Weng, J. Li, J. Zhu, J. Zhao, "Polyester-based nanoparticles for nucleic acid delivery," *Mater. Sci. Eng. C*, vol. 92, no. November 2017, pp. 983–994, 2018, doi: 10.1016/j.msec.2018.07.027.
- [56] M. P. Krafft, "Fluorocarbons and fluorinated amphiphiles in drug delivery and biomedical research," *Adv. Drug*

- Deliv. Rev.*, vol. 47, no. 2–3, pp. 209–228, 2001, doi: 10.1016/S0169-409X(01)00107-7.
- [57] D. O’hagan, “Understanding organofluorine chemistry. An introduction to the C–F bond,” *Chem. Soc. Rev.*, vol. 37, no. 2, pp. 308–319, 2008, doi: 10.1039/b711844a.
- [58] D. A. Tomalia, “Supramolecular chemistry: Fluorine makes a difference,” *Nat. Mater.*, vol. 2, no. 11, pp. 711–712, 2003, doi: 10.1038/nmat1004.
- [59] A. M. Caminade, C. O. Turrin, P. Sutra, J. P. Majoral, “Fluorinated dendrimers,” *Curr. Opin. Colloid Interface Sci.*, vol. 8, no. 3, pp. 282–295, 2003, doi: 10.1016/S1359-0294(03)00051-7.
- [60] S. Hernández-Ainsa, J. Barberá, “Fluorinated liquid crystalline dendrimers,” *J. Fluor. Chem.*, vol. 177, pp. 37–45, 2015, doi: 10.1016/j.jfluchem.2015.02.018.
- [61] M. Suman Chowdhury, W. Zheng, S. Kumari, J. H. Pradip Dey, D. A. Weitz, R. Haag, “Dendronized fluorosurfactant for highly stable water-in-fluorinated oil emulsions with minimal inter-droplet transfer of small molecules,” *Nat. Commun.*, vol. 10, no. 1, 2019, doi: 10.1038/s41467-019-12462-5.
- [62] M. Khayet, C. García-Payo, T. Matsuura, “Superhydrophobic nanofibers electrospun by surface segregating fluorinated amphiphilic additive for membrane distillation,” *J. Memb. Sci.*, vol. 588, no. April, 2019, doi: 10.1016/j.memsci.2019.117215.
- [63] P. Wu, X. Luo, H. Wu, Q. Zhang, Y. Dai, M. Sun, “Efficient and targeted chemo-gene delivery with self-assembled fluoro-nanoparticles for liver fibrosis therapy and recurrence,” *Biomaterials*, vol. 261, pp. 120311–120323, 2020, doi: 10.1016/j.biomaterials.2020.120311.
- [64] M. Wang, H. Xue, M. Gao, Q. Wang, H. Yang, “Synthetic fluorinated polyamides as efficient gene vectors,” *J. Biomed. Mater. Res. - Part B Appl. Biomater.*, vol. 107, no. 6, pp. 2132–2139, 2019, doi: 10.1002/jbm.b.34307.
- [65] M. Wang, Y. Cheng, “The effect of fluorination on the transfection efficacy of surface-engineered dendrimers,” *Biomaterials*, vol. 35, no. 24, pp. 6603–6613, 2014, doi: 10.1016/j.biomaterials.2014.04.065.
- [66] G. Chen, Y. Wang, A. Ullah, Y. Huai, Y. Xu, “The effects of fluoroalkyl chain length and density on siRNA delivery of bioreducible poly(amido amine)s,” *Eur. J. Pharm. Sci.*, vol. 152, no. April, pp. 105433–105440, 2020, doi: 10.1016/j.ejps.2020.105433.
- [67] H. Wang, J. Hu, X. Cai, J. Xiao, Y. Cheng, “Self-assembled fluorodendrimers in the co-delivery of fluorinated drugs and therapeutic genes,” *Polym. Chem.*, vol. 7, no. 13, pp. 2319–2322, 2016, doi: 10.1039/c6py00153j.
- [68] C. Chen, W. Law, C. Chu, N. Chen, L. Lo, “Biodegradable Polymers for Gene-Delivery Applications,” *Int. J. Nanomedicine*, vol. 15, pp. 2131–2150, 2020, doi: <http://doi.org/10.2147/IJN.S222419>.
- [69] R. Bholakant, H. Qian, J. Zhang, X. Huang, D. Huang, J. Feijen, Y. Zhong, W. Chen, “Recent Advances of Polycationic siRNA Vectors for Cancer Therapy,” *Biomacromolecules*, vol. 21, no. 8, pp. 2966–2982, 2020, doi: 10.1021/acs.biomac.0c00438.
- [70] N. Hosseinahli, M. Aghapour, P. H. G. Duijf, B. Baradaran, “Treating cancer with microRNA replacement therapy: A literature review,” *J. Cell. Physiol.*, vol. 233, no. 8, pp. 5574–5588, 2018, doi: 10.1002/jcp.26514.
- [71] Y. Jiao, Z. L. Xia, L. J. Ze, H. Jing, B. Xin, S. Fu, “Research Progress of nucleic acid delivery vectors for gene therapy,” *Biomed. Microdevices*, vol. 22, no. 1, pp. 16–26, 2020, doi: 10.1007/s10544-020-0469-7.
- [72] A. Gigante, M. Li, S. Junghänel, C. Hirschhäuser, S. Knauer, C. Schmuck, “Non-viral transfection vectors: Are hybrid materials the way forward?,” *Medchemcomm*, vol. 10, no. 10, pp. 1692–1718, 2019, doi: 10.1039/c9md00275h.
- [73] W. F. Lai, W. T. Wong, “Design of Polymeric Gene Carriers for Effective Intracellular Delivery,” *Trends Biotechnol.*, vol. 36, no. 7, pp. 713–728, 2018, doi: 10.1016/j.tibtech.2018.02.006.
- [74] H. Yin, R. L. Kanasty, A. A. Eltoukhy, A. J. Vegas, J. R. Dorkin, D. G. Anderson, “Non-viral vectors for gene-based therapy,” *Nat. Rev. Genet.*, vol. 15, no. 8, pp. 541–555, 2014, doi: 10.1038/nrg3763.
- [75] J. Chen, K. Wang, J. Wu, H. Tian, X. Chen, “Polycations for Gene Delivery: Dilemmas and Solutions,” *Bioconjug. Chem.*, vol. 30, pp. 338–349, 2018, doi: 10.1021/acs.bioconjchem.8b00688.
- [76] J. Chen, K. Wang, J. Wu, H. Tian, X. Chen, “Polycations for Gene Delivery: Dilemmas and Solutions,” *Bioconjug. Chem.*, vol. 30, pp. 338–349, 2018, doi: 10.1021/acs.bioconjchem.8b00688.

- [77] H. Wang, Y. Wang, Y. Wang, J. Hu, T. Li, H. Liu, Q. Zhang, Y. Cheng, "Self-Assembled Fluorodendrimers Combine the Features of Lipid and Polymeric Vectors in Gene Delivery," *Angew. Chemie - Int. Ed.*, vol. 54, no. 40, pp. 11647–11651, 2015, doi: 10.1002/anie.201501461.
- [78] J. Hu, K. Hu, Y. Cheng, "Tailoring the dendrimer core for efficient gene delivery," *Acta Biomater.*, vol. 35, pp. 1–11, 2016, doi: 10.1016/j.actbio.2016.02.031.
- [79] M. Wang, H. Liu, L. Li, Y. Cheng, "A fluorinated dendrimer achieves excellent gene transfection efficacy at extremely low nitrogen to phosphorus ratios," *Nat. Commun.*, vol. 5, pp. 3053–3061, 2014, doi: 10.1038/ncomms4053.
- [80] Y. Wang, M. Wang, H. Chen, H. Liu, Q. Zhang, Y. Cheng, "Fluorinated dendrimer for TRAIL gene therapy in cancer treatment," *J. Mater. Chem. B*, vol. 4, no. 7, pp. 1354–1360, 2016, doi: 10.1039/c5tb02712h.
- [81] H. Wang, J. Hu, X. Cai, J. Xiao, Y. Cheng, "Self-assembled fluorodendrimers in the co-delivery of fluorinated drugs and therapeutic genes," *Polym. Chem.*, vol. 7, no. 13, pp. 2319–2322, 2016, doi: 10.1039/c6py00153j.
- [82] B. He, Y. Wang, N. Shao, H. Chang, Y. Cheng, "Polymers modified with double-tailed fluorous compounds for efficient DNA and siRNA delivery," *Acta Biomater.*, vol. 22, pp. 111–119, 2015, doi: 10.1016/j.actbio.2015.04.037.
- [83] H. Wang, S. Ding, Z. Zhang, L. Wang, Y. You, "Cationic micelle: A promising nanocarrier for gene delivery with high transfection efficiency," *J. Gene Med.*, vol. 21, no. 7, 2019, doi: 10.1002/jgm.3101.
- [84] M. A. Kostianen, J. G. Hardy, D. K. Smith, "High-affinity multivalent DNA binding by using low-molecular-weight dendrons," *Angew. Chemie - Int. Ed.*, vol. 44, no. 17, pp. 2556–2559, 2005, doi: 10.1002/anie.200500066.
- [85] S. P. Jones, N. P. Gabrielson, D. W. Pack, D. K. Smith, "Synergistic effects in gene delivery - A structure-activity approach to the optimisation of hybrid dendritic-lipidic transfection agents," *Chem. Commun.*, no. 39, pp. 4700–4702, 2008, doi: 10.1039/b811852c.
- [86] A. Tschiche, A. M. Staedtler, S. Malhotra, H. Bauer, C. Bottcher, S. Sharbati, M. Calderon, M. Koch, T. M. Zollner, A. Barnard, D. K. Smith, R. Einspanier, N. Schmidt, R. Haag, "Polyglycerol-based amphiphilic dendrons as potential siRNA carriers for in vivo applications," *J. Mater. Chem. B*, vol. 2, no. 15, pp. 2153–2167, 2014, doi: 10.1039/c3tb21364a.
- [87] G. Chen, Y. Xu, P. Wu, K. Wang, "Self-assembled PEI nanomicelles with a fluorinated core for improved siRNA delivery," *J. Drug Deliv. Sci. Technol.*, vol. 55, no. August 2019, p. 101403, 2020, doi: 10.1016/j.jddst.2019.101403.
- [88] L. H. Wang, D. C. Wu, H. X. Xu, Y. Z. You, "High DNA-Binding Affinity and Gene-Transfection Efficacy of Bioreducible Cationic Nanomicelles with a Fluorinated Core," *Angew. Chemie - Int. Ed.*, vol. 55, no. 2, pp. 755–759, 2016, doi: 10.1002/anie.201508695.
- [89] V. P. B. Grover, J. M. Tognarelli, M. M. E. Crossey, I. J. Cox, S. D. Taylor-Robinson, M. J. W. McPhail, "Magnetic Resonance Imaging: Principles and Techniques: Lessons for Clinicians," *J. Clin. Exp. Hepatol.*, vol. 5, no. 3, pp. 246–255, 2015, doi: 10.1016/j.jceh.2015.08.001.
- [90] S. Currie, N. Hoggard, I. J. Craven, M. Hadjivassiliou, I. D. Wilkinson, "Understanding MRI: Basic MR physics for physicians," *Postgrad. Med. J.*, vol. 89, no. 1050, pp. 209–223, 2013, doi: 10.1136/postgradmedj-2012-131342.
- [91] T. Kagawa, S. Yoshida, T. Shiraishi, M. Hashimoto, D. Inadomi, M. Sato, T. Tsuzuki, K. Miwa, K. Yuasa, "Basic principles of magnetic resonance imaging for beginner oral and maxillofacial radiologists," *Oral Radiol.*, vol. 33, no. 2, pp. 92–100, 2017, doi: 10.1007/s11282-017-0274-z.
- [92] D. Bartusik, D. Aebisher, "19F applications in drug development and imaging-a review," *Biomed. Pharmacother.*, vol. 68, no. 6, pp. 813–817, 2014, doi: 10.1016/j.biopha.2014.07.012.
- [93] I. Tirota, V. Dichiarante, C. Pigliacelli, G. Cavallo, G. Terraneo, F. Baldelli Bombelli, P. Metrangolo, G. Resnati, "19F magnetic resonance imaging (MRI): From design of materials to clinical applications," *Chem. Rev.*, vol. 115, no. 2, 2015, doi: 10.1021/cr500286d.
- [94] M. H. Cho, S. H. Shin, S. H. Park, D. K. Kadayakkara, D. Kim, Y. Choi, "Targeted, Stimuli-Responsive, and Theranostic 19F Magnetic Resonance Imaging Probes," *Bioconjug. Chem.*, vol. 30, no. 10, pp. 2502–2518, 2019, doi: 10.1021/acs.bioconjchem.9b00582.

- [95] X. Staal, O. Koshkina, M. Srinivas, "In vivo 19-fluorine magnetic resonance imaging," in *Fluorine in Life Sciences: Pharmaceuticals, Medicinal Diagnostics, and Agrochemicals Progress in Fluorine Science Series*, Elsevier, 2018, pp. 397–424. doi: 10.1016/B978-0-12-812733-9.00011-8.
- [96] A. H. J. Staal, K. Becker, O. Tagit, N. K. van Riessen, O. Koshkina, A. Veltien, P. Bouvain, K. R. G. Cortenbach, T. Scheenen, U. Flogel, S. Temme, M. Srinivas, "In vivo clearance of 19F MRI imaging nanocarriers is strongly influenced by nanoparticle ultrastructure," *Biomaterials*, vol. 261, 2020, doi: 10.1016/j.biomaterials.2020.120307.
- [97] I. Tirotta, A. Mastropietro, C. Cordiglieri, L. Gazzera, F. Baggi, G. Baselli, M. G. Bruzzone, I. Zucca, G. Cavallo, G. Terraneo, F. Baldelli Bombelli, P. Metrangolo, G. Resnati, "A Superfluorinated Molecular Probe for Highly Sensitive in Vivo 19 F - MRI," *J. Am. Chem. Soc.*, vol. 136, pp. 8–11, 2014.
- [98] O. Koshkina, P. B. White, A. H. J. Staal, R. Schweins, E. Swider, I. Tirotta, P. Tinnemans, R. Fokkink, A. Veltien, N. K. van Riessen, E. R. H. van Eck, A. Heerschap, P. Metrangolo, F. Baldelli Bombelli, M. Srinivas, "Nanoparticles for " two color " 19 F magnetic resonance imaging: Towards combined imaging of biodistribution and degradation," *J. Colloid Interface Sci.*, vol. 565, pp. 278–287, 2020, doi: 10.1016/j.jcis.2019.12.083.
- [99] L. Jamgotchian, S. Vaillant, E. Selingue, A. Doerflinger, A. Belime, M. Vandamme, G. Pinna, W. Li Ling, E. Gravel, S. Mériaux, E. Doris, "Tumor-targeted super fluorinated micellar probe for sensitive in vivo 19 F-MRI," *Nanoscale*, vol. 13, pp. 2373–2377, 2021, doi: 10.1039/d0nr08200g.
- [100] V. Dichiarante, M. I. Martinez Espinoza, L. Gazzera, M. Vuckovac, M. Latikka, G. Cavallo, G. Raffaini, R. Oropesa-Nuñez, C. Canale, S. Dante, S. Marras, R. Carzino, M. Prato, R. H. A. Ras, P. Metrangolo, "A Short-Chain Multibranch Perfluoroalkyl Thiol for More Sustainable Hydrophobic Coatings," *ACS Sustain. Chem. Eng.*, vol. 6, no. 8, pp. 9734–9743, 2018, doi: 10.1021/acssuschemeng.8b00777.
- [101] Z. Jiang, Y. B. Yu, "The design and synthesis of highly branched and spherically symmetric fluorinated oils and amphiles," *Tetrahedron*, vol. 63, pp. 3982–3988, 2007, doi: 10.1016/j.tet.2007.03.004.
- [102] G. Pozzi, S. Quici, M. C. Raffo, C. A. Bignozzi, S. Caramori, M. Orlandi, "Fluorous Molecules for Dye-Sensitized Solar Cells : Synthesis and Photoelectrochemistry of Unsymmetrical Zinc Phthalocyanine Sensitizers with Bulky Fluorophilic Donor Groups," *J. Phys. Chem. C*, vol. 115, pp. 3777–3788, 2011.
- [103] S. Decato, T. Bemis, E. Madsen, S. Mecozzi, "Polymer Chemistry and their potential application in hydrophobic," *Polym. Chem.*, vol. 5, pp. 6461–6471, 2014, doi: 10.1039/c4py00882k.
- [104] Z. X. Jiang, X. Liu, E. K. Jeong, Y. B. Yu, "Symmetry-Guided Design and Fluorous Synthesis of a Stable and Rapidly Excreted Imaging Tracer for 19F MRI," *Angew. Chemie - Int. Ed.*, vol. 48, no. 26, pp. 4755–4758, 2009, doi: 10.1002/anie.200901005.
- [105] M. B. Taraban, L. Yu, Y. Feng, E. V. Jouravleva, M. A. Anisimov, "Conformational transition of a non-associative fluorinated amphiphile in aqueous solution †," *RSC Adv.*, vol. 4, pp. 54565–54575, 2014, doi: 10.1039/c4ra09752a.
- [106] M. B. Taraban, D. J. Deredge, M. E. Smith, K. T. Briggs, Y. Li, Z.-X. Jiang, P. L. Wintrode, Y. Bruce Yu, "Monitoring dendrimer conformational transition using 19F and 1H2O NMR," *Magn Reson Chem.*, vol. 57, pp. 861–872, 2019, doi: 10.1002/mrc.4849.
- [107] A. M. Huynh, A. Miller, S. M. Kessler, S. Henrikus, C. Hoffmann, A. K. Kiemer, A. Bicker, G. Jung, "Small BODIPY Probes for Combined Dual 19 F MRI and Fluorescence Imaging," *ChemMedChem*, vol. 11, pp. 1568–1575, 2016, doi: 10.1002/cmdc.201600120.
- [108] H. Shi, B. Lai, S. Chen, X. Zhou, J. Nie, J. Ma, "Facile Synthesis of Novel Perfluorocarbon-Modulated 4-Anilinoquinazoline Analogues," *Chin. J. Chem.*, vol. 35, pp. 1693–1700, 2017, doi: 10.1002/cjoc.201700240.
- [109] V. Dichiarante, I. Tirotta, L. Catalano, G. Terraneo, G. Raffaini, M. R. Chierotti, R. Gobetto, F. Baldelli Bombelli, P. Metrangolo, "Superfluorinated and NIR-luminescent gold nanoclusters," *Chem. Commun.*, vol. 53, no. 3, pp. 621–624, 2017, doi: 10.1039/C6CC09324H.
- [110] Q. Peng, Y. Li, S. Bo, Y. Yuan, Z. Yang, S. Chen, X. Zhou, Z.-X. Jiang, "Paramagnetic nanoemulsions with unified signals for sensitive 19 F MRI cell tracking," *Chem. Commun.*, vol. 54, pp. 6000–6003, 2018, doi: 10.1039/c8cc02938e.
- [111] S. Bo, Y. Yuan, Y. Chen, Z. Yang, S. Chen, X. Zhou, Z.-X. Jiang, "In vivo drug tracking with F MRI at

- therapeutic,” *Chem. Commun.*, vol. 54, pp. 3875–3878, 2018, doi: 10.1039/c7cc09898g.
- [112] Z. Y. H. Zhang, S. Bo, K. Zeng, J. Wang, Y. Li, S. Chen, Z.-X. Jiang, X. Zhou, “Fluorinated porphyrin-based theranostics for dual imaging and chemo-photodynamic therapy,” *J. Mater. Chem. B*, vol. 8, pp. 4469–4474, 2020, doi: 10.1039/d0tb00083c.
- [113] M. I. Martínez Espinoza, L. Sori, A. Pizzi, G. Terraneo, I. Moggio, E. Arias, G. Pozzi, S. Orlandi, V. Dichiarante, P. Metrangolo, M. Cavazzini, F. Baldelli Bombelli “BODIPY Dyes Bearing Multibranched Fluorinated Chains: Synthesis, Structural, and Spectroscopic Studies,” *Chem. - A Eur. J.*, vol. 25, no. 38, pp. 9078–9087, 2019, doi: 10.1002/chem.201901259.
- [114] A. A. Bogdanov, S. Thayumanavan, “F MRI of Polymer Nanogels Aided by Improved Segmental Mobility of Embedded Fluorine Moieties,” *Biomacromolecules*, vol. 20, pp. 790–800, 2019, doi: 10.1021/acs.biomac.8b01383.
- [115] Y. Zhang, S. Bo, T. Feng, X. Qin, Y. Wan, S. Jiang, C. Li, J. Lin, T. Wang, X. Zhou, Z.-X. Jiang, P. Huang, “A Versatile Theranostic Nanoemulsion for Architecture- Dependent Multimodal Imaging and Dually Augmented Photodynamic Therapy,” *Adv. Mater.*, vol. 1806444, pp. 1–10, 2019, doi: 10.1002/adma.201806444.
- [116] M. S. Singh, S. Chowdhury, S. Koley, “Advances of azide-alkyne cycloaddition-click chemistry over the recent decade,” *Tetrahedron*, vol. 72, no. 35, pp. 5257–5283, 2016, doi: 10.1016/j.tet.2016.07.044.
- [117] X. Yue, M. B. Taraban, L. L. Hyland, Y. B. Yu, “Avoiding steric congestion in dendrimer growth through proportionate branching: A twist on da Vincis rule of tree branching,” *J. Org. Chem.*, vol. 77, no. 20, pp. 8879–8887, 2012, doi: 10.1021/jo301718y.
- [118] S. Taabache, A. Bertin, “Vesicles from amphiphilic dumbbells and janus dendrimers: Bioinspired self-assembled structures for biomedical applications,” *Polymers (Basel)*, vol. 9, no. 7, 2017, doi: 10.3390/polym9070280.
- [119] H. Ihre, A. Hult, J. M. J. Fréchet, I. Gitsov, “Double-stage convergent approach for the synthesis of functionalized dendritic aliphatic polyesters based on 2,2-bis(hydroxymethyl)propionic acid,” *Macromolecules*, vol. 31, no. 13, pp. 4061–4068, 1998, doi: 10.1021/ma9718762.
- [120] E. Fedeli, A. Lancelot, J. L. Serrano, P. Calvo, T. Sierra, “Self-assembling amphiphilic Janus dendrimers: Mesomorphic properties and aggregation in water,” *New J. Chem.*, vol. 39, no. 3, pp. 1960–1967, 2015, doi: 10.1039/c4nj02071e.
- [121] E. Fedeli, A. Lancelot, J. M. Dominguez, J. L. Serrano, P. Calvo, T. Sierra, “Self-assembling hybrid linear-dendritic block copolymers: The design of nano-carriers for lipophilic antitumoral drugs,” *Nanomaterials*, vol. 9, no. 2, 2019, doi: 10.3390/nano9020161.
- [122] B. Neises, W. Steglich, “Simple Method for the Esterification of Carboxylic Acids,” *Angew. Chemie Int. Ed. English*, vol. 17, no. 7, pp. 522–524, Jul. 1978, doi: 10.1002/anie.197805221.
- [123] J. Ropponen, K. Nättinen, M. Lahtinen, K. Rissanen, “Synthesis, thermal properties and X-ray structural study of weak C-H...O=C hydrogen bonding in aliphatic polyester dendrimers,” *CrystEngComm*, vol. 6, no. 91, pp. 559–566, 2004, doi: 10.1039/b413799j.
- [124] D. Ranganathan, S. Kurur, R. Gilardi, I. L. Karle, “Design and synthesis of AB₃-type (A = 1,3,5-benzenetricarbonyl unit; B = glu diOME or glu₇ octa OMe) peptide dendrimers: Crystal structure of the first generation,” *Biopolymers*, vol. 54, no. 4, pp. 289–295, 2000, doi: 10.1002/1097-0282(20001005)54:4<289::AID-BIP60>3.0.CO;2-7.
- [125] E. Núñez, C. Ferrando, E. Malmström, H. Claesson, P. E. Werner, U. W. Gedde, “Crystal structure, melting behaviour and equilibrium melting point of star polyesters with crystallisable poly(ϵ -caprolactone) arms,” *Polymer (Guildf)*, vol. 45, no. 15, pp. 5251–5263, 2004, doi: 10.1016/j.polymer.2004.05.047.
- [126] C. Tschierske, “Development of Structural Complexity by Liquid- crystal self-assembly,” *Angew. Chem. Int. Ed.*, vol. 52, pp. 8828–8878, 2013, doi: 10.1002/anie.201300872.
- [127] X. Zeng, S. Poppe, A. Lehmann, M. Prehm, C. Chen, F. Liu, H. Lu, G. Ungar, C. Tschierske, “Liquid Crystals A Self-Assembled Bicontinuous Cubic Phase with a Single-Diamond Network,” *Angew. Chem. Int. Ed.*, vol. 58, pp. 7375–7379, 2019, doi: 10.1002/anie.201902677.
- [128] S. Poppe, C. Chen, F. Liu, “A skeletal double gyroid formed by single coaxial bundles of catechol based bolapolyphiles †,” *Chem. Commun.*, vol. 54, pp. 11196–11199, 2018, doi: 10.1039/c8cc06956e.

- [129] Y. Corvis, P. Négrier, J. Soulestin, P. Espeau, “New Melting Data of the Two Polymorphs of Prednisolone,” *J. Phys. Chem. B*, vol. 120, no. 41, pp. 10839–10843, 2016, doi: 10.1021/acs.jpcc.6b07349.
- [130] J. Zhao, Y. Sun, Y. Men, “Melt temperature and initial polymorphs dependencies of polymorphs selection during subsequent crystallization in propylene-ethylene random copolymer,” *Ind. Eng. Chem. Res.*, vol. 56, no. 1, pp. 198–205, 2017, doi: 10.1021/acs.iecr.6b04087.
- [131] T. Tuuttila, M. Lahtinen, N. Kuuloja, J. Huuskonen, K. Rissanen, “Synthesis and thermal behavior of Janus dendrimers, part 1,” *Thermochim. Acta*, vol. 497, no. 1–2, pp. 101–108, 2010, doi: 10.1016/j.tca.2009.08.018.
- [132] S. Ogawa, K. Asakura, S. Osanai, “Thermotropic and glass transition behaviors of n-alkyl β -d-glucosides,” *RSC Adv.*, vol. 3, no. 44, pp. 21439–21446, 2013, doi: 10.1039/c3ra43187h.
- [133] A. Concellón, M. Bucos, J. L. Serrano, P. Romero, M. Marcos, “Supramolecular liquid crystalline dendrimers with a porphyrin core and functional carboxylic acid dendrons,” *RSC Adv.*, vol. 6, no. 69, pp. 65179–65185, 2016, doi: 10.1039/c6ra13604d.
- [134] X. Liu, Y. Yuan, S. Bo, Y. Li, Z. Yang, X. Zhou, S. Chen, Z.-X. Jiang, “Monitoring Fluorinated Dendrimer-Based Self-Assembled Drug-Delivery Systems with ^{19}F Magnetic Resonance,” *European J. Org. Chem.*, vol. 2017, no. 30, pp. 4461–4468, 2017, doi: 10.1002/ejoc.201700566.
- [135] K. Matsuoka, Y. Moroi, “Micellization of fluorinated amphiphiles,” *Curr. Opin. Colloid Interface Sci.*, vol. 8, no. 3, pp. 227–235, 2003, doi: 10.1016/S1359-0294(03)00056-6.
- [136] J. Stetefeld, S. A. McKenna, T. R. Patel, “Dynamic light scattering: a practical guide and applications in biomedical sciences,” *Biophys. Rev.*, vol. 8, pp. 409–427, 2016, doi: 10.1007/s12551-016-0218-6.
- [137] A. Manfredi, N. Mauro, A. Terenzi, J. Alongi, F. Lazzari, F. Ganazzoli, G. Raffaini, E. Ranucci, P. Ferruti, “Self-Ordering Secondary Structure of d - And l -Arginine-Derived Polyamidoamino Acids,” *ACS Macro Lett.*, vol. 6, no. 9, pp. 987–991, 2017, doi: 10.1021/acsmacrolett.7b00492.
- [138] J. Movellan, R. González-Pastor, P. Martín-Duque, T. Sierra, J. M. De La Fuente, J. L. Serrano, “New Ionic bis-MPA and PAMAM Dendrimers: A Study of Their Biocompatibility and DNA-Complexation,” *Macromol. Biosci.*, vol. 15, no. 5, pp. 657–667, 2015, doi: 10.1002/mabi.201400422.
- [139] P. Stenström, D. Manzanares, Y. Zhang, V. Ceña, M. Malkoch, “Evaluation of amino-functional polyester dendrimers based on Bis-MPA as nonviral vectors for siRNA delivery,” *Molecules*, vol. 23, pp. 2028–2043, 2018, doi: 10.3390/molecules23082028.
- [140] N. Feliu, M. V. Walter, M. I. Montañez, A. Kunzmann, A. Hult, A. Nyström, M. Malkoch, B. Fadeel, “Stability and biocompatibility of a library of polyester dendrimers in comparison to polyamidoamine dendrimers,” *Biomaterials*, vol. 33, no. 7, pp. 1970–1981, 2012, doi: 10.1016/j.biomaterials.2011.11.054.
- [141] P. Wu, X. Luo, H. Wu, Q. Zhang, K. Wang, M. Sun, D. Oupicky, “Combined Hydrophobization of Polyethylenimine with Cholesterol and Perfluorobutyrate Improves siRNA Delivery,” *Bioconjug. Chem.*, vol. 31, pp. 698–707, 2020, doi: 10.1021/acs.bioconjchem.9b00834.
- [142] S. Wang, J. Xing, B. Xiong, H. Han, M. Hu, Q. Li, “Fluoropolymer-Mediated Intracellular Delivery of miR-23b for the Osteocyte Differentiation in Osteoblasts,” *Macromol. Biosci.*, pp. 2100024–2100032, 2021, doi: 10.1002/mabi.202100024.
- [143] M. Wang, Y. Cheng, “Structure-activity relationships of fluorinated dendrimers in DNA and siRNA delivery,” *Acta Biomater.*, vol. 46, pp. 204–210, 2016, doi: 10.1016/j.actbio.2016.09.023.
- [144] X. Liu, Y. Wang, C. Chen, A. Tintaru, Y. Cao, J. Liu, F. Ziarelli, J. Tang, H. Guo, R. Rosas, S. Giorgio, L. Charles, P. Rocchi, L. Peng, “A Fluorinated Bola-Amphiphilic Dendrimer for On-Demand Delivery of siRNA, via Specific Response to Reactive Oxygen Species,” *Adv. Funct. Mater.*, vol. 26, no. 47, pp. 8594–8603, 2016, doi: 10.1002/adfm.201604192.
- [145] H. Liu, Y. Wang, M. Wang, J. Xiao, Y. Cheng, “Fluorinated poly(propylenimine) dendrimers as gene vectors,” *Biomaterials*, vol. 35, no. 20, pp. 5407–5413, 2014, doi: 10.1016/j.biomaterials.2014.03.040.
- [146] X. Cai, R. Jin, J. Wang, D. Yue, Q. Jiang, Y. Wu, Z. Gu, “Bioreducible Fluorinated Peptide Dendrimers Capable of Circumventing Various Physiological Barriers for Highly Efficient and Safe Gene Delivery,” *ACS Appl. Mater. Interfaces*, vol. 8, no. 9, pp. 5821–5832, 2016, doi: 10.1021/acsami.5b11545.
- [147] X. Cai, H. Zhu, Y. Zhang, Z. Gu, “Highly Efficient and Safe Delivery of VEGF siRNA by Bioreducible

- Fluorinated Peptide Dendrimers for Cancer Therapy,” *ACS Appl. Mater. Interfaces*, vol. 9, no. 11, pp. 9402–9415, 2017, doi: 10.1021/acsami.6b16689.
- [148] A. Barnard, P. Posocco, S. Pricl, M. Calderon, R. Haag, M. E. Hwang, V. W. T. Shum, D. W. Pack, D. K. Smith, “Degradable Self-Assembling Dendrons for Gene Delivery: Experimental and Theoretical Insights into the Barriers to Cellular Uptake,” *J. Am. Chem. Soc.*, vol. 133, pp. 20288–20300, 2011, doi: 10.1021/ja2070736.
- [149] Y. Zhang, J. Chen, C. Xiao, M. Li, H. Tian, X. Chen, “Cationic dendron-bearing lipids: Investigating structure-activity relationships for small interfering RNA delivery,” *Biomacromolecules*, vol. 14, no. 12, pp. 4289–4300, 2013, doi: 10.1021/bm4011563.
- [150] J. Chen, A. Ellert-Miklaszewska, S. Garofalo, A. K. Dey, J. Tang, Y. Jiang, F. Clément, P. N. Marche, X. Liu, B. Kaminska, A. Santoni, C. Limatola, J. J. Rossi, J. Zhou, L. Peng, “Synthesis and use of an amphiphilic dendrimer for siRNA delivery into primary immune cells,” *Nat. Protoc.*, vol. 16, no. 1, pp. 327–351, 2021, doi: 10.1038/s41596-020-00418-9.
- [151] S. Malhotra, H. Bauer, A. Tschiche, A. M. Staedtler, A. Mohr, M. Calderón, V. S. Parmar, L. Hoeke, S. Sharbati, R. Einspanier, R. Haag, “Glycine-terminated dendritic amphiphiles for nonviral gene delivery,” *Biomacromolecules*, vol. 13, no. 10, pp. 3087–3098, 2012, doi: 10.1021/bm300892v.
- [152] Z. Yuan, X. Guo, M. Wei, Y. Xu, Z. Fang, Y. Feng, W.-E. Yuan, “Novel fluorinated polycationic delivery of anti-VEGF siRNA for tumor therapy,” *NPG Asia Mater.*, vol. 12, no. 1, 2020, doi: 10.1038/s41427-020-0216-9.
- [153] P. Stenström, E. Hjorth, Y. Zhang, O. C. J. Andrén, S. Guette-Marquet, M. Schultzberg, M. Malkoch, “Synthesis and in Vitro Evaluation of Monodisperse Amino-Functional Polyester Dendrimers with Rapid Degradability and Antibacterial Properties,” *Biomacromolecules*, vol. 18, pp. 4323–4330, 2017, doi: 10.1021/acs.biomac.7b01364.
- [154] N. Scholz, T. Behnke, U. Resch-Genger, “Determination of the Critical Micelle Concentration of Neutral and Ionic Surfactants with Fluorometry, Conductometry, and Surface Tension—A Method Comparison,” *J. Fluoresc.*, vol. 28, no. 1, pp. 465–476, 2018, doi: 10.1007/s10895-018-2209-4.
- [155] Ö. Topel, B. A. Çakir, L. Budama, N. Hoda, “Determination of critical micelle concentration of polybutadiene-block-poly(ethyleneoxide) diblock copolymer by fluorescence spectroscopy and dynamic light scattering,” *J. Mol. Liq.*, vol. 177, pp. 40–43, 2013, doi: 10.1016/j.molliq.2012.10.013.
- [156] S. Dong, X. Li, G. Xu, H. Hoffmann, “A cationic fluorocarbon surfactant DEFUMACl and its mixed systems with cationic surfactants: 19F NMR and surface tension study,” *J. Phys. Chem. B*, vol. 111, no. 21, pp. 5903–5910, 2007, doi: 10.1021/jp0705469.
- [157] H. Ivan, O. Reiko, “Gemini surfactants: studying micellisation by 1H and 19F NMR spectroscopy,” *Chem. Commun.*, no. 20, pp. 2025–2026, 1999.
- [158] X. Wang, J. Chen, D. Wang, S. Dong, J. Hao, H. Hoffmann, “Monitoring the different micelle species and the slow kinetics of tetraethylammonium perfluorooctane-sulfonate by 19F NMR spectroscopy,” *Adv. Colloid Interface Sci.*, vol. 246, no. May, pp. 153–164, 2017, doi: 10.1016/j.cis.2017.05.016.
- [159] S. Dong, G. Xu, H. Hoffmann, “Aggregation behavior of fluorocarbon and hydrocarbon cationic surfactant mixtures: A study of 1H NMR and 19F NMR,” *J. Phys. Chem. B*, vol. 112, no. 31, pp. 9371–9378, 2008, doi: 10.1021/jp801216e.
- [160] A. Piloni, R. Simonutti, M. H. Stenzel, “The effect of cationic groups on the stability of 19F MRI contrast agents in nanoparticles,” *J. Polym. Sci. Part A Polym. Chem.*, vol. 57, pp. 1994–2001, 2019, doi: 10.1002/pola.29387.
- [161] D. Jirak, A. Galisova, K. Kolouchova, D. Babuka, M. Hruby, “Fluorine polymer probes for magnetic resonance imaging: quo vadis?,” *Magn. Reson. Mater. Physics, Biol. Med.*, vol. 32, no. 1, pp. 173–185, 2019, doi: 10.1007/s10334-018-0724-6.
- [162] C. Zhang, S. S. Moonshi, Y. Han, S. Puttick, H. Peng, B. J. A. Magoling, J. C. Reid, S. Bernardi, D. J. Searles, P. Král, A. K. Whittaker, “PFPE-Based Polymeric 19F MRI Agents: A New Class of Contrast Agents with Outstanding Sensitivity,” *Macromolecules*, vol. 50, no. 15, pp. 5953–5963, 2017, doi: 10.1021/acs.macromol.7b01285.
- [163] W. Du, A. M. Nystrom, L. Zhang, K. T. Powell, Y. Li, C. Cheng, S. A. Wickline, K. L. Wooley, “Amphiphilic hyperbranched fluoropolymers as nanoscopic 19F magnetic resonance imaging agent assemblies,” *Biomacromolecules*, vol. 9, no. 10, pp. 2826–2833, 2008, doi: 10.1021/bm800595b.

- [164] D. Pezzoli, E. Giupponi, D. Mantovani, G. Candiani, "Size matters for in vitro gene delivery: Investigating the relationships among complexation protocol, transfection medium, size and sedimentation," *Sci. Rep.*, vol. 7, no. August 2016, pp. 1–11, 2017, doi: 10.1038/srep44134.
- [165] C. Malloggi, D. Pezzoli, L. Magagnin, L. De Nardo, D. Mantovani, E. Tallarita, G. Candiani, "Comparative evaluation and optimization of off-the-shelf cationic polymers for gene delivery purposes," *Polym. Chem.*, vol. 6, no. 35, pp. 6325–6339, 2015, doi: 10.1039/c5py00915d.
- [166] N. Bono, F. Ponti, D. Mantovani, G. Candiani, "Non-viral in vitro gene delivery: It is now time to set the bar!," *Pharmaceutics*, vol. 12, no. 2, 2020, doi: 10.3390/pharmaceutics12020183.
- [167] Polyplus, "Transfection protocol JetPEI," no. 103012, pp. 5–6, 2013.
- [168] S. Marcuzzo, D. Kapetis, R. Mantegazza, F. Baggi, S. Bonanno, C. Barzago, P. Cavalcante, N. Kerlero de Rosbo, P. Bernasconi, "Altered miRNA expression is associated with neuronal fate in G93A-SOD1 ependymal stem progenitor cells," *Exp. Neurol.*, vol. 253, pp. 91–101, 2014, doi: 10.1016/j.expneurol.2013.12.007.
- [169] L. K. Hamilton, M. K. V. Truong, M. R. Bednarczyk, A. Aumont, K. J. L. Fernandes, "Cellular organization of the central canal ependymal zone, a niche of latent neural stem cells in the adult mammalian spinal cord," *Neuroscience*, vol. 164, no. 3, pp. 1044–1056, 2009, doi: 10.1016/j.neuroscience.2009.09.006.
- [170] V. Moreno-Manzano, F. J. Rodriguez-Jimenez, M. Garcia-Rosello, S. Lainez, S. Erceg, M. T. Calvo, M. Ronaghi, M. Lloret, R. Planells-Cases, J. M. Sanchez-Puelles, M. Stojkovic, "Activated spinal cord ependymal stem cells rescue neurological function," *Stem Cells*, vol. 27, no. 3, pp. 733–743, 2009, doi: 10.1002/stem.24.
- [171] X. Wei, H. Li, J. Miao, B. Liu, Y. Zhan, D. Wu, Y. Zhang, L. Wang, Y. Fan, H. Gu, W. Wang, Z. Yuan, "MiR-9*- and miR-124a-mediated switching of chromatin remodelling complexes is altered in rat spina bifida aperta," *Neurochem. Res.*, vol. 38, no. 8, pp. 1605–1615, 2013, doi: 10.1007/s11064-013-1062-8.
- [172] K. Nakanishi, T. Nakasa, N. Tanaka, M. Ishikawa, K. Yamada, K. Yamasaki, N. Kamei, B. Izumi, N. Adachi, S. Miyaki, H. Asahara, M. Ochi, "Responses of microRNAs 124a and 223 following spinal cord injury in mice," *Spinal Cord*, vol. 48, no. 3, pp. 192–196, 2010, doi: 10.1038/sc.2009.89.
- [173] N. Bono, C. Pennetta, A. Sganappa, E. Giupponi, F. Sansone, A. Volonterio, G. Candiani, "Design and synthesis of biologically active cationic amphiphiles built on the calix[4]arene scaffold," *Int. J. Pharm.*, vol. 549, no. 1–2, pp. 436–445, 2018, doi: 10.1016/j.ijpharm.2018.08.020.
- [174] G. Cavallo, A. Abate, M. Rosati, G. P. Venuti, T. Pilati, G. Terraneo, G. Resnati, P. Metrangolo, "Tuning of Ionic Liquid Crystal Properties by Combining Halogen Bonding and Fluorous Effect," *Chempluschem*, vol. 86, no. 3, pp. 469–474, 2021, doi: 10.1002/cplu.202100046.
- [175] K. Goossens, K. Lava, C. W. Bielawski, K. Binnemans, "Ionic Liquid Crystals: Versatile Materials," *Chem. Rev.*, vol. 116, no. 8, pp. 4643–4807, 2016, doi: 10.1021/cr400334b.
- [176] K. Salikolimi, A. A. Sudhakar, Y. Ishida, "Functional Ionic Liquid Crystals," *Langmuir*, vol. 36, no. 40, pp. 11702–11731, 2020, doi: 10.1021/acs.langmuir.0c01935.
- [177] H. Wang, H. K. Bisoyi, A. M. Urbas, T. J. Bunning, Q. Li, "The Halogen Bond: An Emerging Supramolecular Tool in the Design of Functional Mesomorphic Materials," *Chem. - A Eur. J.*, vol. 25, no. 6, pp. 1369–1378, 2019, doi: 10.1002/chem.201802927.
- [178] G. Cavallo, P. Metrangolo, R. Milani, T. Pilati, A. Priimagi, G. Resnati, G. Terraneo, "The Halogen Bond," *Chem. Rev.*, vol. 116, pp. 2478–2601, 2016, doi: 10.1021/acs.chemrev.5b00484.
- [179] G. Cavallo, G. Terraneo, A. Monfredini, M. Saccone, A. Priimagi, T. Pilati, G. Resnati, P. Metrangolo, D. W. Bruce, "Superfluorinated ionic liquid crystals based on supramolecular, halogen-bonded anions," *Angew. Chemie - Int. Ed.*, vol. 55, no. 21, pp. 6300–6304, 2016, doi: 10.1002/anie.201601278.
- [180] C. Simocko, Y. Yang, T. M. Swager, K. B. Wagener, "Metathesis step-growth polymerizations in ionic liquid," *ACS Macro Lett.*, vol. 2, no. 12, pp. 1061–1064, 2013, doi: 10.1021/mz4004776.
- [181] H. Liu, H. Yu, "Ionic liquids for electrochemical energy storage devices applications," *J. Mater. Sci. Technol.*, vol. 35, no. 4, pp. 674–686, 2019, doi: 10.1016/j.jmst.2018.10.007.
- [182] A. Turguła, M. Graś, A. Gabryelczyk, G. Lota, J. Pernak, "Long-Chain Ionic Liquids Based on Monoquaternary DABCO Cations and TFSI Anions: Towards Stable Electrolytes for Electrochemical Capacitors," *Chempluschem*, vol. 85, no. 12, pp. 2679–2688, 2020, doi: 10.1002/cplu.202000680.

- [183] G. Vanhoutte, S. D. Hojniak, F. Bardé, K. Binnemans, J. Fransaera, "Fluorine-functionalized ionic liquids with high oxygen solubility," *RSC Adv.*, vol. 8, no. 9, pp. 4525–4530, 2018, doi: 10.1039/c7ra13403g.
- [184] J. M. Vincent, M. Contel, G. Pozzi, R. H. Fish, "How the Horváth paradigm, Fluorous Biphasic Catalysis, affected oxidation chemistry: Successes, challenges, and a sustainable future," *Coord. Chem. Rev.*, vol. 380, pp. 584–599, 2019, doi: 10.1016/j.ccr.2018.11.004.
- [185] M. Hummel, M. Markiewicz, S. Stolte, M. Noisternig, D. E. Braun, T. Gelbrich, U. J. Griesser, G. Partl, B. Naier, K. Wurst, B. Krüger, H. Kopacka, G. Laus, H. Huppertz, H. Schottenberger, "Phase-out-compliant fluorosurfactants: Unique methimazolium derivatives including room temperature ionic liquids," *Green Chem.*, vol. 19, no. 14, pp. 3225–3237, 2017, doi: 10.1039/c7gc00571g.
- [186] R. P. Singh, S. Manandhar, J. M. Shreeve, "New dense fluoroalkyl-substituted imidazolium ionic liquids," *Tetrahedron Lett.*, vol. 43, no. 52, pp. 9497–9499, 2002, doi: 10.1016/S0040-4039(02)02448-6.
- [187] M. Saccone, F. Fernandez Palacio, G. Cavallo, V. Dichiarante, M. Virkki, G. Terraneo, A. Priimagia, P. Metrangolo, "Photoresponsive ionic liquid crystals assembled: Via halogen bond: En route towards light-controllable ion transporters," *Faraday Discuss.*, vol. 203, pp. 407–422, 2017, doi: 10.1039/c7fd00120g.
- [188] L. C. Gilday, S. W. Robinson, T. A. Barendt, M. J. Langton, B. R. Mullaney, P. D. Beer, "Halogen Bonding in Supramolecular Chemistry," *Chem. Rev.*, vol. 115, no. 15, pp. 7118–7195, 2015, doi: 10.1021/cr500674c.

Ringraziamenti

La scrittura della tesi di dottorato segna il concludersi di un periodo complesso fatto non solo di studio e ricerca, ma di crescita sia professionale che personale. Il raggiungimento di tale obiettivo è stato sicuramente possibile grazie all'aiuto dei miei genitori che, anche nei momenti di maggiore difficoltà, mi hanno sempre supportata, al mio ragazzo, Giuseppe, che mi ha supportata e continua a farlo, alle mie amiche storiche, Laura, Alessia e Francesca, e a Maria Giulia, Paolo, Emanuele e Federico, i miei storici compagni del liceo, che tifano sempre per me.

Sono approdata nel mondo della chimica quasi per caso ormai parecchi anni fa, quando ho iniziato la laurea triennale e da allora questo mondo così complesso e articolato mi ha sempre affascinata. Spronata dalla curiosità, che mi ha sempre guidata nelle scelte, sono entrata a far parte del gruppo SupraBioNanoLab del Politecnico di Milano. Ringrazio quindi il professor Pierangelo Metrangolo e le professoressa Francesca Baldelli Bombelli e Gabriella Cavallo grazie ai quali ho potuto avviarmi lungo il percorso del dottorato di ricerca e che mi hanno guidata in questi anni. Durante questo percorso ho conosciuto nuovi amici che mi hanno aiutata nei momenti di sconforto: con piacere ricordo Isabel e Giulia che mi hanno accompagnata nei miei primi passi al Politecnico di Milano e, con loro, Andrea e Valentina che ancora adesso mi aiutano a comprendere meglio e a chiarire molti dubbi. In questi anni ho potuto anche seguire nel loro percorso di tesi magistrale alcuni ragazzi: come non citare Beatrice che ha collaborato a molti degli esperimenti presentati in questa tesi e che, a parte le sue iniziali resistenze verso la sintesi organica, ha dimostrato di essere una valida sintetista di dendroni. Vorrei poi ringraziare tutti coloro che non ho ancora citato e che, come me, sono approdati nel mondo degli alogeni in questi anni; in particolare ringrazio Alessandro, Cristina, Eleonora, Giusy, Giovanni, Lorenzo, Nazeeha, Giorgio, Christian e tutti coloro che hanno fatto parte, anche se per poco, del gruppo SBNLab coi quali continuo a condividere bei momenti e grazie ai quali il percorso di dottorato è sembrato meno impegnativo. Vorrei poi ringraziare tutti coloro che hanno collaborato alla ricerca sperimentale con le loro competenze. Un particolare ringraziamento va quindi alla professoressa Giuseppina Raffaini, al professor Gabriele Candiani e alla dottoressa Nina Bono, al professor Bertrand Donnio, al professor Nonappa, ai collaboratori dell'Istituto Besta e delle Università di Bologna e di Milano il cui contributo è stato fondamentale per comprendere meglio il comportamento dei sistemi mostrati in questa tesi. Ringrazio infine il professor Rainer Haag e la professoressa Debora Berti che hanno revisionato la mia tesi.